Ladder-Type oligo-(*p*-Phenylene)s for Hybrid Optoelectronic Devices based on Resonant Energy Transfer

D i s s e r t a t i o n

zur Erlangung des akademischen Grades
d o c t o r r e r u m n a t u r a l i u m
(Dr. rer. nat.)
im Fach Chemie

eingereicht an der
Mathematisch-Naturwissenschaftlichen Fakultät
der Humboldt-Universität zu Berlin

von
Dipl.-Chem. Björn Kobin

Präsident der Humboldt-Universität zu Berlin
Prof. Dr. Jan-Hendrik Olbertz

Dekan der Mathematisch-Naturwissenschaftlichen Fakultät
Prof. Dr. Elmar Kulke

Gutachter:
1. Prof. Stefan Hecht, Ph.D.
2. Prof. Dr. Jürgen Liebscher
3. Prof. Dr. Ullrich Scherf

Tag der mündlichen Prüfung: 17. April 2015

Die vorliegende Arbeit wurde in der Zeit von Oktober 2011 bis Februar 2015 am Institut für Chemie der Humboldt-Universität zu Berlin unter der Anleitung von Prof. Stefan Hecht, Ph.D. angefertigt.

Teile dieser Arbeit wurden bereits veröffentlicht in: / Parts of this work have already been published in:

[1] B. Kobin, L. Grubert, S. Blumstengel, F. Henneberger, S. Hecht, *J. Mater. Chem.* **2012**, *22*, 4383 - 4390.

[2] B. Kobin, L. Grubert, S. Mebs, B. Braun, S. Hecht, *Isr. J. Chem.* **2014**, *54*, 789 - 795.

[3] B. Kobin, F. Bianchi, S. Halm, J. Leistner, S. Blumstengel, F. Henneberger, S. Hecht, *Adv. Funct. Mater.* **2014**, *24*, 7717 - 7727.

[4] M. Höfner, B. Kobin, S. Hecht, F. Henneberger, *ChemPhysChem* **2014**, *15* 3805 - 3808.

[5] F. Bianchi, S. Sadofev, R. Schlesinger, B. Kobin, S. Hecht, N. Koch, F. Henneberger, S. Blumstengel, *Appl. Phys. Lett.* **2014**, *105*, 233301.

[6] R. Schlesinger, F. Bianchi, S. Blumstengel, C. Christodoulou, R. Ovsyannikov, B. Kobin, K. Moudgil, S. Barlow, S. Hecht, S. R. Marder, F. Henneberger, N. Koch: "Efficient light emission from inorganic and organic semiconductor hybrid structures by energy level tuning", *Nat. Commun.* **2015**, accepted.

Danksagung

Ich möchte mich bei Prof. Stefan Hecht, Ph.D. bedanken, dass ich meine Dissertation in seinem Arbeitskreis zu einem interdisziplinären Thema bearbeiten konnte, das sich in einem sehr interessanten und weiten Spektrum zwischen chemischer Synthese und organischer Elektronik bewegte. Gleichzeitig habe ich stets sehr gute Arbeitsbedingungen vorgefunden und es herrschte kein Mangel an Mitteln, die zur Bewältigung der gestellten Aufgaben nötig waren.
Bei dem gesamten AK Hecht möchte ich mich für die bisherigen Jahre der Zusammenarbeit bedanken, insbesondere bei Jutta Schwarz und Jana Hildebrandt, die mich bei der Synthese unterstützten, bei Sandra Behren, die sowohl in der Synthese, als auch bei der Photochemie zu dieser Arbeit beitrug, bei Dr. Lutz Grubert und Dr. Joachim Leistner, die an der Lösung diverser analytischer Fragestellungen beteiligt waren, sowie Dr. Michael Pätzel, der bei Problemen unterschiedlichster Natur der richtige Ansprechpartner war.
Weiterhin danke ich allen Kooperationspartnern, besonders Francesco Bianchi, Dr. Simon Halm, Moritz Eyer und Dr. Sylke Blumstengel aus dem Institut für Physik der HU, mit denen ich direkt zum Energietransfer und Photoabbau zusammengearbeitet habe und bei Michael Höfner, der die Zielverbindungen in Kavitäten untersuchte; sowie bei Dr. Beatrice Braun und Dr. Stefan Mebs, die etliche Kristallstrukturen der Zielverbindungen lösten.
Der deutschen Forschungsgemeinschaft danke ich für die finanzielle Unterstützung über den SFB 951, der den Rahmen für diese Arbeit vorgab.
Letztendlich bedanke ich mich bei meiner Familie, die mir die Freiheit ließ, die gewünschte Ausbildung zu erhalten und mich besonders während des Studiums auch finanziell unterstützte.

Abstract

Nowadays optoelectronic devices are ubiquitous for illumination purposes, in telecommunication and displays. For a long time, the development for these devices was driven by inorganic semiconductors, later organic semiconductors contributed, as well. Recently concepts have been developed to combine both complementary material classes to exploit the specific advantages of each one. For the hybridization, the properties of the materials, especially the electronic structure, have to match very well. In this work the optimization of ladder-type p-phenylenes towards spectral overlap and energy level alignment with ZnO, vacuum-processability, inertness, as well as layer formation is described. In terms of molecular design the different properties are addressed by site-selective functionalization of the methylene bridges with alkyl, aryl, and fluoro groups. The final products are characterized regarding their optical properties by absorption and fluorescence, their electrochemical properties, as well as their solid-state structure by single crystal X-ray diffraction. Apart from that, a large part of the work is devoted to investigations of the photochemical degradation of fluorene-type structures. New insights are gained into the mechanism of degradation, as well as the origin of the green emission in ladder-type structures The dependence of the rate of degradation is described semi-quantitatively with respect to the substitution pattern. By that, different reaction mechanisms for different substituents are found. Finally, the integration of some products in hybrid structures is discussed.

Zusammenfassung

In der heutigen Zeit sind optoelektronische Bauelemente allgegenwärtig. Sie finden Anwendung für Beleuchtungszwecke, in Anzeigen und für die Telekommunikation. Die Entwicklung dieser Anwendungen wurde lange Zeit von anorganischen Halbleitern getragen, in jüngerer Vergangenheit auch von der organischen Elektronik. Neuerdings werden verstärkt Konzepte entwickelt, um die spezifischen Vorteile der jeweiligen komplementären Materialklassen auszunutzen. Für diese Hybridisierung müssen die Eigenschaften der verschiedenen Materialien, insbesondere die elektronische Struktur, genau auf einander abgestimmt sein. In dieser Arbeit werden Leiter-para-phenylene auf spektrale Überlagerung und angepasste Orbitalenergien mit ZnO, auf chemische Inertheit und auf die Bildung von dünnen Schichten über vakuumbasierte Verarbeitungsmethoden optimiert. Dazu konzentriert sich der synthetische Gesichtspunkt auf die selektive Funktionalisierung der verschiedenen Methylenbrücken mit Alkyl-, Aryl- und Fluorsubstituenten. Die finalen Stufen werden bezüglich ihrer optischen Eigenschaften mittels Absorption und Fluoreszenz, bezüglich ihrer elektrochemischen Eigenschaften und bezüglich ihrer Festkörperstruktur mittels Röntgenstrukturanalyse von Einkristallen charakterisiert. Außerdem widmet sich ein erheblicher Teil dieser Arbeit der Erforschung des photochemischen Abbaus von fluorenbasierten Strukturen. Es werden neue Erkenntnisse zum Abbaumechanismus und der Ursache der grünen Emission gewonnen. Weiterhin werden die Abbauraten von Fluorenstrukturen mit verschiedenen Brückensubstituenten verglichen. Dabei konnten auch verschiedene Reaktionsprodukte und Mechanismen nachgewiesen werden. Letztendlich wird auch die Anwendung einzelner Derivate in Hybridstrukturen diskutiert.

Contents

List of Abbreviations

AFM atomic force microscopy

CBM conduction band minimum

CS charge separated

CT charge transfer

CV cyclic voltammetry

DABCO 1,4-diazabicyclo[2.2.2]octane

DIB dibromoisocyanuric acid

DTBP di-2,6-*tert*-butylphenol

EA electron affinity

EC electrochromic

ECL effective conjugation length

ED extinction difference

EML emissive layer

ETL electron transporting layer

FET field effect transistor

HIOS hybrid inorganic-organic systems

HOMO highest occupied molecular orbital

HTL hole transporting layer

IC internal conversion

IP ionization potential

ISC inter system crossing

ITO indium tin oxide

LED light emitting diode

LOPP ladder-type oligo(*para*-phenylene)

LPPP ladder-type poly(*para*-phenylene)

LUMO lowest unoccupied molecular orbital

MBE molecular beam epitaxy

MIS metal insulator semiconductor

MOM-Cl chloromethyl methyl ether

MOM methoxymethyl

NBS N-bromosuccinimide

NIS N-iodosuccinimide

OFET organic field effect transistor

OLED organic light emitting diode

OMBD organic molecular beam deposition

OPV organic photovoltaics

OTFT organic thin film transistor

OVPD organic vapor phase deposition

PF polyfluorene

PL photoluminescence

PPP poly-*para*-phenylene

PPV poly(*p*-phenylene vinylene)

QW quantum well

RET resonance energy transfer

TCNQ tetracyanoquinodimethane

TEBAC benzyltriethylammonium chloride

THF tetrahydrofuran

TTF tetrathiafulvalene

UHV ultra high vacuum

UPS ultraviolet photoelectron spectroscopy

VBM valence band maximum

XPS X-ray photoelectron spectroscopy

XRR X-ray reflectometry

1 Introduction

In the present-day world people are surrounded by a large variety of technical devices. In many of them light is used or produced, normally by the aid of electrical energy. For example lots of gadgets, such as mobile phones, laptops, tablets, among others, are operated via illuminated, colored displays. In addition, fiber optics are important for telecommunication and huge amounts of energy are consumed for illumination purposes. In all these examples the interaction of light and matter is the central issue. So a better understanding of the underlying processes, as well as the development of new concepts for optoelectronic devices, are key steps to construct devices with better performance, higher efficiency and enhanced sustainability. A novel concept for electroluminescence or solar energy conversion is the use of hybrid devices consisting partly of inorganic, partly of organic semiconductors, which are excitonically coupled to achieve energy transfer and exploit the specific advantages of both material classes.
In this work, the optimization of blue/UV organic emitters for the application in hybrid inorganic-organic devices employing energy transfer by dipolar coupling is described. In the following chapters, tuning of the character and energy of optical transitions, the photochemical degradation of the employed class of compounds, tuning of the frontier orbital energy levels, as well as optimization of the processability are discussed. Finally, some initial examples of application in hybrid structures are given. This chapter gives a broad overview about organic electronics, potential application of hybrid devices and the physical background thereof. Detailed introductions that relate more closely to the respective topics are given in the beginning of each chapter.

1.1 Light and Matter

There have been lots of debates over hundreds of years about the nature of light and how to explain all the effects associated with light. To give an overview about today's understanding of light, it is worth look 150 years into the past. In 1865, Maxwell's paper "A Dynamical Theory of the Electromagnetic Field" was published. One of its important outcomes is, to explain the propagation of light by electromagnetic phenomena. As a result, it was shown, that hypothetical electromagnetic waves have the properties of polarized light. They are propagating approximately with the speed of light and they are transverse waves. Although this is not a proof, it seemed reasonable to describe light in terms of electromagnetic waves.[1] However, there was no experimental proof at the time, that electromagnetic waves can propagate through space (or through luminiferous aether). The key experiments to give this proof were reported by Hertz in 1888. He showed, that electrodynamic trans-

verse waves are existing (in air) and that their velocity is comparable to the speed of light.[2]

Although Hertz could explain the emission of electromagnetic radiation by an oscillating electric dipole in terms of Maxwell's theory, some issues concerning the creation and transformation of light – or the interaction of light and matter – still remained an issue, as later mainly emphasized by Einstein.[3] One of the main problems was the black-body radiation. A black body is absorbing all incident electromagnetic radiation of any wavelength. The question to be solved was to find a function that describes the spectral energy density of the radiation emitted by a system of that kind. One of the first attempts was the Stefan-Boltzmann law, which stated that the integrated energy density is proportional to the temperature by the power of four. Wien could then proof, that the spectral energy density is given by $u(T,\nu) = \nu^3 f(T/\nu)$, in which T is the absolute temperature and ν the frequency. In order to find a proper function f, Planck employed Maxwell's laws on a charged harmonic oscillator being in equilibrium with the surrounding electromagnetic radiation, leading to

$$u(T,\nu) = \frac{8\pi\nu^2}{c^3} E(T,\nu) \quad (I).$$

Here, $E(T,\nu)$ is the mean energy of the oscillator, which can be considered to be in thermal equilibrium with the remaining particles of the system to find the Rayleigh-Jeans law

$$u(T,\nu) = \frac{8\pi\nu^2}{c^3} \frac{R}{N} T$$

(R being the gas constant and N being the Avogadro constant). However, there is one problem with these expressions: Integration over all frequencies ν would give infinite energy density for the radiation. This is also known as 'ultraviolet catastrophe'. Due to improved accuracy of the measurements, it was additionally shown that these laws are not valid for lower frequencies. Therefore Planck introduced, what now is known as Planck's law of black-body radiation:

$$u(T,\nu) = \frac{8\pi\nu^2}{c^3} \frac{b\nu}{\exp(\frac{a\nu}{T}) - 1},$$

a and b being constants. This distribution reproduced experimental data well, but at that point it was only empirical. For the theoretical description, he used (I) again and derived $E(T,\nu)$ via the entropy of the oscillator. Therefore, he used Boltzmann's statistical definition of entropy. But in order to do that, the oscillators may only release radiation energy in discrete multiples of a basic unit, although he still claimed that this has rather formal reasons than physical meaning. At that time mainly Einstein was arguing for the quantization of light. Besides the quantization of the oscillator energies and 'ultraviolet catastrophe', he found several other arguments: If Planck's law is a representation of (I), the Avogadro constant can be determined from a, b, R, and c. Indeed, the found value was relatively precise for that time. Furthermore, he claimed, that the entropy of (gas) particles in a system

behaves similar to the entropy of radiation in a system (according to Wien's law) upon volume change and that the energy of the quanta of radiation is $Ra\nu/N$ ($h\nu$ in today's notation). Furthermore he applied the hypothesis of quantization to explain photoemission with Stokes-shift and the photoelectric effect.[3, 4]

After this rather historic introduction of the beginning of today's models of light, the development of quantum theory will not be discussed further here. But some essential terms and models about the interaction of light and matter will be introduced. Nowadays, it is well accepted that light has both particle and wave character. A quantum of electromagnetic radiation is called photon and has the energy

$$E = h\nu = \frac{hc}{\lambda} \tag{1.1}$$

with h being Planck's constant, c the speed of light and λ the wavelength.[1] If a photon interacts with an electron, the photon may be absorbed and an electronic transition may occur. The probability of electronic transition may be described with the Einstein coefficients. Assuming a two-level system described by the wave functions Ψ_1 and Ψ_2 and the corresponding energy levels E_1 and E_2 ($E_1 < E_2$), three processes can occur: Absorption, stimulated emission and spontaneous emission, which are characterized by the Einstein coefficients B_{12}, B_{21}, and A_{21}, respectively. The rate of absorption is is proportional to the product of B_{12} and the energy density $\rho(\nu)$ of the electromagnetic radiation. The Einstein coefficient can be calculated as

$$B_{12} = \frac{2\pi}{3\hbar}|\langle\Psi_1|\mathrm{M}|\Psi_2\rangle|^2 \tag{1.2}$$

with M being the dipole moment operator, $\langle\Psi_1|\mathrm{M}|\Psi_2\rangle$ is the transition dipole moment and $\hbar = h/2\pi$. From B_{12} the oscillator strength f can be calculated as follows (m_e is the electron mass and e the elementary charge):

$$f = \frac{m_e h\nu}{\pi e^2} B_{12} \tag{1.3}$$

This relation closes the gap between theory and experiment, since f is proportional to the integral of the absorption band. If the system is in thermal equilibrium, it can further be shown by employing Planck's radiation law and Boltzmann's law concerning the population of the states, that $B_{21} = B_{12}$, and

$$A_{21} = \frac{8\pi h\nu^3}{c^3} B_{21}. \tag{1.4}$$

This implies on the one hand, that also the rate of emission is proportional to the oscillator strength, and, on the other hand that under 'typical' experimental (relatively low radiation density) conditions, emission in the UV/visible region is dominated by spontaneous emission.[5, 6]

At this point, the focus will shift to matter and the processes mediating its interaction with light. Once a photon is absorbed, it can create an exciton in the

[1] In contrast to the equations above, from here on a modern notation is used.

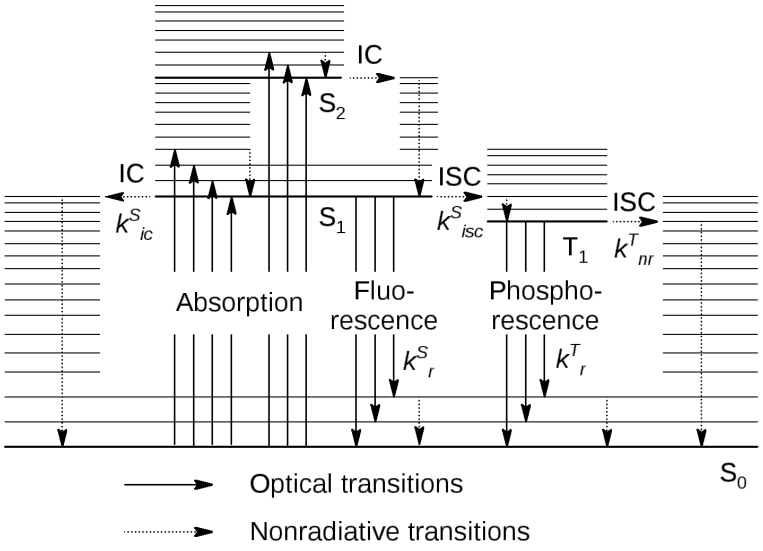

Figure 1.1. Jablonski diagram representing the processes of absorption, emission and some nonradiative transitions and the corresponding rate constants. IC: internal conversion, ISC: inter system crossing, S_0: electronic ground state, S_1, S_2: lowest and second excited singlet state, T_1 lowest triplet state.

material. An exciton is a quasiparticle, consisting of a bound electron hole pair, which can move though the material. There are two limiting cases to describe the exciton. The first one is the Wannier-Mott exciton. It is the typical case for inorganic semiconductors. Due to the large dielectric constant of the material, the Coulomb interaction between electron and hole is weak. Thus the binding energy is low and the binding radius is large. Since at room temperature the binding energy is typically smaller than k_bT, electron and hole dissociate fast and form free charge carriers. The other case is the Frenkel exciton, which is mainly found in organic materials. Here, the dielectric constant is much smaller and the Coulomb interaction is stronger. The binding radius is smaller and the exciton binding energy is normally much larger than k_bT.[7]

If a molecule is in the electronically excited state, there is a number of processes that can occur. Some are depicted in Figure 1.1 (photoreactions, electron transfer processes and intermolecular processes are omitted here). Absorption of a photon proceeds in about 10^{-15} s from the lowest vibrational state S_0 (the thermal energy at room temperature is normally too low to excite molecular vibrations) to vibrationally excited S_1 and higher electronic states according to the Franck-Condon principle. This gives rise to the characteristic shape of absorption spectra, for example different intensities of different vibronic peaks, if they are resolved. From there, vibrational relaxation to the lowest vibrational level of the electronically excited states happens quickly. From S_2 to S_1 or from higher excited states, internal conversion (IC) is efficient, which is a non-radiative transition between two electronic states. From S_1 to S_0 IC is normally less efficient because of the larger energy gap. Hence, typically molecules relax to the vibrational level 0 of S_1 and from that point other processes can compete with IC. One of these processes is fluorescence, which is a radiative

transition between states of the same spin. Although the 0-0 transition of absorption and fluorescence is the same, according to the the Jablonski diagram, the emission is redshifted because to relaxation/reorganisation in the excited state. According the the Franck-Condon principle, fluorescence does also populate vibrationally excited states of S_0. The energy difference between the maximum of the first absorption band and the maximum of the fluorescence spectrum is called Stokes shift. Furthermore, inter system crossing (ISC) can occur from S_1, populating the triplet T_1. The radiative transition between T_1 (or other states with a spin different from S_0) and S_0 is called phosphorescence. In solution at room temperature, phosphorescence can usually not compete with further ISC and non-radiative relaxation. As depicted in figure 1.1, all the processes described above are associated with rate constants k. The rate constants for the non-radiative de-excitaion of S_1 can be combined as follows:

$$k_{nr}^S = k_{ic}^S + k_{isc}^S \tag{1.5}$$

For spontaneous emission, the evolution of the concentration of excited molecules $[^1A^*]$ from the initial concentration $[^1A^*]_0$ follows an exponential decay:

$$[^1A^*] = [^1A^*]_0 \cdot e^{-\frac{t}{\tau_s}} \tag{1.6}$$

The excited state lifetime τ_S (of S_1) can be calculated from the radiative and non-radiative rate constants:

$$\tau_S = \frac{1}{k_r^S + k_{nr}^S} \tag{1.7}$$

From these numbers, the fluorescence quantum yield Φ_F can be determined by:

$$\Phi_F = k_r^S \tau_S = \frac{\tau_S}{\tau_r} \tag{1.8}$$

with τ_r being the radiative lifetime.[5]

1.2 Organic Electronics

Any electronic device has an inherent demand for charge transport by conductive materials. Initially, this was accomplished by metals or inorganic semiconductors. On the contrary, organic materials are typically employed as insulating materials. Of course, this is related to the fact, that most organic materials are indeed insulators and the processability of plastics is better than that of ceramic insulators. But this perspective changed dramatically with the discovery of conducting polymers. The first famous example is poly-acetylene[2]. When thin films of poly-acetylene were first treated with ammonia to eliminate defect-related conductivity and were afterwards doped with electron acceptors, such as halogens or AsF_5 an increase in conductivity of 11 orders of magnitude was achieved. Upon increasing the amount of dopant, an insulator-to-metal transition was observed. Later it was also shown, that high conductivity can also be achieved with the electron donating dopant sodium naphthalide and that the conductivity of those materials is electronic.[8–10] Although the ability for charge transport is essential, the important application of semiconductors is located in active devices to modulate conductivity or to absorb or emit light.
From that point onwards, many promises have been made about future devices and applications of organic electronics. But one should keep in mind, that the primary aim of research in this field in not to replace inorganic semiconductors in their established applications. Instead, it is an objective to find new or alternative applications based on the specific advantages of organic electronics, which rather stand out for low-end products. For example many products of consumer electronics have a short life cycle today. So there is no need for long lasting devices, but demands for low-cost fabrication in large scale are rising. Especially the issue of abundant raw materials and simple strategies for disposal speak for that material class. Organic electronic devices can be produced in thin film on plastic foil from hydrocarbon materials. On the one hand, the amount of spent material is small in that case, on the other hand, most hydrocarbon materials do not exhaust scarce resources. Furthermore, the materials can be processed at low temperature from solution, which reduces both costs and energy consumption compared classical semiconductors. Related to the materials and processing techniques, it is possible to produce flexible large area devices for photovoltaics or illumination, which might even be applied as a coating of products. Based on the specific advantages of organic semiconductors, three typical basic devices are very common: cells for organic photovoltaics (OPV), the organic field effect transistor (OFET) (resp. organic thin film transistor (OTFT)s), and the organic light emitting diode (OLED). Deduced from the latter two, thin film displays up to the size of a TV screen are being produced and commercially available.[11–16]

[2]The development of conductive polymers by Alan J. Heeger, Alan G. MacDiarmid, and Hideki Shirakawa was rewarded with the Nobel price in chemistry 2000. See: "The Nobel Prize in Chemistry 2000". Nobelprize.org. Nobel Media AB 2014. Web. 17 Dec 2014. `http://www.nobelprize.org/nobel_prizes/chemistry/laureates/2000/`

1.2.1 Introduction to (Inorganic) Semiconductors

Commonly, inorganic semiconductors are crystalline materials, thus the basic theories describing them are also related to an ordered, crystalline state. In the ideal case, they are treated as an infinite periodic lattice. The electronic structure of semiconductors is described by energy bands. Two of the most common models about the formation of energy bands are the nearly free electron model and the tight binding model. The first one expands the established model of the uniform electron gas, which gives a parabolic potential in the momentum space (energy E vs. wave vector $\vec{k}$), and adds a periodic potential in real space, representing the atomic nuclei in a lattice. The perturbation of the electrons by the periodic potential leads to energy discontinuities, which are known as band gaps. The tight-binding model considers atomic orbitals and the overlap to the nearest neighbors. Solutions are periodic curves in E vs. $\vec{k}$ that depend on the properties of the atomic orbital, the lattice constant and the strength of the interaction. In real semiconductors, the minimum of the conduction band may have the same position in k-space as the valence band maximum, giving a direct band gap and a direct semiconductor. If this is not the case, the material has an indirect band gap.[17]

Semiconductors are categorized in intrinsic and extrinsic semiconductors. Intrinsic semiconductors possess latent charge carriers (i. e. electrons from the valence band), which can be excited by thermal energy to generate free charge carriers. The density of electrons in the conduction band (and of holes in the valence band, respectively) can be calculated from the product of the density of states in the bands and the Fermi-function, which gives the energy distribution of electrons and holes. Extrinsic semiconductors are generated by the introduction of small amounts of electron donors or acceptors into the material. This creates some density of states in the band gap. Either donor levels are introduced slightly below the conduction band (n-type materials) or acceptor levels slightly above the valence band (p-type). The density of charge carriers can again be calculated from the product of density of states and a modified Fermi-function. From that, the conductivity σ of the semiconductor can be calculated, which is a product of (free) charge carrier density, charge carrier mobility μ and elementary charge. The charge carrier mobility is defined as the quotient of the drift velocity and the electric field $\mu = v_d/E$ and it is proportional to the relaxation time τ, which is a decay constant for the decay of current, after an electric field is removed. There are two main reasons for the decay, which are thermal motion of the lattice atoms and impurities of the material.[18]

The optical properties of semiconductors are governed by several different mechanisms for absorption and emission. In the case of fundamental absorption, an electron is directly excited from the valence band to the conduction band. In semiconductors with a direct gap this occurs without a change of the momentum of the electron. For indirect gap absorption, an additional phonon has to be absorbed or emitted, to ensure momentum conservation. In the first case onset of absorption with increasing energy is steeper than for the latter case. Examples for additional mechanisms of absorption are exciton absorption (electron and hole do not dissociate), free carrier absorption (electrons or holes absorb energy within their band),

interband absorption (transitions between two conduction or valence bands), or absorption at impurity centers (defects). Emission of light occurs due to radiative recombination of an electron and a hole. The rate of this process is approximately proportional to the densities of electrons and holes and the absorption coefficient. Accordingly, direct gap materials can also be efficient emitters, indirect materials, such as silicon, are rather not emissive. However, in some cases impurities acting as recombination centers can lead to emissive recombination.[19]

1.2.2 Materials and Processing Techniques

Organic semiconductors are carbon based π-conjugated materials. Depending on the application they are optimized for a certain function, for example transport of charge carriers, emission or absorption of light. The band gap (or the distance from the highest occupied molecular orbital (HOMO) to lowest unoccupied molecular orbital (LUMO)), the absorption coefficient, the photoluminescence (PL) quantum yield or the charge carrier mobility are important parameters for applicability. But also the absolute position of the bands or energy levels plays an important role concerning charge or energy transfer at the interfaces of different materials. From the practical point of view, the materials are separated into two classes: Low molecular weight materials and polymers. While the low molecular weight materials can in principle both be processed from the gas phase and solution, polymers can only be processed from solution.

For thin film growth of small molecules on surfaces from the gas phase, organic molecular beam deposition (OMBD) and organic vapor phase deposition (OVPD) are the most prominent techniques. OMBD is carried out in ultra high vacuum (UHV) to ensure sufficiently low evaporation temperatures and long mean free path. The molecules are evaporated from evaporation cells, which are heated to temperatures of up to 400 °C, depending on the thermal stability and vapor pressure of the molecules. Typically the evaporation temperature is also kept below the melting temperature of the organic compounds. In OVPD the source material is evaporated into a stream of inert carrier gas, which is widened towards the substrate. The pressure of the carrier gas is kept slightly below 1 mbar. All the parts of the apparatus, that are in contact with the stream of gas need to be heated to prevent the molecules from deposition on the walls. The substrate is cooled. The flow of the molecules can be regulated by the gas flow, furthermore precise mixing of different compounds is possible. The main advantage in comparison to OMBD are the ability to coat large areas homogeneously and that a large fraction of the source molecules is deposited to the substrate.[20]

Solution based processing covers a large variety of techniques ranging from very simple laboratory scale methods such as drop casting or spin coating to industrially applied large-area coating and printing techniques. This section will not give an overview about all different techniques, but some examples for state-of-the-art technology. For fast, large area coatings on flexible substrates, roll-to-roll processing

is desirable. There is a certain number of coating techniques that are employed in roll-to-roll processing or are at least compatible. The techniques for one-dimensional large area coatings are slot-die coating, knife-coating, and spray coating. In knife-coating the ink is supplied in front of a knife, which is placed very close to the substrate. As the substrate is moved, a homogeneous film is formed behind the knife. Slot-die coating works quite similar, but here the ink is pumped through a slot. This gives more control of the process. In spray coating the ink is, optionally supported by pressurized gas, sprayed though nozzles onto the moving substrate.
Printing techniques, which are commonly used are gravure printing, flexographic printing, screen printing, and inkjet printing. While for the first three techniques physical printing forms need to be manufactured, for inkjet printing this is not the case. Patterning is achieved by the use of pixels. A droplet of ink is deposited on each pixel or not, which is referred to as drop-on-demand. The droplets are produced in a nozzle with a piezo actuator. Although the technique is very adaptive in terms of changing the pattern, the formulation of the ink is relatively demanding. In screen printing the ink is forced through a pre-patterned grid, which may either be done step-wise in flat screen printing or continuously in rotary screen printing. In flexographic printing the ink is transferred from the higher areas of the soft printing cylinder to the substrate, similar to stamping. Gravure printing is used for high processing speed and high output. Here, the ink is transferred from cavities of the printing cylinder to the substrate.
For the production of OPV devices, slot-die coating is commonly employed in roll-to-roll processing, but also screen printing and flexographic printing. For OTFTs gravure, inkjet and screen printing have been employed, but mainly not in roll-to-roll processing. OLEDs and electrochromic (EC) devices have been produced by all the above mentioned techniques, but in most of the cases not in roll-to-roll.[21]
The method of processing is also strongly connected to materials, which are used for the fabrication of a device. This is not only related to the solubility of a material in the processing solvent, but the processing has an impact on the morphology of the layers in a device. For example the material can be crystalline or amorphous, or semi-crystalline, there might be mixing or de-mixing phenomena. Since the morphology determines the solid state properties, the techniques and conditions of material processing may influence the performance of a device as much as the intrinsic properties of the chemical species.[22, 23]

Small molecules for semiconductor devices, theoretically promise better purity and higher quality (single) crystalline materials. However, from a practical point of view, which involves processing to commercial devices, the development is behind that of polymeric materials. The morphology problem (i. e. the dependence of the material's electronic properties on the processing) is more serious for small molecule semiconductors. The electronic structure of the material is governed by the one of the single molecule, most importantly by the frontier energy levels, the π and π^* level. When the molecules are oriented in a periodic lattice and and the π orbitals are overlapping to some extent, a band structure can be formed with a conduction band originating from the LUMO and a valence band originating from the HOMO. The energy dispersion is of course strongly dependent on the crystal structure. For

single component crystals this behavior can for example be observed at planar aromatic molecules with few or no side groups, such as pentacene. Another strategy to form conducting materials, is the co-crystallization of organic donors and acceptors to form charge transfer complexes. This approach can give materials with metallic behavior and high conductivity, as shown for tetracyanoquinodimethane (TCNQ) and tetrathiafulvalene (TTF), for example. Due to their transport properties, small molecules have been applied in OFETs, but their application as emitter in electroluminescent devices or absorbing material in OPV devices is more common. [24] The variety of materials is huge and will not be discussed, here. For some examples of monomer aromatic systems and aryl, alkenyl, alkynyl and mixed oligomers see e.g.[25].

When differentiating between small molecules and conjugated polymers there is one characteristic feature about polymers: they are normally – via covalent bonding – one dimensional periodic systems consisting of numerous repetitions of the monomer unit. This could in theory enforce a band structure. However, in terms of 3D structure, conjugated polymers do not form a perfect lattice. Normally, the structures are to some extent kinked, twisted or bent and double bonds are partly localized. This gives rise to finite conjugation and therefore to extended molecular orbitals instead of real bands. Even in structurally perfect polymers, there is a limited extend of conjugation. This behavior can be studied regarding the optical or electronic properties upon increasing oligomer size. When the optical gap $E(n)$ (n being the number of repeat units) is plotted against the inverse number of repeat units, there is a nearly linear relationship for a small number of repeat units. For larger systems the optical gap is converging to a certain value. The actual behavior of the optical gap can better be described using a converging e-function:

$$E(n) = E_\infty + (E_1 - E_\infty) \cdot e^{-a(n-1)} \tag{1.9}$$

E_∞ is the optical gap for a polymer of infinite length, and E_1 for the monomer. The parameter a is a measure of, how fast the optical gap converges and $\Delta E = E_1 - E_\infty$ is a measure for the effect of conjugation, which depend on the particular polymer. From that, the effective conjugation length (ECL) can be defined, which is reached, when n is sufficiently large, so that E_∞ is nearly approached.[26]
In general, polymers are preferred for solution based processing techniques, since they tend to form thin films easily. This relates to their ability of glass formation and thus easier control over the morphology is reached, although crystalline domains may also be wanted on polymeric materials. If the glass transition temperature is sufficiently high, the thin film morphology is also expected to be stable. The variety of conjugated polymers is at least as high as for small molecule semiconductors. Apart from poly-acetylene, which lacks processability, some prominent examples are poly-*para*-phenylene (PPP) derivatives (including polyfluorenes and ladder-type poly(*para*-phenylene) (LPPP)), poly-*para*-phenylene-vinylene, polythiophenes, polypyrroles, numerous co-polymers etc. For some examples, see [27–29].

1.2.3 Devices

In this section, some devices commonly made from organic semiconductors are introduced, concerning their device structure, physical principles of operation and their requirements for the materials. The three device types presented here are OFETs, OPV devices, and OLEDs.

1.2.3.1 Organic Field Effect Transistors

The first solid-state OFET was reported by A. Tsumura, H. Koezuka, and T. Ando in 1986. It consisted of gold electrodes (source and drain), a SiO_2 insulation layer and polythiophene, which was prepared electrochemically from bithiohene, as semiconductor.[30]
The typical design of OFETs is that of a metal insulator semiconductor (MIS) field effect transistor (FET) (see figure 1.2). The semiconducting layer is situated between two metal electrodes. This part of the structure is isolated from the metal gate electrode by a thin layer of a dielectric. In combination with a support material, there are several different possible arrangements for these components.
When a voltage is applied between the semiconductor and the gate electrode, charges are generated at the interface of the semiconductor and the dielectric. By varying the voltage, the number of charge carriers and thereby the conductivity between source and drain can be adjusted. Conventional silicon FETs are operated in the inversion mode. By differently doped areas, there is for example a p-n-p junction between the source and drain contacts, by applying an electric field, the n-region gets inverted near the dielectric and the device becomes conductive. OFETs are normally operated in the accumulation mode with intrinsic semiconductors. This means, that positive charge carriers are accumulated at the interface of the semiconductor to the dielectric and form a conducting channel, when a negative voltage is applied to the gate, or the other way around. An important parameter characterizing FETs is the transconductance g_m which is defined as

$$g_m = \frac{\partial I_D}{\partial V_{GS}} \text{ with } V_{DS} = const. \tag{1.10}$$

It characterizes the response of the device on changing the gate-source voltage V_{GS} with I_D being the drain current and V_{DS} being the drain-source voltage. The transconductance can also be calculated from the charge carrier mobility of the semiconductor, the device dimensions, V_{DS} and the gate dielectric capacitance.[23, 31]

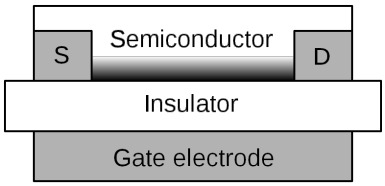

Figure 1.2. Schematic structure of a MISFET. S: source electrode, D: drain electrode, highlighted area in semiconductor: accumulation zone at $V_{DS} = 0$.

1.2.3.2 Organic Photovoltaics

There are several different concepts about including organic materials as active components in solar cells. Here, the main focus will be on all-organic solid state devices with a p-n heterojunction. Before discussing the different device types and their specific advantages, the processes (see figure 1.3) taking place during device operation will be discussed. The first process is the absorption of a photon ((A) in figure 1.3).In this context it is one of the advantages of organic π-conjugated materials compared to inorganic semiconductors, that their absorption bands are intense and broad, and they can be tuned relatively easy to match the solar spectrum. After absorption of a photon, the system relaxes thermally to a minimum of the first exited state and an exciton is formed. In contrast to inorganic semiconductors the exciton-binding energy is relatively high and thus at room temperature no free charge carriers are formed. In the next step the excitons need to move to the donor-acceptor interface to dissociate before they decay ((B) in figure 1.3.). Since excitons are not charged, they are not affected by an electric field. Thus they diffuse by random hopping via Förster or Dexter type coupling. Important factors governing the efficiency of this process are the exciton diffusion length and the lifetime of the exciton. Once

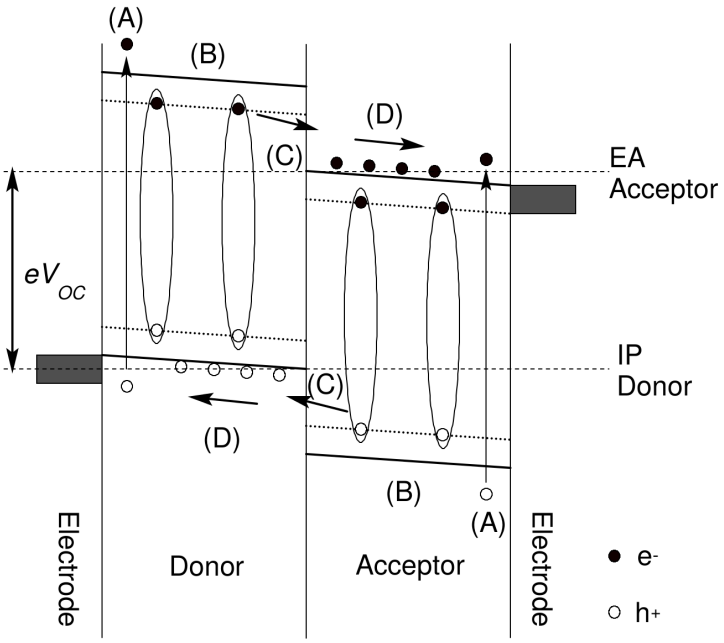

Figure 1.3. Energy level diagram for an organic donor-acceptor solar cell with heterojunction displaying the basic physical processes of operation of the device. (A) Absorption of a photon and creation of an electron hole pair followed by thermal relaxation and formation of an exciton with the energy of the optical gap (denoted by the ellipses), (B) diffusion of the excitons to the donor-acceptor interface, (C) exciton dissociation, electrons (e^-) remain in the acceptor LUMO and holes (h^+) in the donor HOMO, (D) transport of the charges to the electrodes. V_{OC}: open circuit voltage, EA: electron affinity, IP: ionization potential.

an exciton reaches the donor-acceptor interface, it can dissociate into free charge carriers if its energy is higher than that of the final state ((C) in figure 1.3).
Although the charge separation at the interface is not yet fully understood, there are some important states and processes to be mentioned. When one of the charge carriers crosses the interface, the electron is situated at the LUMO of the acceptor and the hole is at the HOMO of the donor, but they are still bound by Coulomb forces. This is referred to as the charge transfer (CT) state, which has excess thermal energy. Depending on the rate constants, this state can dissociate to the charge separated (CS) state or relax thermally to the lowest CT state, which is also lower than the CS state. This state can either be dissociated or it can be deactivated by charge recombination, which is a loss channel. Finally, the free charges can drift to the electrodes ((D) in figure 1.3). This can be understood by radical ions hopping from site to site.
The performance of a solar cell can be described by a number of parameters. The first one is the open circuit voltage V_{OC}, which is related to the difference between the electron affinity (EA) of the acceptor and the ionization potential (IP) of the donor. The short circuit current density J_{SC} is the maximum current per unit area under standardized illumination conditions. V_{max} and J_{max} are the voltage and current density of maximum output power of the cell. The power conversion efficiency η is given by

$$\eta = \frac{V_{max} J_{max}}{P_{inc}} = \mathrm{FF} \frac{V_{OC} J_{SC}}{P_{inc}}. \tag{1.11}$$

P_{inc} is the incident power density and the fill factor FF is the fraction of actual power output $V_{max} \cdot J_{max}$ related to the hypothetical power output at rectangular current-voltage characteristics $V_{OC} \cdot J_{SC}$.

The device structure of solid sate OPV usually consists of a transparent glass or plastic substrate, a transparent conducting electrode, for example indium tin oxide (ITO), some organic layers and metal back electrodes. In figure 1.4 a) a two-layer device with planar heterojunction is shown. In these devices, the thickness of the organic layer plays a crucial role. On the one hand, it should be sufficiently thick to absorb the majority of the incident light, on the other hand the thickness of the layers is limited by the exciton diffusion length, because in thick layers losses via recombination of excitons are significant. For most organic materials this issue is not

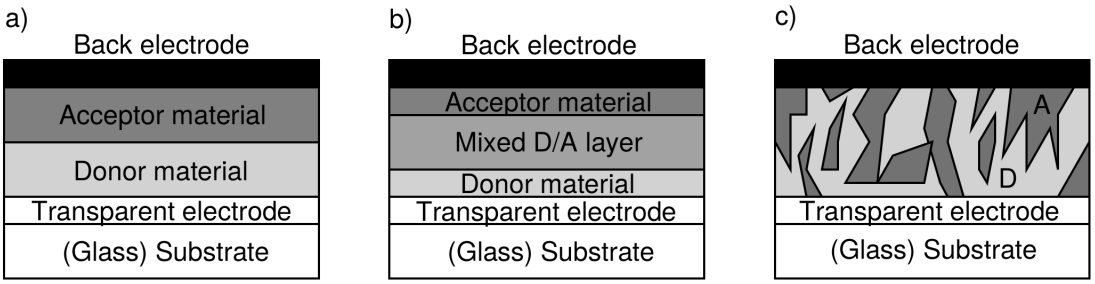

Figure 1.4. Typical device structures of OPV cells. a) Planar heterojunction, b) mixed donor-acceptor layer, c) bulk heterojunction.

solved sufficiently well for this devices type. To overcome the issue, devices with a non-planar heterojunction were developed. Donor and acceptor material are mixed, forming an interpenetrating phase-separated network. Thereby the average distance to the donor-acceptor interface is independent of the thickness of the organic layer. The fabrication can be carried out by co-deposition, leading to mixed interlayer devices (figure 1.4 b) or bulk heterojunction devices (figure 1.4 c). However, for these devices the extraction of charge carriers may become a problem.[32]

A concept to overcome some limitations of the above mentioned device types is the employment of organic tandem- or multijunction solar cells. Tandem cells consist of a stack of two or more planar heterojunction cells that are usually connected in series via a recombination zone. In that way, not only more light can be absorbed, as compared to a device with a single organic layer, but also high-energy photons can be converted more efficiently by the use of materials with a wider band gap. Due to the series connection, the output voltage of the device is higher and the current lower, which reduces resistive losses. However, the subcells must match very well in terms of absorption and output current, which requires very precise manufacturing of the different layers.[33]
A very different concept from the above mentioned examples are dye-sensitized solar cells, which became well-known with a paper by Grätzel.[34] The so-called Grätzel cells can be considered as hybrid devices. TiO_2 nanostructures are coated with a dye. Upon absorption of a photon, the dye transfers an electron to the inorganic material, which is responsible for the charge transport. The oxidized dye gets re-reduced by an electrolyte in solution. In later designs, the electrolyte solution was replaced by polymeric organic hole transporting materials to fabricate all-solid state devices.[35, 36]

1.2.3.3 Light Emitting Devices

Inorganic LEDs The usage of light to generate electricity was described in the prior section. When the process is reverted, light can be generated, which is known as electroluminescence. The most prominent electroluminescent device is the light emitting diode (LED). In a very simple case a LED consists of a p-n-junction, just like a normal diode. Applying an appropriate voltage results in a current through the device, giving rise to recombination of holes and electrons in the vicinity of the p-n-junction. If this recombination is radiative to some extent, the device can emit light. Of course the efficiency of emission and the wavelength of the emitted light is dependent on the material. Normally, there is an active layer of a (slightly) different material between the p and n semiconductors to enhance the efficiency of radiative recombination and to confine the emission of light. Most commonly, III-V semiconductors, but also II-VI and IV-materials are used. States within the band gap can be introduced by doping, which can be used for color tuning But more importantly, these defects act as recombination centers leading to higher rates for radiative recombination in materials with an indirect band gap.[37]

1st Generation OLED: Singlet Emitter Concerning the basic principle of operation, OLEDs do not differ very much from LEDs. The most important issue is to find an active material with a high luminescence efficiency, and to properly inject both types of charge carriers into that material. But as pointed out above, the properties of inorganic and organic semiconductors are quite different, which is also expressed in the design of the device. Especially the emission of light in most inorganic LEDs is confined to a small spot, in contrast, OLED devices emit over a larger area.

While the emission properties of many organic semiconductors are favorable, charge transport and especially the injection of charge carriers accompanied by unreasonably high driving voltages remained a serious problem for a long time. The first example of an OLED with a high brightness at a relatively low operating voltage was presented by Tang and VanSlyke in 1987.[38] They employed tris(8-hydroxyquinolinato)aluminium as emissive layer (EML) and a bis(triarylamine) as hole transporting layer (HTL) between a low-work function metal cathode and an ITO anode (for comparison see figure 1.5 a). The device was fabricated by vacuum deposition techniques and emitted green light for several tens of hours of operation.[38] In an early example for a polymeric OLED, poly(*p*-phenylene vinylene) (PPV), of which a precursor can be deposited from solution, was used as EML. But without electron transporting layer (ETL) or HTL, the operating voltage was still quite high and the efficiency relatively low.[39] Furthermore, the fabrication of an OLED on a flexible substrate (polyethylene terephthalate) was achieved, using a soluble derivative of PPV as EML and polyaniline as HTL.[40]

As already stated before, the efficiency of an OLED is on the one hand dependent on the emission properties of the EML and the further light output of the device, and on the other hand on an efficient and balanced injection of charge carriers into the EML. The latter condition is strongly affected by the properties of the interfaces between the different materials. In the simplest case an OLED consists of an EML which is in contact to a high work function anode and a low work function metal cathode (this structure is similar to figure 1.5 without ETL and HTL). The organic

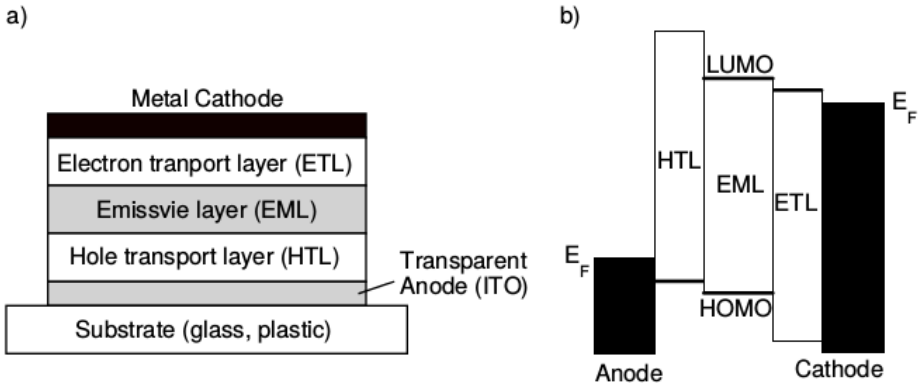

Figure 1.5. Schematic representation of an OLED. a) Device structure showing the different layers, b) Energy level diagram at flat-band conditions (E_F: Fermi energy).

semiconductor in the EML is intrinsic, thus the charge carrier density is low, which results in a relatively large depletion depth. Usually, the depletion depth is larger than the thickness of the material. Thus, the electronic structure of the bulk organic semiconductor can be described in terms of the rigid band model, which means that the built-in electric field causes a uniform slope in the energy of the states. At zero bias the Fermi levels of cathode and anode are equal and the energy of the states of the EML are highest at the anode and decrease linearly towards the cathode. If a bias is applied, this slope in energy gets less steep. At a certain value the flat-band condition is reached (see figure 1.5 b) and charge carrier injection can occur. When the bias is increased further, the slope is reverted and triangular barriers are formed. With increasing bias or increasing electric field, the thickness of the barrier decreases. Charge carriers can tunnel through these barriers by Fowler-Nordheim field emission tunneling. The tunnel current is strongly dependent on the electric field, which causes the necessity of very thin and even films. The tunnel current is also affected by the barrier height, for low operating voltages, the barriers should be kept as low as possible. For optimal operating conditions of the device, both the anode and the cathode material should match the energy levels of the material of the EML equally and very well. If this is not case, injection of one type of charge carriers can be much more efficient than the other type, which would lead to a current of majority charge carriers crossing the EML without recombination. This problem can be encountered by the introduction of ETL (or hole blocking layers) and HTL (or electron blocking layers, see figure 1.5). When the flow of majority carriers is blocked at the interface of two materials, the electric field at the electrode for the minority carriers increases, which leads to enhanced injection of minority carriers. Furthermore the introduction of additional layers reduces the heights of the barriers.[41–43]

2nd Generation OLED: Triplet Emitter In the above mentioned examples only singlet emitters were used in the EML, but electron spin was not considered, yet. When electron and hole, both having a spin of $\pm\frac{1}{2}$, approach and form a bound exciton in the EML, there are four possibilities to combine the spins, three of them being a triplet. Accordingly, the statistical probability of triplet formation is 75%. Therefore, in devices made solely from singlet emitters, at least 75% of the excitons are converted to heat, the maximum efficiency of electron-to-photon conversion is 25%. To achieve higher efficiency, triplet emitters were employed in OLEDs. Usually, the $T_1 \rightarrow S_0$ transition is strictly spin forbidden and thus very slow, leading to non-radiative de-excitation. However, some transition metal complexes (for example complexes of Ir, Ru, and Pt) exhibit relatively strong spin-orbit coupling and therefore singlet character is mixed into the triplet states. Especially metal-to-ligand charge transfer states ($d\pi^*$) are involved. In the end, radiative lifetimes down to 1 μs can be reached for phosphorescence, which can compete with non-radiative processes to give a high luminescence quantum yield. The device structure of phosphorescent OLEDs is quite similar to the ones described above, but the EML does not consist of pure triplet emitter. Triplet emitters need to be specially separated to suppress non-radiative de-excitation pathways, such as triplet-triplet annihilation. Therefore they are applied as dopands in a host matrix. In such a system there

are three ways to excite the emitter in the matrix. If the energies of the electronic states are situated in the band gap of the host material, the emitter can be excited directly by trapping of charge carriers. Secondly triplet excitons that were already formed in the host material can be transferred to the emitter by Dexter transfer. In that case it is important to chose a host material which a (optical) band gap, that is sufficiently high, since the lowest triplet energy of a conjugated polymer can be below the lowest excited singlet by up to 1 eV. Finally singlet excitons can be transferred to the emitter by Förster transfer. The triplet emitters are also known to have very high ISC rates. So the formation of a triplet followed by phosphorescence is more likely than direct fluorescent emission.[44, 45]

1.3 Hybrid Optoelectronic Devices

The term 'hybrid' is oftentimes used nowadays to describe materials or devices, that consist of very different classes of substances. Here, the combination of organic and inorganic semiconductors is named hybrid. By this, all the above mentioned devices may be called hybrid. But there is one additional point: In the following the focus will be on devices that transfer energy, or more precisely, excitons between the different types of materials in order to generate their function. First, some physical background will be given on the different regimes and mechanisms of excitonic coupling. Afterwards some examples from the literature will be given to lead to the hybrid inorganic-organic systems (HIOS) project, which surrounds this work. One of the main goals of this project is, to combine the advantages of the different materials to increase the performance and efficiency of opto-electronic devices.

1.3.1 Regimes of Coupling

In a system of two molecules of which the donor D^* is excited and the acceptor A is in the ground state[3], there are several ways of exciton transfer. If the system is not coupled, because the distance of the molecules is in the order of the optical wavelength or larger, the donor relaxes by the emission of a photon which then can be absorbed by the acceptor. For this type of energy transfer, some spectral overlap between the donor emission and acceptor absorption is needed. Typically, a decrease in intensity of the donor emission is observed in the region of spectral overlap, while the decay time remains unchanged.
For non-radiative energy transfer, spectral overlap of the donor emission and the acceptor absorption is a primary requirement, as well. The participating transitions have to be strictly of the same energy or in resonance. Therefore, the non-radiative energy transfer is also termed resonance energy transfer (RET). The two parts of the system have to interact. The strength of that coupling can be expressed as an energy which is related to the perturbation of the uncoupled system by the coupling. This interaction has Coulombic and exchange contributions. The Coulombic interactions have a relatively long range and can be described in Förster's model for dipol-dipol interactions. For shorter ranges models including mono- and multipolar interactions are better suited. The exchange contribution is related to Dexter's mechanism of RET. Since the wave functions of the involved states of donor and acceptor have to overlap for exchange energy transfer, these contribution is only significant for short ranges and if Förster-type transfer is forbidden. Non-radiative energy transfer is evidenced, when the excited state lifetime of the donor is reduced, while the spectral shape is preserved.
Depending on the energy of the interaction, three regimes of coupling can be differentiated: the strong coupling regime, weak coupling and very weak coupling. Here, only the first and the latter one are discussed.[4] Since weak coupling relates to the

[3] Exciton or energy transfer can also take place between the same type of molecules. The factors that govern the efficiency of the process are similar to the D-A case, but some characteristic observations related to energy transfer are different.

[4] In the literature sometimes only strong and weak coupling is differentiated, but then the meaning of 'weak' is what here is referred to as very weak coupling. For comparison see ref. [46]

typical electronic structure of larger organic molecules or π-systems. In the case of strong coupling or coherent coupling the coupling strength is larger than the energy offset between the donor and acceptor transitions and also larger than the corresponding bandwidth or linewidth of the spectrum. As a result the absorption spectrum of the coupled system is different from that of its parts: Two new absorption bands have formed, that are split by the twofold coupling energy corresponding to the in-phase and out-of-phase components. The energy transfer time is extremely short (shorter than vibrational relaxation, for example) and the exciton is truly delocalized over both parts of the system. Within the dipole approximation, the energy transfer rate is inversely proportional to the distance of the two parts by the power of three. In the case of very weak coupling, the interaction energy is smaller than the energetic separation of donor and acceptor and the spectral bandwidth and the absorption spectrum is not altered. The transfer time is generally longer than vibrational relaxation, so that energy transfer takes place from the lowest vibrational level of the first excited state. The transfer rate is proportional to r^{-6} (r being the distance) but it can have a range up to 100 Å.
The rate constant of Förster type dipolar energy transfer k_T^F can be calculated as follows:

$$k_T^F = k_D \left[\frac{R_0}{r}\right]^6 = \frac{1}{\tau_0^D}\left[\frac{R_0}{r}\right]^6 \tag{1.12}$$

In this equation k_D is the emission rate constant for spontaneous emission of the donor or τ_0^D the corresponding decay time and R_0 is the Förster radius at which the rates of energy transfer and spontaneous decay are equal. The Förster radius R_0 (in Å) can also be calculated from spectroscopic data:

$$R_0 = 0.2108 \left[\kappa^2 \Phi_D n^{-4} \int_0^\infty I_D(\lambda)\varepsilon_D(\lambda)\mathrm{d}\lambda\right]^{1/6} \tag{1.13}$$

Φ_D is the fluorescence quantum yield of the donor, n the refractive index of the medium, $I_D(\lambda)$ (λ in nm) the fluorescence intensity of the donor (normalized by $\int_0^\infty I_D(\lambda)\mathrm{d}\lambda = 1$), and $\varepsilon_D(\lambda)$ is the molar absorption coefficient in L mol^{-1} cm^{-1}. The orientation factor κ^2 can reach an average value of $2/3$ for an ensemble where free rotation of the dipoles is faster than energy transfer. The quantum efficiency Φ_T of the energy transfer can be calculated by

$$\Phi_T = 1 - \frac{\tau_D}{\tau_D^0} \tag{1.14}$$

from the decay time in absence of an acceptor (τ_D^0) and with acceptor (τ_D). Concerning the selection rules for Förster RET, one has to consider, that the optical transition of the acceptor has to be allowed and that the donor has to have a non-zero quantum yield for the emission. Accordingly, a singlet excited donor can transfer its energy to a ground state acceptor to create a singlet excited acceptor, or to a triplet excited acceptor to create a higher triplet. But also phosphorescent donors can transfer their energy under spin conservation of the acceptor.
The rate constant for Dexter RET in the very weak coupling regime can be calculated as follows:

$$k_T^{ex} = \frac{2\pi}{h} K \int_0^\infty I_D(\lambda)\varepsilon_D(\lambda)\mathrm{d}\lambda \cdot e^{-2r/L} \tag{1.15}$$

with the normalization condition $\int_0^\infty I_D(\lambda)\mathrm{d}\lambda = 1$. L is the average Bohr radius and K is a constant that is not accessible from spectroscopic data and limits the usability of this formula. The selection rules for Dexter's mechanism are not as restrictive as for Förster's mechanism. The most important additional transitions are the transfer from a triplet excited donor to an acceptor which is initially in the ground state, to create a triplet excited acceptor, and the triplet-triplet annihilation.[47]
The different mechanisms of coupling described above for molecular systems can in principle also occur in hybrid structures composed of inorganic quantum wells and quantum dots, and organic chromophores. However, the coupling between 'inorganic' Wannier-Mott excitons and 'organic' Frenkel excitons, as well as the non-0-dimensionality of the structures may lead to new effects. In the [very] weak coupling regime energy can be transferred incoherently from organic layers to to inorganic semiconductors or vice versa, depending on the optical band gaps of the involved materials. Hence, the preferable absorbing or emitting properties of the organic materials can be combined with the superior ability of charge carrier injection and transport of the inorganic semiconductors. In this way, RET LED or RET solar cells can be constructed. At this point, it should also be noted, that the rate constant for energy transfer decays less steeply with the distance between donor and acceptor than the r^{-6} dependence for two point dipoles. In the case of strong coupling, hybrid Frenkel-Wannier-Mott excitons are expected to be formed, which are characterized by the oscillator strength of the Frenkel exciton and the radius of the Wanner-Mott exciton, leading to enhanced nonlinear optical effects.[46]

1.3.2 Examples for Energy Transfer Devices

In this section a few examples are given for structures or devices that investigate or exploit RET between the different classes of materials. The idea of hybrid LEDs consisting of an inorganic quantum well of II-VI materials and an organic emitting layer separated by a barrier of a defined width, was first explored on the theoretical level. Using typical parameters of the materials, it was shown that energy transfer from the quantum well to the organic layer can be faster than the intrinsic excitation decay time of the quantum well. Therefore non-radiative decay channels in the quantum well play a smaller role and the overall emission quantum yield of the structure is increased, provided that the emission quantum yield of the organic material is high.[48]
The first inorganic-organic structure that was well studied experimentally, is a ZnO quantum well with $Zn_{0.9}Mg_{0.1}O$ barriers with an organic layer of 2,2-*p*-phenylenebis-(5-phenyloxazole). By evaluation of the PL transients of the bare quantum well and the hybrid structure, it was shown that excitons are transferred from the quantum well to the organic part with an efficiency of up to 0.5 at a temperature of 5 K.[49] Using 2,7-bis(biphenyl-4-yl)-2',7'-di-*t*-butyl-9,9'-spirobifluorene as organic layer, the efficiency of the exciton transfer was increased to 0.75, but electron transfer from the organic material to the inorganic part quenched the emission to some extent.[50] In some later studies the energy transfer between InGaN/GaN or GaN/AlGaN quantum wells and organic (polymeric) layers was investigated.[51–55] There are also some examples of energy transfer between inorganic quantum dots and inorganic

layers or quantum wells in both directions to form hybrid solar cells or LEDs.[56, 57] While in all the above mentioned exsamples the energy transfer is mediated by long-range dipolar interactions, there are also some cases of Dexter type exchange transfer. Triplet excitons were either transferred from $PbBr_6$ layers in a perovskite structure to naphthalene layers[58] or from pentacene to PbSe nanocrystals.[59]

1.3.3 The HIOS Project

As already stated above, the work presented in this thesis has been carried out in the framework of the collaborative research center 951 of the DFG, 'HIOS' (hybrid inorganic/organic systems for opto-electronics). In the previous sections, the optical and electronic properties of different classes of materials were described, as well as their applicability, processing techniques, and typical device structures. The specific advantages and disadvantages of the different types of materials were depicted and, to some extent, possible ways to combine or hybridize these materials were introduced. It is now the goal of the project to study and systematically improve the opto-electronic performance of hybrid structures that exploit the specific advantages of the employed materials, while specific disadvantages are eliminated. The three components are organic semiconductors, inorganic semiconductors, and metal nanostructures. The latter ones are not discussed here, because that part of the project is not related to this work. For the part of inorganic semiconductors ZnO and GaN were considered. Here, the focus will be on ZnO.
With regard to their opto-electronic function, the structures may be very sensitive towards morphology and defects. Especially the interface of the materials plays an important role, since inorganic semiconductors often form surface reconstructions or the surfaces are reactive and the organic material can bind in different ways. However, to understand the fundamental optical and electronic processes in HIOS, reproducible fabrication of high quality structures is essential. Thus, one of the key research areas is the controlled assembly of HIOS. To achieve high structural quality, high purity materials need to be processed under controlled conditions. Therefore, all-UHV techniques as molecular beam epitaxy (MBE) for the inorganic semiconductors, and OMBD for the organic layers were chosen as growth methods for the initial phase of the project. For later stages, solution processing is planned, as it should broaden the scope of molecular compounds used tremendously.
Once high quality samples can be grown and structurally characterized, the electronic coupling and hybridization of quantum states of the different materials can be investigated. Here, the investigations mainly concern the excitonic coupling, which is analyzed by transient PL measurements and the energy level alignment, which is analyzed by ultraviolet photoelectron spectroscopy (UPS) or X-ray photoelectron spectroscopy (XPS).

1.3.3.1 ZnO

ZnO is the prototypical inorganic semiconductor investigated in the HIOS project. It is a non-toxic, low-cost, relatively abundant material. Bulk ZnO crystallizes in the wurtzite structure ($P6_3mc$, see figure 1.6). Macroscopic crystals of ZnO are

transparent and colorless to yellow. In figure 1.6 b) some different ideal crystal faces are depicted (before reconstruction or passivation), the oxygen terminated (000-1), the zinc terminated (0001) and the mixed terminated 10-10) surface. Depending on the surface, molecular adsorption geometries and energy level alignment may be different (see for example [60]). ZnO is a direct semiconductor with a wide band gap (3.44 eV at low temperature, 3.37 eV at room temperature) and thus a strong absorption in the UV region. Due to a relatively large exciton binding energy of 60 meV, ZnO can also emit at room or higher temperatures. Crystalline bulk or thin film ZnO can be grown with a large variety of techniques from solution, from the melt, or from the gas phase. Most growth techniques lead to n-type conducting ZnO. Furthermore, band gap tuning is possible. By alloying CdO for lower and MgO for higher band gaps, a variation of the band gap between roughly 3 eV and 4 eV is possible, which is also applied in heterostructures.[61]

In terms of application in electronic devices, ZnO is widely discussed as material for transparent electrodes. By doping with aluminum or gallium a relatively low resistivity can be achieved that is comparable to ITO, while retaining the material's transparency. As a low-cost material, it is a potential candidate to replace expensive ITO.[63, 64]

In principle, bulk ZnO can also emit light, however quantum well structures present some advantages. In addition the formation of subbands, the charge carriers and the excitons are spatially confined. If the barrier of the quantum well is thin, the excitons are confined very close to the surface of the device, which is important for non-radiative energy transfer. High quality ZnO/ZnMgO quantum wells can be grown by epitaxial methods under high vacuum conditions. The emission of such quantum wells is situated between 3.3 and 3.5 eV and the peak width at half maximum can be as small as 7 meV in some cases. Furthermore the thickness of the capping layer (respectively the barrier thickness at the interface) can be reduced down to 2.5 nm without losing the emissive properties of the quantum well, which

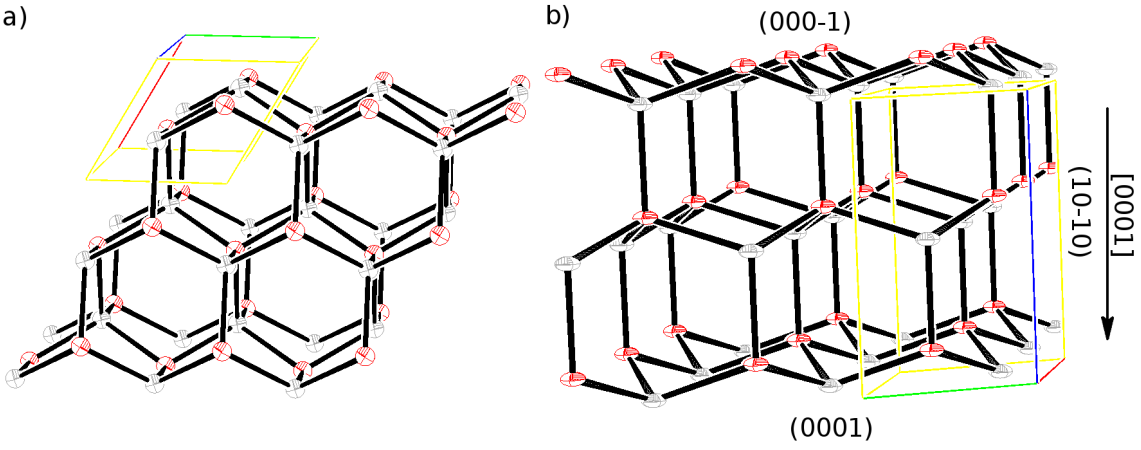

Figure 1.6. Crystal structure of ZnO (Wurtzite, O: red, Zn: gray) a) view along [0001] of a crystal fragment. b) Crystal fragment displaying the different surfaces of ZnO: oxygen terminated (000-1) (top), zinc terminated (0001) bottom, and mixed terminated (10-10) surface. Crystallographic data are taken from ref. [62].

enables dipolar coupling to organic semiconductors.[65, 66]

1.3.3.2 Requirements for the Organic Component in HIOS

To construct hybrid devices with an efficient energy transfer, the organic component has to fulfill several requirements, that are not only associated with parameters of the energy transfer process. Factors concerning the processability of the material, as well as a stable device structure are important, as well. Below, several requirements are listed, starting with the ones related to the energy transfer:

- **Spectral overlap.** As apparent from equations 1.13 and 1.15, the spectral overlap of the donor emission and the acceptor absorption is of major importance in the very weak coupling regime. Most obviously, the energy of both transitions has to be equal and it is advantageous if the spectral shapes are similar, to achieve maximal overlap of the normalized spectra. Since the emission of the inorganic quantum well is very sharp, the organic component should also display narrow transitions. In that context, one should keep in mind, that both the PL quantum yield of the donor, which can not be influenced by the organic component employed as acceptor, as well as the absorption coefficient ε in the region of spectral overlap influence the transfer rate. Thus, organic chromophores with a maximum ε exactly and ideally only at the donor emission are required. In a scenario of coherent coupling, a small width of the transitions is even more important.

- **High PL quantum yield.** The efficiency of a hybrid LED depends on the quantum yield of the emitter. Hence, the organic component should have a PL quantum yield Φ_{PL}, that is close to 1.

- **Small Stokes-shift.** A small stokes shift is advantageous because of two reasons. The first one is energy efficiency. To generate high-energy photons with a minimum driving voltage, energy should not be lost via thermal relaxation and reorganization of molecules. Secondly, a small Stokes-shift assures a relatively high exciton diffusion length mediated by intermolecular donor-donor RET.

- **Energy level alignment.** Since inorganic semiconductor and organic material are in close proximity, electron transfer processes may occur. While this process is desired in photovoltaic devices, it would quench the emission of an hybrid LED. Therefore the HOMO of the emitter and the valence band maximum of the inorganic semiconductor, as well as the LUMO and the conduction band minimum should have the same energies, respectively.

- **Inertness.** When applied in a device structure, the organic component should be as durable as possible. This relates to thermal, as well as photochemical and electrochemical degradation processes.

- **Tolerant to gas phase processing.** In the initial phase of the project, the device fabrication is mainly limited to UHV based techniques. The organic

components are processed by OMBD, which requires molecules, which can be evaporated. To ensure the vacuum processability, the molecules should be thermally very stable and the molecular mass should not exceed approximately 1000 g/mol, to keep the evaporation temperature sufficiently low. Furthermore it is advantageous, if the melting point is above the evaporation temperature in the pressure regimes used. These requirements limit the use of solubilizing groups.

- **Thin film formation.** In layered devices, it is important, that the components can be grown in closed, homogeneous films. These may either be of high crystalline quality or totally amorphous and have to be stable over time. Stable films can either be formed if the interaction between sample and substrate is sufficiently strong or if the sample molecules are not mobile and do not diffuse.

- **Assembly on a given substrate surface.** The interaction between the different materials can depend on the orientation of the molecules with respect to the surface. Therefore, the orientation of the optical transition dipole is significant. In a target molecule, it should be in a pronounced direction, which can be addressed by chemical functionalization to guide the self assembly on the substrate surface by dipoles or anchoring groups.

1.3.3.3 Potential Organic Building Blocks

The variety of absorbing and emitting organic molecules is large. Nearly every conjugated molecule has a pronounced absorption and a large fraction of them is also emissive. But it is rather demanding, to find a class of molecules, that meets all the requirements stated above. An additional point should be addressed here, as well. Once a molecule is found, that is suitable regarding most of the requirements, there should still be some freedom for chemical variation without disturbing the system such, that its favorable properties get lost. On the other hand, some perturbation should be possible to allow for fine-tuning of the chromophore.
Typical examples of simple fluorescent molecules, which are applied in organic electronics are polycyclic aromatic hydrocarbons, such as pyrene, perylene, naphthalene, anthracene, or higher acenes. Due to their fully planar and rigid π-system they posses narrow absorption and emission bands and some of them also a high fluorescence quantum yield. But the optical HOMO-LUMO-transition in the near UV in combination with a very high absorption coefficient is hard to find. Furthermore, some of these compounds are very sensitive to (photo) oxidation and the possibilities for chemical functionalization are limited. Regarding the point of assembly on surfaces, rod-like molecules can have some advantages. In this case, oligo(*p*-phenylene)s are an interesting class of organic semiconductors. They have a strong absorption in the UV region and high PL quantum yields. But the bands are relatively broad because of the rotational degrees of freedom between the phenylene units. However, this problem can be eliminated by locking the angle between phenylene units by covalent bridging. This was accomplished with a methylene bridge (figure 1.7 a), with a ethane, or ethene in the bridge (1.7 b and c), or with a bridging nitrogen (1.7

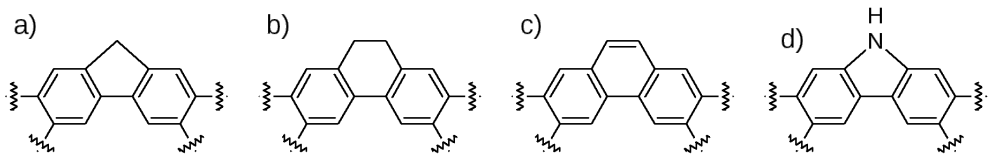

Figure 1.7. Different types of ladder-type oligo-*p*-phenylenes.

d, for an overview see e.g. [67]). Except for the ethane bridge, these structures are planar. But in case of the nitrogen and ethene bridge, the optical transitions have already relatively long wavelengths for very short oligomers and the lowest vibronic transition is not very pronounced. Accordingly, the ladder-type oligo(*p*-phenylene)s with the methylene bridge are most promising for hybrid structures with ZnO quantum wells. They posses a strong 0-0 transition in the UV and a rough tuning of the optical band gap can be conducted with a variation of the oligomer length. Furthermore, a large variety of functionalization can be carried out at the different methylene groups and at the terminal aromatic positions.

1.3.3.4 Ladder-Type *para*-Phenylenes

The synthetic route to LPPPs and longer ladder-type oligo(*para*-phenylene) (LOPP)s[5] was first described by Scherf and Müllen in 1991 (figure 1.8).[68] To build up the polymer strand, a substituted 1,4-phenylenebis(boronic acid) **1** (R^1 = H, alkyl) was reacted in a Suzuki polycondensation with a derivative of 1,4-dibromobenzene carrying two keto units for later intramolecular bridging in *para* position with respect to each other (**2**, R^2 = (alky substituted) phenyl units). The initial polymer **3** was reduced to the polyalcohol **4**, which was condensed to the LPPP **5** in a intramolecular Friedel-Crafts reaction. This synthetic route is not limited to *para*-phenylenes, structures with *meta* connections of the phenyl units have also been synthesized. But the synthetic route displays more versatility. Keto groups as in **3** can be reacted with metalorganic reagents to yield a polyalcohol. In that way, mixed alkyl-aryl substituted were synthesized, which are more resistant towards degradation than **5**, since the hydrogen in the methylene bridge is quite reactive. If instead of ketones, esters are used, they can also be reacted with metalorganic reagents to finally yield LPPPs with bis(alkyl) or bis(aryl) substituted methylene bridges. Furthermore, the ester groups can be saponified and reacted in Friedel-Crafts acylations, to give LOPPs carrying the fluorenone motif. These keto groups can further be converted into spirobifluorene units or dicyanovinyl groups.[67, 69–73]
It was shown, that LPPPs are higly luminescent, easily processable materials. The optical and excited state properties have been examined on a theoretical[74] and experimental basis. Site selective fluorescence studies revealed, that the Stokes shift in LOPPs is maily related to spectral diffusion and not to reorganization.[75] Solid state optical properties have been discussed[76] and LPPPs have successfully been employed as active layer in OLEDs.[77]

[5]From here on, LPPP and LOPP only refers to structures with methylene bridge as shown in figure 1.7 a).

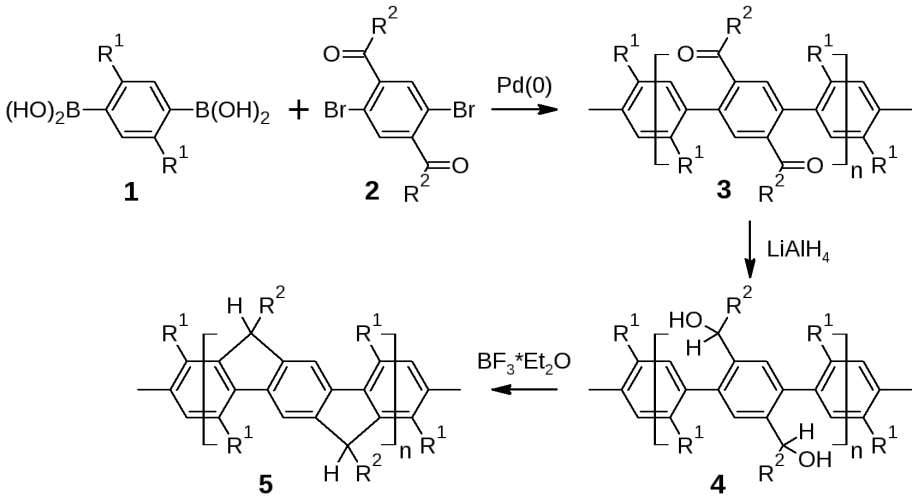

Figure 1.8. Initial synthetic route to LPPP **5**.

1.4 Challenges

The challenges for this work are already pre-defined by the requirements for the organic component, which were stated above. However, some of the requirements are most likely already accomplished by the choice of LOPPs as target molecules, such as high PL quantum yield and a small stokes shift, some are more specific, especially concerning the synthesis. In the following the different points are reformulated and summarized.

- **Spectral overlap.** As LOPPs already display strong and narrow optical 0-0-transitions, the remaining task is to bring this transition in resonance with the emission of the ZnO quantum well structures ($\approx$ 3.4 eV). A rough tuning of the optical gap can be achieved by adjustment of the oligomer length. Fine tuning might be possible by a variation of the substitution pattern, however, this might interfere with other parameters.

- **Vacuum processing.** For the application of the organic materials in evaporation based processing techniques, solubilizing groups based on long alkyl chains should be omitted. The related lack of solubility for larger planar, π-conjugated molecules has two consequences for the synthesis: First, the planarization of the molecule should be carried out as late as possible, to keep the intermediates easy to handle. And secondly, purification techniques have to be employed, that do not or only marginally depend on the solubility of the substances, such as crystallization and sublimation techniques.

- **Energy level alignment.** It is relatively simple to achieve shifts in the frontier orbital energies by introduction of donating or accepting groups. The optical properties have to remain unchanged, however. This excludes any conjugated group, such as cyano, dicyanovilyl, nitro or carbonyl groups. Hence, the focus will be on fluorine and fluorinated substituents.

- **Inertness.** The reactivity of hydrocarbon LOPPs towards surfaces is expected to be rather low. So inertness was initially not considered as a serious problem. But in the course of the experiments it turned out, that photooxidation is seriously interfering with the analysis of the energy transfer. Hence, a lot of effort was put into the generation of new insights into the products and mechanisms of photodegradation.

- **Layer formation.** If the interaction between substrate and organic layer is weak, the organic component might tend to form crystalline islands. To form either crystalline or amorphous layers without a strong interaction to the substrate, intermolecular interactions should be weakened and diffusion should be hampered.

- **Molecular orientation.** To control the orientation of molecules on a surface, the attachment of anchoring groups on specific positions or the introduction of a molecular dipole is necessary.

- **Site selective functionalization.** In most of the previous points, a very distinct functionalization needs to be realized in order to achieve a fine tuning of the properties of the organic material. In that context synthetic routes have to be developed, which make is possible to specifically address every methylene bridge with a variety of different substituents.

The following chapters will address these points in combination or sometimes only one of them. In the second chapter some general points of the synthesis and processing of LOPPs and their properties will be compared to non-bridged *p*-phenylenes. In the third chapter the effects of the fluorination of the methylene bridges on the frontier orbital energies, the intermolecular arrangement, and the optical properties will be addressed. The fourth and fifth chapter have a focus on the photodegradation of structures carrying the fluorene motif. While the former one is related to reaction conditions, kinetics and potential products of the degradation of ladder-type structures, the latter one focuses on the influence of different substituents in the methylene bridge of 2,7-diphenylfluorenes on the rates of photodegradation. In the sixth chapter the influence of spirobifluorene on the optical properties, solid state structures and thin film forming ability will be discussed, as well as the influence of isomerism on the optical properties. In the final chapter a short overview over first integration into hybrid devices will be presented.

2 Vacuum-Processable *p*-Phenylenes and Effects of Bridging and Planarization[6]

2.1 Introduction

Optoelectronic devices incorporating organic semiconducting materials are heavily investigated to achieve higher device efficiencies and longer durability in combination with their light weight, flexibility, and potentially low cost.[16] The integration of organic and inorganic semiconductor materials to unite specific favorable properties of both material classes is particularly promising. To achieve proper interaction of both semiconductor materials in order to promote either energy or electron transfer between the two device components, the energy level alignment at the interface and hence the organization of the molecular building blocks is crucial.[60] In order to gain a detailed understanding of these important processes it is essential to construct well-defined inorganic–organic hybrid structures. Such model systems can be realized by thin-film growth of organic molecules on semiconductor surfaces by vapor deposition or molecular beam deposition techniques.[80] The most important prerequisites for the molecular building blocks to be employed are therefore their thermal stability beyond the evaporation temperatures. Clearly, the organic material should possess the desired opto-electronic properties, such as high absorption coefficients and luminescence efficiencies, narrow absorption and luminescence bands as well as a small Stokes shift to enable efficient exciton migration within the organic layer. Furthermore, the organic component should resist any type of optically or electrochemically induced degradation.

One of the prime organic semiconductors, meeting many but not all of the aforementioned conditions, is p-sexiphenyl **6P**–the 'fruitfly' of organic electronics. Besides studies on the application in OLEDs[77, 81] there are many reports about its crystallographic structures on a variety of metallic and dielectric surfaces,[82] notably also on the electronic structure at the interface with ZnO.[60] Furthermore, non-radiative energy transfer between ZnO and a spiro-derivative of **6P** has been demonstrated.[50] However, due to its intrinsic flexibility, in particular its rotational degrees of freedom along the aryl-aryl connections, oligo- and poly(*p*-phenylene)s in general display rather broad absorption and emission spectra and a significant Stokes shift. To overcome these restrictions, focusses on LOPPs, which due to their fixed planar geometry should exhibit the desired optical features. Note that to date a large number of typically odd-numbered oligomers as well as polymers of that type has been synthesized and studies of their optical and electronic properties as well as their applicability in OLEDs, photovoltaic cells, and electronic materials have been

[6]This chapter has already been published in a similar manner in ref. [78], initial work has been carried out in the framework of a diploma thesis [79].

described in the literature,[67, 70, 72, 83–87] yet all these examples necessitate long alkyl chains to provide sufficient solubility for solution processing. However, the significant weight bestowed by the side chains prohibits their evaporation without thermal degradation and therefore it is not surprising that thus far there is no report on vacuum-processable LOPPs.[7] Furthermore, note that even-numbered oligomers have been synthesized only up to four phenylene units. Herein, we disclose a new synthetic route to even-numbered LOPPs, designed specifically for vacuum-based deposition techniques. We describe both the synthesis and characterization with regard to their optical and electrochemical properties in solution as well as the growth of thin films on alumina surfaces by OMBD. These molecules should enable the realization of the targeted organic–inorganic semiconductor hybrid structures to allow for efficient exciton and charge transfer across the organic-inorganic interface.

2.2 Results and Discussion

2.2.1 Synthesis

The synthesis to even-numbered LOPPs is based on a central fluorene unit, which is connected to two terminal aromatic moieties via cross-coupling reactions. The bridging, leading to an extended aromatic system and hence extremely low solubility, represents the penultimate step of the sequence. The functional groups to induce the bridging reaction are incorporated in the central building block and hence access to the highly functionalized fluorene derivative **8** (figure 2.1) is required.
Since attempts to direct functionalization of 2,7-dibromo-9,9-dimethylfluorene in its 3- and 6-position were not successful, phenanthrene-9,10-dione **1** was chosen as the starting material as it is regioselectively brominated using bromine and dibenzoyl peroxide in nitrobenzene.[89] Ring contraction of 3,6-dibromo-phenanthrene-9,10-

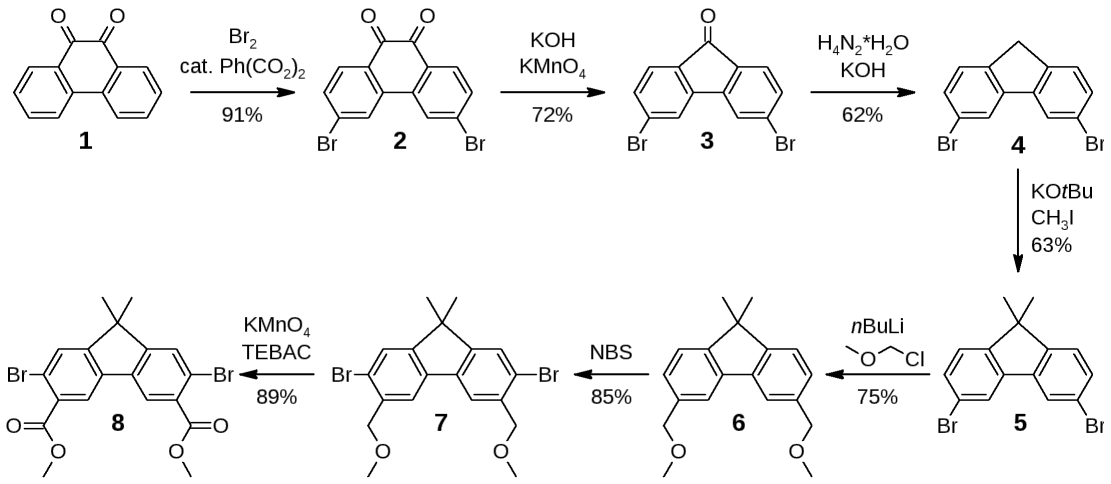

Figure 2.1. Synthesis of highly functionalized fluorene **8** (TEBAC :triethyl benzyl ammoniumchloride).

[7]The only exception known to the author is a patent: See ref. [88]. But some of the data presented there are questionable.

dione **2** followed by decarboxylation using aqueous KOH and $KMnO_4$ provided 3,6-dibromofluorenone **3**,[90] which was reduced via a Wolff–Kishner reduction[91] and the formed 3,6-dibromofluorene **4** was subsequently methylated employing CH_3I and KO*t*Bu[92] to provide 3,6-dibromo-9,9-dimethylfluorene **5**. Two-fold lithiation using *n*-butyl lithium and subsequent reaction with chloromethyl methyl ether chloromethyl methyl ether (MOM-Cl) gave **6** in 75% yield. Note that other electrophiles, such as dimethyl carbonate or acetone, gave lower yields. Diether **6** was brominated with N-bromosuccinimide in propylene carbonate[93] and the formed 2,7-dibrominated fluorene **7** was oxidized[94] to the corresponding diester building block **8**.

The core unit **8** was reacted with 9,9-dimethylfluorene-2-boronic acid, which was readily generated by lithiation of **9** followed by reaction with tributylborate (figure 2.2), in a Suzuki cross-coupling reaction employing catalytic amounts of $Pd(PPh_3)_4$ and Na_2CO_3 in a biphasic water-tetrahydrofuran (THF) solvent mixture. Diester **10** was treated with excess CH_3MgI to yield diol **11**. Final bridging via intramolecular Friedel–Crafts alkylation[69] provides ladder-type sexiphenyl **L6P**, readily visible by its characteristic blue fluorescence appearing within a few seconds of the reaction. Purification of the final product **L6P** was achieved by precipitation, extensive washing of the solid, and final sublimation. Interestingly, the solubility of **L6P** in $CHCl_3$ and CH_2Cl_2 is much better as compared to *p*-sexiphenyl **6P** enabling characterization by standard solution techniques, such as NMR, UV/vis absorption and fluorescence measurement as well as cyclic voltammetry (CV). It appears that the methyl groups at the sp^3-hybridized bridging carbon atoms projecting out of plane prevent efficient π-π stacking, at least to some degree.

The synthesis of the ladder-type quarterphenyl **L4P** was carried out following an analogous route but employing phenylboronic acid (figure 2.3). Intermediate diester

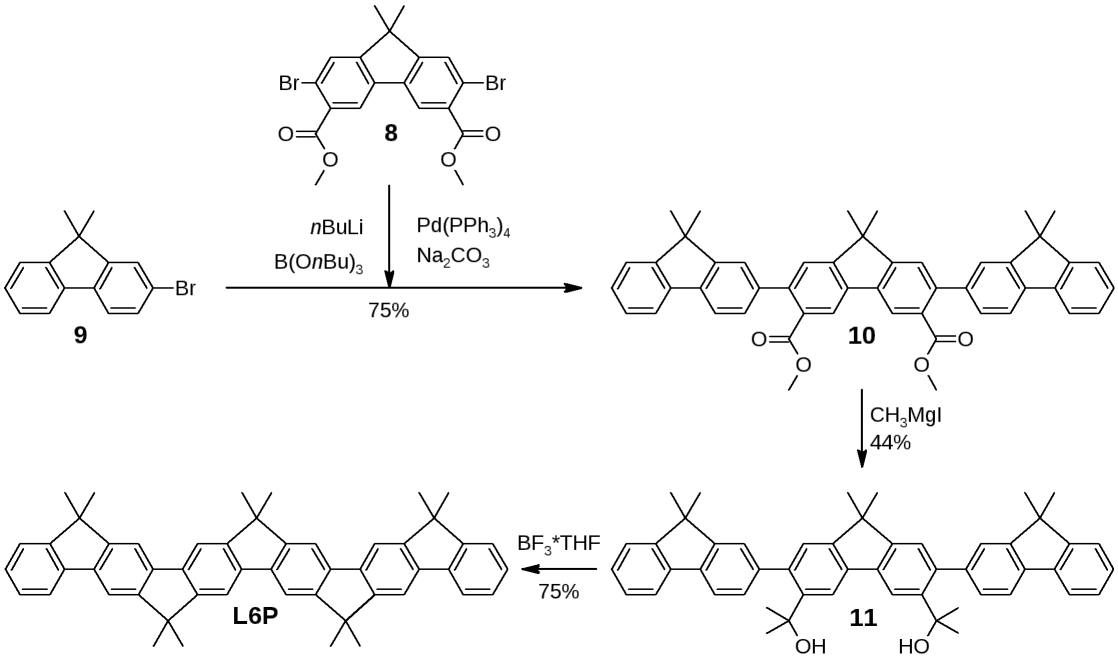

Figure 2.2. Synthesis of ladder oligomer **L6P**.

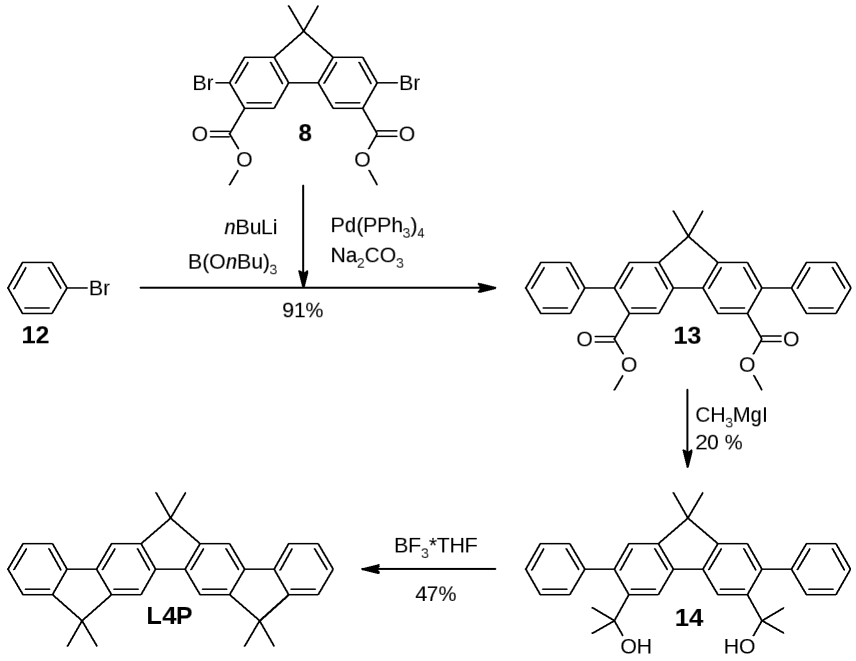

Figure 2.3. Synthesis of ladder oligomer **L4P**.

13 was reacted with CH_3MgI to afford diol **14**, which was converted to **L4P** via two-fold intramolecular Friedel–Crafts alkylation. Purification of **L4P** was achieved by recrystallization and sublimation. For comparison purposes, bifluorene **2F** was synthesized by cross-coupling **9** with its corresponding boronic acid while terfluorene **3F** was synthesized according to literature procedures.[95]

2.2.2 Optical and Electrochemical Properties[8]

The optical and electrochemical behavior of the newly synthesized oligomers was investigated in solution, in particular to determine the influence of increasing rigidity, i.e. loss of rotational degrees of freedom, in a series ranging from **6P** over **3F** to **L6P** as well as the effect of extending the π-system in even-numbered LOPPs in a series ranging from **1F** over **L4P** to **L6P** (figure2.4).
Both absorption (λ_{abs}) and fluorescence emission (λ_{em}) maxima are bathochromically shifted with increasing degree of bridging, i.e. going from **6P** via **3F** to **L6P** (Fig. 2.5). This is in good agreement with the fact that bridging forces adjacent phenylene units into coplanarity hence leading to an increased effective π-conjugation. In addition, the maximum extinction coefficients ε_{max} are significantly increased upon bridging, i.e. it is more than doubled when going from **4P** to **L4P** and again from **3F** to **L6P** as well as more than tripled going from **6P** to **L6P** (Table 2.1). The absorption and excitation spectra of **3F** and **6P**,[9] respectively, are rather broad and unstructured when compared to **L6P**. In addition to having a very high extinction coefficient ε_{max} the absorption maximum of **L6P** is very sharp, in

[8]Electrochemical measurements were carried out by Dr. Lutz Grubert (HU Berlin, Institut für Chemie).

[9]For **6P** only excitation spectra are available due to its poor solubility

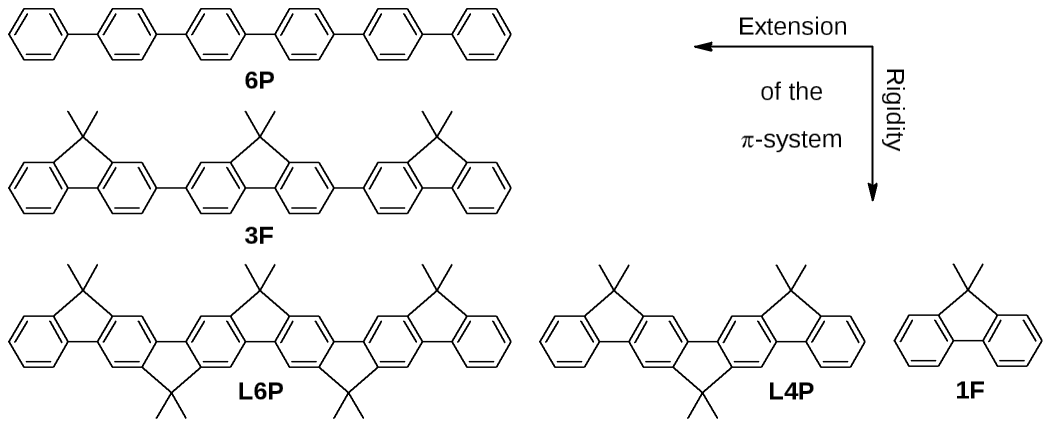

Figure 2.4. Characterized compounds and variation of their structural parameters.

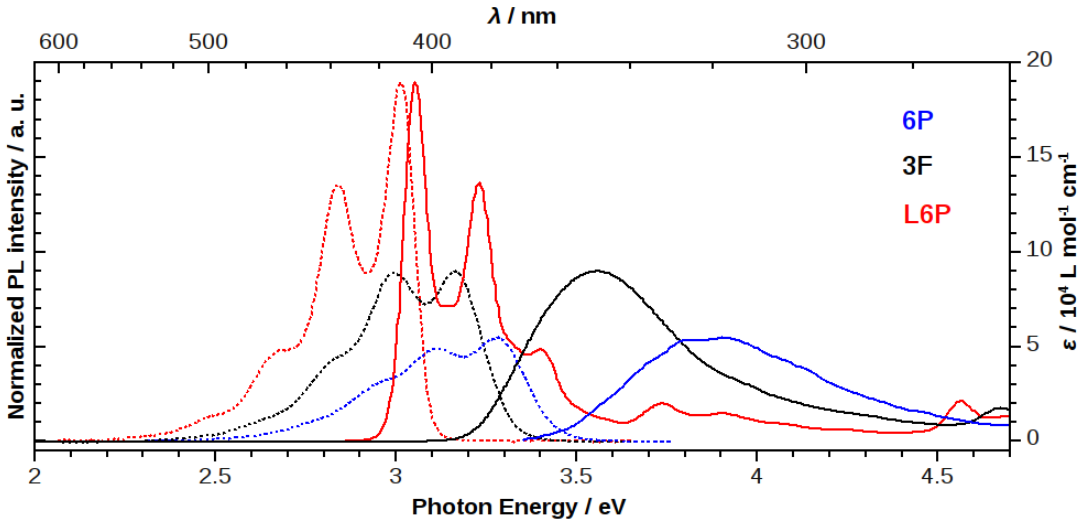

Figure 2.5. Spectral properties of *p*-phenylenes in solution: Absorption (solid line), and fluorescence (dotted) spectra of **3F** (black), and **L6P** (red), as well as excitation (solid line, scaled with ε from ref. [96]) and fluorescence (dotted) spectra of **6P** in CH_2Cl_2. The intensity of the fluorescence is normalized to the corresponding maximum absorption coefficient.

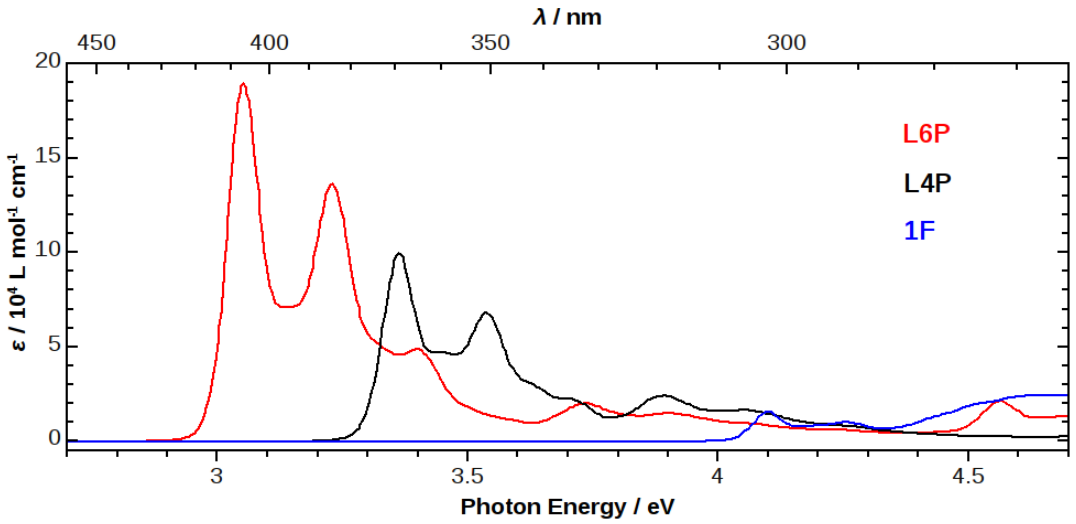

Figure 2.6. Spectral properties of *p*-phenylenes in solution: absorption spectra of **1F** (blue), **L4P** (black), and **L6P** (red) in CH_2Cl_2.

particular on the low-energy edge. The degree of bridging has perhaps the most profound effect on the Stokes shift (ΔE), i.e. the energy offset between absorption and emission maxima, which is significantly decreased when going from **6P** (580 meV) via **3F** (250 meV) to **L6P** (40 meV). These observations are readily explained by the fact that oligo(*p*-phenylene)s can freely rotate about the phenylene–phenylene bonds in the ground state in solution, leading to absorption of various rotamers and hence spectral broadening. Upon excitation the unbridged oligo(*p*-phenylene)s can undergo relaxation on their excited state potential energy surface by adopting a more planar conformation,[100] hence giving rise to a large Stokes shift. In contrast, the geometry of the rigidified **L6P** in its ground and excited states is almost identical leading to a vanishing Stokes shift, while **3F** represents a somewhat intermediate case. Furthermore, rigidification in **L6P** is reflected by the clearly visible vibronic coupling. In this regard, analysis of the absorption spectra of the bridged series, i.e. **1F**, **L4P**, and **L6P** (figure 2.6), shows that in all cases the 0,0-transition is favored.

Table 2.1. Optical properties of the investigated *p*-phenylenes in solution.

	λ_{max} / nm	ϵ_{max} / L mol^{-1} cm^{-1}	λ_{Em} / nm	Φ_{PL}	ΔE / meV
6P	320[a]	55 000[b]	377	0.93[b]	580
3F	349	90 000	393	0.9	250
L6P	407	190 000	412	1.0	40
L4P	369	100 000	374	0.7	40
1F	301	16 000	303	0.53 - 0.80[c]	30
4P[d]	295	41 000		0.9	

Spectra were recorded in CH_2Cl_2 at 25 °C. [a]Maximum of excitation spectrum. [b]Values according to ref. [96]. [c]Values for non-methylated fluorene according to ref. [97] and [98]. [d]Values according to ref. [99].

The distance between the 0,0- and 0,1-transitions varies between 150 and 180 meV. Importantly, the fluorescence quantum yield Φ_{PL} of both **L6P** and **3F** is close to unity.[10] With increasing size of the π-system, the quantum yields seem to increase only slightly (Table 2.1).

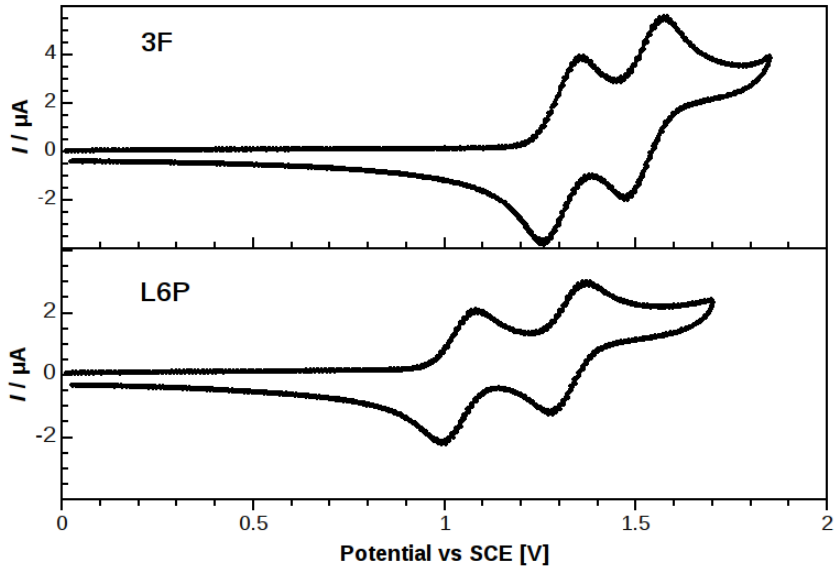

Figure 2.7. Cyclovoltammogram of **3F** (top) and **L6P** (bottom) in CH_2Cl_2 (0.1 mol L^{-1} Bu_4NPF_6), dE/dt = 1 V s^{-1}.

In addition to the optical properties, the electrochemical behavior of the newly synthesized LOPPs has been investigated and compared to their respective compounds. The cyclo-voltammograms of **3F** (figure 2.7, top) and **L6P** (figure 2.7, bottom) show that both compounds can reversibly be oxidized in two successive one-electron steps to their respective radical cations and dications. The bridged structure in **L6P** facilitates the first oxidation event, as it occurs at a 300 mV lower oxidation potential as compared to **3F** (table 2.2). Furthermore, the enhanced π-

Table 2.2. Oxidation potentials of investigated *p*-phenylenes.

	E_p^{a1} / V	E_p^{a2} / V	ΔE_p^a / V
3F	0.793	1.009	0.216
L6P	0.492	0.778	0.286
L4P	0.687	1.193[a]	0.506
1F	1.276[a]	–	–
2F	0.894	1.248[a]	0.354

Potentials vs. Fc/Fc^+ in CH_2Cl_2 (0.1 mol L^{-1} Bu_4NPF_6), dE/dt = 1 V s^{-1}. [a]Irreversible oxidation.

[10]Due to its low solubility, no fluorescence quantum yield could be determined for **6P** by the employed method.

conjugation and therefore stronger coupling lead to a greater separation of the two oxidation peaks (ΔE_p^a) in **L6P** (table 2.2). The same trends are observed when comparing **2F** with its bridged analogue **L4P**. Therefore, the completely bridged structures become more electron-rich, which could in part be attributed to their smaller HOMO–LUMO gap, and their radical cations are more stabilized by the enhanced π-conjugation as compared to their dications. Furthermore, the number of reversible one-electron oxidation steps of LOPPs as a function of the number of phenylene units is basically the same as reported for oligofluorenes.[101, 102] Thus, whereas the oxidation of **1F** is irreversible, **L4P** forms a stable radical cation yet undergoes an irreversible second electron transfer, and **L6P** exhibits two reversible oxidation steps.

While performing the cyclovoltammetric measurements with **L6P** UV/vis absorption spectra were recorded (figure 2.8). The formation of the radical cation **L6P**$^{+}$ is indicated by a newly formed absorption band maximum located at 581 nm. Moving to higher potential the absorption band of the dication **L6P**$^{2+}$ can be observed with a maximum at 1084 nm. Note that the spectral shape of the three species remains rather similar as all three compounds display three maxima, due to vibronic transitions, and the distance between the first and second absorption maximum remains at about 180 meV.

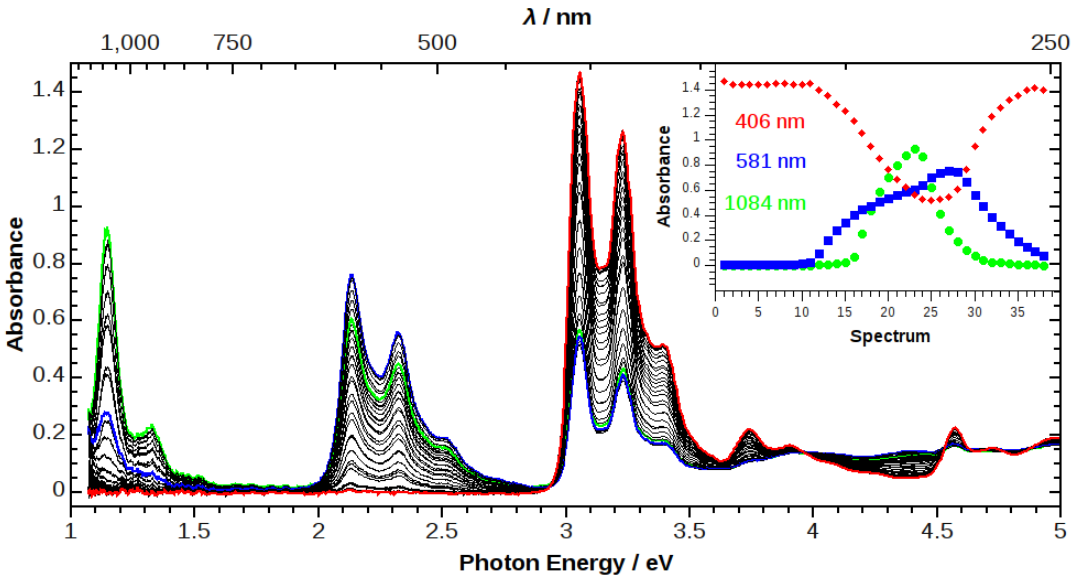

Figure 2.8. Spectral change of **L6P** during electrochemical oxidation: formation of radical cation and dication (c = $8 \cdot 10^{-5}$ mol L^{-1} in CH_2Cl_2). Recorded in a 1 mm quartz cuvette using a platinum grid electrode, 0.1 mol L^{-1} Bu_4NPF_6, dE/dt = 10 mV s^{-1}, 0 $\longrightarrow$ 1.3 $\longrightarrow$ 0 V vs. $Ag/AgNO_3$, spectra recorded every 70 mV. Highlighted spectra at the beginning (red), at maximum absorption of the cation (blue) and at maximum absorption of the dication (green). Inset: evolution of the absorption at 406 nm (red, associated to **L6P**), 581 nm (blue, associated to **L6P**$^{+}$) and 1084 nm (green, associated with **L6P**$^{2+}$).

2.2.3 Thin Film Growth[11]

Thin films of **L6P** were prepared on Al_2O_3 (0001) substrates by OMBD in an UHV ($5 \cdot 10^{-9}$ Torr) deposition chamber. The deposition rate as measured by a quartz microbalance was 0.1 nm min^{-1}. The substrate was kept at room temperature. The morphology of a **L6P** submonolayer at a coverage of 0.27 is depicted in the atomic force microscopy (AFM) image of figure 2.9. Extended flat molecular islands with a height corresponding approximately to the length of the **L6P** are visible. Thus, the islands are comprised of upright standing molecules. Such morphology is typical for molecules crystallizing in a herringbone structure on chemically inert substrates (such as sapphire). It was found also for **6P** molecules deposited on ZnO (0001)[60] and TiO_2.[103]

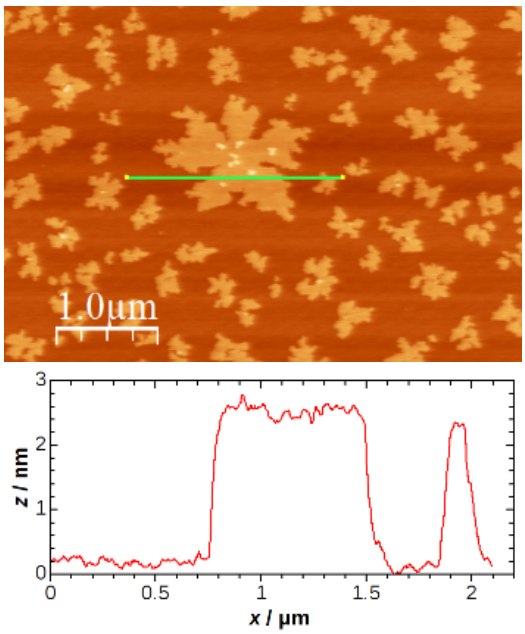

Figure 2.9. AFM image of **L6P** deposited on an Al_2O_3 (0001) surface (top) and the corresponding height profile (bottom).

2.3 Conclusion

A new synthetic route to yield even-numbered LOPPs has been developed based on the use of a highly functionalized central fluorene building block. Direct comparison with the structurally related non-bridged oligo(*p*-phenylene)s as well as partially bridged oligofluorenes shows that the newly synthesized LOPPs exhibit outstanding photophysical properties, such as sharp and intense optical transitions characterized by narrow absorption bands and very small Stokes shifts as well as large extinction coefficients and high fluorescence quantum yields. The origin of the observed optical properties can clearly be linked to their rigid structure maximizing π-conjugation.

[11] Work in this section has been carried out by Dr. Sylke Blumstengel in the group of Prof. Fritz Henneberger (HU Berlin, Institut für Physik).

Furthermore, oxidation of LOPPs is more facile as compared to their non-bridged counterparts. Initial investigations demonstrate that these materials are applicable to OMBD techniques allowing the controlled generation of organic (ultra)thin films on solid substrate surfaces.

However, in following experiments it turned out, that **L4P**, which is indeed resonant to ZnO, is applicable to OMBD, but it rather forms crytallites on oxide surfaces, than closed, thin layers. In applied in a polymer matrix, it is too sensitive to photooxidation in studies concerning the energy transfer.

2.4 Experimental

Absorption measurements were carried out on a Varian Cary 50 Bio UV/vis spectrometer in 1 cm quartz cuvettes. Fluorescence spectra were obtained on a Varian Cary Eclipse spectrofluorimeter. Solutions of a concentration of about 10^{-6} mol L^{-1} (for dimethylfluorene **1F** about 10^{-5} mol L^{-1}) were used for the absorption measurements. Perylene (Φ = 94%, ref. [97]) was used as reference for the measurement of the fluorescence quantum yields. It was dissolved in cyclohexane, the other products in CH_2Cl_2. The solutions were diluted 1 by 30 for the measurement of fluorescence spectra. The reference solution was degassed with argon before carrying out the measurements. Electrochemical measurements were carried out using a HEKA-Elektronik PG310 potentiostat or an Autolab PGSTAT128N and an Ava Spec-2048x14 spectrometer equipped with an Avalight-DH-S-BAL lamp. ^{1}H-NMR and ^{13}C-NMR spectra were referenced to 7.26 ppm and 77.16 ppm, respectively, for $CDCl_3$ and 5.32 ppm and 53.8 ppm, respectively, for CD_2Cl_2. Thin films of **L6P** were grown in an OMBD system by CreaPhys. The AFM image was recorded in tapping mode with a Nanoscope 3a controller, Veeco, USA.

Organic Synthesis

3,6-Dibromophenanthrene-9,10-dione (2)
The literature procedure (ref. [89]) was adapted to large scale synthesis: Phenanthrene-9,10-dione **1** (52 g, 250 mmol) and dibenzoyl peroxide (2 g, 8.3 mmol) were dissolved in nitrobenzene (250 mL). An initial amount of bromine (14.5 g, 90 mmol) was added to the mixture and heated to 120 °C. When the formation of gaseous HBr started, the remaining bromine (72 g, 450 mmol, in sum 86.4 g, 540 mmol) was added drop-wise. After heating for one hour, the mixture was cooled and ethanol (250 mL) was added. The precipitated product was filtered and washed with ethanol until the washing solution turned colourless. After drying under vacuum 83.4 g (228 mmol, 91% yield) of 3,6-dibromophenanthrene-9,10-dione **2** were obtained as an orange powder.
^{1}H-NMR (500 MHz, $CDCl_3$) δ [ppm] = 8.12 (d, J = 1.8 Hz, 2H), 8.07 (d, J = 8.3 Hz, 2H), 7.67 (dd, J = 8.3, 1.7 Hz, 2H).
^{13}C-NMR (126 MHz, $CDCl_3$) δ [ppm] = 179.0, 136.1, 133.6, 132.3, 130.0, 127.6.

3,6-Dibromo-9-fluorenone (3)
The literature procedure(ref. [90]) was used: KOH (101 g, 2.2 mol) was dissolved in 150 mL of water and heated to 130 °C. Then, 3,6-dibromophenanthrene-9,10-dione **2** (61.9 g, 169 mmol) was suspended in the solution. After stirring for 30 min, the mixture turned black and very viscous. Within a period of 2 h $KMnO_4$ (141.5 g, 895 mmol) was added carefully. The mixture was stirred at 130 °C for one hour and cooled to room temperature, followed by neutralization with concentrated sulfuric acid. Sodium bisulfite was added carefully to the (slightly acidic!) mixture until it turned light yellow. The precipitate was filtered off and washed with water. 3,6-Dibromo-9-fluorenone **3** (41.1 g, 121.6 mmol, 72% yield) was obtained as a light yellow powder.
^{1}H-NMR (500 MHz, $CDCl_3$) δ [ppm] = 7.67 (d, J = 1.6 Hz, 2H), 7.55 (d, J = 7.8 Hz, 2H), 7.50 (dd, J = 7.8, 1.6 Hz, 2H).

3,6-Dibromofluorene (4)
The literature procedure(ref. [91]) was modified concerning workup and purification: 3,6-Dibromo-9-fluorenone **3** (33.8 g, 100 mmol) was dispersed in 300 mL of triethylene glycol and hydrazine hydrate (100%, 21.8 mL, 450 mmol) was added. While stirring overnight at 100 °C the solution slowly turned clear. Then, KOH (33 g in 90 mL of water) was added. Stirring was continued for 2 h at 130 °C. After cooling to room temperature, the mixture was poured into 1.2 L of water and neutralized with HCl. The orange precipitate was filtered off, dried and purified by sublimation (10^{-3} mbar, heater at 220 °C). 3,6-Dibromofluorene **4** (20.2 g, 62.3 mmol, 62% yield) was obtained as a nearly white solid.
^{1}H-NMR (500 MHz, $CDCl_3$) δ [ppm] = 7.87 (d, J = 1.7 Hz, 2H), 7.44 (dd, J = 8.0, 1.8 Hz, 2H), 7.40 (d, J = 8.0 Hz, 2H), 3.80 (s, 2H).
^{13}C-NMR (126 MHz, $CDCl_3$) δ [ppm] = 142.8, 142.3, 130.4, 126.7, 123.5, 121.2, 36.4.

3,6-Dibromo-9,9-dimethylfluorene (5)
The literature procedure (ref. [92]) was adapted to the substrate: 3,6-Dibromofluorene **4** (17.8 g, 55 mmol) was dissolved in dry THF (150 mL) and cooled to 0 °C. KOtBu (18.5 g, 165 mmol), and after stirring for 10 min, CH_3I (10.3 mL, 165 mmol) were added. The solution was allowed to warm to room temperature and it was stirred overnight. Then water was added and the mixture was extracted with ethyl acetate. The organic phase was dried with $MgSO_4$. Upon removing the solvent, the crude product remained as an orange solid. Column chromatography (cyclohexane) gave 12.2 g (34.7 mmol, 63% yield) 3,6-dibromo-9,9-dimethylfluorene **5** as a white solid.
^{1}H-NMR (500 MHz, $CDCl_3$) δ [ppm] = 7.80 (d, J = 1.8 Hz, 2H), 7.45 (dd, J = 8.0, 1.8 Hz, 2H), 7.29 (d, J = 8.0 Hz, 2H), 1.45 (s, 6H).
^{13}C-NMR (126 MHz, $CDCl_3$) δ [ppm] = 152.7, 140.2, 130.9, 124.4, 123.6, 121.2, 46.8, 26.9.

3,6-Bis(methoxymethyl)-9,9-dimethylfluorene (6)
3,6-Dibromo-9,9-dimethylfluorene **5** (12 g, 34 mmol) was dissolved under argon in 200 mL of dry THF and the solution was cooled to -78 °C. n-BuLi (2.2 M in cyclohexane, 42 mL, 92 mmol) was added and the solution was stirred for 30 min.

Then, chloromethyl methyl ether (MOM-Cl, 8.5 mL, 112 mmol) was added and stirring was continued for 30 min at -78 °C and overnight (solution turned clear after 10 min) at room temperature. The mixture was poured into water. It was extracted with ethyl acetate, dried ($MgSO_4$) and the solvent was removed. Column chromatography (petroleum ether /ethyl acetate) gave 7.2 g (25.5 mmol, 75% yield) of 3,6-bis(methoxymethyl)-9,9-dimethylfluorene **6**.
^{1}H-NMR (500 MHz, $CDCl_3$) δ [ppm] = 7.73 (d, J = 0.7 Hz, 2H), 7.41 (d, J = 7.7 Hz, 2H), 7.29 (dd, J = 7.7, 1.3 Hz, 2H), 4.54 (s, 4H), 3.44 (s, 6H), 1.48 (s, 6H).
^{13}C-NMR (126 MHz, $CDCl_3$) δ [ppm] = 153.6, 139.5, 137.2, 127.1, 122.6, 119.7, 95.8, 75.1, 58.3, 46.7, 27.3.

2,7-Dibromo-3,6-bis(methoxymethyl)-9,9-dimethylfluorene (7)
The literature procedure(ref. [93]) was adapted to substrate **6**: In 30 mL of propylene carbonate 3,6-bis(methoxymethyl)-9,9-dimethylfluorene **6** (1.9 g, 6.7 mmol) was dissolved and N-bromosuccinimide (NBS) (2.4 g, 13.4 mmol) was added. The mixture was stirred for 16 h at 60 °C. Then, water was added and the precipitate was filtered off. Purification by column chromatography (petroleum ether/ethyl acetate) gave 2.5 g (5.7 mmol, 85% yield) of 2,7-dibromo-3,6-bis(methoxymethyl)-9,9-dimethylfluorene **7** as a colorless solid.
^{1}H-NMR (500 MHz, $CDCl_3$) δ [ppm] = 7.82 (s, 2H), 7.57 (s, 2H), 4.59 (s, 4H), 3.53 (s, 6H), 1.46 (s, 6H).
^{13}C-NMR (126 MHz, $CDCl_3$) δ [ppm] = 154.4, 138.0, 136.6, 127.1, 121.8, 120.7, 74.3, 58.9, 47.1, 27.1.

Dimethyl 2,7-dibromo-9,9-dimethylfluorene-3,6-dicarboxylate (8)
The literature procedure (ref. [94]) was adapted to substrate **7**: In 10 mL of CH_2Cl_2 2,7-dibromo-3,6-bis(methoxymethyl)-9,9-dimethyl-fluorene **7** (0.16 g, 0.36 mmol), benzyltriethylammonium chloride (TEBAC) (0.49 g, 2.16 mmol) and $KMnO_4$ (0.34 g, 2.16 mmol) were dissolved and stirred for 5 h at reflux. Then an aqueous solution of sodium thiosulfate was added until the purple color disappeared. The mixture was extracted with CH_2Cl_2, dried ($MgSO_4$) and the solvent was removed. Column chromatography (cyclohexane/ethyl acetate) gave 0.15 g (0.32 mmol, 89% yield) of dimethyl 2,7-dibromo-9,9-dimethylfluorene-3,6-dicarboxylate **8**.
^{1}H-NMR (500 MHz, $CDCl_3$) δ [ppm] = 8.13 (s, 2H), 7.69 (s, 2H), 3.97 (s, 6H), 1.48 (s, 6H).
^{13}C-NMR (126 MHz, $CDCl_3$) δ [ppm] = 166.7, 157.7, 136.9, 131.4, 129.2, 123.3, 121.5, 52.7, 47.8, 26.6.

2-Bromo-9,9-dimethylfluorene (9)
2-Bromofluorene (10 g, 40.8 mmol) was dissolved in 200 mL of DMSO and cooled to 0 °C. Then, CH_3I (6.1 mL, 97.9 mmol), TEBAC (0.46 g, 2 mmol) and 25 mL of 50% aqueous NaOH were added. After stirring for 30 min, the solution was poured into water and extracted with ethyl acetate. The organic phase was washed with diluted HCl, dried with $MgSO_4$ and the solvent was removed. Column chromatography (petroleum ether/ethyl acetate) gave 11 g (40.2 mmol, 99% yield) of 2-bromo-9,9-dimethylfluorene **9**.

^{1}H-NMR (300 MHz, $CDCl_3$) δ [ppm] = 7.73 - 7.68 (m, 1H), 7.61 - 7.57 (m, 2H), 7.50 - 7.42 (m, 2H), 7.38 - 7.33 (m, 2H), 1.49 (s, 6H).
^{13}C-NMR (75 MHz, $CDCl_3$) δ [ppm] = 155.8, 153.4, 138.3, 138.2, 130.2, 127.8, 127.3, 126.2, 122.8, 121.5, 121.1, 120.2, 47.2, 27.1.

Terfluorene (10)
General procedure for the Suzuki coupling: 2-Bromo-9,9-dimethylfluorene **9** (4.8 g 17.5 mmol) was dissolved under an argon atmosphere in 50 mL of dry THF and cooled to -78 °C. Subsequently *n*-BuLi (2.2 M in cyclohexane, 8.9 mL, 19.6 mmol) was added and the mixture was stirred for 30 min. It turned brown and turbid. Upon adding tributylborate (5.7 mL, 21 mmol), the solution was stirred for one hour at room temperature.
Meanwhile dimethyl 2,7-dibromo-9,9-dimethylfluorene-3,6-dicarboxylate **8** (3.3 g, 7 mmol) was dissolved in 50 mL of THF and degassed using argon. Then, $Pd(PPh_3)_4$ (0.65 g, 0.56 mmol) was added. After stirring for 15 min, 40 mL of 2 M aq. sodium carbonate solution was added and the temperature was raised to 60 °C.
Both solutions were combined and stirred overnight at 60 °C. After cooling to room temperature, water was added and the mixture was extracted with ethyl acetate. The organic phase was dried ($MgSO_4$) and the solvent was removed. The crude product was first purified by column chromatography and then dissolved in a mixture of CH_2Cl_2 and ethyl acetate. The CH_2Cl_2 was removed under reduced pressure and the product precipitated. Upon filtration and drying under vacuum 3.6 g (5.2 mmol, 74% yield) of terfluorene **10** were obtained.
^{1}H-NMR (500 MHz, $CDCl_3$) δ [ppm] = 8.26 (s, 2H), 7.81 (d, J = 8.1 Hz, 2H), 7.80 - 7.77 (m, 2H), 7.56 (s, 2H), 7.50 - 7.46 (m, 2H), 7.46 - 7.42 (m, 4H), 7.41 - 7.33 (m, 4H), 3.67 (s, 6H), 1.61 (s, 6H), 1.56 (s, 12H).
^{13}C-NMR (126 MHz, $CDCl_3$) δ [ppm] = 169.9, 156.9, 153.9, 153.7, 142.5, 140.8, 139.0, 138.6, 137.4, 130.9, 127.5, 127.4, 127.2, 125.1, 123.0, 122.8, 122.0, 120.3, 120.0, 52.2, 47.8, 47.0, 27.4, 27.1.

Dimethyl 2,7-diphenyl-9,9-dimethylfluorene-3,6-dicarboxylate (13)
Starting from bromobenzene **12** (0.47 g, 3 mmol) and dimethyl 2,7-dibromo-9,9-dimethylfluorene-3,6-dicarboxylate **8** (0.47 g, 1 mmol), 0.42 g (0.91 mmol, 91% yield) dimethyl 2,7-diphenyl-9,9-dimethylfluorene-3,6-dicarboxylate **13** was obtained without the above mentioned crystallization step.
^{1}H-NMR (500 MHz, $CDCl_3$) δ [ppm] = 8.24 (s, 2H), 7.47 - 7.42 (m, 6H), 7.41 - 7.37 (m, 6H), 3.69 (s, 6H), 1.54 (s, 6H).
^{13}C-NMR (126 MHz, $CDCl_3$) δ [ppm] = 169.2, 156.8, 142.5, 141.7, 137.3, 130.3, 128.4, 128.1, 127.3, 125.2, 121.9, 52.0, 47.6, 26.9.

Terfluorene diol (11)
General procedure for the reaction of diesters with Grignard reagents to diols: Terfluorene **10** (0.9 g, 1.3 mmol) was dissolved in 50 mL of dry THF under argon and CH_3MgI (3 M in diethyl ether, 10.8 mL, 32.5 mmol) was added. After refluxing for 2 h, water was added and the mixture was extracted with diethyl ether. The organic phase was dried with $MgSO_4$ and the solvent was removed. Column chromatogra-

phy (cyclohexane/ethyl acetate) gave 0.40 g (0.58 mmol, 44% yield) of terfluorene **11**.
^{1}H-NMR (500 MHz, CD_2Cl_2) δ [ppm] = 8.16 (s, 2H), 7.80 - 7.76 (m, 4H), 7.51 - 7.46 (m, 4H), 7.36 (m, 6H), 7.21 (s, 2H), 2.12 (s, 2H), 1.53 (s, 12H), 1.52 (s, 12H), 1.49 (s, 6H).
^{13}C-NMR (75 MHz, CD_2Cl_2) δ [ppm] = 154.2, 153.5, 152.0, 146.3, 143.7, 140.0, 139.2, 138.6, 138.3, 129.0, 127.7, 127.4, 126.6, 124.8, 123.0, 120.3, 119.5, 117.8, 74.4, 47.2, 46.8, 33.0, 27.4, 27.2.

2,7-Diphenyl-3,6-bis(1,1-dimethylhydroxymethyl)-9,9-dimethylfluorene (14)
Starting from dimethyl 2,7-diphenyl-9,9-dimethylfluorene-3,6-dicarboxylate **13** (0.4 g, 0.87 mmol), 0.08 g (0.17 mmol, 20% yield) of 2,7-diphenyl-3,6-bis(1,1-dimethylhydroxymethyl)-9,9-dimethylfluorene **14** were obtained.
^{1}H-NMR (500 MHz, CD_2Cl_2) δ [ppm] = 8.10 (s, 2H), 7.43 - 7.36 (m, 10H), 7.10 (s, 2H), 1.82 (s, 2H), 1.51 (s, 12H), 1.43 (s, 6H).

Ladder-type sexiphenyl (L6P)
General procedure for the intramolecular Friedel–Crafts reaction to ladder-type *p*-phenylenes according to ref. [69]: terfluorene **11** (0.4 g, 0.57 mmol) was dissolved in 50 mL of CH_2Cl_2 and $BF_3 \cdot THF$ (50% in THF, 1.9 mL, 8.5 mmol) was added. After stirring for 30 min at room temperature, ethanol and aqueous $NaHCO_3$ were added. The organic phase was concentrated and the product was separated by centrifugation. The yellowish precipitate was washed with ethyl acetate several times. Finally, 0.28 g (0.42 mmol, 75% yield) of the ladder-type sexiphenyl **L6P** were obtained.
^{1}H-NMR (500 MHz, $CDCl_3$) δ [ppm] = 7.84 (s, 6H), 7.80 - 7.77 (m, 4H), 7.46 (d, J = 7.3 Hz, 2H), 7.36 (td, J = 7.4, 0.9 Hz, 2H), 7.31 (td, J = 7.2, 0.9 Hz, 2H), 1.66 (s, 6H), 1.65 (s, 12H), 1.59 (s, 12H).
^{13}C-NMR (126 MHz, $CDCl_3$) δ [ppm] = 154.2, 153.8, 153.8, 153.7, 153.3, 139.7, 139.3, 139.0, 138.9, 138.6, 127.1, 127.0, 122.7, 119.8, 114.3, 114.0, 114.0, 113.9, 46.7, 46.5, 29.9, 27.9, 27.6.

Ladder-type quarterphenyl (L4P)
Starting with 2,7-diphenyl-3,6-bis(1,1-dimethylhydroxymethyl)-9,9-dimethylfluorene **14** (0.07 g, 0.15 mmol), 0.03 g (0.07 mmol, 47% yield) of the ladder-type quarterphenyl **L4P** were obtained after recrystallization from ethyl acetate.
^{1}H-NMR (500 MHz, $CDCl_3$) δ [ppm] = 7.83 (s, 2H), 7.79 - 7.76 (m, 4H), 7.46 (d, J = 7.2 Hz, 2H), 7.36 (td, J = 7.4, 1.2 Hz, 2H), 7.31 (td, J = 7.3, 1.1 Hz, 2H), 1.62 (s, 6H), 1.58 (s, 12H).
^{13}C-NMR (75 MHz, $CDCl_3$) δ [ppm] = 154.0, 153.6, 153.1, 139.5, 139.0, 138.5, 127.0, 126.9, 122.6, 119.7, 114.2, 113.9, 46.6, 46.3, 27.7, 27.4.

3 Gradual Fluorination of Ladder-type Quarterphenyl[12]

3.1 Introduction

The introduction of fluorine into organic molecules has received ever-increasing attention over the years[105] due to the advantageous properties of fluorinated compounds with regard to their use in positron emission tomography[106, 107] and their unique noncovalent interactions[108–110] in biological environments as well as man-made materials. Thereby, the unique C-F bond imparts enhanced chemical stability (e.g., Teflon) and strongly altered electronic properties, and therefore, fluoroorganic chemistry has made vital contributions to materials chemistry in general and to organic electronics in particular. This is exemplified by the use of the perfluorinated versions of pentacene or tetracyanobenzoquinone (TCNQ), namely, perfluoropentacene and F4-TCNQ, as n-type semiconductors[111] or strongly accepting dopants for organic semiconductors,[112, 113] respectively.

For fluorene-type structures, there is one example of perfluorinated oligomers of 9,9-dimethylfluorene, which exhibits good electron mobility.[114] In the case of LPPPs, which offer enhanced optical properties compared with nonbridged polyfluorenes, both substituents in the benzylic methylene positions are typically functionalized with aryl or alkyl groups,[83] in some cases also with a ketone.[72] To the best of my knowledge, there is only one report of fluorination, namely, in the case of indenofluorene.[115] This is surprising because fluorination in these positions is supposed to

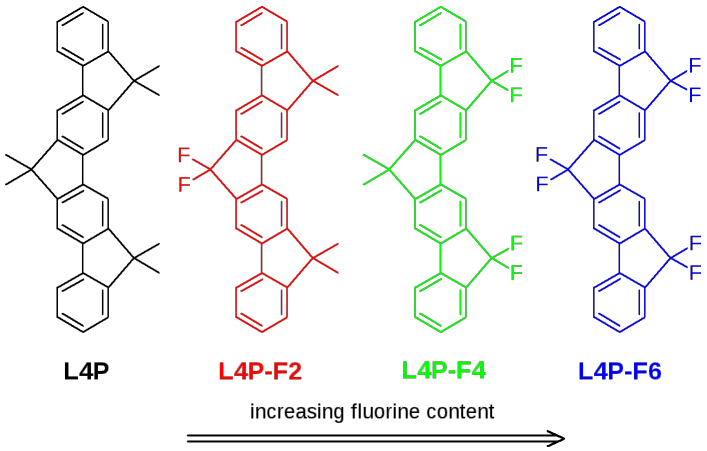

Figure 3.1. Ladder-type quarterphenyls (L4Ps) with increasing fluorine content studied herein.

[12]This chapter has already been published in a similar manner in ref. [104].

have a larger impact on the electronic structure than at an aromatic position, since p-π repulsion in fluorine bound to sp^2 carbon has a destabilizing effect. In particular, negative charges are better stabilized by trifluoromethyl groups and the same argument should also be valid for the difluoromethylene groups discussed herein.[13] Furthermore, the introduction of the fluorine substituent by nucleophilic substitution is straightforward.[116]
To investigate the influence of fluorine substitution on the molecular and assembly structure, and the resulting optical and electrochemical properties of LPPPs, we developed a series of ladder-type quarterphenyls (L4Ps), in which symmetry-equivalent methyl groups were gradually substituted by fluorine (figure 3.1). Herein, we report on the synthesis of the respective successively fluorinated derivatives **L4P-F2**, **L4P-F4**, and **L4P-F6**, and compare their optical spectra and redox properties with the parent **L4P**. Furthermore, their structure in the crystalline solid is discussed.

3.2 Results and Discussion

3.2.1 Synthesis

In general, the synthesis of L4Ps involves two mayor steps: cross-coupling of a central fluorene unit with two terminal phenyl units, and subsequent twofold intramolecular annulation in a Friedel-Crafts-type reaction. In the more simple case, the bridging functionality is originally located on the outer, typically less-substituted phenyl units and attacks the central fluorene unit ("out-side→in"), but occasionally it is necessary to reverse the direction of annulation ("inside→out"). Furthermore, it is useful to achieve as much of the final functionalization as possible prior to the bridging reaction due to the dramatically decreased solubility of the formed L4Ps. Nevertheless, in our syntheses, the introduction of fluorine substituents was carried out after planarization of the π-system, since ketones **L4P-O** and **L4P-O2**[14] could be readily converted into the difluoromethylene derivatives. The fluorination protocol via 1,3-dithiolanes was adapted from that reported by Katzenellenbogen and Sondej,[116] yet the procedure was simplified. Reactions were carried out in air between 0 °C and room temperature using low-cost polypropylene vials.
The synthesis of L4P has already been described.[78] For the synthesis of the two partially fluorinated derivatives **L4P-F2** and **L4P-F4** (figure 3.2), ketone **L4P-O** and diketone **L4P-O2** served as the key starting materials. In the first step, the ketones were transformed into the corresponding 1,3-dithiolanes **1** and **2** in excellent yields. The conversion of **1** and **2** to the di- and tetrafluoride, respectively, was carried out using 70 % HF/pyridine and N-iodosuccinimide (NIS) as the oxidant. The use of other reagents, such as NBS, gave rise to additional electrophilic substitution at the aromatic core. Both products **L4P-F2** and **L4P-F4** were obtained in good yields and fully characterized, including X-ray single-crystal structural analyses (see below).

[13] These effects can be explained by 'negative hyperconjugation' and 'the special fluorine effect' described in ref. [105] pp. 48 - 50

[14] The synthesis of the ketones **L4P-O** and **L4P-O2** is described in ref. [117] and will be discussed in the following chapter.

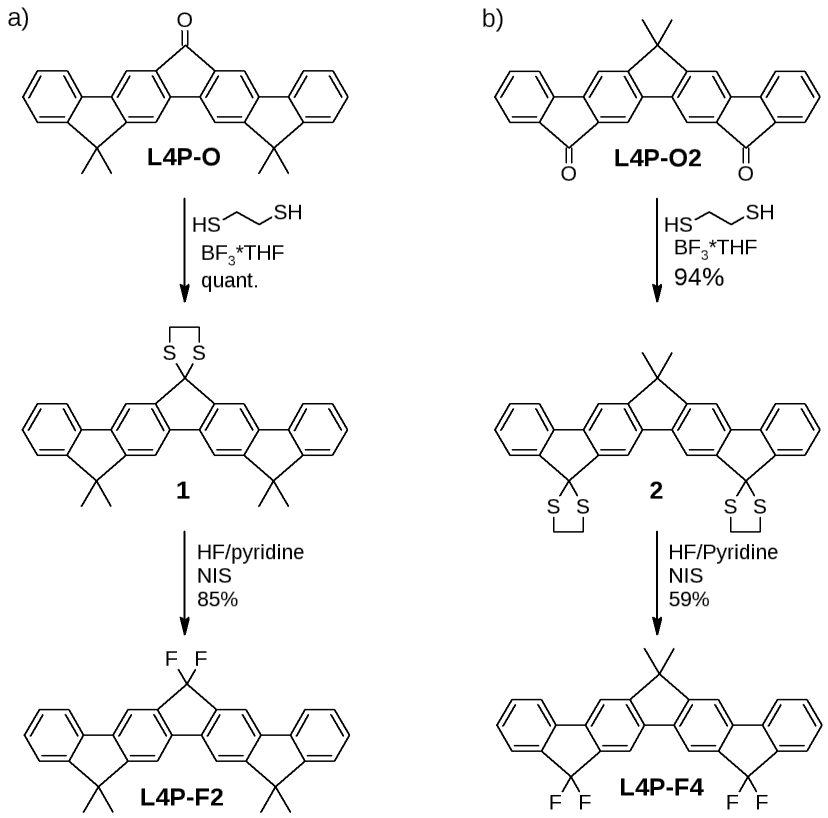

Figure 3.2. Synthesis of a) **L4P-F2** and b) **L4P-F4**.

The synthesis of **L4P-F6** turned out to be more complicated, although the individual reaction steps were similar to the ones discussed above. Initially, a route involving standard bridging from the terminal phenyl units to the central fluorene, that is, "outside→in", was attempted (figure 3.3). Therefore, 9,9-difluorofluorene **3** was coupled to iodobenzoate **4** to give the corresponding diester **5**.[15] A sequence of ester hydrolysis, followed by twofold Friedel-Crafts acylation, conversion to the corresponding 1,3-dithiolanes, and final fluorination was attempted, yet due to their very low solubility none of the products could be purified and analyzed in a satisfactory way. In particular, it remains unclear whether the twofold intramolecular Friedel-Crafts reaction involving the electron-deficient difluorofluorene core was successful or if isomers or different side products were formed.

To prevent detrimental deactivation in the electrophilic aromatic substitution step, the ester groups were placed at the central fluorene unit, and therefore, the direction of the bridging reaction was reversed, that is, "inside→out" in key intermediate **12** (figure 3.4). In addition, only the desired L4P products and no structural isomers can be formed due to the equivalence of the *ortho* positions of the terminal phenyl units. Therefore, the main challenge of this route is the synthesis of the central fluorene unit, which carries functionalities for cross-coupling and bridging as well as the desired fluorine substitution. In the case of fluorene, direct functional-

[15] Protocols for cross-coupling were adapted from ref. [118].

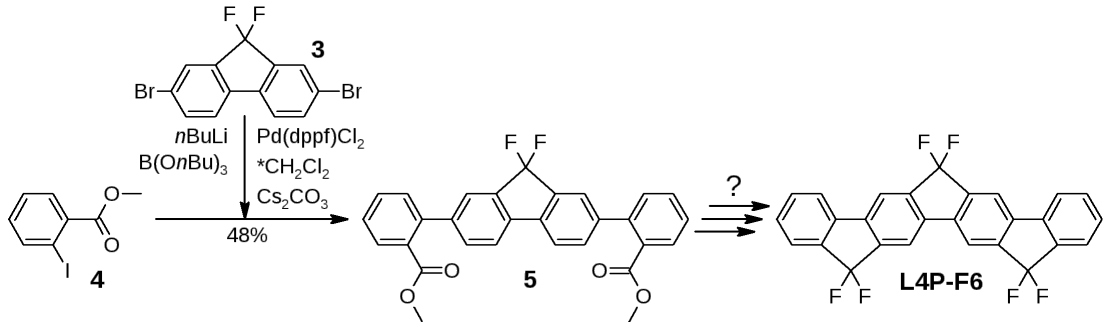

Figure 3.3. Attempted synthesis of **L4P-F6**.

ization of the 3- and 6-positions cannot be achieved; hence 3,6-dibromofluorenone **6** was used, which could be prepared from 3,6-dibromophenanthrenequinone.[90] 3,6-Dibromofluorenone **6** was converted into dithiolane **7** in quantitative yield, followed by reaction with 70 % HF/pyridine and NIS to give difluoride **8**. Subsequent halogen-metal exchange and quenching with chloromethyl methyl ether yielded diether **9**. In the next step, bromination was complicated due to the electron-deficient nature of the 9,9-difluorofluorene moiety. Most of the tested bromination conditions either led to no reaction or to decomposition of the substrate by defluorination.

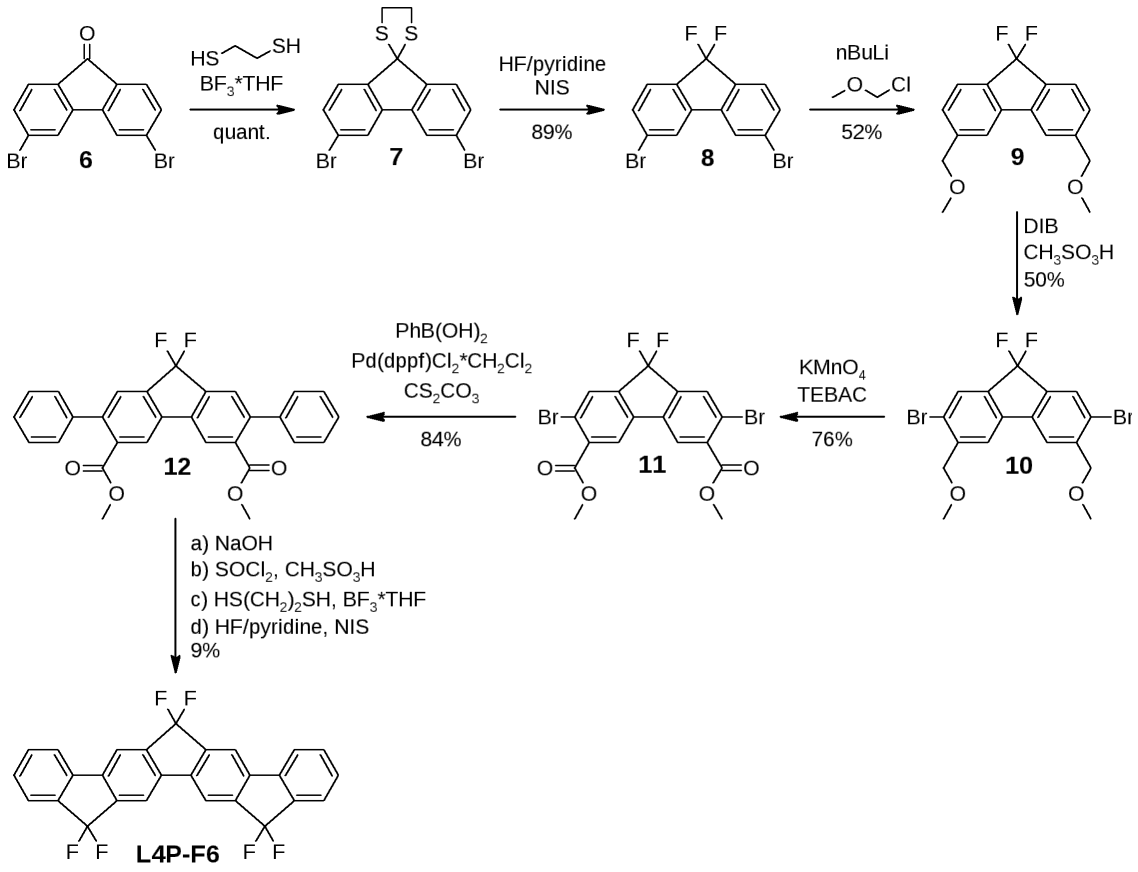

Figure 3.4. Synthesis of **L4P-F6**.

Luckily, the use of dibromoisocyanuric acid (DIB)[119] in acetic acid, employing catalytic amounts of methanesulfonic acid, provided dibromide **10** in moderate yields. Then, the two ether functionalities were oxidized to give diester **11**, which was coupled with phenylboronic acid to yield **12**. The final reaction steps had to be carried out without intermediate purification and analysis due to the low solubility of the formed L4P scaffold: First, the diester was saponified and a Friedel-Crafts acylation was performed to give a red-pinkish powder. Subsequent conversion to the bis(dithiolane) needed to be performed in tetrachloroethane at elevated temperatures, whereupon the color of the product vanished. Finally, fluorination was carried out using our established conditions to yield the target compound as a crude product with low solubility. After several steps of column chromatography with preheated solvents and recrystallization, **L4P-F6** could be isolated in low yield and was successfully characterized.

3.2.2 Molecular Structure and Packing in the Crystal[16]

X-ray diffraction is able to yield high-resolution images of each molecule's chemical structure and in addition, yet often neglected, it provides detailed insights into the supramolecular organization of the crystalline solid. Besides the intrinsic electronic structure at the molecular level, the solid-state structure is key to harnessing the macroscopic material properties, in particular related to charge injection and transport. Of course, a necessary precondition to utilize X-ray diffraction is the availability of crystalline material, ideally single crystals. Gratifyingly, for three of the four compounds (figure 3.1), crystals suitable for X-ray analysis could be grown from solutions in THF or $CHCl_3$/ethanol. The resulting crystal structures of **L4P**, **L4P-F2**, and **L4P-F4** reveal that the aromatic system in all three of these molecules is planar (figure 3.5). Otherwise, the measured bond lengths and angles show no noticeable deviation from commonly observed values in related systems.

Analysis of the molecular packing shows that there are no similarities between the intermolecular arrangements in the three crystal structures. In **L4P**, the voids between molecules within the crystal packing are filled by (disordered) THF molecules, forming channels in the crystallographic a direction (figure 3.6). The shortest intermolecular interactions between methyl groups and the centers of gravity of the aryl rings, belonging to symmetry-equivalent neighboring molecules, amount to 3.5389(16) and 3.7487(16) Å (C28 to Cg C25*→C30* and C6 to Cg C1**→C5**, respectively, in which * defines the symmetry operation $-1/2+X, 1/2-Y, -Z$ and ** defines the symmetry operation $1/2+X, Y, 1/2-Z$).
L4P-F2 crystallizes in a herringbone structure with a herringbone angle of 90 ° (figure 3.7a). The offset of the molecules along their long axis is such that the fluorine atoms are always pointing into the gap between two other molecules (figure 3.7b). The shortest intermolecular contacts amount to 2.63 and 2.75 Å, respectively (F1-H15*, F2-H15*), and no classical hydrogen bonds are present. The space filling

[16]Collection of diffraction data and crystal structure refinement were carried out by Dr. Beatrice Braun and Dr. Stefan Mebs (HU Berlin, Institut für Chemie).

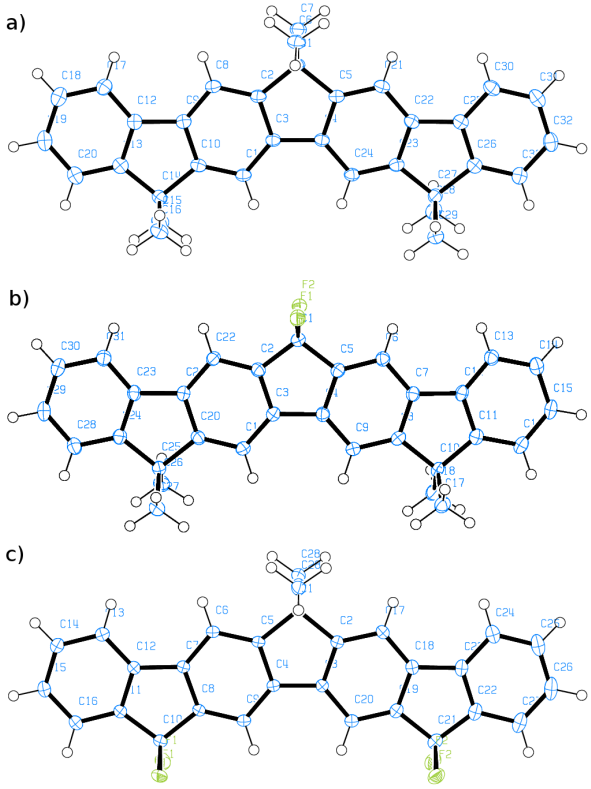

Figure 3.5. Atomic displacement parameters (ADP) plots[120] of the crystal structures of a) **L4P** (CCDC 985904), b) **L4P-F2** (CCDC 985905), and c) **L4P-F4** (CCDC 985906). The ellipsoids are drawn at the 50 % probability level.

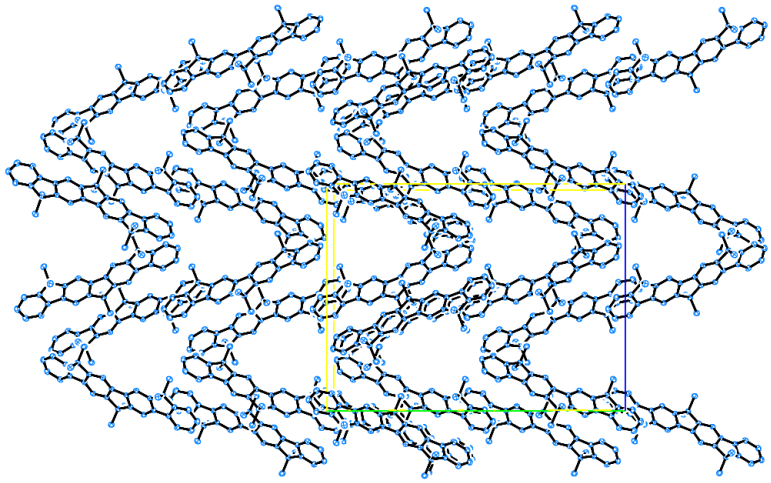

Figure 3.6. Packing of the **L4P** molecules within the unit cell: View along the *a* axis. Disordered THF molecules are excluded for clarity.

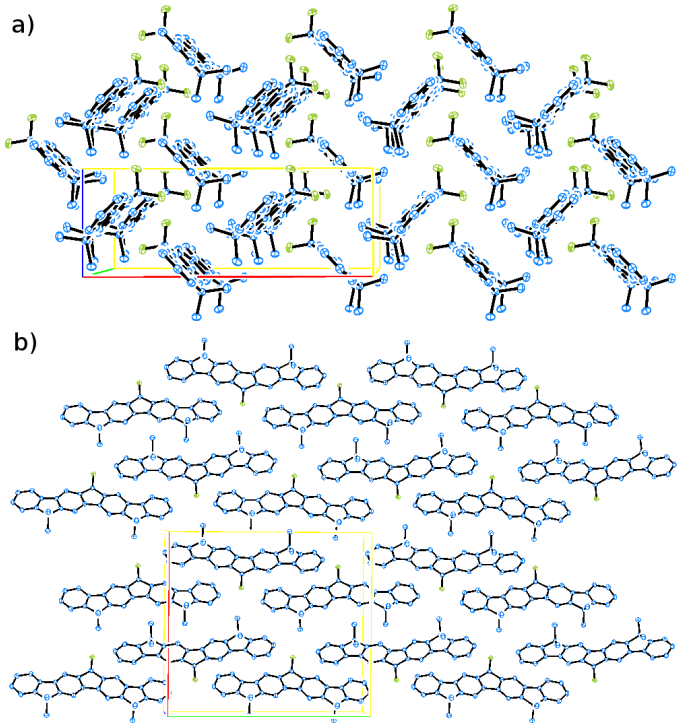

Figure 3.7. Packing of the **L4P-F2** molecules within the unit cell: a) View along the *b* axis, showing the herringbone structure and b) along the *c* axis, showing the structural offset.

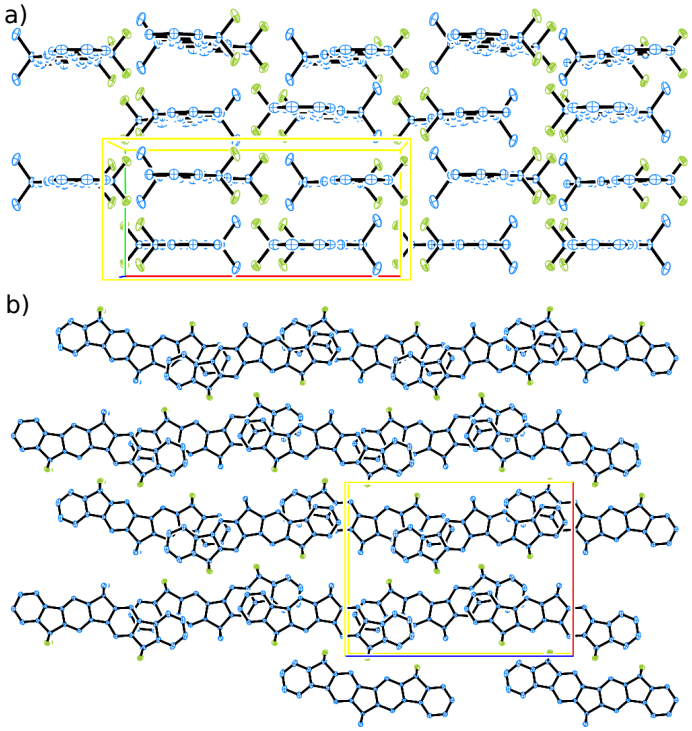

Figure 3.8. Packing of **L4P-F4** within the unit cell: a) view along the crystallographic *c* axis, showing the layered structure, and b) along the *b* direction, showing the structural offset.

is 66.4%.
L4P-F4 crystallizes in a layered structure (figure 3.8a). Within each layer, all molecular dipoles are more or less oriented in a parallel manner, yet between two adjacent layers the dipoles are oriented in an antiparallel fashion. This gives rise to the fact that the planes of the π-systems coincide with mirror planes. The distance between individual layers is 3.46 Å (figure 3.8a) and the stacked molecules exhibit an offset (Figure 3.8b). There are short intermolecular contacts between F and CH_3 substituents: 2.62 Å (F1-H28a*, in which * refers to the symmetry operation $-1/2+x, 1/2-y, 1/2-z$) and 2.75 Å (F2-H20**, in which ** refers to the symmetry operation $1-x, -1/2+y, 1-z$). No classical hydrogen bonds are present. The space filling is 68.8%.
At first, the C-H$\cdots$F interactions, with distances ranging from 2.62 to 2.75 Å and being associated with an estimated gain in interaction energy in the order of 1 kJ/mol, do not seem to be significant. However, since other dominating interactions are absent, one can try to explain the structure formation in the series of compounds by several small contributions.[108, 109] Looking at **L4P-F2**, the edge-to-face orientation leads to a stabilizing interaction between the rather negatively polarized aromatic core and the positively polarized periphery of the aromatic system. A destabilizing interaction between fluorine and the core of the aromatic hydrocarbon is avoided by the offset of half a length of a molecule and in addition weak C-H$\cdots$F contacts are formed. In contrast, one can hardly imagine a herringbone-like structure of **L4P-F4** without F-π interactions. Furthermore, the molecular dipole of **L4P-F4** is expected to be larger, and hence, the combination of these effects can explain the observed antiparallel face-to-face orientation.

3.2.3 Electrochemistry[17]

The introduction of fluorine into conjugated organic compounds has a large influence on the energy levels, which have to be matched with other materials and interfaces to achieve the desired functions in organic electronic devices. By means of cyclic voltammetry, one can determine the oxidation and reduction potentials in solution, and thereby, get a relative measure for the position of the relevant frontier molecular orbital levels. Several solvents have been employed during the course of the measurements, since both the solubility of the sample and sufficient electrochemical inertness of the solvent have to be assured.
Although the first one-electron reduction of **L4P** was reversible or quasi-reversible in all of the used solvents, it was irreversible for the fluorinated counterparts (figure 3.9 and Table 3.1). The generated radical anion probably undergoes further chemical transformations, potentially fluoride dissociation. Because of the irreversible nature of the reduction, the comparability between the potential measured and the actual position of the LUMO is limited. Regarding the reduction potentials in THF, there is a relatively large gap between **L4P** and **L4P-F2**, as well as between **L4P-F4** and **L4P-F6** ($\Delta E_p^c \approx$ 400 - 500 mV). In contrast, the gap between **L4P-F2** and **L4P-F4**

[17]Electrochemical measurements were carried out by Dr. Lutz Grubert (HU Berlin, Institut für Chemie).

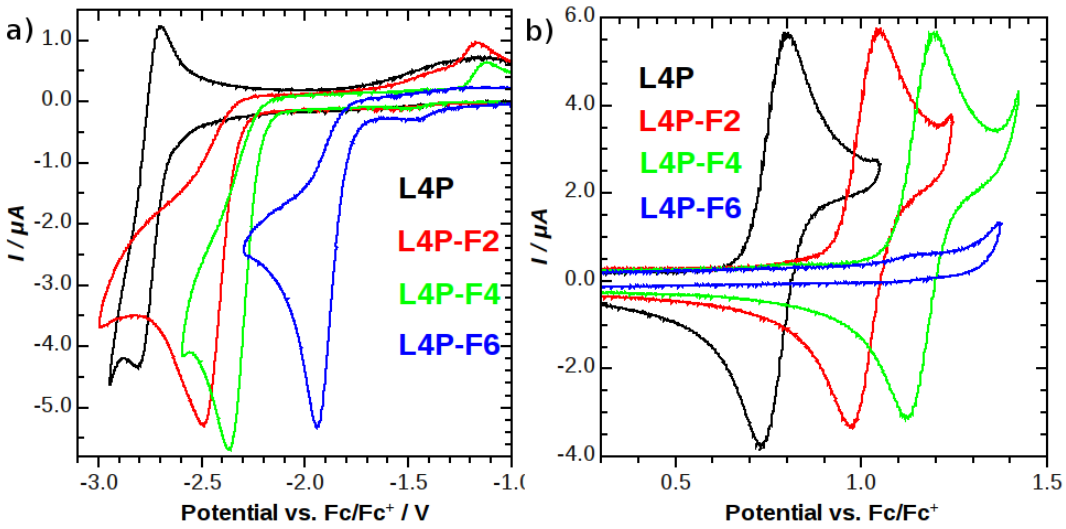

Figure 3.9. Cyclic voltammetry results for **L4P**, **L4P-F2**, **L4P-F4**, and **L4P-F6** (0.1 mol L^{-1} Bu_4NPF_6; dE/dt = 1 V s^{-1}). a) Cathodic, 10^{-3} mol L^{-1} or saturated in DMF, b) anodic, 10^{-3} mol L^{-1} or saturated in acetonitrile.

is much smaller (ΔE_p^c = 130 mV). Accordingly, the influence of the central fluorine substitution seems to be stronger than that in the terminal position. The position of the LUMO of **L4P** can be approximated to be situated between -1.8 and -2.0 eV.[18] The overall potential shift between **L4P** and **L4P-F6** is significant (approximately 1 V), and thus, it is reasonable to assume that the LUMO shifts by at least 1 eV. Due to the irreversible nature of the electrochemical reduction, an estimation of the actual LUMO was hindered. When carrying out the measurements in acetonitrile and DMF, the findings were similar (table 3.1).

Of the three suitable solvents employed, only acetonitrile (figure 3.9b) was somewhat suited to investigate the oxidation behavior of the compounds. In acetonitrile,

Table 3.1. Reduction and oxidation potentials (vs. the ferrocene couple Fc/Fc^+) as well as frontier molecular orbital levels of the investigated compounds.

	E_p^c (THF) V	E_p^c (MeCN) V	E_p^c (DMF) V	E_p^a (MeCN) V	E_{HOMO}[iii] eV	E_{LUMO}[iv] eV
L4P	-3.006	-	-2.814	0.797	-5.6	-2.2[v]
L4P-F2	-2.532[i]	-2.482[i]	-2.496[i]	1.045	-5.8	-2.4
L4P-F4	-2.400[i]	-2.249[i]	-2.372[i]	1.192	-6.0	-2.6
L4P-F6	-1.994[i]	-1.859[i]	-1.944[i]	1.2[i,ii]	-	-

[i]Irreversible peak. [ii]Low-intensity signal. [iii]Estimated from reversible reduction waves using $E_{LUMO} = -4.8 - E_p^c$ (vs. Fc/Fc^+)[121]. [iv]Estimated using $E_{LUMO} = E_{HOMO}$ + optical gap (from UV/Vis absorption spectroscopy). [v]Alternatively, using the (quasi)reversible reduction potential in DMF and $E_{LUMO} = -4.8 - E_p^c$ (vs. Fc/Fc^+),[121] yields an estimated LUMO level at -2.0 eV.

[18]The frontier orbital level can be estimated by subtracting the (reversible) peak potential from -4.8 eV ($E_{LUMO} = -4.8 - E_p^c$ vs. Fc/Fc^+) according to ref. [121].

L4P, **L4P-F2**, and **L4P-F4** undergo reversible one-electron oxidation steps and the trend of the potentials is similar to that observed for their reduction. Notably, the value measured for **L4P-F6** has to be considered with great care due to the compound's low solubility in acetonitrile.

3.2.4 Optical Properties

The influence of fluorine substitution on the optical properties of conjugated organic molecules may be very variable. Depending on the interplay of the opposing -I and the + M effects, that is, σ-accepting versus π-donating properties of fluorine, a change in the position of the absorption bands (hypso- or bathochromic shifts), their widths (broadening), and their extinction coefficients (hypo- or hyperchromicity) may occur.[122, 123]
Non-fluorinated **L4P** (figure 3.10, table 3.2, black lines) has an absorption maximum at 369 nm (3.4 eV) with ε = 100000 L mol^{-1} cm^{-1}. The absorption and emission spectra of **L4P** display a relatively narrow vibronic fine structure; the first 0,0-transition is the most intense (see table 3.3). The fluorescence quantum yield in solution (CH_2Cl_2) is practically unity ($\Phi \approx 1$). In the case of **L4P-F2** and **L4P-F4** (Figure 3.10, red and green lines, respectively), the first two vibronic bands have about the same intensity between ε = 55000 and 60000 L mol^{-1} cm^{-1} and are slightly hypsochromically shifted with respect to **L4P**. For **L4P-F4**, the absorption and emission spectra are as expected mirror images of each other, whereas, in the case of **L4P-F2**, the intensity variation of the vibronic bands in both spectra is completely opposite to what would be expected based on the mirror image rule. Perhaps more importantly, the fluorescence quantum yield decreases significantly and is be-

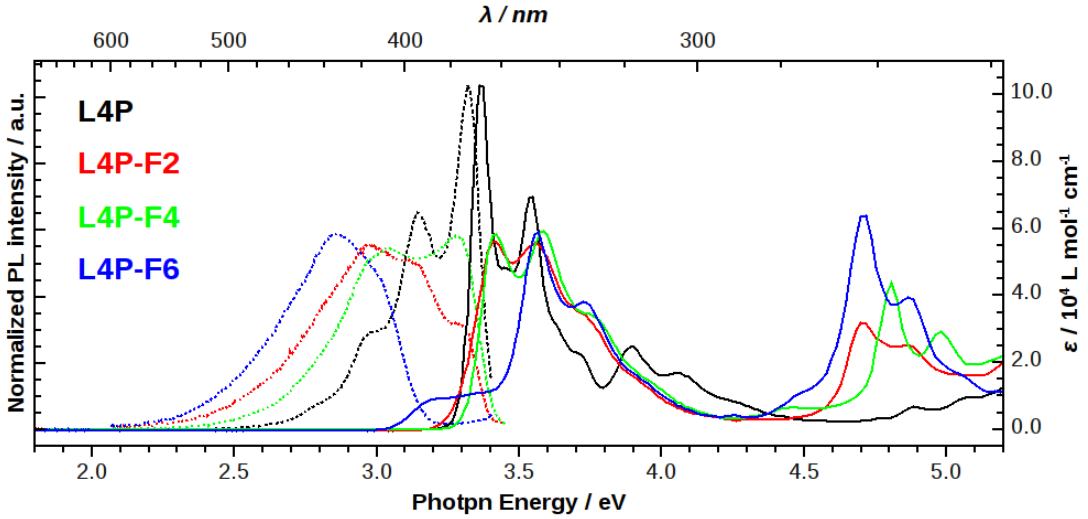

Figure 3.10. Absorption (solid line, $\approx 10^{-5}$ mol L^{-1}; $4 \cdot 10^{-6}$ mol L^{-1} for **L4P-F6**) and emission (dotted line, normalized to the corresponding absorption maxima, $\approx 5 \cdot 10^{-7}$ mol L^{-1} for **L4P** and **L4P-F6**; $\approx 10^{-5}$ mol L^{-1} for **L4P-F2** and **L4P-F4**) spectra of **L4P**, **L4P-F2**, **L4P-F4**, and **L4P-F6** in CH_2Cl_2.

low 1 % in both cases, that is, **L4P-F2** and **L4P-F4**. The optical properties of **L4P-F6** are quite different from the other derivatives. The first intense vibronic transition is hypsochromically shifted to about the same position as the second transition of the other molecules. However, there is also a broad shoulder tailing far into the visible region. The emission spectrum is broad without vibronic fine structure and the most bathochromically shifted of all three derivatives. **L4P-F6** displays a fluorescence quantum yield of about 20 %. Furthermore, all three of the fluorinated molecules exhibit a strongly enhanced transition between 4.5 and 5 eV that is most likely associated with the S_2 excited state.
Considering the changes in the optical properties upon fluorine substitution, again the influence of the substituent on the central methylene bridge seems to be stronger than that of the outer ones. Already **L4P-F2** differs more strongly from **L4P** than **L4P-F4**. Surprisingly, the fluorescence quantum yield of **L4P-F6** is far higher than those for the mixed substituted molecules, although the spectral features are mostly altered. At this point, it can only speculated about potential reasons for the observed behavior, which may be a result of the stronger dipole perpendicular to the optical transition in the **L4P-Fx**, relative to **L4P**, which, together with the mesomeric and inductive effects, could cause an alteration to the electronic and vibrational states.[122, 123]

Table 3.2. Absorption data of investigated compounds.

compound	solvent	λ_{max} / nm	ϵ_{max} / 10^3 L mol^{-1} cm^{-1} (λ / nm)
L4P	CH_2Cl_2	369, 350, 319	104 (369)
L4P-F2	CH_2Cl_2	364, 349, 264	56 (364)
L4P-F4	CH_2Cl_2	363, 346, 258	59 (363)
L4P-F6	CH_2Cl_2	348, 333, 263	59 (348)

λ_{max}: Absorption maxima; ϵ_{max} (λ): Absorption maximum and corresponding wavelength.

Table 3.3. Emission data of investigated compounds.

compound	solvent	λ_{Em} / nm	λ_{Ex} / nm (Φ)	λ_{Ex} / nm (Graph)	Φ_{PL}
L4P	CH_2Cl_2	374, 395	354	354	1.0
L4P-F2	CH_2Cl_2	376, 415	354	350	<0.01
L4P-F4	CH_2Cl_2	378, 408	354	350	<0.01
L4P-F6	CH_2Cl_2	434	354	354	0.2

λ_{Em}: Emission maxima; λ_{Ex} (Φ): Excitation wavelength for the determination of the quantum yield; λ_{Ex} (Graph): Excitation wavelength for the production of the graph; Φ_{PL}: Photoluminescence quantum yield.

3.3 Conclusions

Four different L4Ps with varying degrees of fluorination in their three benzylic methylene bridge positions, namely, **L4P-Fn** (n = 0, 2, 4, 6), have been prepared. The increasing amount of fluorine, leading to a dipole orthogonal to the long axis of the molecule, had a strong influence on its packing in the crystalline phase. The introduction of fluorine led to largely decreased reduction potentials by up to 1 eV in the case of **L4P-F6**, compared with **L4P**. Fluorination furthermore affected the relative intensities of vibronic transitions and their positions in the absorption and emission spectra and led to largely reduced fluorescence quantum yields. With regard to both electrochemical and optical properties, fluorination of the central methylene bridge seemed to have a more pronounced effect than fluorination of the terminal methylene groups. Concerning potential applications of these and related fluorinated derivatives, we conclude that they are not suitable as emitters in OLED-type devices due to their poor fluorescence quantum yields, yet their low-lying LUMO levels and the possibility to engineer their packing behavior might render them interesting for other organic electronic applications.

3.4 Experimental

3.4.1 Organic Synthesis

^{1}H-NMR and ^{13}C-NMR spectra were referenced to 7.26 ppm and 77.16 ppm, respectively, for $CDCl_3$ and 5.32 ppm and 53.8 ppm, respectively, for CD_2Cl_2. ^{19}F-NMR-spectra were referenced to 0.00 ppm for $CFCl_3$.

12,12,15,15-Tetramethyl-12,15-dihydrospiro[cyclopenta[2,1-*b*:3,4-*b'*]difluorene-6,2'-[1,3]dithiolane] (1)
Ethane dithiol (0.25 mL, 8.28 g, 3 mmol) and 50% BF_3·THF (0.33 mL, 0.42 g, 1.5 mmol) were added to a stirred suspension of **L4P-O** (0.41 g, 1.0 mmol) in CH_2Cl_2 (20 mL) and stirring was continued over night at room temperature. Then, aqueous NaOH (≈ 10%) was added to the mixture, which had turned colorless before. After stirring for another hour, the mixture was extracted with CH_2Cl_2. The organic phase was dried ($MgSO_4$) and the solvent was removed. Dithiolane **1** (0.49 g, 1.0 mmol) was obtained as a nearly colorless solid in quantitative yield.
^{1}H-NMR (300 MHz, CD_2Cl_2) δ [ppm] = 8.04 (d, J = 0.7 Hz, 2H), 7.82 - 7.77 (m, 2H), 7.76 (d, J = 0.7 Hz, 2H), 7.50 - 7.45 (m, 2H), 7.41 - 7.30 (m, 4H), 3.93 (s, 4H), 1.56 (s, 12H).
^{13}C-NMR (75 MHz, CD_2Cl_2) δ [ppm] = 155.3, 154.4, 150.9, 140.0, 139.3, 138.5, 127.6, 127.4, 123.0, 120.3, 117.1, 114.2, 47.0, 43.0, 27.5.

6,6-Difluoro-12,12,15,15-tetramethyl-12,15-dihydro-6*H*-cyclopenta[2,1-*b*:3,4-*b'*]difluorene (L4P-F2)
In a polypropylene screw-cap beaker a suspension of NIS (0.47 g, 2.1 mmol) in CH_2Cl_2 (20 mL) was cooled to 0 °C and 70% HF/pyridine (0.51 mL, 0.56 g, 20 mmol

HF) was added. Then, **1** (0.49 g, 1.0 mmol) was added and the mixture was stirred for 15 min, followed by the addition of an excess of basic alumina. The mixture was diluted with CH_2Cl_2 and filtered through a pad of silica. The resulting solution was washed with aqueous $Na_2S_2O_3$ and subsequently with aqueous $NaHCO_3$. The organic phase was dried ($MgSO_4$) and the solvent was removed. The crude product was purified by column chromatography (petroleum ether bp. 40 – 60 °C / CH_2Cl_2) to give **L4P-F2** (0.37 g, 0.85 mmol, 85% yield) as a colorless solid.
^{1}H-NMR (300 MHz, $CDCl_3$) δ (ppm) = 7.97 (s, 2H), 7.80 - 7.73 (m, 2H), 7.68 (s, 2H), 7.49 - 7.42 (m, 2H), 7.42 - 7.31 (m, 4H), 1.57 (s, 12H).
^{1}H-NMR (300 MHz, CD_2Cl_2) δ (ppm) = 8.00 - 7.95 (m, 2H), 7.81 - 7.76 (m, 2H), 7.74 (d, J = 0.8 Hz, 2H), 7.51 - 7.45 (m, 2H), 7.42 - 7.33 (m, 4H), 1.56 (s, 12H).
^{13}C-NMR (75 MHz, CD_2Cl_2) δ (ppm) = 158.7 (s), 154.2 (s), 140.4 (s), 139.5 (t, J = 5.1 Hz), 138.6 (s), 138.0 (t, J = 25.1 Hz), 128.1 (s), 127.6 (s), 123.0 (s), 120.5 (s), 115.7 (s), 115.2 (s), 47.4 (s), 27.1 (s).
^{19}F-NMR (282 MHz, CD_2Cl_2) δ (ppm) = -110.53 (s).

6',6'-Dimethyl-6'*H*-dispiro[[1,3]dithiolane-2,12'-cyclopenta[2,1-*b*:3,4-*b'*]difluorene-15',2"-[1,3]dithiolane] (2)
A solution of **L4P-O2** (0.33 g, 0.83 mmol), ethane dithiol (0.35 mL, 0.39 g, 4.15 mmol), and 50% BF_3·THF (0.92 mL, 1.16 g, 4.15 mmol) in $CHCl_3$ (40 mL) was refluxed over night, whereupon the orange color vanished. After cooling to room temperature, aqueous NaOH (≈ 10%) was added and the mixture was stirred for another hour. Then, it was diluted with CH_2Cl_2, water was added and the phases were separated. Ethyl acetate was added to the organic phase and it was filtered through silica. After adding some ethanol, the major amount of solvent was removed and the precipitate was filtered off and dried under vacuum. Thioketal **2** (0.43 g, 0.78 mmol, 94% yield) was obtained as a nearly colorless solid.
^{1}H-NMR (300 MHz, CD_2Cl_2) δ (ppm) = 8.10 (d, J = 0.7 Hz, 2H), 7.73 – 7.66 (m, 6H), 7.36 (pd, J = 7.4, 1.4 Hz, 4H), 3.98 – 3.80 (m, 8H), 1.60 (s, 6H).
^{13}C-NMR (75 MHz, CD_2Cl_2) δ (ppm) = 155.6, 151.7, 150.3, 139.9, 138.8, 138.4, 128.9, 128.4, 125.5, 119.9, 117.3, 114.5, 68.8, 46.9, 42.9, 27.5.

12,12,15,15-Tetrafluoro-6,6-dimethyl-12,15-dihydro-6*H*-cyclopenta[2,1-*b*:3,4-*b'*]difluorene (L4P-F4)
In a polypropylene screw-cap beaker a stirred mixture of NIS (0.68 g, 3.04 mmol) and CH_2Cl_2 (20 mL) was cooled to 0 °C and 70% HF/pyridine (0.39 mL, 0.43 g, 15.2 mmol HF) was added. Then, **2** (0.42 g, 0.76 mmol) was added and stirring was continued for 45 min. Afterwards the reaction was quenched with excess basic alumina and diluted with CH_2Cl_2. It was filtered through a pad of silica and washed with aqueous $Na_2S_2O_3$. The organic phase was dried ($MgSO_4$) and the solvent was removed. The crude product was purified by column chromatography (cyclohexane / ethyl acetate) to give **L4P-F4** (0.20 g, 0.45 mmol, 59% yield) as a colorless solid.
^{1}H-NMR (500 MHz, $CDCl_3$) δ (ppm) = 7.99 (d, J = 0.5 Hz, 2H), 7.67 – 7.61 (m, 6H), 7.49 (t, J = 7.5 Hz, 2H), 7.35 (td, J = 7.5, 0.9 Hz, 2H), 1.59 (s, 6H).
^{13}C-NMR (126 MHz, $CDCl_3$) δ (ppm) = 158.3 (s), 139.7 (t, J = 4.7 Hz), 139.4 (s),

138.6 (t, J = 25.1 Hz), 137.9 (t, J = 25.2 Hz), 132.2 (s), 128.8 (s), 124.0 (s), 123.0 (t, J = 242.6 Hz), 120.3 (s), 115.9 (s), 115.0 (s), 47.4 (s), 27.0 (s).
^{19}F-NMR (282 MHz, $CDCl_3$) δ (ppm) = -110.25 (s).

Diethyl 2,2'-(9,9-difluoro-9*H*-fluorene-2,7-diyl)dibenzoate (5)
Under an argon atmosphere *n*BuLi (15 mL, 33 mmol, 2.2 mol/L in cyclohexane) was added to a solution of 2,7-dibromo-9,9-difluorofluorene **3** (5.4 g, 15 mmol) in dry THF (40 mL) at -78 °C. After stirring for 1 h, tributyl borate (9.6 mL, 8.3 g, 36 mmol) was added and stirring was continued for 1 h at room temperature. The resulting solution was combined with a mixture of **4** (9.8 g, 37.5 mmol), Cs_2CO_3 (19.6 g, 60 mmol) and Pd(dppf)Cl_2·CH_2Cl_2 (0.33 g, 0.45 mmol) in ethanol (40 mL) and DMF (10 mL) and stirred for 12 h at 60 °C. Then, the mixture was poured into water and the precipitate was filtered off carefully[19]. It was dissolved in CH_2Cl_2, dried ($MgSO_4$) and the solvent was removed. The crude product was purified by column chromatography (cyclohexane / ethyl acetate) to give **5** (3.6 g, 7.2 mmol) in 48% yield.
^{1}H-NMR (300 MHz, $CDCl_3$) δ (ppm) = 7.92 (dd, J = 7.7, 1.1 Hz, 2H), 7.68 – 7.55 (m, 6H), 7.52 – 7.40 (m, 6H), 4.16 (q, J = 7.1 Hz, 4H), 1.05 (t, J = 7.1 Hz, 6H).
^{13}C-NMR (75 MHz, $CDCl_3$) δ (ppm) = 168.6, 142.6, 141.6, 138.2, 132.4, 131.6, 131.2, 130.6, 130.3, 127.9, 124.3, 120.2, 61.3, 27.1, 13.8.
^{19}F-NMR (282 MHz, $CDCl_3$) δ (ppm) = -111.07 (s).

3,6-Dibromospiro[fluorene-9,2'-[1,3]dithiolane] (7)
Ethane dithiol (7.5 mL, 8.5 g, 90 mmol) and 50% BF_3·THF (13.3 mL, 16.8 g, 60 mmol) were added to a suspension of **6** (20.3 g, 60 mmol) in CH_2Cl_2 (100 ml). After stirring the mixture for 3 days at 40 °C, it turned nearly colorless and aq. NaOH (≈ 10%) was added. The mixture was stirred for another hour and then extracted with CH_2Cl_2. The organic phase was dried ($MgSO_4$) and the solvent was removed to give 25 g (60 mmol, quantitative yield) of thioketal **7**.
^{1}H-NMR (300 MHz, $CDCl_3$) δ (ppm) = 7.70 (d, J = 1.7 Hz, 2H), 7.54 (d, J = 8.2 Hz, 2H), 7.46 (dd, J = 8.2, 1.8 Hz, 2H), 3.76 (s, 4H).
^{13}C-NMR (75 MHz, CDCl3) δ (ppm) = 149.8, 139.3, 132.0, 126.9, 123.4, 122.9, 68.0, 42.6.

3,6-Dibromo-9,9-difluoro-9*H*-fluorene (8)
In a polypropylene screw cap beaker, thioketal **7** (10.9 g, 26.3 mmol) was slowly added to a mixture of 70% HF/pyridine (4.0 mL, 4.4 g, 158 mmol HF) and NIS (17.8 g, 78.9 mmol) in CH_2Cl_2 (60 mL) at 0 °C. After stirring for 1 h, excess basic alumina was added and the mixture was stirred for another 15 min. The mixture was diluted (CH_2Cl_2) and the solids were filtered off. The solution was washed with aqueous $Na_2S_2O_3$, dried ($MgSO_4$), and the solvent was removed. Column chromatography (petroleum ether / CH_2Cl_2) gave **8** (8.4 g, 23.3 mmol, 89% yield) as a colorless solid.
^{1}H-NMR (300 MHz, $CDCl_3$) δ (ppm) = 7.66 (m, 2H), 7.49 (m, 4H).
^{13}C-NMR (75 MHz, $CDCl_3$) δ (ppm) = 140.2 (t, J = 5.0 Hz), 136.9 (t, J = 25.7 Hz),

[19] In case the product mixture remains oily, extraction with CH_2Cl_2 may be necessary.

132.5 (s), 126.8 (s), 125.4 (s), 124.3 (s), 122.2 (t, J = 236.9 Hz).
^{19}F-NMR (282 MHz, $CDCl_3$) δ (ppm) = -111.56 (s).

9,9-Difluoro-3,6-bis(methoxymethyl)-9*H*-fluorene (9)
Under an argon atmosphere *n*BuLi (28 mL, 60.7 mmol, 2.2 mol/L in cyclohexane) was added to a stirred solution of **8** (9.1 g, 25.3 mmol) in dry THF (150 mL) at -78 °C. After stirring for 1 h at that temperature, chlormethyl methylether (5.8 mL, 6.2 g, 75.9 mmol, MOM-Cl) was added and the solution was allowed to warm to room temperature. The reaction was stirred for another hour, until it was quenched with aqueous $NaHCO_3$. The mixture was extracted with ethyl acetate. The organic phase was dried ($MgSO_4$) and the solvent was removed. The crude product was purified by column chromatography (cyclohexane / ethyl acetate) to give **9** (3.8 g, 13.1 mmol) in 52% yield.
^{1}H-NMR (300 MHz, $CDCl_3$) δ (ppm) = 7.62 – 7.55 (m, 4H), 7.28 (d, J = 7.9 Hz, 2H), 4.52 (s, 4H), 3.43 (s, 6H).
^{13}C-NMR (75 MHz, $CDCl_3$) δ (ppm) = 142.9 (s), 139.8 (t, J = 4.8 Hz), 137.7 (t, J = 25.3 Hz), 127.9 (s), 123.8 (s), 123.2 (t, J = 228.9 Hz), 119.6 (s), 74.4 (s), 58.5 (s).
^{19}F-NMR (282 MHz, $CDCl_3$) δ (ppm) = -111.22 (s).

2,7-Dibromo-9,9-difluoro-3,6-bis(methoxymethyl)-9*H*-fluorene (10)
Mathanesulfonic acid (0.5 mL) was added to a mixture of **9** (2.9 g, 10.0 mmol) and DIB[20] (5.7 g, 20 mmol) in acetic acid (50 mL). After stirring the mixture for 30 min at room temperature, it was poured on cold aqueous NaOH and extracted with CH_2Cl_2. The organic phase was washed with aqueous $Na_2S_2O_3$, dried ($MgSO_4$), and the solvent was removed. The crude product was purified by column chromatography (petroleum ether / ethyl acetate) to give **10** (2.23 g, 5.0 mmol) in 50% yield.
^{1}H-NMR (300 MHz, CD_2Cl_2) δ (ppm) = 7.79 – 7.73 (m, 4H), 4.54 (d, J = 0.9 Hz, 4H), 3.52 (s, 6H).
^{13}C-NMR (75 MHz, CD_2Cl_2) δ (ppm) = 143.0 (s), 138.5 (t, J = 4.8 Hz), 138.1 (t, J = 25.2 Hz), 128.2 (s), 122.4 (t, J = 244.4 Hz), 122.3 – 122.2 (m), 120.8 (s), 74.0 (s), 59.1 (s).
^{19}F-NMR (282 MHz, CD_2Cl_2) δ (ppm) = -110.94 (s).

Dimethyl 2,7-dibromo-9,9-difluoro-9*H*-fluorene-3,6-dicarboxylate (11)
A mixture of **10** (1.8 g, 4.0 mmol), TEBAC (5.5 g, 24 mmol) and $KMnO_4$ (3.8 g, 24 mmol) in CH_2Cl_2 (20 mL) was refluxed over night. After cooling to room temperature, the reaction was quenched with aqueous $Na_2S_2O_3$ and extracted with CH_2Cl_2. The organic phase was dried ($MgSO_4$) and the solvent was removed. The crude product was purified by column chromatography (cyclohexane / ethyl acetate) to give **11** (1.45 g, 3.2 mmol) in 76% yield.
^{1}H-NMR (300 MHz, $CDCl_3$) δ (ppm) = 7.96 (s, 2H), 7.91 (t, J = 1.4 Hz, 2H), 3.98 (s, 6H).
^{13}C-NMR (75 MHz, $CDCl_3$) δ (ppm) = 165.9 (s), 140.9 (t, J = 25.4 Hz), 137.0 (t, J = 4.7 Hz), 136.4 (s), 130.3 (s), 123.4 (s), 122.9 (s), 121.1 (t, J = 247.0 Hz), 53.1

[20] DIB was synthesized according to ref. [119].

(s).
^{19}F-NMR (282 MHz, $CDCl_3$) δ (ppm) = -110.88 (s).

Dimethyl 9,9-difluoro-2,7-diphenyl-9*H*-fluorene-3,6-dicarboxylate (12)
A mixture of **11** (1.43 g, 3.0 mmol), phenylboronic acid (1.46 g, 12 mmol), Cs_2CO_3 (4.9 g, 15 mmol), and Pd(dppf)Cl_2·CH_2Cl_2 (0.08 g, 0.09 mmol) was stirred in ethanol/THF/DMF (40/40/10 mL) under an argon atmosphere at 65 °C for 15 min. After cooling to room temperature, the mixture was diluted with water and extracted with CH_2Cl_2. The organic phase was dried ($MgSO_4$) and the solvent was removed. The crude product was purified by column chromatography (cyclohexane / ethyl acetate) to give **12** (1.19 g, 2.53 mmol, 84% yield) as a colorless solid.
^{1}H-NMR (300 MHz, $CDCl_3$) δ (ppm) = 8.05 (s, 2H), 7.69 (m, 2H), 7.49 – 7.32 (m, 10H), 3.68 (s, 6H).
^{13}C-NMR (75 MHz, $CDCl_3$) δ (ppm) = 168.6 (s), 144.0 (s), 140.4 (t, J = 25.3 Hz), 140.3 (s), 137.4 (t, J = 4.8 Hz), 135.1 (s), 128.5 (s), 128.3 (s), 128.1 (s), 126.4 (s), 122.1 (s), 52.5 (s).
^{19}F-NMR (282 MHz, $CDCl_3$) δ (ppm) = -111.10 (s).

6,6,12,12,15,15-hexafluoro-12,15-dihydro-6*H*-cyclopenta[2,1-b:3,4-*b'*]difluorene (L4P-F6)
A solution of 6 g NaOH in 15 mL of water was added to a suspension of **12** (0.94 g, 2.0 mmol) in ethanol (60 mL). The mixture was stirred over night at 55 °C. After cooling to room temperature, water and HCl were added and the precipitate that formed thereupon was filtered off. After drying in air, and subsequently under high vacuum 0.80 g of crude acid have been obtained as a nearly colorless powder.
The crude product was suspended in $SOCl_2$ (40 mL) and refluxed for 1 h. Then, $MeSO_3H$ (1 mL) was added and refluxing was continued for 30 min. After cooling to room temperature, the precipitate was filtered off. Upon air-drying, 0.72 g of crude product have been obtained as a pink powder.
Then, it was suspended in 1,1,2,2-tetrachloroethane (25 mL) and ethane dithiol (0.6 mL, 0.75 g, 8.0 mmol), as well as 50% BF_3·THF (1.8 mL, 2.24 g, 8.0 mmol) were added. The mixture was stirred for 2 h at 120 °C, whereupon the red color disappeared. After cooling to room temperature, the reaction was carefully quenched with aqueous NaOH ($\approx$ 10%) and extracted with CH_2Cl_2. The major amount of solvent was removed from the organic phase and the precipitate was filtered off. Air-drying gave 1.1 g of crude material as a nearly colorless powder.
A mixture of NIS (2.25 g, 10.0 mmol) and HF/pyridine (70% HF; 3.5 mL) in CH_2Cl_2 (30 mL) was cooled to 0 °C. Then, the crude product of the last stage was added and the reaction was stirred for 1 h. Finally, it was carefully quenched with excess basic alumina and sodium bisulfite and filtered through a pad of celite, using CH_2Cl_2 to purge. The solvent was removed. Pre-purification was achieved by column chromatography using cyclohexane / ethyl acetate and again using hot tetrachloromethane as eluant. Then, the crude product was subsequently crystallized from chlorobenzene and THF. Finally **L4P-F6** (0.08 g, 0.2 mmol, 9% yield) was obtained as pale yellow crystals.
^{1}H-NMR (500 MHz, THF-D_8) δ (ppm) = 8.20 (s, 2H), 8.09 (s, 2H), 7.85 (d,

J = 7.6 Hz, 2H), 7.68 (d, J = 7.5 Hz, 2H), 7.58 (td, J = 7.5, 0.6 Hz, 2H), 7.44 (td, J = 7.5, 0.9 Hz, 2H).
^{19}F-NMR (471 MHz, THF-D_8) δ (ppm) = -112.59 (s), -112.73 (s).
EI-MS: m/Z = 450.08434 (calculated: 450.08432).

3.4.2 Crystal Structure Analysis

The diffraction data were collected on a STOE IPDS 2Θ diffractometer at 100 K. Crystallographic data are depicted in the crystallographic table. The structures were solved by direct methods (SHELXS-97)[124] and were refined with the full-matrix least-squares method on F^2 (SHELX-97 and SHELXL-2013)[21]. The hydrogen atoms were placed at the calculated positions and were refined by using a riding model. The data, which contain the supplementary crystallographic information, can be obtained free of charge from The Cambridge Crystallographic Data Centre via `www.ccdc.cam.ac.uk/data_request/cif`.

[21] [124]; Sheldrick, G. M., *SHELXL, Crystal Structure Refinement*, **2013** University of Göttingen, Germany.

Crystallographic Table

compound	**L4P**·(THF)	**L4P-F$_2$**	**L4P-F$_4$**
Formular	$C_{37}H_{38}O$	$C_{31}H_{24}F_2$	C29 H18 F4
Formular weight / g·mol^{-1}	498.67	434.50	442.43
λ / Å	0.71073	0.71073	0.71073
Crystal system	Orthorhombic	Orthorhombic	Orthorhombic
Space group	*Pbca*	$Pna2_1$	*Pnma*
a / Å	10.8148(3)	17.7321(7)	15.1402(5)
b / Å	26.1707(9)	19.5341(6)	6.9271(3)
c / Å	19.8964(5)	6.6038(2)	19.8487(7)
α / °	90	90	90
β / °	90	90	90
γ / °	90	90	90
V / Å^3	5631.3(3)	2287.43(13)	2081.69(14)
Z	8	4	4
Density / g·cm^{-3}	1.176	1.262	1.412
μ / mm^{-1}	0.068	0.083	0.106
$F(000)$	2144.0	912.0	912.0
Θ range / °	3.17 - 29.58	3.26 - 27.20	2.05 - 29.55
Reflections collected	60986	21843	16607
Independent reflections	7855	4797	3118
Completeness to Θ	0.99	0.99	1.00
R_{int}	0.0610	0.0483	0.0355
GoF on F^2	1.064	1.018	0.880
R_1 [I > 2σ(I)]	0.0558	0.0324	0.0339
wR_2 [I > 2σ(I)]	0.1493	0.0766	0.0872
R_1 (all data)	0.0796	0.0374	0.0507
wR_2 (all data)	0.1598	0.0787	0.0914
$\Delta\rho_{max}/\Delta\rho_{min}$ / e·Å^{-3}	0.77 / -0.51	0.12 / -0.21	0.386 / -0.167
CCDC	985904	985905	985906

3.4.3 Cyclic Voltammetry

Cyclic voltammetry was performed using a PG310 USB (HEKA Elektronik) potentiostat interfaced to a PC with PotMaster v2x43 (HEKA Elektronik) software for data evaluation. A three-electrode configuration contained in a non-divided cell consisting of a platinum disc (d = 1 mm) as working electrode, a platinum plate as counter-electrode and a saturated calomel electrode (SCE) with an agar-agar-plug in a Luggin capillary with a diaphragm as reference electrode was used. Measurements were carried out in *N,N*-dimethylformamide (anhydrous, SIGMA-ALDRICH), THF (anhydrous, inhibitor-free, SIGMA-ALDRICH), or Acetonitrile (HPLC-Grade, VWR, distilled from CaH) containing 0.1 M Bu_4NPF_6 (FLUKA – for electrochemical analysis) using a scan rate of dE/dt = 1 V s^{-1}. The data are given in reference to the ferrocene redox couple (Fc/Fc^+), which was used as external standard.

3.4.4 UV-Vis Spectroscopy

Absorption spectra were recorded on a Varian Cary 50 Bio UV-Visible spectrometer and fluorescence spectra on a Varian Cary Eclipse Fluorescence spectrometer using 10.0 x 10.0 mm quartz cuvettes.

3.4.4.1 Fluorescence Quantum Yield

The fluorescence quantum yield was determined according to

$$\Phi_S = \Phi_R \cdot \frac{\int I_S(\lambda_S) d\lambda_S}{\int I_R(\lambda_R) d\lambda_R} \cdot \frac{[1 - 10^{-E_R(\lambda_{Ex})}]}{[1 - 10^{-E_S(\lambda_{Ex})}]} \cdot \frac{n_S^2}{n_R^2}.$$

In the equation Φ depicts the fluorescence quantum yield, $\int I(\lambda) d\lambda$ the Area under the fluorescence spectrum, $E(\lambda_{Ex})$ the extinction (absorbance) at the excitation wavelength (which was kept the same for sample and reference), and n the refractive index of the solvents used. Index R denotes properties of reference, and S of the unknown sample. 9,10-Diphenylanthracene in cyclohexane, assuming Φ = 1[125], was used as reference.[126, 127]

4 Green Emission in Ladder-Type Quarterphenyl[22]

4.1 Introduction

In the past years there has been a lot of research in the field of organic electronics with the prospect of fabricating low-cost, light-weight, and flexible devices.[16, 128] However, in OPV and in OLED, especially the blue emitting ones, the lifetimes of the devices remains a critical issue. Polyfluorenes, as well as LPPPs[68] have already been exploited in blue emitting OLEDs for some time,[129, 130] but they suffer from relatively fast degradation. There are several studies on the degradation of such compounds. The degradation can be initiated thermally, photochemically or electrochemically. In polyfluorene (PF) the emerging green emission has been attributed to excimers and fluorenone defects, which are capable of trapping the excitation energy.[131–145] Furthermore chain end defects, such as hydroxyl groups, which originate from Suzuki cross couling polymerization, may lead to green emission as well.[146] In LPPPs a break of the bridging units of the polymer backbone was taken into consideration, as well as fragments, such as arylketones and fluorenones were identified by vibrational spectroscopy[147–150] The optical properties of these fragments have also been characterized by means of quantum-chemical calculations and compared to the properties of thermally degraded LPPP films.[150] The most prominent mechanisms of degradation proposed in the literature involve a 9-fluorenylhydroperoxide formed from synthetic defect sites, such as residual 9-hydrogen-substituted such as residual 9-hydrogen-substituted fluorene.[131] In addition, free-radical autoxidation leading to fluorenone type defects has been proposed for thermally[151, 152] as well as photochemically[153, 154] induced degradation, typically necessitating synthetic defect-sites. There is also at least one report on highly purified oligo(alkylfluorene)s, which alternatively claims that gradual degradation of the side chains due to singlet oxygen leads to the fluorenone defect.[155] In contrast to most of these studies dealing with PF, we focus on small molecules, such as the ladder-type quarterphenyl **L4P**, which in combination with ZnO is supposed to be a potent candidate for creating hybrid inorganic-organic systems for opto-electronic devices.[46, 50, 60, 78] In order to assemble these systems, **L4P** was designed to be compatible with organic molecular vapor-deposition, and therefore the molecular weight was minimized by limiting the number of repeat units and omitting solubilizing side chains. In this context it should be emphasized that the small-molecule approach–after proper purification by gradient-sublimation and crystallization–provides a pure sample compound of one well-defined molecular entity, which can be unambiguously structurally characterized. Here, a detailed study

[22] This chapter has already been published in a similar manner in ref. [117].

of the photodegradation of **L4P** is presented, with detailed insights into its kinetics in solution as well as the chemical structure of formed degradation products. Particular attention is on the active species of oxygen being responsible for degradation. The optical properties of the isolated structural defects, deliberately synthesized fluorenone-type defects, and crude degraded mixtures are being compared, showing that the observed absorption and emission characteristics of the degraded samples cannot explained conventional be by the fluorenone-type defect in LPPPs. Finally, time-dependent PL measurements show that intact **L4P** is efficiently transferring its excitation energy to defects.

4.2 Organic Synthesis

The synthesis of the two ketones **L4P-O** and **L4P-O2**[23] involves in both cases cross-coupling of properly substituted phenyl residues to a central fluorene building block (figures 4.1 and 4.2). In the first case of **L4P-O**, annulation proceeds by twofold Friedel-Crafts alkylation of the protected fluorenone core. On the other

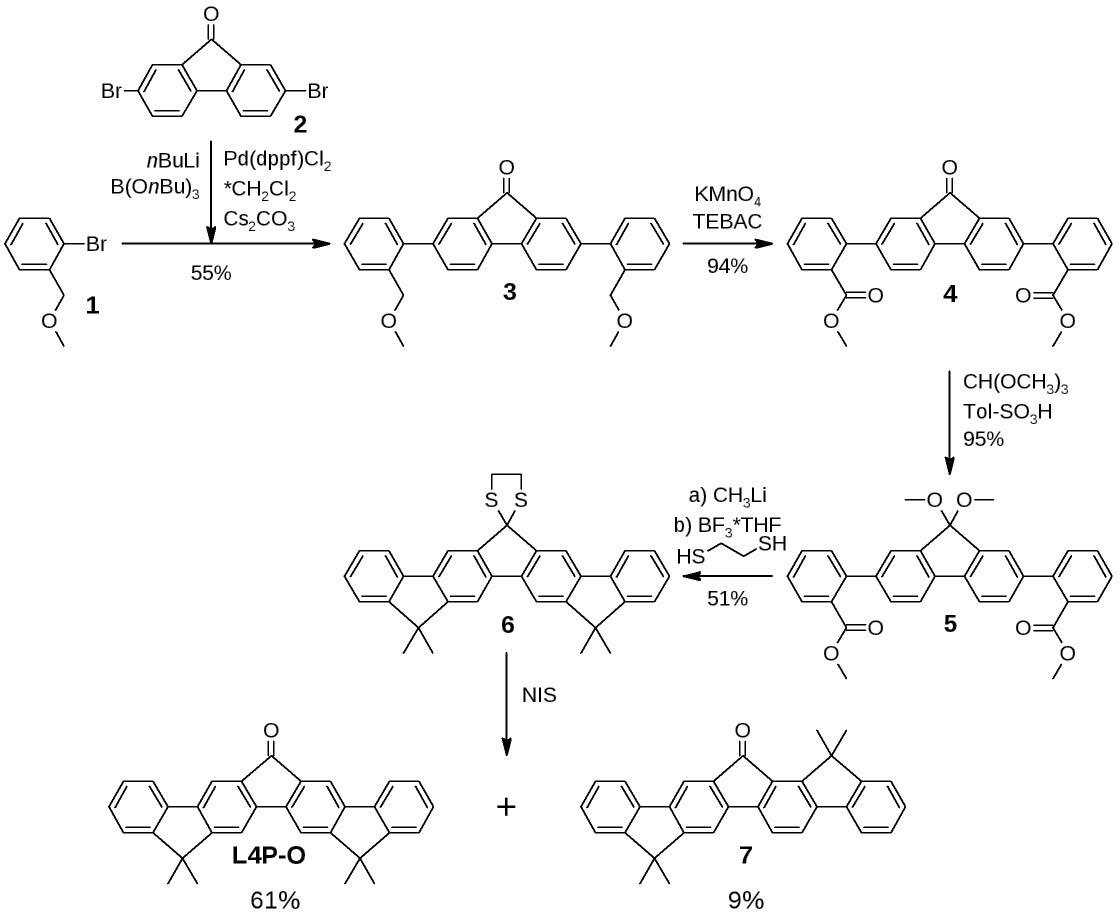

Figure 4.1. Synthesis of **L4P-O**.

[23] **L4P**,as well as **L4P-O2** have been described in ref.[88]; however the synthetic route involves harsh conditions, and characterization data for the intermediates were not provided.

hand, twofold Friedel-Crafts acylation of a central fluorene building block creates the two terminal ketone functionalities in **L4P-O2**. Recently, also a synthesis yielding **L4P** was published,[78] which has been designed to prepare longer oligomers and therefore involves many reaction steps. Comparing the different syntheses, the route via diester **10** described herein for facile access of **L4P** is recommended.

For the synthesis of **L4P-O** (figure4.1), 2,7-dibromofluorenone **2** was chosen as the central building block as well as 2-(methoxymethyl)-bromobenzene as the outer building block carrying the masked groups for intramolecular cyclization. Ether **1** was synthesized from 2-bromobenzyl bromide and sodium methoxide. The synthesis of 2,7-dibromofluorenone was adapted from an old, yet simple protocol by Goldschmiedt and Schranzhofer.[156] Ether **1** was converted to a boronic ester via lithiation and coupled twice to **2** via Suzuki crosscoupling using conditions, which were adapted from a paper by Knochel involving $Pd(dppf)Cl_2$ as catalyst and Cs_2CO_3 as base.[118] Oxidation of diether **3** with $KMnO_4$ yielded diester **4** in good yield.[94] Then, the ketone was protected as its dimethyl ketal using trimethyl orthoformate and toluenesulfonic acid. Subsequently, the ester-functionalities of **5** were reacted with methyl lithium to yield a tertiary alcohol intermediate, which was not isolated. For the twofold condensation to the desired ring-closed product, a Lewis acid needs to be employed, which – if used alone – was found to deprotect the ketone and eliminate the tertiary alcohols, followed by further decompostion. In contrast, addition of 1,2-ethanedithiol (in the presence of the Lewis acid) led to conversion of the ketone to 1,3-dithiolane **6**, which is stable in the presence of the Lewis acid, as well as a minor amount of isomers (that have not been separated). Deprotection with NIS and acetic acid gave the desired **L4P-O** as the main product as well as traces

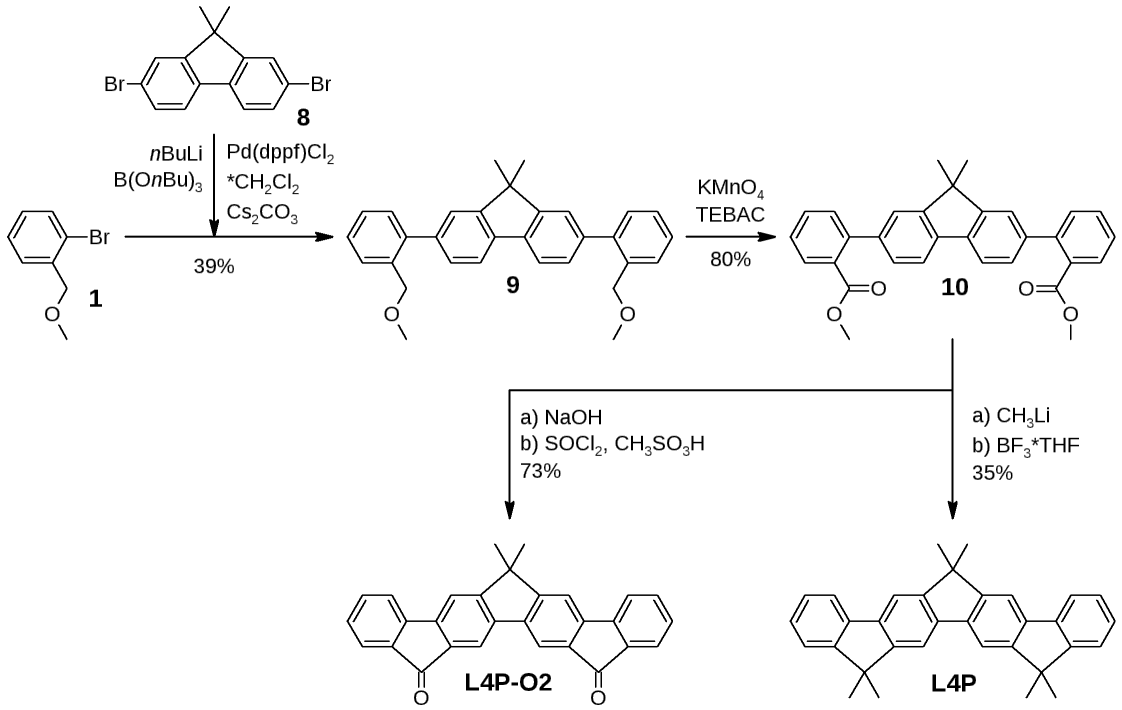

Figure 4.2. Synthesis of **L4P-O2**.

of **7**, which can easily be separated by column chromatography or crystallization.
The synthesis of **L4P-O2** (figure 4.2) is rather straightforward: Ether **1** was coupled to 2,7-dibromofluorene **8** to yield diether **9**, which was subsequently oxidized to the diester **10** and hydrolyzed to the free acid. Condensation to **L4P-O2** was achieved by reaction of the bisacid with thionyl chloride and methanesulfonic acid as catalyst. Depending on the purity and morphology, **L4P-O2** appears as orange powder or deep orange to reddish crystals.
The semi-bridged **DPF-O** was obtained by coupling phenylboronic acid **11** and 2,7-dibromofluorenone **2** (figure 4.3). During this reaction only few amounts of side-products were formed and hence **DPF-O** could be crystallized from the crude product in good yields.

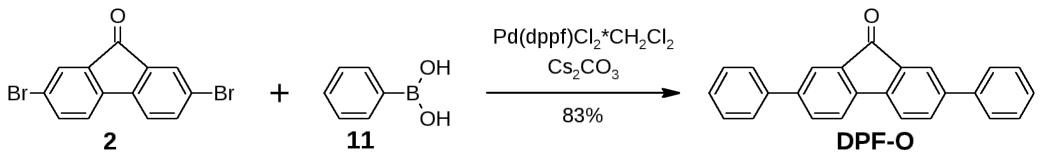

Figure 4.3. Synthesis of **DPF-O**.

4.3 Photodegradation in Solution

To investigate the chemical reactions, which give rise to photodegradation of samples containing **L4P**, some initial experiments were carried out in solution. In contrast to thin films it is relatively simple to keep the samples homogeneous and hence the experimental conditions are defined more precisely while at the same time chemical analysis is facilitated. In an initial set of experiments, the influence of different solvents on the process of photodegradation was analyzed by exposing the respective solutions to strong UV-irradiation while acquiring PL spectra. Photodegradation is strongly dependent on the solvent, for example in toluene and THF it is relatively slow whereas solutions in methylene chloride and ethyl acetate degrade much more rapidly (over the course of few hours). By far the fastest photodegradation (over the course of few minutes) occurs in chloroform associated with a rapidly increasing green PL.

4.3.1 Degradation Kinetics from Absorption and Emission Spectroscopy

Based on these initial experiments, methylene chloride and ethyl acetate were chosen for further investigation assuming that in these solvents a general representation of the degradation behavior of **L4P** can be achieved in a reasonable duration of UV-irradiation. To get a better understanding of the process of degradation, kinetic studies of three observables were carried out: The absorbance, the blue PL (excited at 330 nm), which is related to native defect-free **L4P**, and the green emission,

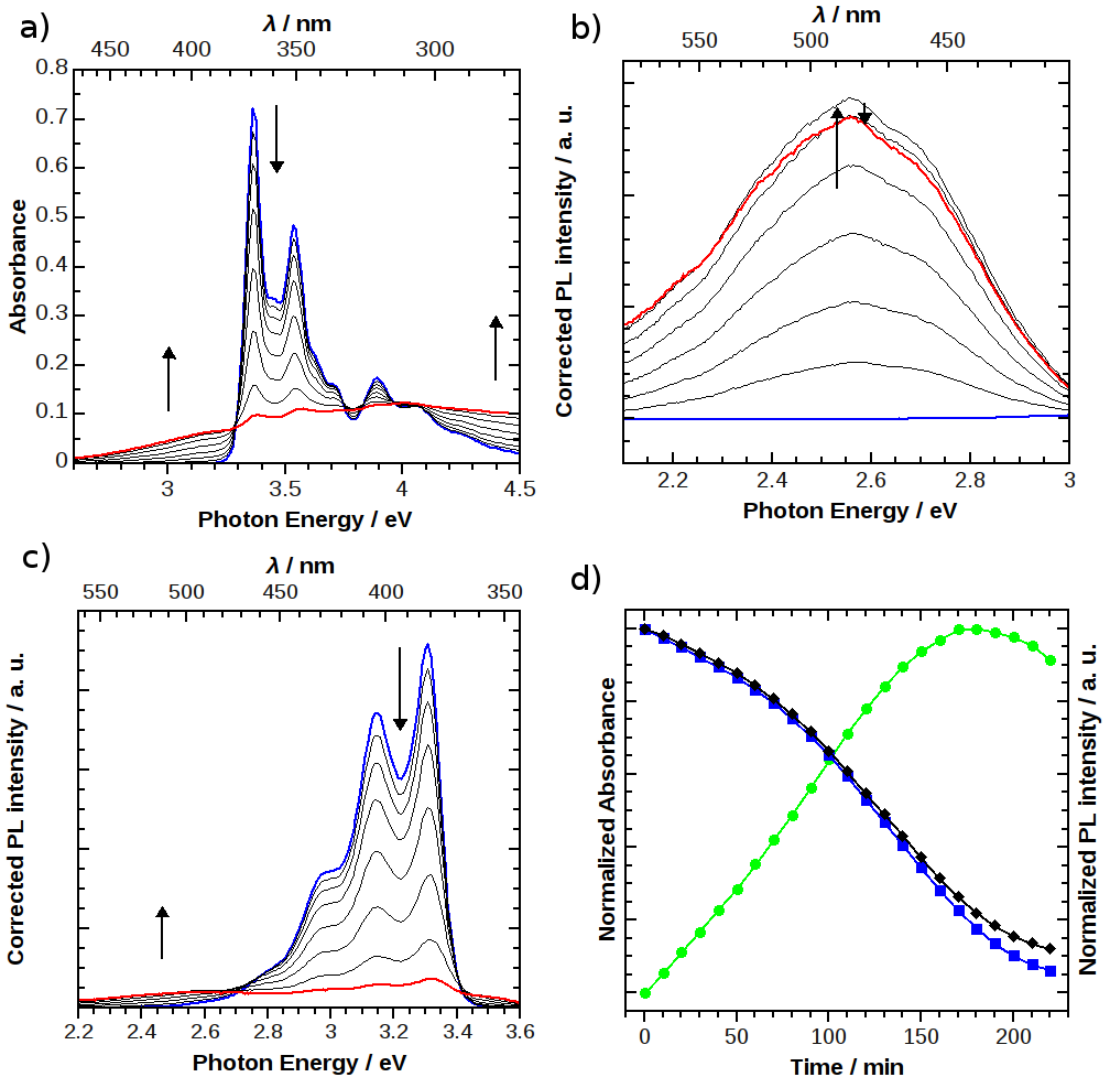

Figure 4.4. Spectral changes upon irradiation of a $6.8 \cdot 10^{-6}$ mol L^{-1} solution of **L4P** in CH_2Cl_2 (25 °C) with 300 - 400 nm light: a) Absorbance spectra, b) corrected PL spectra in green region upon 400 nm excitation, and c) corrected PL spectra in blue region upon 330 nm excitation. Spectra shown in a) - c) were recorded every 30 min. The initial spectra are shown in blue, the final ones in red. d) Resulting plot of changes in absorbance at 369 nm (black diamonds), blue PL detected at 394 nm (blue squares), and green PL detected at 500 nm (green circles) as a function of irradiation time.

which is excited below the absorption edge of **L4P** (at 400 nm) for addressing defect-related states directly. As will be detailed below, energy transfer between **L4P** and the defects is an additional process reducing the LOPP's radiative yield. Therefore, in order to elucidate the primary photodegradation mechanism, the measurements have to be carried out at concentrations sufficiently low to neglect energy transfer. Over the course of irradiation, the narrow absorption peaks around 350 and 370 nm strongly decrease and a broad featureless absorption between 380 and 500 nm

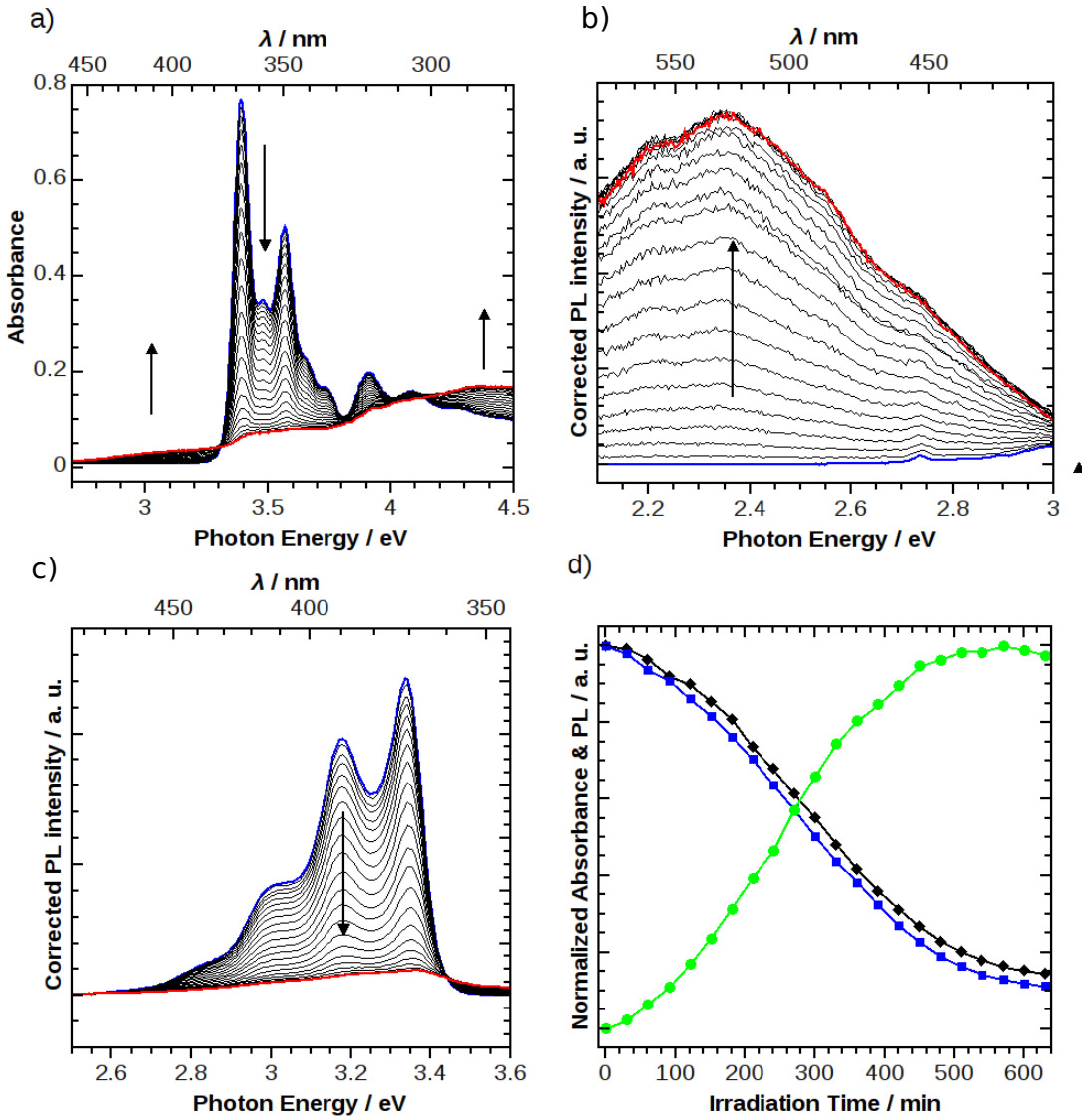

Figure 4.5. Degradation of **L4P** in ethyl acetate (initial concentration $6.8 \cdot 10^{-6}$ mol L^{-1}, time interval: 30 min): a) Changes in the absorption spectrum; b) Changes in the blue emission (excitation at 330 nm); c) Evolution of green emission (excitation at 400 nm), The initial spectra in a) - c) are shown in blue, the final ones in red. d) Absorption (black) and green (detected at 550 nm), as well as blue (detected at 380 nm) PL intensity vs. duration of degradation.

rises (figure 4.4a). In a similar manner the blue **L4P** emission between 370 and 450 nm decreases and loses its vibronic structure (figure 4.4c). Simultaneously, a broad green PL appears with a maximum at 480 nm (figure 4.4b). The time dependent decrease of both the absorption at the 0-0 transition as well as the blue PL is very similar (Figure 4.4d), suggesting that these two spectroscopic signatures correspond to one and the same molecular structure, i.e. **L4P**. Interestingly, after the **L4P** is mostly consumed and the maximum concentration of the primary photoproduct is reached, the green emission eventually also starts to decay.

These findings agree somehow with the common photodegradation mechanisms proposed in the literature that involve formation of carbonyl (C=O) group defects, typically at the bridging benzylic sites.[151–155] If photodegradation would therefore follow this kind of mechanism, structures carrying the fluorenone motif, such as **L4P-O** and **L4P-O2** (figures 4.1 and 4.2) should be formed. However, the product mixture of degraded **L4P** in methylene chloride or ethyl acetate displays very different optical spectra as compared to the synthesized ketones **L4P-O** and **L4P-O2** (figure 4.6). The photodegraded mixtures (figure 4.6b) show a broad absorption down to 2.5 eV, signifying the presence of transitions with considerable strength below the absorption edge of **L4P** (3.3 eV, see figures 4.4a, 4.5a). This low energy absorption is still substantial in the region of **L4P** emission, suggesting that energy transfer might be quite efficient, if donor (**L4P**) and acceptor (defect) are in close proximity. The defect emission is bright and at around 2.5 eV. In contrast, the near-UV absorption (3.3 - 3.9 eV) of the ketones **L4P-O** and **L4P-O2** (figure 4.6a) resembles the absorption of **L4P** (figures 4.4a, 4.5a), although the extinction coefficient ε is significantly smaller and the maxima are blue-shifted. Additionally there is a low-energy absorption between 2.5 and 3.3 eV, making these compounds appear orange. Yet this broad transition has a very low oscillator strength such that energy transfer for this type of defects is rather unlikely. Additionally the orange emission of these compounds is farther in the low-energy region than observed for any degradation product or mixture and the emission quantum yield is extremely low. From these data it becomes apparent that both quantum yield of these ketones as well as their spectral overlap with **L4P** is rather low and hence such fluorenone structures are most likely not involved in the observed defect emission.

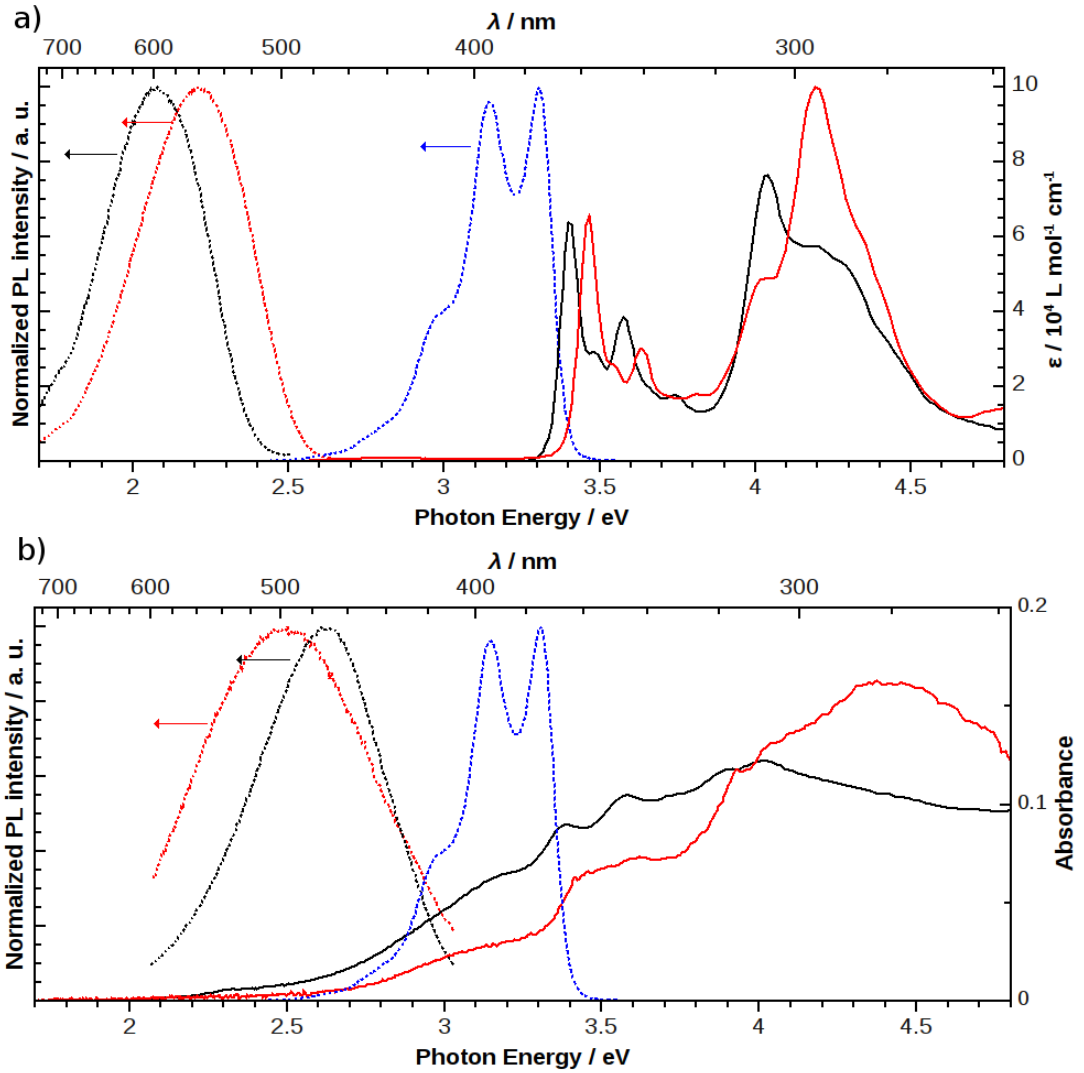

Figure 4.6. a) Absorption spectra of **L4P-O** (solid, black) and **L4P-O2** (solid, red) as well PL spectra of **L4P** (dotted, blue), **L4P-O** (dotted, black), and **L4P-O2** (dotted, red) upon excitation at 330 nm (25 °C, CH_2Cl_2). The spectral region between 2.5 and 3.3 eV is not shown because a cutoff filter was used to remove the 2nd harmonic of the excitation source and PL of residual, highly emissive **L4P** in the samples. b) Absorption (solid lines) and PL spectra (dotted lines) of **L4P** after irradiation with 300 - 400 nm light in CH_2Cl_2 (black, initial concentration: $6.8 \cdot 10^{-6}$ mol L^{-1}) and ethyl acetate (red, initial concentration: $6.8 \cdot 10^{-6}$ mol L^{-1}).

4.3.2 Chemical Analysis of Photodegradation Products[24]

Another indication arises from comparison with the non-bridged *p*-quarterphenyl **4P**, which should behave very different in case photodamage would occur at the benzylic bridges. However, when analogous degradation experiments were carried out in methylene chloride **4P** behaves similarly to **L4P** (see figure 4.7) providing

[24]Product separation by semi-preparative HPLC was carried out by Dr. Joachim Leistner (HU Berlin, Institut für Chemie).

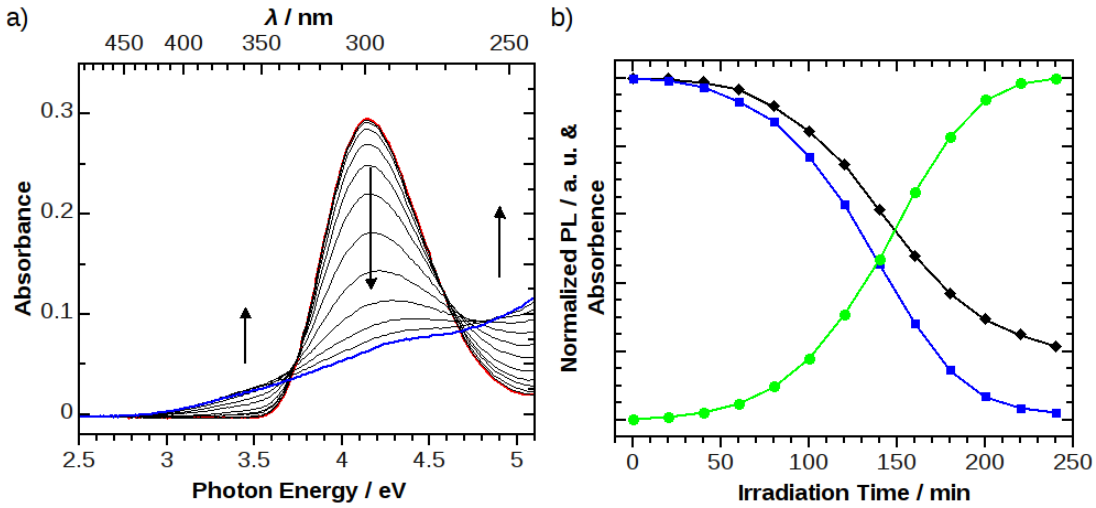

Figure 4.7. Photodegradation of **4P** in CH_2Cl_2 (initial concentration $7 \cdot 10^{-6}$ mol L^{-1}): a) Changes in the absorption spectrum, 20 min time interval between each spectrum; b) Evolution of absorption (at 300 nm, black), blue PL (370 nm, blue), and green PL (560 nm, green) over time.

another piece of evidence that the formation of fluorenone defects is rather unlikely to be the main photodegradation process.

In order to elucidate the origin of the defect emission, product formation over time was studied once again in methylene chloride at concentrations compatible with analysis by means of chromatography coupled to mass spectrometry (UPLC-MS). Using UV detection (Figure 4.8) the main peak at a retention time of 6.86 min is

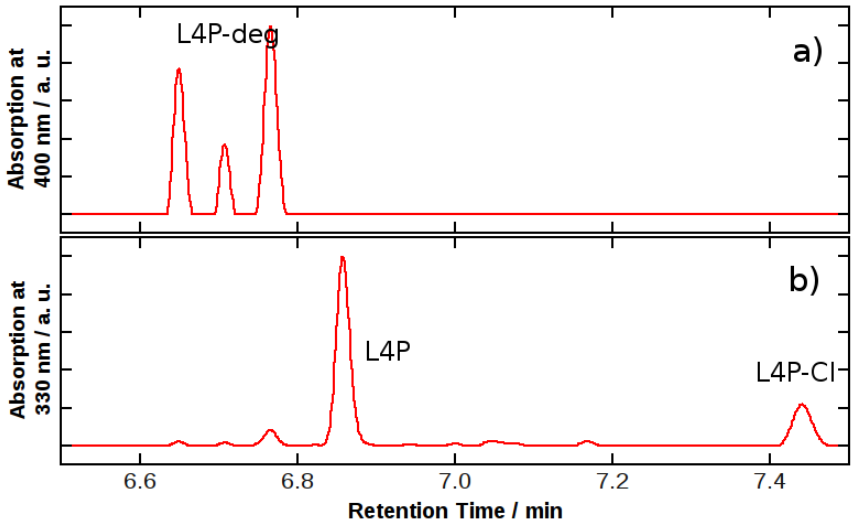

Figure 4.8. Chromatography traces of **L4P** after irradiation with 350 nm light in CH_2Cl_2 solution using UV-detection at a) 390 - 410 nm and b) 325 - 375 nm giving rise to **L4P-deg** and **L4P-Cl**.

attributed to the starting material **L4P**. Upon irradiation, the first product, which is formed relatively rapidly, exhibits a $m/z = 460.2$ and a characteristic isotopic pattern, such that it can be assigned to the monochlorinated product **L4P-Cl** (peak at 7.44 min in Figure 4.8b). Within the proceeding degradation also a relatively large amount of dichlorinated **L4P-Cl2** was formed. However, the influence of the chlorination on the optical properties of **L4P** is rather negligible as can be concluded from the transparency at long wavelength. In addition to the singly and doubly chlorinated products, three low-energy absorbing defect-species **L4P-deg** were formed (intense peaks between 6.65 and 6.76 min in Figure 4.8a, also seen in 4.8b). All of them show the same $m/z = 455.2$, which corresponds to a gain of 28 mass units as compared to **L4P**. It turned out to be very difficult to correlate the observed gain in mass with any oxidation process and therefore the chemical nature of the defect cannot be derived from the above analysis. To rule out fragmentation or complex formation upon ionization the ketone **L4P-O** was also analyzed via UPLC-MS, but only a peak at $m/z = 413$ was found, which corresponds to the [**L4P-O**+H]$^+$-ion. Accordingly, no evidence was found in the photodegraded samples for the presence of the ketones **L4P-O** or **L4P-O2**.

To resolve the chemical structure of the photodegradation products, two of the three main defects **L4P-deg** identified via UPLC-MS monitoring (figure 4.8) were isolated on a scale sufficient for subsequent analysis by NMR spectrocopy (figure 4.9). Comparison of the ^{1}H-NMR spectra of one isomer of the photodegradation products (**L4P-deg**) with **L4P** shows the presence of an additional singlet slightly above 10 ppm, the loss of one proton signal in the aromatic region and the reduced symmetry of the latter. The aliphatic proton signals also indicate a reduction of the molecular symmetry. The corresponding ^{13}C-NMR spectra may be interpreted the same way and furthermore show the presence of a carbonyl signal. Based on this spectral information, we conclude that upon irradiation of **L4P** in chloroform or methylene chloride a formylation reaction (figure 4.9) occurs, that somewhat resembles the thermal Reimer-Tiemann reaction[157, 158] and gives rise to formation of various monoformylated regioisomers. This would also explain the much more rapid degradation in chloroform as compared to methylene chloride. In the latter, **L4P** primarily undergoes of chlorination while methylene chloride is being chlorinated itself to in-situ generate chloroform, which is the more reactive formylation agent. Although we can only speculate about the mechanism of this photochemical conversion (potentially involving dichlorocarbenes or precursors of phosgene), it becomes clear now, why especially chloroform, but also methylene chloride, are not suited to process polyfluorenes, polyphenylenes, and ladder-type polyphenylenes (since residual solvent is difficult to be removed completely).

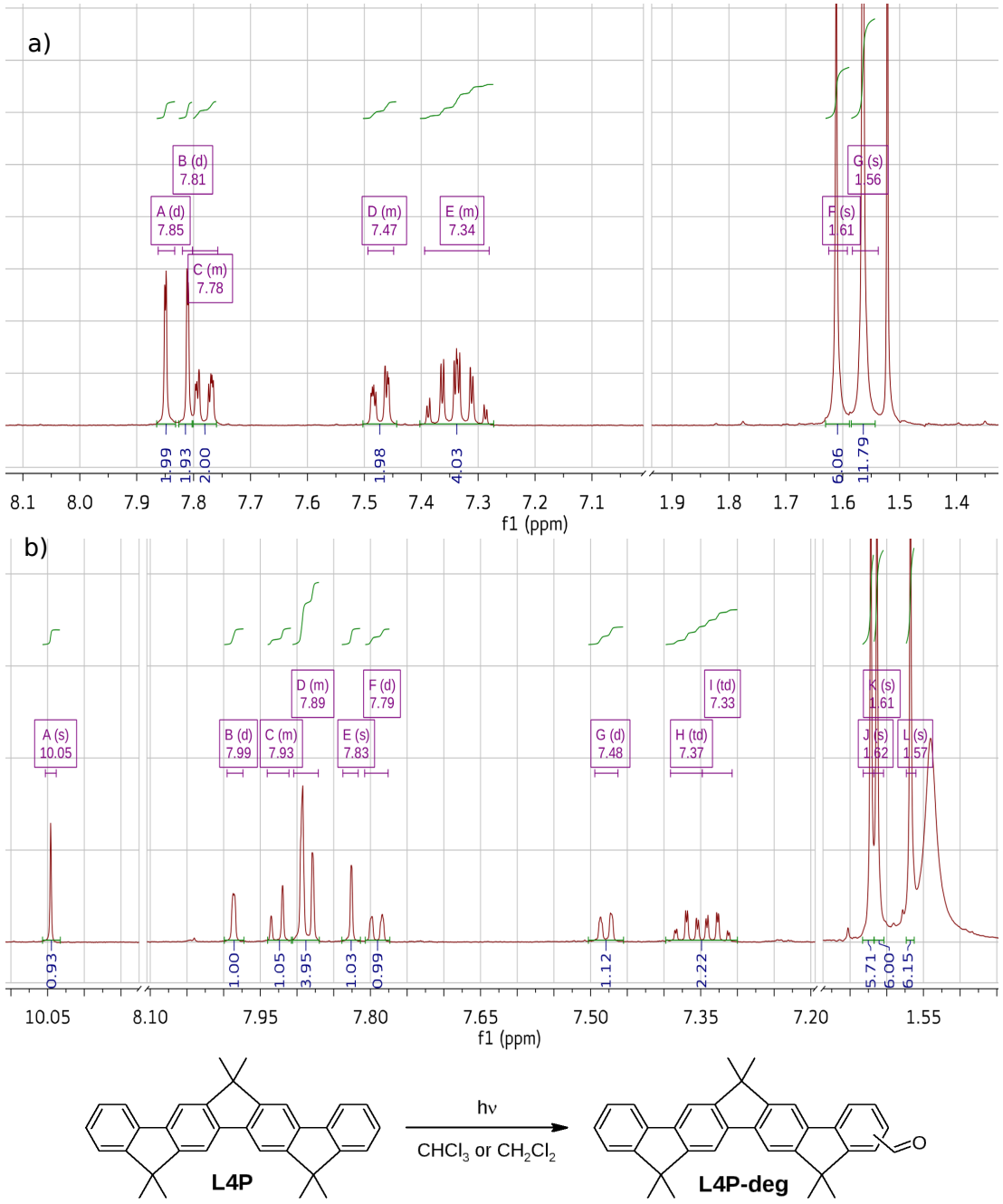

Figure 4.9. Formylation of **L4P** during irradiation in CH_2Cl_2 or $CHCl_3$. ^{1}H-NMR spectra of a) pristine **L4P** (300 MHz, CD_2Cl_2) and b) one isomer of defect **L4P-deg** (500 MHz, CD_2Cl_2), as well as proposed photochemical formylation reaction to explain the observed photodegradation products.

4.3.3 Optical Properties of Isolated Photodegradation Products

Naturally, the spectra of the isolated defects resemble the mixture of photodegraded products (Figure 4.6b). The absorption spectra of the isolated defects overlap extensively with the emission of **L4P** in the region between 3.0 and 3.5 eV (Figure 4.10a) and, as already mentioned above, energy transfer is expected to occur efficiently. Furthermore the efficiency of the PL of the isolated defects is much higher than that of the ketones **L4P-O** and **L4P-O2** and the emission is situated in the green to yellow region (2.6 - 2.7 eV). In this context it is interesting to note that careful comparison of the absorption and emission spectra can provide some further insight into the molecular origin of the defects. In the case of **L4P-O** there is a very weak low-energy absorption between 2.3 and 3.2 eV (depicted in Figure 3.10b in tenfold amplification), which can be attributed to the symmetry-forbidden n$\rightarrow \pi^*$ transition of the ketone. In stark contrast, in **DPF-O**, which has exactly the same π-system in terms of connectivity, the same transition is significantly stronger, although the $\pi \rightarrow \pi^*$ transition is much weaker. This can readily be explained by the freely rotatable phenyl groups providing more flexibility to the molecule and hence some mixing of the in-plane $\pi \rightarrow \pi^*$ transition and the out-of-plane n$\rightarrow \pi^*$ may occur thereby enhancing the low-energy transition.[159] This influence of backbone rigidity is not only observed in absorption but also in emission: In contrast to **L4P-O**, in **DPF-O** some of the PL is recovered and the quantum yield amounts at least to a few per cent ($\approx$4%) in CH_2Cl_2. This implies that the reason for strong low-energy emission of the isolated photodegradation products is not the broken symmetry due to the reduced planarity of the aromatic system but instead the ability of the carbonyl group to rotate out-of-plane.

Although in chlorinated solvents such as chloroform and methylene chloride the formation of a formylation product was proven, the general validity of these findings and their applicability to explain photodegradation in different solvents or films needed to be investigated. For this purpose, the aging behavior of solutions in methylene chloride and ethyl acetate was compared by means of absorption and PL measurements as well as UPLC-MS analysis. In the case of methylene chloride, three main products absorbing around 400 nm were found and are attributed to the three isomers of the formylated product **L4P-deg**. In ethyl acetate there is a large variety of products that absorb above 400 nm, making it – at least by the means that were available for us – not feasible to isolate and characterize them. However, the overall absorption spectra of the irradiated solutions in ethyl acetate (figure 4.6b) show qualitatively the same behavior when compared to methylene chloride: Upon irradiation the sharp peaks of the **L4P** absorption are vanishing and a broad tail below 3.3 eV appears, which again overlaps with the **L4P** emission. Even the kinetics of the degradation in ethyl acetate (see figure 4.5) is similar to that in methylene chloride (see figure 4.5).

A very thorough theoretical analysis of the optical properies of potential degradation products of larger oligomers of **LPPP** is given in ref. [150] that discusses three types of defects: a) a “ketonic defect”, resembling fluorenone-type defect and hence the structure of L4P-O, b) a “phenol defect”, and c) a “phenolate defect”.[150] While

for the first, the calculations of the optical transitions are in good agreement with our findings, the latter two defects arise from the oxidative cleavage of a methylene bridge, resulting in a freely rotatable arylketone fragment adjacent to the phenol unit. Interestingly, in the excited state, these types of structure show allowed transitions below the pristine **LPPP** and in the case of deprotonated species, i.e. the "phenolate defect",[150] the energy of the transition is even below the fluorenone-type defect. In view of our observations and employed experimental conditions as well as the fact that the π-system of the "phenol defect" somehow resembles **L4P-deg**, which indeed shows low energy emission, even compared to the longer oligomer

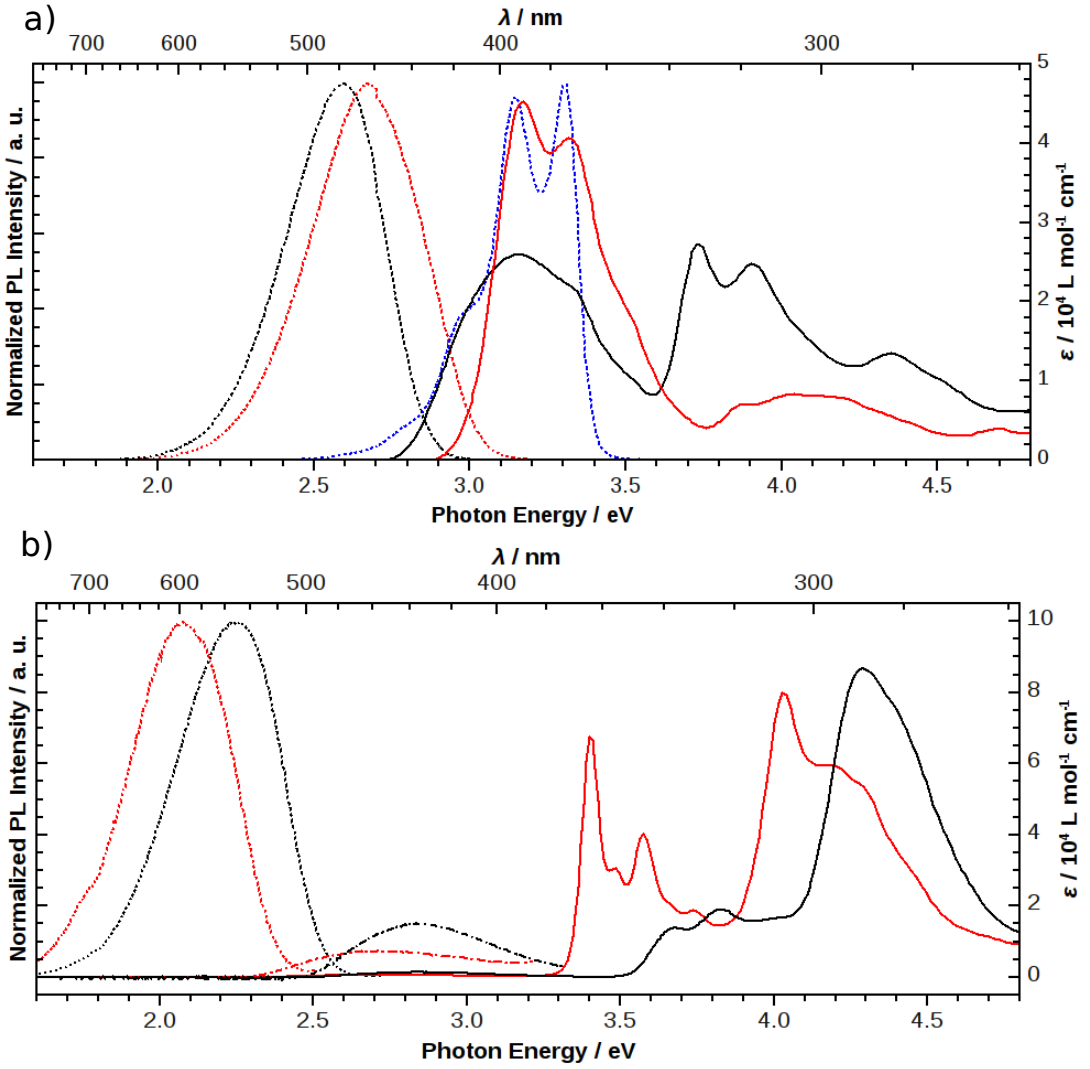

Figure 4.10. a) Absorption (solid lines) and PL (dotted lines) of two different isolated formyl defects (**L4P-deg** in Figure 4.9, excitation at 380 and 395 nm, respectively) and PL of **L4P** (dotted blue, excitation at 330 nm) in CH_2Cl_2 (25 °C). b) Absorption (solid and dashed dotted (zoomed 10x) lines) and PL spectra (dotted lines) of **L4P-O** (red, excitation at 330 nm) and **DPF-O** (black, excitation at 435 nm) in CH_2Cl_2 (25 °C).

L6P,[78] it seems most likely that structures related to the "phenol defect"[150] are responsible for the green emission under the conditions employed by us.
Although the products formed in ethyl acetate behave in a very similar manner they are not the same than the ones formed in methylene chloride, as for example proven by their mass spectra. Because typically degradation is referred to an oxidation process in the literature,[131, 151–155] the influence of oxygen on photodegradation was evaluated. Samples of **L4P** in different solvents, each of them under Argon as well as under air, were irradiated at 350 nm at equal conditions. In several solvents (methylene chloride, ethyl acetate, tetrahydrofuran) bubbling Argon through the solution prior to irradiation leads to a significant slow-down of the degradation. The most pronounced difference was found for methylene chloride, where in the Argon-saturated solution the typical **L4P** absorption decreased much more slowly as compared to the aerated sample (figure 4.11a). Clearly, the absence of oxygen inhibits photodegradation or at least it slows it down (also knowing that water was present in all the samples).
To get another hint towards the oxidation mechanism, different quenchers for active species of oxygen were added to solutions of **L4P** in ethyl acetate prior to irradiation. Namely di-2,6-*tert*-butylphenol (DTBP) was added, which is a known scavenger for radical auto-oxidation processes, as well as 1,4-diazabicyclo[2.2.2]octane (DABCO), which is a quencher for singlet oxygen.[160] Surprisingly, the addition of DTBP did not lead to a longer lifetime of the **L4P** in solution and in contrast the aging even seemed to accelerate (figure 4.11b). However, upon addition of DABCO practically

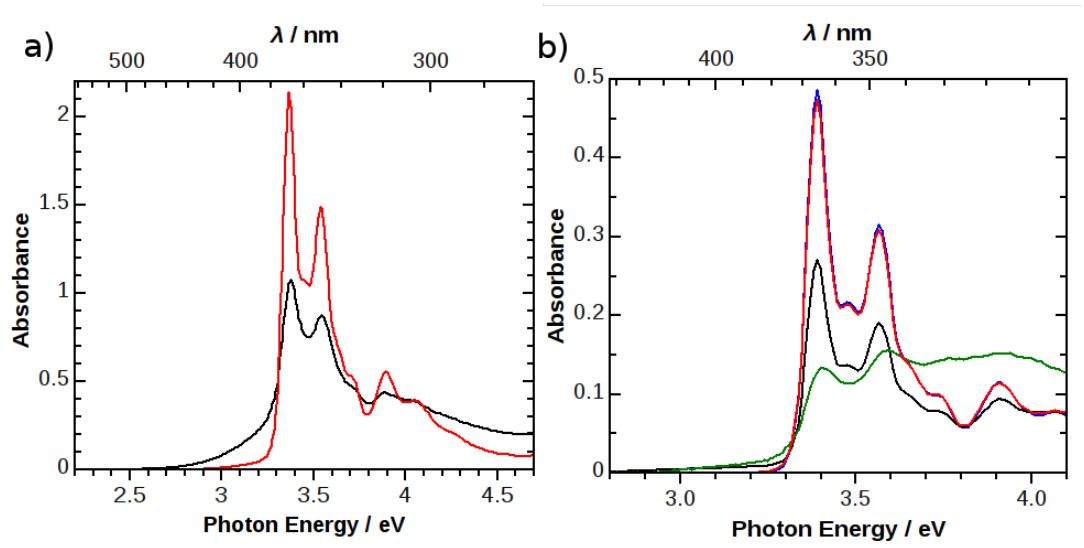

Figure 4.11. a) Absorption (0.2 mm path length) of **L4P** in CH_2Cl_2 (initial concentration 10^{-3} mol L^{-1}) after irradiation with 350 nm light under Argon (red) and under air (black). b) Absorption (1 mm path length) of **L4P** solutions in ethyl acetate (initial concentration $4.4 \cdot 10^{-5}$ mol L^{-1}) after irradiation with 350 nm light in the presence of DTBP (green, 0.02 mol L^{-1}) or DABCO (red, 0.02 mol L^{-1}), without an additive (black) as well as the original solution (blue). For solutions containing additives, proper background correction has been carried out.

no photodegradation was observed after the same duration of irradiation. Hence, photodegradation of **L4P** in solution primarily seems to involve singlet oxygen as the main active oxidant. Singlet oxygen engages in variety of reactions, mainly [2+2]- and [4+2]-cycloadditions as well as ene-reactions, involving mostly olefins or dienes, in some cases even aromatic systems, as substrates. Primarily (endo)peroxides and oxetanes are formed in these reactions, which eventually would lead to the formation of ketones and aldehydes.[161–163] **L4P** does not display one of these particularly priviledged substrate structures giving rise to rather low selectivity during oxidation and the large number of different degradation products obtained in ethyl acetate.

4.4 Degradation in the Solid State and Energy Transfer[25]

To study degradation and energy transfer in the solid state, **L4P** has been embedded in a polystyrene matrix at 1%, 10% and 20% (w/w) and spin cast to sapphire substrates. In comparison to dilute solutions the 0-1 transition is the most prominent one in the PL spectrum due to reabsorption of the 0-0 emission. Upon increasing concentration, a broad emission in the blue-to green region is rising. Extended UV-irradiation of the layers leads similarly to the experiments in solution to an increase in the intensity of the green emission and a broadening and flattening of the absorption. The PL excitation spectrum of the green emission resembles the absorption spectrum of **L4P** with a certain amount of defects, strongly indicating an energy transfer from **L4P** to the defects. The dynamics of the energy transfer was studied by means of time-resolved PL spectroscopy and evaluated with a model for Förster-type RET. At higher concentrations (20%), the emission of **L4P** shows a non-exponential decay and in the emission of the defect a feeding process can be observed and the evaluation shows, that the decay of the excited donor is dominated by energy transfer.

4.5 Conclusion

It is demonstrated that small, ladder-type L4P molecules dispersed in solution or a solid matrix degrade upon UV irradiation in the presence of oxygen. This photodegradation results in green-yellow emitting defects, which for sufficiently small intermolecular distances are efficiently excited via energy transfer from the original L4P. The overall emission process from the defect traps agrees well with previous extensive studies on photodegraded polyfluorene-type polymers.[133, 139, 164]
Considering the process of photodegradation, our system at first appears to be rather similar to what has been proposed for polyfluorenes in the literature (i.e., greenish-yellow emission upon extensive irradiation). But already kinetic studies with **L4P** suggest that neither the fluorenyl anion mechanism,[131, 136] which should follow

[25]The work described in this section was carried out by Francesco Bianchi, Dr. Simon Halm, and Dr. Sylke Blumstengel in the group of Prof. Fritz Henneberger (HU Berlin, Institut für Physik).

typical first order photokinetics, nor the radical chain mechanism[151, 152] may explain our observations. The inhibition of photodegradation by adding DABCO to the samples proved, that singlet oxygen is the major source of decomposition, as has already been proposed by Abbel.[155] Thereby, the accelerating kinetics can readily be explained: At the beginning the **L4P** substrate acts as singlet oxygen sensitizer, yet with a rather low sensitization quantum yield.[165] But as soon as the aromatic carbonyl defect has been formed, it acts as a much more efficient singlet oxygen sensitizer due to the enhanced intersystem crossing leading to efficient population of the carbonyl triplet,[166] and hence the photochemical degradation process is autocatalytic in nature.

4.6 Experimental

4.6.1 Analytical Instrumentation and Light Sources for Degradation in Solution

Absorption spectra were recorded on a Varian Cary 50 Bio UV-Visible Spectrometer and fluorescence spectra on a Varian Cary Eclipse Fluorescence Spectrometer. Fluorescence, i.e. photoluminescence, spectra were corrected for variations in photomultiplier response over wavelength using correction curves generated on the instrument. For the kinetic measurements a 1000 W Oriel Xe arc lamp was used equipped with a water-filter and an UG1-filter for **L4P** or an UG11-filter for **4P**. For preparative degradation and for comparative measurements on the influence of oxygen or additives a Rayonet Photoreactor equipped with 350 nm fluorescent lamps was used. During irradiation the samples were rotated using a Rayonet Marry-Go-Round sample-holder. Analytical LC was performed on a Waters Acquity UPLC equipped with a Waters LCT Premier XE Mass detector for high-resolution MS (HR-MS, ESI+-ionization) and with Waters Alliance systems (consisting of a Waters Separations Module 2695, a Waters Diode Array Detector 996 and a Waters LCT Premier XE Mass Detector).

4.6.2 Organic Synthesis

^{1}H-NMR and ^{13}C-NMR spectra were referenced to 7.26 ppm and 77.16 ppm, respectively, for $CDCl_3$ and 5.32 ppm and 53.8 ppm, respectively, for CD_2Cl_2.

Bromo-2-(methoxymethyl)benzene (1) After sodium (8.07 g, 351 mmol) was reacted with methanol (120 mL; Evolution of heat: Use reflux condenser!), 2-bromobenzyl bromide (74.7 g, 300 mmol) was added slowly. Upon stirring the mixture for 3 h at room temperature, water was added, followed by extraction with CH_2Cl_2. The organic phase was dried ($MgSO_4$) and the solvent was removed to yield 59.5 g (296 mmol, 99% yield) of **1** as yellowish oil.
^{1}H-NMR (300 MHz, $CDCl_3$) δ [ppm] = 7.55 (dd, J = 7.9, 1.1 Hz, 1H), 7.50 - 7.44 (m, 1H), 7.32 (td, **J** = 7.5, 1.2 Hz, 1H), 7.15 (td, **J** = 7.7, 1.8 Hz, 1H), 4.54 (s, 2H),

3.48 (s, 3H).

2,7-Dibromo-9*H*-fluoren-9-one (2)
a) In medium scale: Bromine (24.7 g, 7.9 mL, 154 mmol) was added to powdered 9-fluorenone (11.6 g, 64.4 mmol; vigorous formation of HBr!). After 5 min the temperature of the cake-like reaction mixture was raised to 150 °C and held there for 30 min. Upon cooling to 80 °C, THF (ca. 250 mL) was added until the entire product was dissolved. The mixture was cooled to room temperature, the precipitate was filtered off and washed with ethanol. The residual solution was concentrated and the precipitate was filtered off again. After drying under vacuum, 2,7-dibromofluorenone **2** (19.2 g, 56.8 mmol, 88% yield) was obtained as a yellow solid.
b) In large scale: In a round-bottom flask equipped with addition-funnel, condenser and gas-washing bottle (aq. NaOH) fluorenone (32 g, 178 mmol) was melted. At 140 °C the drop-wise addition of bromine (68.4 g, 427 mmol) was started. Meanwhile the temperature was raised to 200°C. After the addition of Bromine was finished, the mixture was stirred another 45 min at 200 °C. Afterwards the mixture was cooled to room temperature and residual bromine and HBr were removed by purging air through the apparatus. The crude product was crystallized from chloroform/methanol to give 42.6 g (126 mmol, 71%yield) of pure 2,7-dibromofluorenone **2**, as well as a mixture of mono- and dibrominated product, which was stored for subsequent brominations.
^{1}H-NMR (300 MHz, $CDCl_3$) δ [ppm] = 7.77 (d, J = 1.8 Hz, 2H), 7.63 (dd, J = 7.9, 1.9 Hz, 2H), 7.39 (d, J = 7.9 Hz, 2H).

2,7-Bis(2-(methoxymethyl)phenyl)-9H-fluoren-9-one (3)
Under an argon atmosphere, a solution of **1** (5.03 g, 25 mmol) in dry THF (50 mL) was cooled to -78 °C. *n*BuLi (12.3 mL, 27 mmol, 2.2 M in cyclohexane) was added to the reaction mixture and it was stirred for 1 hour at -78 °C. Upon adding $B(OBu)_3$ (6.21 g, 7.22 mL, 27 mmol), the mixture was allowed to warm to room temperature and stirring was continued for another hour.
Then, the solution of the boronate was added to a mixture of **2** (3.38 g, 10 mmol), Cs_2CO_3 (14.63 g, 45 mmol), and $Pd(dppf)Cl_2 \cdot CH_2Cl_2$ (0.17 g, 0.2 mmol) in ethanol (50 mL) and DMF (10 mL). The reaction was stirred overnight at 65 °C. After cooling to room temperature, water was added and the mixture was extracted with CH_2Cl_2. The organic phase was dried ($MgSO_4$) and all volatiles were removed. The crude product was purified by column chromatography (cyclohexane/ethyl acetate) to obtain **3** as a yellow solid (2.3 g, 5.5 mmol, 55% yield).
^{1}H-NMR (300 MHz, $CDCl_3$) δ [ppm] = 7.72 (dd, J = 1.6, 0.6 Hz, 2H), 7.62 (dd, J = 7.7, 0.6 Hz, 2H), 7.58 - 7.53 (m, 4H), 7.44 - 7.36 (m, 4H), 7.35 - 7.31 (m, 2H), 4.36 (s, 4H), 3.36 (s,6H).
^{13}C-NMR (75 MHz, $CDCl_3$) δ [ppm] = 193.9, 143.2, 142.1, 140.9, 135.8, 135.4, 134.6, 129.8, 129.8, 128.2, 128.2, 125.3, 120.3, 72.7, 58.3.

Dimethyl 2,2'-(9-oxo-9*H*-fluorene-2,7-diyl)dibenzoate (4)
A mixture of **3** (2.1 g, 5 mmol), $KMnO_4$ (4.74 g, 30 mmol), and TEBAC (6.84 g, 30 mmol) in CH_2Cl_2 (50 mL) was refluxed overnight. After cooling to room temperature, the reaction was quenched with aqueous $Na_2S_2O_3$, diluted with water and extracted with CH_2Cl_2. The organic phase was dried ($MgSO_4$) and the solvent was removed. The crude product was crystallized from chloroform/ethanol, to give **4** (2.1 g, 4.7 mmol, 94% yield) as a yellow solid.
^{1}H-NMR (300 MHz, $CDCl_3$) δ [ppm] = 7.92 (dd, J = 7.7, 1.3 Hz, 2H), 7.63 (d, J = 1.2 Hz, 2H), 7.61 - 7.54 (m, 4H), 7.49 - 7.42 (m, 4H), 7.39 (dd, J = 7.6, 1.1 Hz, 2H), 3.71 (s, 6H).
^{13}C-NMR (75 MHz, $CDCl_3$) δ [ppm] = 168.6, 143.3,142.7, 141.8, 134.9, 134.6, 131.8, 130.7, 130.5, 130.4, 127.9, 124.6, 120.2, 52.3.

Dimethyl 2,2'-(9,9-dimethoxy-9H-fluorene-2,7-diyl)dibenzoate (5)
A solution of **4** (0.45 g, 1 mmol) and trimethyl orthoformate (1.3 mL, 1.16 g, 8 mmol), and a catalytic amount of methanesulfonic acid in methanol (10 mL) and chloroform (10 mL) was refluxed overnight, whereupon the yellow color disappeared. Then, the reaction mixture was quenched with aqueous $NaHCO_3$ and extracted with ethyl acetate. The organic phase was dried ($MgSO_4$) and the solvent was removed to give **5** (0.47 g, 0.95 mmol, 95% yield) as a nearly colorless solid.
^{1}H-NMR (300 MHz, $CDCl_3$) δ [ppm] = 7.88 - 7.83 (m, 2H), 7.67 (dd, J = 7.8, 0.5 Hz, 2H), 7.59 - 7.53 (m, 2H), 7.50 - 7.40 (m, 6H), 7.38 (dd, J = 7.8, 1.7 Hz, 2H), 3.67 (s, 6H), 3.38 (s, 6H).
^{13}C-NMR (75 MHz, $CDCl_3$) δ [ppm] = 169.2, 142.3, 141.9, 141.2, 139.0, 131.5, 131.0, 130.8, 130.3, 130.1, 127.5, 125.1, 120.1, 52.2, 51.9.

12,12,15,15-Tetramethyl-12,15-dihydrospiro[cyclopenta[2,1-b:3,4-*b'*]difluorene-6,2'-[1,3]dithiolane] (6)
Under an argon atmosphere CH_3Li (14.7 mL, 44 mmol, 3.0 M in dimethoxymethane) was added to a solution of **5** (2.17 g, 4.4 mmol) in dry THF (100 mL). After stirring for 1.5 h, the reaction was quenched with methanol, water was added and the mixture was extracted with ethyl acetate. The organic phase was dried ($MgSO_4$) and the solvent was removed. The crude product was dissolved in CH_2Cl_2 (100 mL) and ethane dithiol (1.47 mL, 1.65 g, 17.6 mmol), as well as $BF_3 \cdot$ THF (50% in THF, 7.8 mL, 9.83 g, 35 mmol) were added. After the reaction was stirred for 1 h at room temperature and for 1 h at 40 °C, it was carefully quenched with excess aqueous NaOH (≈10%). After stirring was continued for further 30 min, the mixture was extracted with CH_2Cl_2. The organic phase was dried ($MgSO_4$) and the solvent was removed. The crude product was purified by column chromatography (petroleum ether/ethyl acetate) to give **6** (1.1 g, 2.3 mmol, 51% yield) as a white to yellowish solid.
^{1}H-NMR (300 MHz, CD_2Cl_2) δ [ppm] = 8.04 (d, J = 0.7 Hz, 2H), 7.82 - 7.77 (m, 2H), 7.76 (d, J = 0.7 Hz, 2H), 7.50 - 7.45 (m, 2H), 7.41 - 7.30 (m, 4H), 3.93 (s, 4H), 1.56 (s, 12H).
^{13}C-NMR (75 MHz, CD_2Cl_2) δ [ppm] = 155.3, 154.4, 150.9, 140.0, 139.3, 138.5, 127.7, 127.4, 123.0, 120.3, 117.1, 114.2, 47.0, 43.0, 27.5.

12,12,15,15-Tetramethyl-12,15-dihydro-6*H*-cyclopenta[2,1-*b*:3,4-*b'*]difluoren-6-one L4P-O

NIS (2.03 g, 9.0 mmol) was added to a solution of **6** in CH_2Cl_2 (40 mL) and acetic acid (40 mL). Upon stirring the reaction for 10 min at room temperature, it was poured on cold aqueous NaOH. The mixture was extracted with CH_2Cl_2, the organic phase was dried ($MgSO_4$) and the solvent was removed. The crude product was purified by column chromatography (CH_2Cl_2) to give **L4P-O** (0.57 g, 1.4 mmol, 61% yield) as orange crystals, as well as **7** (0.08 g, 0.2 mmol, 9% yield).

L4P-O: ^{1}H-NMR (300 MHz, CD_2Cl_2) δ [ppm] = 7.98 (d, J = 0.7 Hz, 2H), 7.81 - 7.74 (m, 2H), 7.67 (d, J = 0.8 Hz, 2H), 7.51 - 7.44 (m, 2H), 7.42 - 7.32 (m, 4H), 1.56 (s, 12H).

^{13}C-NMR (75 MHz, CD_2Cl_2) δ [ppm] = 161.5, 153.9, 144.8, 140.6, 138.5, 135.0, 128.1, 127.7, 123.0, 120.5, 116.1, 115.2, 47.6, 27.0.

7: ^{1}H-NMR (300 MHz, $CDCl_3$) δ [ppm] = 7.99 (d, J = 0.7 Hz, 1H), 7.82 (d, J = 7.6 Hz, 1H), 7.79 - 7.70 (m, 2H), 7.58 (dd, J = 4.1, 3.5 Hz, 2H), 7.51 - 7.43 (m, 2H), 7.42 - 7.32 (m, 4H), 1.73 (s, 6H), 1.56 (s, 6H).

^{13}C-NMR (75 MHz, $CDCl_3$) δ [ppm] = 193.9, 161.2, 154.6, 154.0, 153.6, 144.8, 144.2, 141.9, 140.3, 138.4, 137.9, 134.0, 130.4, 128.2, 127.9, 127.5, 127.1, 125.1, 122.9, 122.7, 120.4, 119.9, 119.1, 116.1, 114.5, 48.2, 47.4, 27.1, 24.7.

2,7-Bis(2-(methoxymethyl)phenyl)-9,9-dimethyl-9*H*-fluorene (9)

Under an argon atmosphere, a solution of **1** (5.03 g, 25 mmol) in dry THF (50 mL) was cooled to -78 °C. *n*BuLi (28 mmol, 12.7 mL, 2.2 M in cyclohexane) was slowly added and the mixture was stirred for 1 h. Then, tributyl borate (6.44 g, 7.49 mL, 28 mmol) was added and upon warming to room temperature, the solution was stirred for another 30 min.

Subsequently the solution of the boronate was added to a mixture of **8** (3.52 g, 10 mmol), $Pd(dppf)Cl_2 \cdot CH_2Cl_2$ (0.17 g, 0.2 mmol), and Cs_2CO_3 (14.6 g, 45 mmol) in ethanol (50 mL) and DMF (10 mL). The reaction was stirred overnight under an Argon atmosphere at 65 °C. After cooling to room temperature, water was added and the mixture was extracted with CH_2Cl_2. The organic phase was dried ($MgSO_4$) and all volatiles were removed. Column chromatography (cyclohexane/ethyl acetate) gave 1.7 g (3.9 mmol, 39% yield) of diether **9** as a colorless resin.

^{1}H-NMR (300 MHz, $CDCl_3$) δ [ppm] = 7.82 (d, J = 7.8 Hz, 2H), 7.61 - 7.55 (m, 2H), 7.54 (d, J = 1.1 Hz, 2H), 7.45 - 7.38 (m, 8H), 4.39 (s, 4H), 3.40 (s, 6H), 1.58 (s, 6H).

^{13}C-NMR (75 MHz, $CDCl_3$) δ [ppm] = 153.8, 142.6, 140.0, 138.0, 135.5, 130.2, 129.8, 128.3, 128.0, 127.5, 124.0, 119.7, 72.9, 58.4, 47.1, 27.3.

Dimethyl 2,2'-(9,9-dimethyl-9*H*-fluorene-2,7-diyl)dibenzoate (10)

A mixture of **9** (1.52 g, 3.5 mmol), $KMnO_4$ (3.32 g, 21 mmol), and TEBAC (4.79 g, 21 mmol) in CH_2Cl_2 (50 mL) was refluxed overnight. After cooling to room temperature, the reaction was quenched with aqueous $Na_2S_2O_3$. The mixture was transferred into a separation funnel and diluted with CH_2Cl_2 and water. Upon adding HCl to dissolve MnO_2, the phases were immediately separated. The organic phase was dried

($MgSO_4$) and the solvent was removed. The crude product was purified by column chromatography (cyclohexane/ethyl acetate) to give 1.3 g (2.8 mmol, 80% yield) of diester **10** as a colorless solid.
^{1}H-NMR (300 MHz, $CDCl_3$) δ [ppm] = 7.83 (dd, J = 7.7, 1.0 Hz, 2H), 7.78 (dd, J = 7.7, 0.6 Hz, 2H), 7.60 - 7.52 (m, 2H), 7.49 (dd, J = 7.7, 1.1 Hz, 2H), 7.46 - 7.39 (m, 2H), 7.39 - 7.33 (m, 4H), 3.62 (s, 6H), 1.53 (s, 6H).
^{13}C-NMR (75 MHz, $CDCl_3$) δ [ppm] = 169.8, 153.8, 142.6, 140.5, 138.2, 131.4, 131.3, 130.8, 129.9, 127.5, 127.3, 123.0, 120.0, 52.1, 47.0, 27.4.

6,6-Dimethyl-6*H*-cyclopenta[2,1-*b*:3,4-*b'*]difluorene-12,15-dione L4P-O2
A solution of NaOH (8 g in 20 mL of water) was added to the solution of **10** (2.36 g, 5.1 mmol) in ethanol (300 mL). The mixture was stirred for 16 h at 75 °C. After cooling to room temperature, the main amount of solvent was removed. Water, as well as ethyl acetate were added until phase separation was observed. The aqueous phase was washed with ethyl acetate and subsequently acidified (HCl). The precipitate was filtered off and dried under vacuum.
The crude acid was added to $SOCl_2$ (100 mL) and stirred for 4 h at 60 °C. Afterwards methanesulfonic acid (2 mL) was added and $SOCl_2$ was subsequently removed by distillation. Aqueous $NaHCO_3$ was added to the residue and it was extracted with (a large quantity of) CH_2Cl_2. The organic phase was dried ($MgSO_4$) and the solvent was removed. The crude product was dispersed in few hot chloroform and after stirring for some minutes, it was filtered off to give 1.4 g (3.5 mmol, 69% yield) of **L4P-O2** as an orange powder.
^{1}H-NMR (300 MHz, $CDCl_3$) δ [ppm] = 7.99 (d, J = 0.7 Hz, 2H), 7.70 - 7.64 (m, 2H), 7.61 - 7.55 (m, 4H), 7.51 (td, J = 7.4, 1.1 Hz, 2H), 7.30 (td, J = 7.4, 1.1 Hz, 2H), 1.61 (s, 6H).

6,6,12,12,15,15-hexamethyl-12,15-dihydro-6*H*-cyclopenta[2,1-*b*:3,4-*b'*] difluorene L4P
Under an argon atmosphere methyllitium (8 mL, 24 mmol, 3 M in dimethoxymethane) was added to a solution of **10** (0.924 g, 2.0 mmol) in dry THF (60 mL). The reaction was stirred for one hour at room temperature and subsequently quenched with water. The mixture was extracted with ethyl acetate, the organic phase was dried ($MgSO_4$) and the solvent was removed. The crude intermediate was dissolved in CH_2Cl_2 (100 mL) and $BF_3 \cdot$ THF (50% in THF, 2 mL, 8 mmol) was added. After stirring the reaction for 10 min at room temperature, it was quenched with aqueous $NaHCO_3$ and little ethanol. The mixture was extracted with CH_2Cl_2, the organic phase was dried ($MgSO_4$), filtered through a pad of silica and the solvent was removed. After crystallization from chloroform/ethanol, **L4P** (0.30 g, 0.7 mmol, 35% yield) was obtained as a colorless powder.
^{1}H-NMR (300 MHz, CD_2Cl_2) δ [ppm] = 7.85 (d, J = 0.7 Hz, 2H), 7.81 (d, J = 0.7 Hz, 2H), 7.80 - 7.76 (m, 2H), 7.50 - 7.45 (m, 2H), 7.40 - 7.28 (m, 4H), 1.61 (s, 6H), 1.56 (s, 12H).

2,7-diphenyl-9H-fluoren-9-one DPF-O
A mixture of **2** (1.01 g, 3.0 mmol), phenylboronic acid **11** (0.88 g, 7.2 mmol), $Pd(dppf)Cl_2 \cdot CH_2Cl_2$ (0.13 g, 0.15 mmol), and Cs_2CO_3 (2.44 g, 7.5 mmol) in ethanol (30 mL), THF (30 mL) and DMF (10 mL) was stirred overnight under an argon atmosphere at 60°C. After cooling to room temperature, the mixture was poured into water and the precipitate was filtered off. The crude product was dissolved in warm THF and filtered through a pad of celite. The solvent was removed and **DPF-O** (0.83 g, 2.50 mmol, 83% yield) was obtained by crystallization from THF.
^{1}H-NMR (300 MHz, $CDCl_3$) δ [ppm] = 7.94 (d, J = 1.3 Hz, 2H), 7.75 (dd, J = 7.8, 1.8 Hz, 2H), 7.67 - 7.59 (m, 6H), 7.52 - 7.44 (m, 4H), 7.43 - 7.35 (m, 2H).
^{13}C-NMR (75 MHz, $CDCl_3$) δ [ppm] = 143.2, 142.4, 140.0, 135.4, 133.5, 129.1, 128.1, 127.0, 123.2, 120.9.

4.6.3 Isolation of Degradation Products

For the isolation of the defects solutions of **L4P** in CH_2Cl_2 and chloroform ($\approx 10^{-3}$ mol L^{-1}) have been irradiated in a Rayonet photoreactor until the deep-blue fluorescence vanished. Then the solvent was removed and excess **L4P** was removed by crystallization from ethyl acetate. The residue was purified by column chromatography over silica using a mixture of petroleum ether (b.p. 40 – 60 °C) and ethyl acetate. The pre-purified samples have been further purified by semi-prep HPLC: Waters 600 prep. HPLC pump, Waters 996 diode array detector, Waters fraction collector III, Phenomenix Luno 10u Phenyl-Hexyl 250 x 21.2 mm; 22 mL/min 75% AcCN, 25% H_2O.
L4P-deg-a: ^{1}H-NMR (300 MHz, CD_2Cl_2) δ [ppm] = 11.20 (s, 1H), 8.05 (d, J = 0.7 Hz, 1H), 8.01 (s, 1H), 7.86 (dd, J = 6.8, 0.7 Hz, 1H), 7.83 - 7.79 (m, 2H), 7.50 - 7.46 (m, 2H), 7.40 - 7.33 (m, 4H), 1.71 (s, 6H), 1.63 (s, 6H), 1.55 (s, 6H).
^{13}C-NMR (75 MHz, CD_2Cl_2) δ [ppm] = 194.0, 156.0, 155.5, 155.1, 154.9, 153.5, 152.8, 140.0, 139.7, 139.5, 139.2, 137.8, 137.8, 130.6, 128.2, 127.8, 127.4, 127.4, 123.1, 122.8, 120.3, 119.9, 119.4, 118.4, 114.5, 49.1, 47.1, 45.9, 27.8, 27.5, 26.8.
L4P-deg-c: ^{1}H-NMR (300 MHz, CD_2Cl_2) δ [ppm] = 10.05 (s, 1H), 7.99 (d, J = 0.4 Hz, 1H), 7.93 (d, J = 7.8 Hz, 1H), 7.91 - 7.86 (m, 4H), 7.83 (d, J = 0.5 Hz, 1H), 7.81 - 7.77 (m, 1H), 7.50 - 7.46 (m, 1H), 7.35 (pd, J = 7.3, 1.4 Hz, 2H), 1.62 (s, 6H), 1.61 (s, 6H), 1.57 (s, 6H).
^{1}H-NMR (500 MHz, CD_2Cl_2) δ [ppm] = 10.05 (s, 1H), 7.99 (d, J = 0.7 Hz, 1H), 7.94 - 7.91 (m, 1H), 7.90 - 7.87 (m, 4H), 7.83 (s, 1H), 7.79 (d, J = 7.0 Hz, 1H), 7.48 (d, J = 6.8 Hz, 1H), 7.37 (td, J = 7.4, 1.3 Hz, 1H), 7.33 (td, J = 7.3, 1.2 Hz, 1H), 1.62 (s, 6H), 1.61 (s, 6H), 1.57 (s, 6H).

5 Kinetics of Photodegradation of Various 2,7-Diphenylfluorenes

5.1 Introduction

As already pointed out in the last chapter, green emission in PF and related structures has widely been discussed. The most prominent explanation for the green emission is the formation of fluorenone type (or at least keto) defects. (see e. g. refs. [131, 132]). The formation of these fluorenone defects was mainly rationalized by oxidation processes involving radicals or hydroperoxides at synthetic defect sites, but also the influence of singlet oxygen was discussed.[151–155] In the previous chapter it was shown, that under certain conditions, the main source of degradation was rather singlet oxygen, than some auto-oxidation process. While the focus of that chapter was mainly related to the conditions surrounding the degrading molecules, this chapter will deal with the influence of the molecular structure on the degradation.

A crucial role in the efficiency of the degradation process is related to the substitution pattern of the fluorene-type material, namely to the substituent in 9-position of the 9*H*-fluorene. In the above mentioned examples synthetic defect sites, such as hydrogen instead of an alkyl substituent are identified to be sensitive towards degradation. On the other hand, attempts have been made to introduce aryl units, especially the spirobifluorene motif, to obtain fluorene-type materials, that are more stable towards thermal, as well as photochemical degradation.[71, 153, 167–173]

However, these studies lack a quantification of the stability. Here, the stability of a variety of differently substituted fluorene-type materials (Scheme 1) towards photochemical degradation in solution will be compared in a quantitative manner. But what exactly does 'stable' mean? According to the IUPAC Gold Book "the term [stable] expresses a thermodynamic property, which is quantitatively measured by relative molar standard Gibbs energies".[174] So one chemical species is more stable if it liberates less Gibbs free energy as compared to a reference system. Since photoreactions are not strictly governed by the principle of minimizing the Gibbs free energy, the term reactivity could rather be used, which "expresses a kinetic property".[175] Furthermore, the rate of a photoreaction is dependent on the intensity of absorbed light, so the sensitivity towards photodegradation would very explicitly be described by a reaction quantum yield. Since the absolute quantum yield is very low and thus difficult to measure, only a relative quantum yield will be determined in the following, which is referenced to the most unreactive derivative in the series of investigated compounds.

To keep the following considerations as simple as possible, it was decided to use a small molecule that carries only one fluorene unit and accordingly only one methylene bridge. To shift the optical transitions to lower energies, the fluorene core was

substituted by phenyl units in positions 2 and 7 leading to the 2,7-diphenylfluorene (DPF) as central structural motif (figure 5.1). The methylene bridge was substituted with a variety of groups, including methyl (**DPF-Me2**), hydrogen (**DPF**)[176], phenyl (**DPF-Ph2**), spirobifluorene (**DPF-sp**), fluorine (**DPF-F2**), as well as oxo substituents (**DPF-O**).[176, 177]

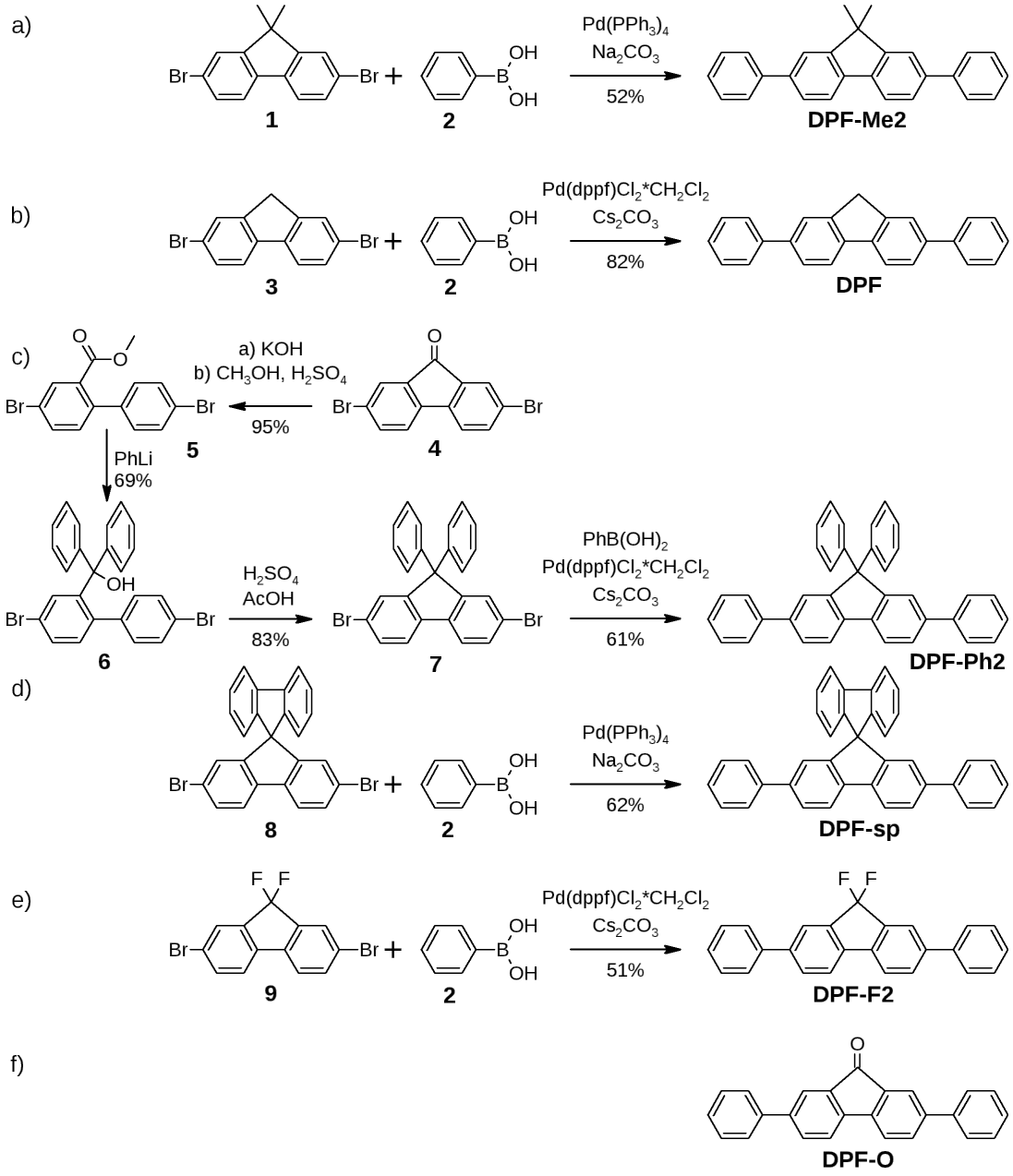

Figure 5.1. Investigated compounds and synthesis thereof.

5.2 Synthesis and Crystal Structures[26]

The synthesis of the different compounds was achieved by Suzuki cross-coupling of phenylboronic acid with the appropriate central 2,7-dibromofluorene unit either in a two phase system employing $Pd(PPh_3)_4$ as catalyst and Na_2CO_3 as base or in a one phase system with $Pd(dppf)Cl_2 \cdot CH_2Cl_2$ and Cs_2CO_3 (see figure 5.1). The reaction conditions were mainly adapted from ref [118]. The reaction yields range from 50 % (**DPF-Me2** and **DPF-F2**) up to more than 80% (**DPF**, **DPF-O**). It turned out, that the solubility of **DPF** is surprisingly low compared to the other products. The synthesis of 2,7-dibromo-9,9-diphenylfluorene **7** starts with 2,7-dibromofluorenone **4** (figure 5.1c), which was ring-opened with KOH in anisole

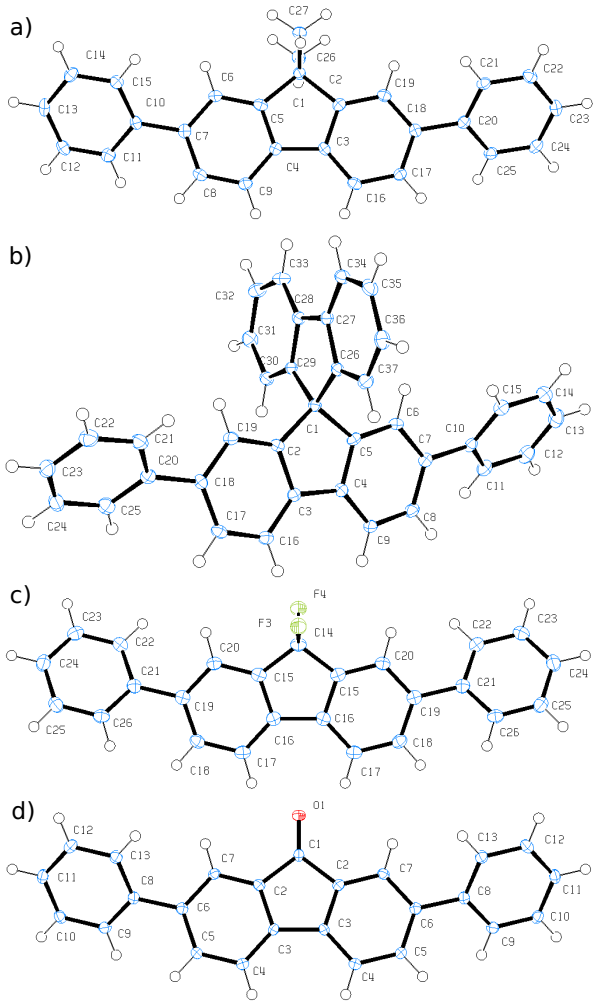

Figure 5.2. Molecular structures of a) **DPF-Me2**, b) **DPF-sp**, c) **DPF-F2**, and d) **DPF-O** from single crystal X-ray analysis. Thermal ellipsoides are drawn at the 50% probability level.

[26]The Synthesis of **DPF-Ph2** was carried out by Sandra Behren in the framework of her bachelor thesis. Collection of diffraction data and crystal structure refinement were carried out by Dr. Beatrice Braun (HU Berlin, Institut für Chemie).

and subsequently esterified with methanol in good yields to intermediate **5**. The ester was then reacted with phenyllithium to alcohol **6**, which was ring-closed to 2,7-dibromo-9,9-diphenylfluorene **7**.[168, 178]
For four of the derivatives it was possible to obtain single crystal X-ray structures (see figure 5.2). **DPF-Me2** and **DPF-sp** crystallize in $Pna2_1$ (orthorhombic), **DPF-F2** in $P2_1/m$ (monoclinic), and **DPF-O**[27] in $Cmc2_1$ (orthorhombic). None of the structures incorporates solvent molecules. **DPF-F2** and **DPF-O** posses mirror symmetry with respect to the orientation of the phenyl units. In **DPF-F2** there are two molecules with slightly different conformation in the unit cell: The angle between the fluorene plane and the phenyl plane is 26.95 ° for the one and 31.89 ° for the other one. For **DPF-O** they it amounts 35.71 °. For the other two molecules, the orientation of the two phenyl units with respect to the fluorene plane is not equal. In **DPF-Me2** they measure 36.77 ° and 31.76 °. In **DPF-sp** the phenyl-fluorene angles amount 43.89 ° and 40.32 °. Accordingly **DPF-F2** can be considered the most planar of these structures in the solid state and **DPF-sp** the least planar one.

5.3 Optical Properties

In terms of application, the main purpose of fluorene type materials is the emission of light. In that context the optical properties for the absorption and emission are of major importance. Figure 5.3 shows the absorption and PL spectra of the different DPFs (see also table 5.1 and 5.2).

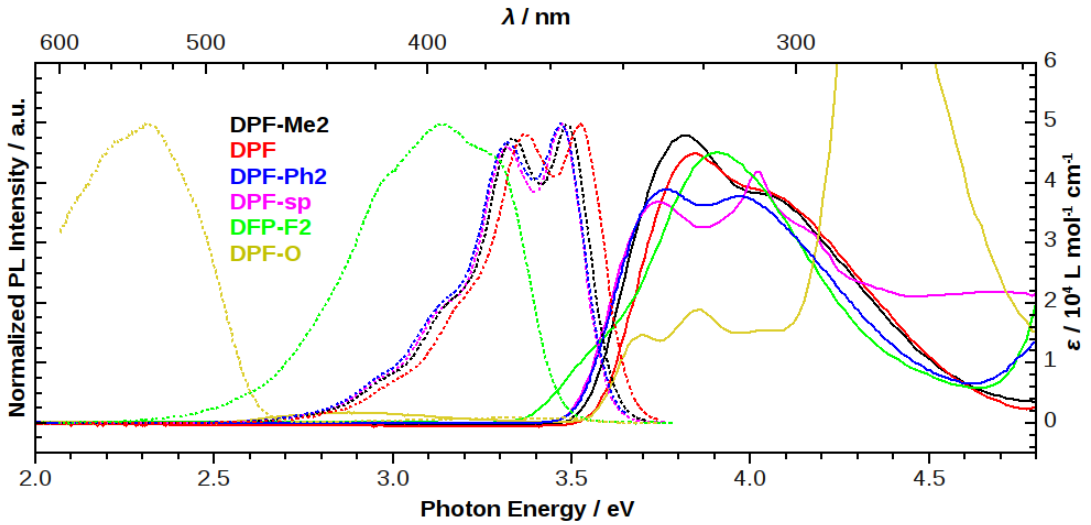

Figure 5.3. Absorption (solid line) and normalized PL spectra of **DPF-Me2** (black), **DPF** (red), **DPF-sp** (magenta), **DPF-Ph2** (blue), **DPF-F2** (green), and **DPF-O** (yellow) in ethyl acetate, $\approx 10^{-5}$ mol L^{-1}.

[27]The crystal structure of **DPF-O** has recently been published in ref. [177] and the space group agrees with our findings. However, the dimensions of the unit cell slightly deviate, which may be related to a different temperature during the measurement.

The all-hydrocarbon compounds (**DPF-Me2**, **DPF**, **DPF-Ph2**, and **DPF-sp**) show more or less the same behavior in absorption: There are two maxima or one maximum and one shoulder between 310 and 330 nm. The first maximum is slightly stronger than the second one, except for **DPF-sp**. Here, the stronger absorption in the second maximum can be attributed to the additional absorption of the spirobifluorene unit. The shape of the emission spectrum is even more similar: There

Table 5.1. Absorption Data

compound	solvent	λ_{max} / nm	ϵ_{max} / 10^3 L mol^{-1} cm^{-1} (λ / nm)
DPF-Me2	ethyl acetate	325	48 (325)
	CH_2Cl_2	326	46 (326)
DPF	ethyl acetate	322	45 (322)
	CH_2Cl_2	325	47 (325)
DPF-Ph2	ethyl acetate	313, 330	39 (330)
	CH_2Cl_2	314, 331	38 (331)
DPF-sp	ethyl acetate	309, 332	42 (309)
	CH_2Cl_2	310, 333	44 (310)
DPF-F2	ethyl acetate	317	45 (317)
	CH_2Cl_2	320	43 (320)
DPF-O	ethyl acetate	286, 322, 335, 431	19 (322)
	CH_2Cl_2	289, 324, 337, 437	19 (324)

λ_{max}: Absorption maxima; ϵ_{max} (λ): Absorption maximum and corresponding wavelength.

Table 5.2. Emission Data

compound	solvent	λ_{Em} / nm	λ_{Ex} / nm	Φ_{PL}
DPF-Me2	ethyl acetate	356, 372	325	
	CH_2Cl_2	355, 372	303	0.8
DPF	ethyl acetate	352, 369	322	
	CH_2Cl_2	356, 372	303	0.5
DPF-Ph2	ethyl acetate	357, 374	330	
	CH_2Cl_2	361, 376	303	<0.01
DPF-sp	ethyl acetate	357, 374	320	
	CH_2Cl_2	360, 376	310	1.0
DPF-F2	ethyl acetate	396	318	
	CH_2Cl_2	395	310	<0.01
DPF-O	ethyl acetate	538	322	
	CH_2Cl_2	≈550	310	0.04

λ_{Em}: Emission maxima; λ_{Ex}: Excitation wavelength; Φ_{PL}: Photoluminescence quantum yield.

are two main peaks with nearly equal intensity between 350 and 380 nm, and two shoulders at lower energies. This vibronic progression is related to lower flexibility of the molecules in the excited state. Except for a slight blue shift of **DPF**, the normalized PL spectra are very similar, but the effect of the substituent in the methylene bridge on the PL quantum yield Φ_{PL} in CH_2Cl_2 is dramatic: For **DPF** Φ_{PL} is about 0.5, methylation (**DPF-Me2**) increases Φ_{PL} to 0.8, and for the spiro compound **DPF-sp** it is roughly unity. But removing the spiro linkage between the two phenyl substituents in the 9-position leads to a drop of Φ_{PL} below one per cent for **DPF-Ph2**. This may be attributed to the ability of free rotation of the 9-phenyl in the excited state[28] . **DPF-F2** has an absorption maximum around 320 nm and a shoulder at the low-energy side and the emission is shifted to lower energies compared to the hydrocarbons, having its maximum around 400 nm and Φ_{PL} is very low ($< 1\%$). The ketone **DPF-O** shows a behaviour, which is typical for the fluorenone-defect. In the region between 350 and 300 nm the absorption is decreased compared to the other compounds, but below 300 nm it is strongly increased. Below the 'normal' absorption edge, a new, weak absorption band can be found, which reaches far into the visible region. There is also a low energy emission related to that transition with a maximum around 540 nm and a Φ_{PL} of about 0.04.

5.4 Photochemical Degradation[29]

5.4.1 Theoretical Considerations Concerning the Kinetics of Degradation

Regarding a simple photoreaction

$$A \xrightarrow{h\upsilon} B$$

the change in concentration of A can be expressed in the following way:

$$\frac{\mathrm{d}a}{\mathrm{d}t} = \varphi_A I_A. \tag{5.1}$$

In this equation φ_A denotes the quantum yield of the above mentioned reaction and I_A the number of absorbed (only by A) photons per unit time and unit volume.[30] The intensity of the absorbed light is given by

$$I_A(z) = \varepsilon_A^* a I(z) \tag{5.2}$$

with z being the length of the path, the light traveled through the solution, ε^* being the natural absorption coefficient and $I(z)$ being the intensity of light at the position

[28]Note: The 2,7-phenyls are not supposed to be freely rotatable in the excited state due to partial double bond character of the phenyl-fluorene bond.

[29]The majority of kinetic degradation experiments was carried out by Sandra Behren in the framework of her bachelor thesis.

[30]Ref. [179], p.135.

z.[31] Assuming that the absorption of B can be neglected,[32] the Lambert-Beer-Law ($I(z) = I_0 e^{-z\varepsilon_A^* a}$) can be substituted into 5.2. This gives a measure for the intensity of absorbed light after a path length z in the absorbing medium:

$$I_A(z) = \varepsilon_A^* a I_0 e^{-z\varepsilon_A^* a} \tag{5.3}$$

To obtain the mean intensity of absorbed light I_A in the cuvette, $I_A(z)$ has to be integrated over the length l of the cuvette and divided by l:

$$I_A = \frac{1}{l}\int_0^l I_A(z)\mathrm{d}z = \frac{I_0}{l}\left[1 - e^{-\varepsilon_A^* a l}\right] \tag{5.4}$$

For practical reasons, the natural extinction coefficient ε^* is substituted by the decadic extinction coefficient ε:

$$I_A = \frac{I_0}{l}\left[1 - 10^{-\varepsilon_A a l}\right] \tag{5.5}$$

Now, I_A in equation 5.1 can be substituted by equation 5.5 and $\varepsilon_A a l$ by the extinction E_A:

$$\frac{\mathrm{d}a}{\mathrm{d}t} = \frac{-\varphi_A I_0}{l}\left[1 - 10^{-E_A}\right] \tag{5.6}$$

Equation 5.6 only accounts for monochromatic light. In our setup, a broader range of wavelengths was used. Assuming, that φ_A is independent of the wavelength of irradiation, the term for the absorbed light (denoted by the index $_{ir}$) can be summed up as follows:[33]

$$\boxed{\frac{\mathrm{d}a}{\mathrm{d}t} = \frac{-\varphi_A}{l}\sum_{\lambda_{ir}} I_0(\lambda_{ir})\left[1 - 10^{-E_A(\lambda_{ir})}\right]} \tag{5.7}$$

The change of concentration of $\frac{\mathrm{d}a}{\mathrm{d}t}$ was determined by means of UV/Vis absorption spectroscopy. Regarding the reaction $A \xrightarrow{h\upsilon} B$, the absorbance (normalized over the length) for the sample is given by

$$\frac{1}{l}E = a\varepsilon_A + b\varepsilon_B \tag{5.8}$$

with $a = a_0 - \alpha a_0 = a_0(1-\alpha)$ and $b = a_0\alpha$, with a_0 being the initial concentration of A and α being the degree of reaction. This leads to the following expression for the absorbance during the reaction:

$$\frac{1}{l}E = a_0(1-\alpha)\varepsilon_A + a_0\alpha\varepsilon_B = a_0\left[\varepsilon_A + \alpha(\varepsilon_B - \varepsilon_A)\right]. \tag{5.9}$$

[31] Ref. [179], pp.167.

[32] This assumption is valid at the very beginning of the photoreaction and if ε_B is considerably smaller than ε_A. Here, we only used the first few per cent of conversion for the analysis of the kinetics.

[33] Integration would be the formally correct operation at this point, the summation accounts for the numeric processing of the recorded spectral data.

The time derivative of equation 5.9 is given by:

$$\frac{1}{l}\frac{\mathrm{d}E}{\mathrm{d}t} = (\varepsilon_B - \varepsilon_A)a_0\frac{\mathrm{d}\alpha}{\mathrm{d}t} \tag{5.10}$$

The time derivative of the concentration $\frac{\mathrm{d}a}{\mathrm{d}t} = -a_0\frac{\mathrm{d}\alpha}{\mathrm{d}t}$ allows for further simplification:

$$\frac{1}{l}\frac{\mathrm{d}E}{\mathrm{d}t} = (\varepsilon_a - \varepsilon_B)\frac{\mathrm{d}a}{\mathrm{d}t} = \varepsilon_A\beta\frac{\mathrm{d}a}{\mathrm{d}t} \tag{5.11}$$

with $\beta = \frac{\varepsilon_A - \varepsilon_B}{\varepsilon_A}$ being a factor that describes to which extent a change in concentration of A leads to a change in absorbance. In case ε_B is not known, β was determined by UPLC-UV/Vis-spectroscopy. In Eqn. 5.7, $\frac{\mathrm{d}a}{\mathrm{d}t}$ was substituted according to Eqn. 5.11, leading to the following expression for the reaction quantum yield (λ_{obs} is the wavelength at which the change of absorbance is detected):

$$\boxed{\varphi_A = -\frac{\mathrm{d}E(\lambda_{obs})}{\mathrm{d}t}\cdot\frac{1}{\varepsilon_A(\lambda_{obs})\beta}\cdot\frac{1}{\sum_{\lambda_{ir}} I_0(\lambda_{ir})\left[1-10^{-E_A(\lambda_{ir})}\right]}} \tag{5.12}$$

Unfortunately we were not able to determine the actual intensity I_0 at the cuvette. However, for the determination of the proportion of the quantum yield of the different compounds, the relative intensity of the irradiation wavelengths is suited, as well. The relative intensity will be referred to as I_0^*. The output power (power per area and wavelength interval) of the Xenon arc lamp is more or less constant over the range of irradiation wavelengths ($\approx$ 300 - 400 nm) we used.[34] This was converted to photons per area and time and multiplied by the transmittance of the UG1 filter to give the relative light intensity I_0^* (see figure 5.4).

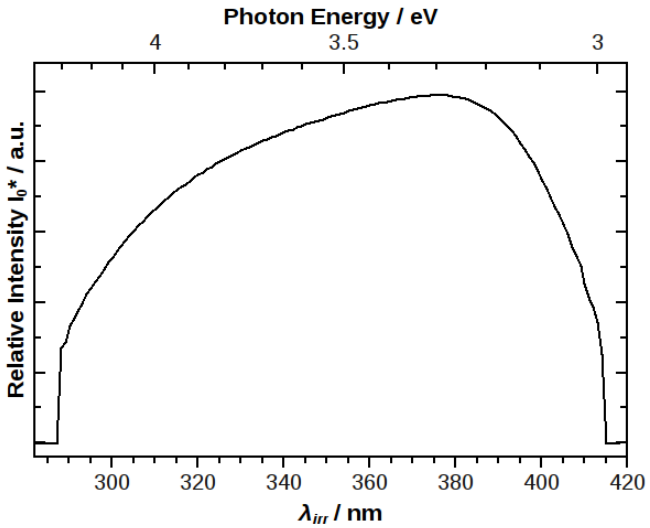

Figure 5.4. Estimated relative light intensity for the degradation experiments.

[34]ORIEL PRODUCT TRAINING: Spectral Irradiance, p. 26, downloaded June 12, 2014 at `http://assets.newport.com/webDocuments-EN/images/Light_Sources.pdf`

Now, a number φ^* can be determined, that is in linear relationship to the actual quantum yield:

$$\varphi_A^* = -\frac{\mathrm{d}E(\lambda_{obs})}{\mathrm{d}t} \cdot \frac{1}{\varepsilon_A(\lambda_{obs})\beta} \cdot \frac{1}{\sum_{\lambda_{ir}} I_0^*(\lambda_{ir})\left[1 - 10^{-E_A(\lambda_{ir})}\right]}. \tag{5.13}$$

5.4.2 Phenomenological Findings

To get a quantitative measure for the efficiency of degradation, the changes of concentration are monitored after the sample has absorbed a certain amount of photons, which is achieved by irradiation for a certain time with a constant light intensity. In this case a Xenon arc lamp equipped with a UG1 filter (transmission ≈ 300 - 400 nm) was used, to irradiate a cuvette with the corresponding solution of the DPF at a concentration slightly above 10^{-5} mol L^{-1} in ethyl acetate under air. But before doing a quantitative analysis, some phenomenological findings are discussed. In figure 5.5 the change of absorption of two typical samples is shown. In both cases the main absorption band decreases and a low-energy tail and some higher energy band are building up. In one of the cases (figures 5.5 a and c), which is discussed by **DPF-Me2** as example, but also represents **DPF-sp** and **DPF-Ph2**, the degradation is relatively slow. At the beginning, there are only slight changes and the process seems to accelerate. The extinction difference (ED) plot[180] (figure 5.5 a), inset) does not give an obvious linear relationship. At first sight, this might be attributed to the small EDs above 4.5 eV and below 3.5 eV, but also linear fitting does not give lines through the origin, especially the positive slope contradicts a uniform reaction. This kinetic behavior may be related to an auto-catalytic degradation process involving singlet oxygen, as we just proposed for methylated ladder-type oligo-*para*-phenylenes.[117] In later stages of the degradation process (not shown here) the absorption is broad and flat, evenly decreasing upon further irradiation. UPLC-UV/Vis-Absorption analysis (figure 5.5 e) of degraded solutions shows a large variety of products. This is in agreement to the ED plots, demonstrating the manifoldness of the involved photoreactions.

In the second case (figure 5.5 b, d, and f), which is represented by **DPF**, the conversion is way faster. The reaction starts rapidly, decelerates over time, and stops more or less at a certain point. The ED plot clearly shows a linear relationship and linear fitting gives lines, which – more or less – cross the origin. This kind of kinetics may be related to a first-order reaction, as expected for a uniform photoreaction of the type A→B. Furthermore, the final absorption spectrum (red line in figure 5.5 b) looks very much like the absorption spectrum of **DPF-O**. This finding was also confirmed by UPLC-analysis (figure 5.5f). The degradation of **DPF-F2** (figure 5.6) seems even faster, also giving **DPF-O** as reaction product. However, the ED plot, which is not strictly linear, as well as the initial increase and subsequent decrease of the band at 3 eV do rather suggest a two-step process with some intermediate being formed. In summary, UV-irradiation of **DPF** and **DPF-F2** leads to relatively rapid conversion to **DPF-O** (figure 5.7) without formation of significant amounts of side products, while the samples with carbon-carbon bonds in the methylene bridge only slowly undergo photodegradation and form a large variety of products. The photodegradation of **DPF-O** was also investigated, but it is much slower than all the

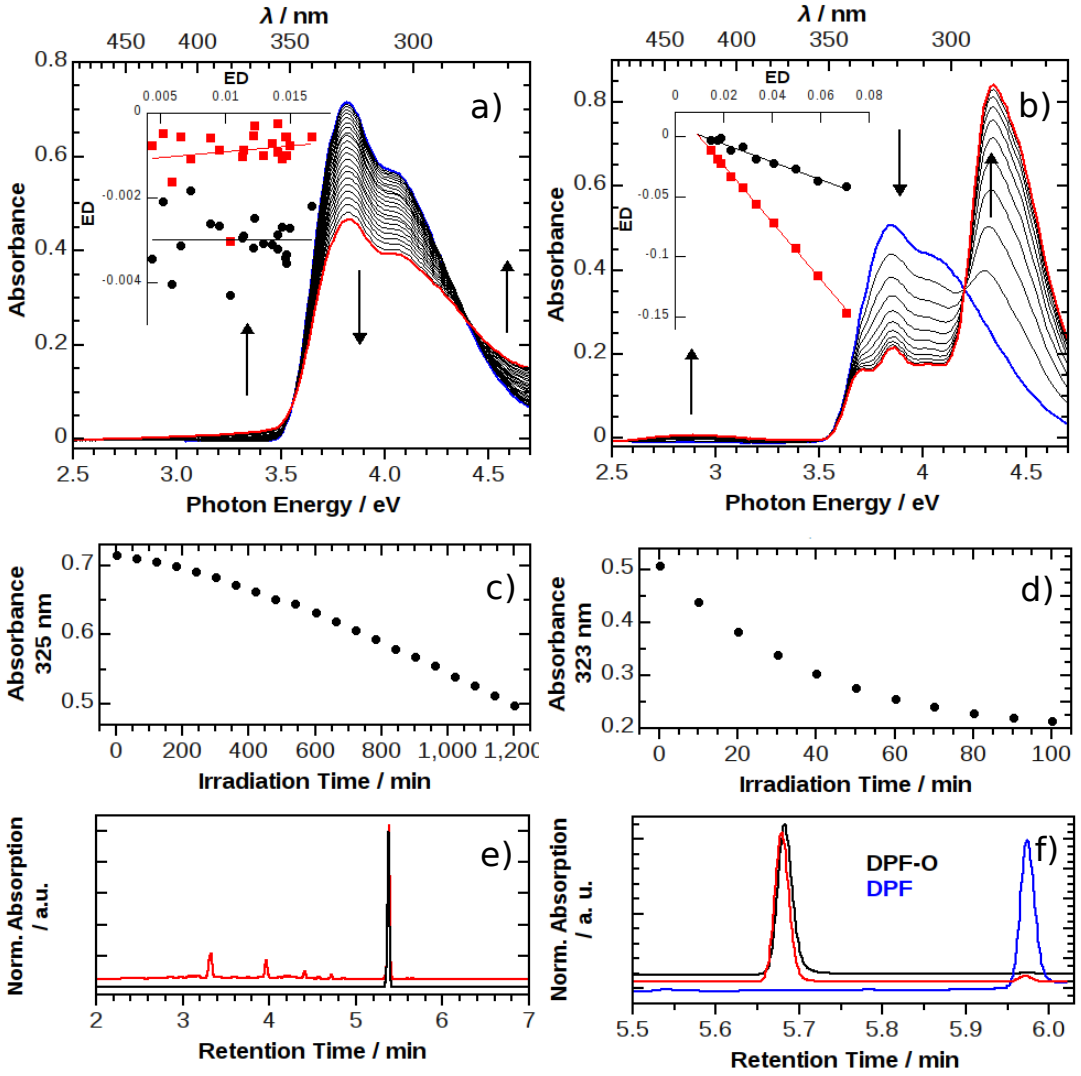

Figure 5.5. Change in absorption upon photochemical degradation in ethyl acetate with light of 290 - 410 nm: a) Changes in the absorption spectrum of **DPF-Me2**, initial concentration $1.50 \cdot 10^{-5}$ mol L^{-1}, time interval: 1 h. Inset: ED plot, ED at 370 nm vs. ED at 325 nm (red squares, solid line: linear fit), ED at 270 nm vs. ED at 325 nm (black circles, solid line: linear fit). b) Changes in the absorption spectrum of **DPF**, initial concentration $1.12 \cdot 10^{-5}$ mol L^{-1}, time interval: 10 min. Inset: ED plot, ED at 285 nm vs. ED at 325 nm (red squares, solid line: linear fit), ED at 430 nm vs. ED at 325 nm (black circles, zoomed x10, solid line: linear fit). c) Absorbance of **DPF-Me2** at 325 nm vs. irradiation time. d) Absorbance of **DPF** at 323 nm vs. irradiation time. e) Absorption trace (330 ± 5 nm) of a liquid chromatography run of pristine (black) and photodegraded (red) **DPF-Me2**. f) Absorption trace (280 ± 5 nm) of a liquid chromatography run of pristine **DPF** (blue), **DPF-O** (black) and degraded **DPF** (red).

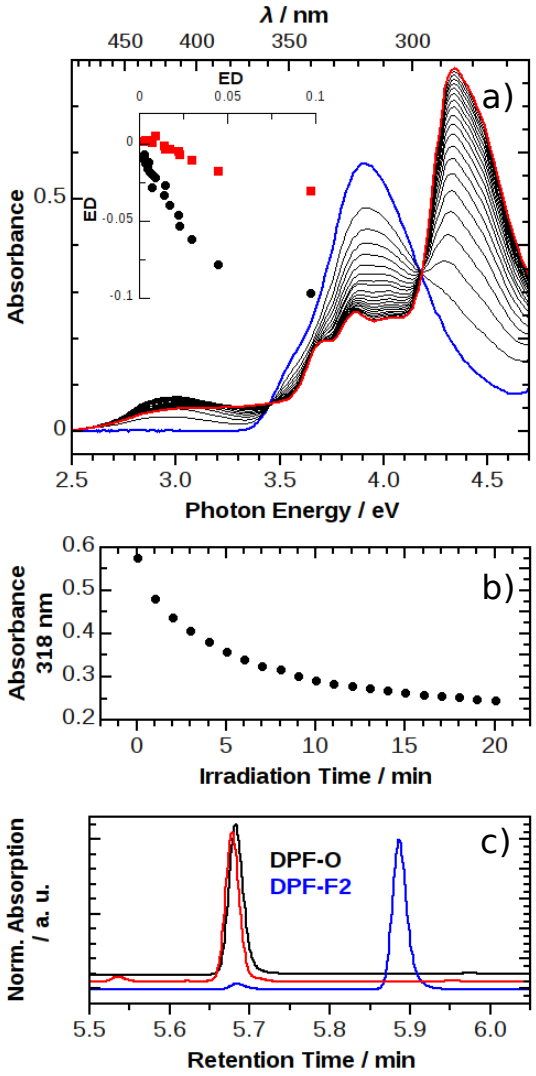

Figure 5.6. Photochemical degradation of **DPF-F2** in ethyl acetate with light of 290 - 410 nm. a) Changes in the absorption (initial concentration: $1.30 \cdot 10^{-5}$ mol L^{-1}), time interval: 1 min. Inset: ED plot, ED at 285 nm vs ED at 320 nm (black circles), ED at 420 nm vs. ED at 320 nm (red squares). b) Absorbance at 317 nm vs. irradiation time. c) Absorption trace (280 ± 5 nm) of liquid chromatography runs of pristine **DPF-F2** (blue), degraded **DPF-F2** (red), as well as **DPF-O** (black).

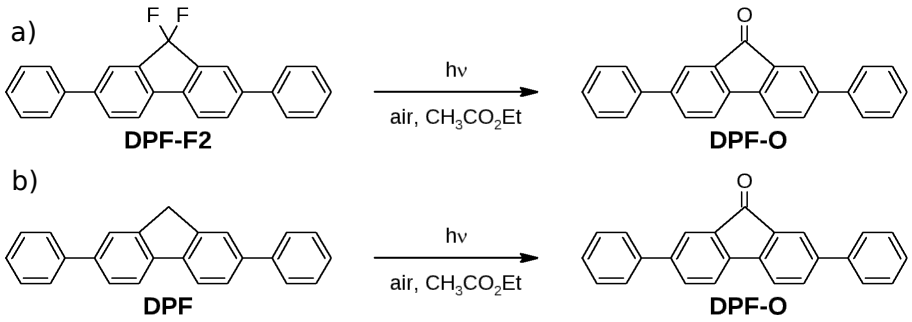

Figure 5.7. Identified reaction products of photodegradation of a) **DPF-F2** and b) **DPF**.

other examples, which might at least partly be due to the lower extinction coefficient at the irradiation wavelengths. In the end, it was too slow to generate quantitative information about its degradation in a reasonable irradiation time.

5.4.3 Evaluation of Kinetic Studies

The strict determination of a quantum yield of the accelerating **DPF-Me2**-type kinetics is somewhat difficult, because the knowledge of the exact reaction mechanism is needed and the critical photochemical step has to be identified. Furthermore this number would possibly not be comparable to the simpler mechanism. Accordingly, it was decided to treat the different reactions, as if they were of the simple type A $\rightarrow$ B. From a practical point of view, this should be appropriate to answer the question: How fast do the first few per cent of a material degrade? The quantum yield of that photoreaction can be determined according to equation 5.13. In this equation, $\frac{\mathrm{d}E(\lambda_{obs})}{\mathrm{d}t}$ denotes the change of absorbance at the observation wavelength and can easily be monitored during irradiation. $\varepsilon_A(\lambda_{obs})\beta$ gives the relation of the first term to a change in concentration and the last term accounts for the amount of absorbed light. The asterisk (*) in I_0^* and φ_A^* denotes, that the absolute light intensity I_0 is not known, but $I_0^*(\lambda_{ir})$ is at least proportional to the actual intensity. Hence, φ_A^* is also not the actual quantum yield, but a number that is proportional to it. Later it will be normalized to the slowest degrading compound, to give a relative efficiency of degradation. β is a factor, that describes, to which extent a change of the concentration of the starting material leads to a change in absorbance. It can be calculated as $\beta = \frac{\varepsilon_A - \varepsilon_B}{\varepsilon_A}$, when the extinction coefficient of the product is known and the product is stable. So for **DPF** β is 0.58 and for **DPF-F2** it is 0.64 (see table 5.3). In the case of the other three compounds, the determination of β is more demanding: On the one hand, there is a large variety of degradation products, which would still allow for the determination of an effective ε_B of the product mixture. But on the other hand, the process does not 'stop' at a certain stage, or with other words the primary degradation products degrade, as well at a velocity that is not negligible. However, it is possible to find a relationship between the concentration of the starting material and the absorbance in an experimental

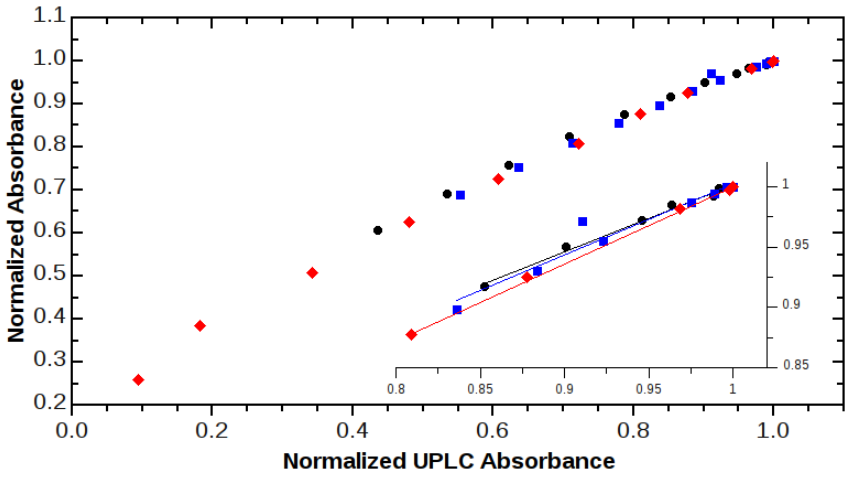

Figure 5.8. Determination of β by absorbance and UPLC. The normalized absorbance of the product mixture is plotted versus the normalized concentration, which was determined by UPLC (integrated absorption trace) for **DPF-Me2** (red diamonds), **DPF-Ph2** (black circles), and **DPF-sp** (blue squares). Inset: Zoom into the zone of the linear fits.

way. Therefore, solutions of $\approx 10^{-4}$ mol L^{-1} of the DPFs in ethyl acetate have been irradiated in a photoreactor at 300 nm. From time to time the absorption spectrum of the solutions was recorded and the corresponding concentration of the starting material was monitored by UPLC (integration of the absorption peak in the chromatogram). In figure 5.8 the normalized absorbance of the sample is plotted versus the concentration of the starting material. Luckily, it turned out that there is nearly a linear relationship. Hence, β is given by the slope of the linear fit. To account for the fact, that only the first few per cent of conversion were used to determine $\frac{\mathrm{d}E(\lambda_{obs})}{\mathrm{d}t}$, also here only the range of the first 20% conversion was fitted (see figure 5.8, inset). According to this procedure, for **DPF-Me2** a β of 0.64 was found, for **DPF-Ph2**, it is 0.55 and for **DPF-sp** 0.59. These values are also in the range of the ones, which were calculated by the extinction coefficient of the known product for **DPF** and **DPF-F2**.

Finally, the relative efficiencies of the photodegradation of the different DPFs were determined according to equation 5.13. The two aryl substituted compounds **DPF-Ph2** and **DPF-sp** degrade equally slowest ($\varphi^* = 1$). The methyl substituted one

Table 5.3. Comprehensive efficiencies of photodegradation relative to **DPF-sp**.

Compound	β	φ^*
DPF-Me2	0.64	3.3
DPF	0.58	290
DPF-Ph2	0.55	1.0
DPF-sp	0.59	1.0
DPF-F2	0.64	2200

DPF-Me2 degrades roughly tree times faster. The hydrogen substituted **DPF** degrades another 100 times faster, reaching a φ^* of 290. Surprisingly, the degradation of the fluorinated compound is by far the fastest with a φ^* of 2200.

5.5 Conclusion

In this chapter a method for the quantification of the inertness of fluorene type materials towards photodegradation was presented. Regarding the kinetics of photodegradation of a series of differently bridge substituted 2,7-diphenylfluorenes as model compounds for polyfluorenes, it turned out, that this the reaction is governed by two very different mechanisms. While hydrogen or fluorine substituents in the bridge (represented by **DPF** and **DPF-F2**) give a typical decelerating first-order photokinetics, leading to the fluorenone-product **DPF-O**, aryl and alkyl substitution (represented by **DPF-Me2**, **DPF-Ph2**, and **DPF-sp**) leads to a degradation, which accelerates in the beginning and gives a large variety of products. The latter ones are also way more inert. Aromatic substituents are the most inert ones, no matter if phenyl or spirobifluorene. However, the phenyl substituents in the bridge reduce the fluorescence quantum yield (in solution) dramatically. The methyl substituted compound degrades about three times more efficient. Finally, the spirocompound is the best one, taking into account both inertness and luminescence. But also alkyl substitution still shows acceptable inertness towards degradation combined with a good fluorescence quantum yield, if it is properly purified. These findings may help to understand substituent effects in fluorene type materials in a general way.

5.6 Experimental

5.6.1 Analytical Instrumentation

Analytical LC was performed on a Waters Acquity UPLC equipped with a Waters LCT Premier XE Mass detector for high-resolution MS (HR-MS, ESI^+-ionization) and with Waters Alliance systems (consisting of a Waters Separations Module 2695, a Waters Diode Array Detector 996 and a Waters LCT Premier XE Mass Detector).

5.6.2 UV-Vis Spectroscopy

Absorption spectra were recorded on a Varian Cary 50 Bio UV-Visible spectrometer and fluorescence spectra on a Varian Cary Eclipse Fluorescence spectrometer using 10.0 x 10.0 mm quartz cuvettes. For the studies on degradation a 1000 W Oriel Xe high pressure arc lamp was used equipped with a water-filter and an UG1-filter.

5.6.2.1 Fluorescence Quantum Yield

The fluorescence quantum yield was determined according to

$$\Phi_S = \Phi_R \cdot \frac{\int I_S(\lambda_S) d\lambda_S}{\int I_R(\lambda_R) d\lambda_R} \cdot \frac{[1 - 10^{-E_R(\lambda_{Ex})}]}{[1 - 10^{-E_S(\lambda_{Ex})}]} \cdot \frac{n_S^2}{n_R^2}. \tag{5.14}$$

In the equation Φ depicts the fluorescence quantum yield, $\int I(\lambda) d\lambda$ the area under the fluorescence spectrum, $E(\lambda_{Ex})$ the extinction (absorbance) at the excitation wavelength (which was kept the same for sample and reference), and n the refractive index of the solvents used. Index R denotes properties of the reference, and S of the unknown sample. p-quarterphenyl in cyclohexane, assuming $\Phi = 0.89$[99], was used as reference.[126, 127]

5.6.3 Organic Synthesis

^{1}H-NMR and ^{13}C-NMR spectra were referenced to 7.26 ppm and 77.16 ppm, respectively, for $CDCl_3$ and 5.32 ppm and 53.8 ppm, respectively, for CD_2Cl_2.

9,9-Dimethyl-2,7-diphenyl-9*H*-fluorene DPF-Me2
Under an argon atmosphere $Pd(PPh_3)_4$ (0.116 g, 0.10 mmol) was added to a stirred solution of **1** (1.76 g, 5.0 mmol) in THF (100 mL). The mixture was stirred for 10 min. Then, phenylboronic acid **2** (1.46 g, 12.0 mmol), as well as aqueous Na_2CO_3 (40 mL, 2.0 mol L^{-1}) were added and the reaction was stirred for 4 h at 65 °C. After cooling to room temperature, water was added and the mixture was extracted with ethyl acetate. The organic phase was dried ($MgSO_4$) and the solvent was removed. Purification by column chromatography (petroleum ether/ethyl acetate), recrystallization (CH_2Cl_2/cyclohexane), and sublimation yielded 0.9 g (2.6 mmol, 52% yield) of **DPF-Me2**.
^{1}H-NMR (300 MHz, $CDCl_3$) δ [ppm] = 7.81 (d, J = 7.8 Hz, 2H), 7.72 - 7.65 (m, 6H), 7.60 (dd, J = 7.9, 1.6 Hz, 2H), 7.48 (t, J = 7.5 Hz, 4H), 7.37 (t, J = 7.3 Hz, 2H), 1.59 (s, 6H).
^{13}C-NMR (75 MHz, $CDCl_3$) δ [ppm] = 154.7, 141.7, 140.6, 138.3, 128.9, 127.4, 127.3, 126.4, 121.6, 120.5, 47.2, 27.5.

2,7-Diphenyl-9*H*-fluorene DPF
Under argon, a mixture of 2,7-dibromo-9*H*-fluorene **3** (1.62 g , 5.0 mmol), phenylboronic acid **2** (1.53 g, 12.5 mmol), $Pd(dppf)Cl_2 \cdot CH_2Cl_2$ (0.83 g, 0.10 mmol), and Cs_2CO_3 (4.88 g, 15.0 mmol) in THF/ethanol/DMF (40/40/10 mL) was stirred at 65 °C for 2 h. After cooling to room temperature, water was added and the mixture was extracted with CH_2Cl_2 (>400 mL, low solubility). The organic phase was dried ($MgSO_4$) and the major amount of solvent was removed. The precipitate was filtered off and purified by gradient sublimation. **DPF** (1.3 g, 4.1 mmol, 82% yield) was obtained as a nearly colorless solid.
^{1}H-NMR (300 MHz, CD_2Cl_2) δ [ppm] = 7.89 (d, J = 8.0 Hz, 2H), 7.84 - 7.81 (m, 2H), 7.72 - 7.63 (m, 6H), 7.51 - 7.43 (m, 4H), 7.40 - 7.32 (m, 2H), 4.05 (s, 2H).

Methyl-4,4'-dibromo-[1,1'biphenyl]-2-carboxylate (5)
The literature procedure[178] was modified: A stirred suspension of 2,7-dibomofluorenone **4** (10.4 g, 30.8 mmol) in anisole (100 mL) was heated to 100 °C. Then, KOH

(12.0 g, 214 mmol) was added and the solution was heated to 160 °C. The mixture was stirred at that temperature, until a white precipitate had formed and the yellow color of the solution had vanished. The precipitate was filtered from the hot solution, washed with petroleum ether and dissolved in water. Upon adding conc. hydrochloric acid, the product precipitated. It was filtered off and dried.
The crude carboxylic acid was dissolved in methanol (200 mL) at 65 °C. After adding conc. sulfuric acid (8 mL), the mixture was stirred over night at that temperature. Then, methanol was removed and the residue was dissolved in ethyl acetate. The solution was washed with aqueous $NaHCO_3$ and water (3x). The organic phase was dried and the solvent was removed. The crude product was purified by column chromatography (petroleum ether/ethyl acetate) to give 11.0 g (29.6 mmol, 95% yield) of methyl ester **5**.
^{1}H-NMR (300 MHz, CD_2Cl_2) δ [ppm] = 7.98 (d, J = 2.2 Hz, 1H), 7.68 (dd, J = 8.2, 2.2 Hz, 1H), 7.58 - 7.49 (m, 2H), 7.23 (d, J = 8.2 Hz, 1H), 7.20 - 7.12 (m, 2H), 3.67 (s, 3H).
^{13}C-NMR (75 MHz, CD_2Cl_2) δ [ppm] = 167.4, 140.1, 139.6, 134.8, 133.2, 132.6, 131.6, 130.4, 122.1, 121.8, 52.6.

(4,4'-Dibromo-1,1'-biphenyl-2-yl)diphenylmethanol (6)[35]
Under an argon atmosphere *n*BuLi (3.2 mL, 7.0 mmol, 2.2 mol L^{-1} in cyclohexane) was added to a solution of bromobenzene (1.1 g, 7 mmol) in THF (10 mL) at -78 °C. After stirring the mixture at that temperature for 30 min, it was added to a solution of **5** (1.1 g, 3.0 mmol) in THF (20 mL). The reaction was stirred at 60 °C for one hour. After cooling to room temperature, the reaction was quenched with diluted aqueous NH_4Cl and extracted with CH_2Cl_2. The organic phase was dried ($MgSO_4$), the solvent was removed and the product was crystallized from CH_2Cl_2/ethanol. **6** (1.02 g, 2.06 mmol, 69% yield) was obtained as colorless crystals.
^{1}H-NMR (300 MHz, CD_2Cl_2) δ [ppm] = 5.46 (dd, J = 8.1, 2.1 Hz, 1H), 5.34 - 5.21 (m, 8H), 5.16 - 5.07 (m, 4H), 4.97 (dd, J = 5.1, 2.9 Hz, 2H), 4.68 - 4.59 (m, 2H).
^{13}C-NMR (75 MHz, CD_2Cl_2) δ [ppm] = 146.9, 140.6, 134.3, 133.0, 131.5, 131.1, 130.5, 129.4, 128.3, 128.2, 127.9, 121.8, 121.3, 110.4, 83.2.

2,7-Dibromo-9,9-diphenyl-9*H*-fluorene (7)[36]
Concentrated sulfuric acid (0.5 mL) was added to a stirred solution of **6** (0.5 g, 1.0 mmol) in acetic acid (15 mL) at 100 °C. The mixture was stirred at that temperature for one hour and finally poured into water. The precipitate was filtered off and crystallized from chloroform/ethanol to give **7** (0.4 g, 0,84 mmol, 83% yield) as white powder.
^{1}H-NMR (300 MHz, CD_2Cl_2) δ [ppm] = 7.69 - 7.62 (m, 2H), 7.52 (m, 4H), 7.30 - 7.23 (m, 6H), 7.19 - 7.10 (m, 4H).
^{13}C-NMR (75 MHz, CD_2Cl_2) δ = 153.4, 144.8, 138.5, 131.4, 129.6, 128.9, 128.3, 127.6, 122.2, 110.4, 66.0.

[35] According to ref. [168].
[36] The synthesis was carried out according to a slightly modified literature procedure from ref. [168]

2,7,9,9-Tetraphenyl-9*H*-fluorene DPF-Ph2
A mixture of **7** (0.4 g, 0.84 mmol), phenylboronic acid **2** (0.26 g, 2.1 mmol), Cs_2CO_3 (1.26 g, 3.8 mmol), and Pd(dppf)$Cl_2 \cdot CH_2Cl_2$ (0.014 g, 0.017 mmol) in THF/ethanol/DMF (10/10/2.5 mL) was stirred under an argon atmosphere for 30 min at 70 °C. Then, it was poured into water and extracted with ethyl acetate. The organic phase was dried ($MgSO_4$) and the solvent was removed. The crude product was purified by column chromatography (petroleum ether/ethyl acetate) to give **DPF-Ph2** (0.24 g, 0.51 mmol, 61% yield) as white powder.
^{1}H-NMR (300 MHz, CD_2Cl_2) δ [ppm] = 7.95 - 7.88 (m, 2H), 7.72 - 7.64 (m, 4H), 7.64 - 7.56 (m, 4H), 7.48 - 7.39 (m, 4H), 7.38 - 7.22 (m, 12H).
^{13}C-NMR (75 MHz, CD_2Cl_2) δ [ppm] = 152.5, 146.2, 141.4, 141.2, 139.4, 129.1, 128.7, 128.5, 127.7, 127.4, 127.2, 127.2, 125.2, 121.0, 66.1.

2,7-Diphenyl-9,9'-spirobi[fluorene] DPF-sp
Under an argon atmosphere Pd(PPh_3)$_4$ (0.18 g, 0.16 mmol) was added to a solution of 2,7-dibromospirobifluorene **8** (0.75 g, 1.6 mmol) in THF (40 mL). After stirring for 10 min, aqueous Na_2CO_3 (12.6 mL, 2.0 mol L^{-1}) and phenylboronic acid **2** (0.46 g, 3.8 mmol) were added. The reaction was stirred for 24 h at 65 °C. After cooling to room temperature, water was added and the mixture was extracted with ethyl acetate. The organic phase was dried ($MgSO_4$) and the solvent was removed. The crude product was purified by column chromatography (petroleum ether/ethyl acetate) and subsequent crystallization (ethyl acetate) to give **DPF-sp** (0.50 g, 1.1 mmol, 68% yield) as colorless solid.
^{1}H-NMR (300 MHz, $CDCl_3$) δ [ppm] = 7.93 (d, J = 7.9 Hz, 2H), 7.87 (d, J = 7.6 Hz, 2H), 7.63 (dd, J = 7.9, 1.7 Hz, 2H), 7.46 - 7.21 (m, 12H), 7.12 (td, J = 7.5, 1.1 Hz, 2H), 6.94 (d, J = 1.6 Hz, 2H), 6.83 (d, J = 7.6 Hz, 2H).
^{13}C-NMR (75 MHz, $CDCl_3$) δ [ppm] = 150.1, 148.9, 142.1, 141.2, 140.9, 128.8, 128.1, 128.0, 127.4, 127.3, 127.2, 124.5, 123.0, 120.6, 120.3, 66.3.

9,9-Difluoro-2,7-diphenyl-9*H*-fluorene DPF-F2
Under an argon atmosphere, phenylboronic acid **2** (0.36 g, 3.0 mmol) was added to a mixture of **9** (0.40 g, 1.1 mmol), Pd(dppf)$Cl_2 \cdot CH_2Cl_2$ (0.06 g, 0.09 mmol) and Cs_2CO_3 (0.89 g, 2.75 mmol) in THF/ethanol/DMF (8/8/2 mL). After stirring the mixture for 2 h at 65 °C, water was added and the (cooled) mixture was extracted with CH_2Cl_2. The organic phase was dried ($MgSO_4$) and all volatiles were removed. Column chromatography (petroleum ether/ethyl acetate) gave 0,20 g (0.56 mmol, 51% yield) of **DPF-F2**.
^{1}H-NMR (300 MHz, $CDCl_3$) δ [ppm] = 7.88 (*d*, J = 1.1 Hz, 2H), 7.72 (dd, J = 7.9, 1.6 Hz, 2H), 7.68 - 7.62 (m, 6H), 7.53 - 7.44 (m, 4H), 7.44 - 7.36 (m, 2H).
^{13}C-NMR[37] (75 MHz, $CDCl_3$) δ [ppm] = 142.2, 140.3, 139.0, 138.3, 131.1, 129.1, 128.0, 127.2, 122.8, 120.92.
For further purification **DPF-F2** was crystallized from THF.

[37] spectrum incomplete/multiplets not assigned

5.6.4 Crystal Structure Analysis

The diffraction data were collected on a STOE IPDS 2Θ diffractometer at 100 K. Crystallographic data are depicted in the crystallographic table. The structures were solved by direct methods (SHELXS-97)[124] and were refined with the full-matrix least-squares method n F^2 (SHELX-97 and SHELXL-2013)[38]. The hydrogen atoms were placed at the calculated positions and were refined by using a riding model. The data, which contain the supplementary crystallographic information, can be obtained free of charge from The Cambridge Crystallographic Data Centre via `www.ccdc.cam.ac.uk/data_request/cif`.

[38][124]; Sheldrick, G. M., *SHELXL, Crystal Structure Refinement*, **2013** University of Göttingen, Germany.

compound	**DPF-Me2**	**DPF-sp**	**DPF-F2**	**DPF-O**
Formular	$C_{27}H_{22}$	$C_{37}H_{24}$	$C_{25}H_{16}F_2$	$C_{25}H_{16}O$
Formular weight / g·mol^{-1}	346.45	468.56	354.38	332.38
λ / Å	0.71073	0.71073	0.71073	0.71073
Crystal system	Orthorhombic	Orthorhombic	Monoclinic	Orthorhombic
Space group	$Pna2_1$	$Pna2_1$	$P2_1/m$	$Cmc2_1$
a / Å	12.1659(5)	13.7193(3)	9.6134(4)	34.7372(18)
b / Å	21.9295(12)	16.2571(4)	19.636(1)	6.7517(3)
c / Å	7.1708(3)	11.2574(4)	9.8168(4)	7.1631(3)
α / °	90	90	90	90
β / °	90	90	110.275(3)	90
γ / °	90	90	90	90
V / Å^3	1913.11(15)	2510.81(12)	1738.29(14)	1680.00(13)
Z	4	4	4	4
Density / g·cm^{-3}	1.203	1.240	1.354	1.314
μ / mm^{-1}	0.068	0.070	0.092	0.079
$F(000)$	736.0	984.0	736.0	696.0
Θ range / °	2.50 - 27.50	4.68 - 27.50	4.70 - 27.50	3.49 - 27.49
Reflections collected	17895	35448	27855	11906
Independent reflections	2372	5731	4091	1953
Completeness to Θ	1.00	0.99	0.99	1.00
R_{int}	0.0744	0.0393	0.0736	0.0337
GoF on F^2	1.080	0.999	0.992	1.088
R_1 [I > 2σ(I)]	0.0442	0.0389	0.0383	0.0299
wR_2 [I > 2σ(I)]	0.0837	0.1109	0.0682	0.0769
R_1 (all data)	0.0590	0.0411	0.0714	0.0301
wR_2 (all data)	0.0873	0.1127	0.0731	0.0771
$\Delta\rho_{max}/\Delta\rho_{min}$ / e·Å^{-3}	0.366 / -0.251	0.283 / -0.256	0.229 / -0.242	0.333 / -0.272
CCDC	1036983	1036985	1036984	1036986

6 Spiro-Bridged Ladder-Type oligo(*para*-Phenylene)s

6.1 Introduction

In the field of organic electronics oligo and poly(*para*-penylene)s have attracted great interest for more than two decades now. Because of their relatively wide band gap and their strong optical transitions, these materials have been employed as singlet emitters for blue OLEDs very early.[77, 128–130, 181] Within this class of materials Scherf and Müllen introduced the ladder-type poly(*para*-phenylene)s by bridging each phenylene unit with a five-membered ring to overcome the limited processability of unsubstituted poly(*para*-phenylene). But in contrast to polyfluorenes, these polymers possess a very planar conjugated backbone.[67, 68, 70] This molecular design leads to unique electronic structures and optical properties for fully conjugated polymers.[74–76, 84–86] Similarly to polyfluorenes,[133] LPPPs also suffer from parasitic green defect emission, which is mainly related to oxidative degradation in general and espacially at synthetic defect sites accompanied by distortion of the backbone planarity[117, 147–150, 182] One way to affect the sensitivity towards degradation is the substituion pattern. It was shown for polyfluorenes, as well as for LPPPs, that aromatic bridge substitution gives the most inert structures,[71, 153, 167, 169–172] which was also proven in the previous chapter. In the case of LPPPs the most common motif for aromatic bridge substituents is the spirobifluorene. It was incorporated into polymers[173, 183], 'linear' oligomers,[72, 184] as well as oligomers (trimers) deviating from the the usual *para*-phenylene structure with the bridging moiety on alternating sides of the ribbon.[185–187]

Due to their narrow and strong optical transitions, **LPPP**s and the corresponding oligomers are favorable building blocks for hybrid resonant optoelectronic devices[46] exploiting dipolar coupling to excitons in inorganic semiconductors. The all-methylated **L4P** (R^1=R^2=CH_3 in figure 6.1) matches the emission of ZnO quantum wells, and thus is suited for the production of resonant devices.[49, 50, 78]

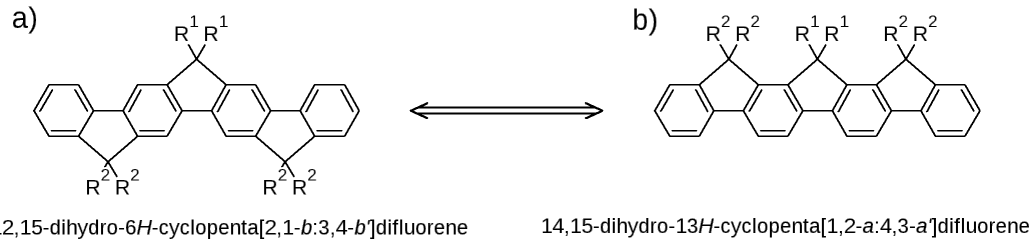

Figure 6.1. Backbone structures of target molecules.

However, in practice the photochemical inertness and the processability of **L4P** still remained an issue. Since aromatic substitution leads to enhanced photochemical stability and the introduction of spirobifluorene units may affect the thin film morphology, the effects of subsequent increments of the number of spiro groups in the target molecules is analyzed.
In this chapter the synthetic routes to subsequently exchanged symmetry equivalent methyl groups by spiro-bifluorene units in the 'linear' **L4P** (figure 6.1a, cyclopenta[2,1-*b*:3,4-*b'*]difluorene core, referred to as **L4P** in the following) are presented. These structures are related to refs. [72, 184], although solubilizing groups are omitted to guarantee vacuum processability. Here, we discuss the influence of the spiro-groups on the molecular packing in solid state by X-ray crystal structures, as well as the influence on the optical properties. Furthermore the potential of band gap engineering by on-purpose synthesis of the 'bent' isomer of LOPPs (figure 6.1b, cyclopenta[1,2-*a*:4,3-*a'*]difluorene core, referred to as ***iso*-L4P** in the following) will be discussed. This work is related to refs.[185, 186], but it was never demonstrated for oligomers of this size.

6.2 Results and Discussion

6.2.1 Synthesis of Spiro-LOPPs[39]

The synthesis of ladder-type oligo or poly(*para*-phenylene)s involves two major steps: buildup of the *para*-phenylene backbone by cross-coupling reactions and subsequent bridging by Friedel-Crafts type reactions. In case of the linear tetramer (figure 6.1a) it is suitable to couple two terminal phenyl units to a central fluorene unit. The functional units for the intramolecular bridging reaction may ether be located at the central fluorene or at the phenyl groups, the latter route being simpler but not applicable in every case.[78, 104] Ideally the bridging is the last step of the synthesis, since the rigid products typically possess a low solubility. However, post-bridging functionalization is carried out here, as well. To obtain the spiro compounds 2-metalbiphenyl is added to the corresponding ketones and the intermediate carbinols are reacted in acetic acid/HCl as described already very early for 9,9'-spirobifluorene.[188]
The synthesis of **L4P** has already been described.[78, 117] In a first attempt (figure 6.2) of synthesizing **L4P-sp**, 2,7-dibromospirobifluorene **1** was used as central building block and coupled to boronic ester **2**. The product was oxidized to the ester **3** and reacted with methyl lithium. The resulting alcohol was converted to the fully bridged structure using $BF_3 \cdot THF$. But after initial purification of the product, it turned out that also unwanted isomers have been formed. Although the low regioselectivity in the bridging reaction is unusual, it is not unknown.[186] However, in this particular case the substitution pattern favors very low selectivity. The isomeric mixture contained only 55% of the target isomer **L4P-sp**. Since quantitative purification was not possible with reasonable effort, another synthetic strategy had to

[39]Some stages of the synthesis of ***iso*-L4P-sp2** were carried out by Jutta Schwarz (HU Berlin, Institut für Chemie).

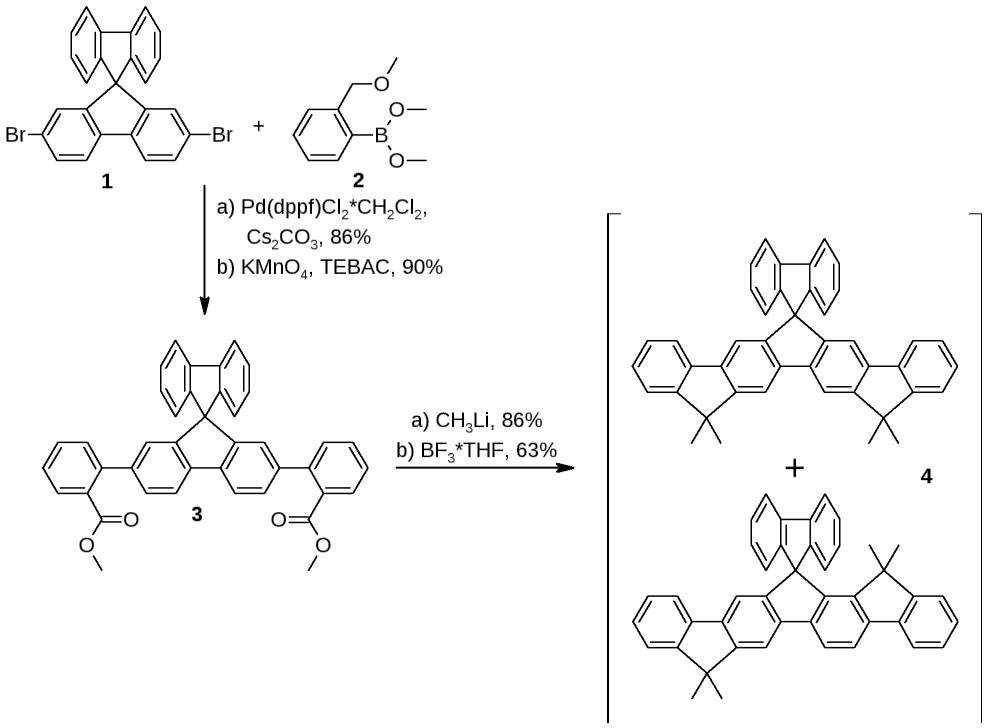

Figure 6.2. Attempted synthesis of **L4P-sp**.

be employed. When the isomerically pure ketone **L4P-O** once was available (figure 6.3a),[117] the synthesis of **L4P-sp** became relatively facile and good yields were found for the introduction of the spiro group. **L4P-sp2** was synthesized in the same manner from the diketone **L4P-O2**. Initially the synthesis of **L4P-sp3** was also planned via a bridged diketone but due to solubility issues in the keto stage and the low regioselectivity in the case of **L4P-sp**, it was decided to follow a route that does not need further functionalization after the bridging step. This was achieved by using methoxymethyl (MOM) protected (9-(2-Bromophenyl)-9*H*-fluoren-9-yl)methanol **6** as terminal building block[189] and 2,7-dibromospirobifluorene **1** as the central one. Cross coupling and final intramolecular Friedel-Crafts alkylation were carried out without purification of intermediates in relatively low yields. But, although the purification is demanding, **L4P-sp3** can be synthesized on a gram scale.

As it turned out, the introduction of the spirobifluorene units shifts the absorption off-resonance with respect to ZnO, the necessity for slightly blue shifted derivatives emerged. For indenofluorene derivatives it was already shown, that the relative position of the bridges shifts the absorption spectra.[185] Furthermore the UV-Vis absorption traces of analytical LC runs of the isomeric mixture **4** showed a blue shift for the unwanted isomer of **L4P-sp**. For that reason an on-purpose synthesis for derivatives with the cyclopenta[1,2-*a*:4,3-*a'*]difluorene (***iso*-L4P**) core was developed (figure 6.4). The desired regio isomer may ether be synthesized by attaching the bridging functionalities at the central fluorene unit in 1- and 8-position or by protecting the usual 3- and 6-position of the fluorene and using terminal phenyl units with the bridging functionality. Here, it was decided to use the latter one and bromine was employed as protecting group. 3,6-dibromo-9,9-dimethylfluorene

7 was diiodinated in 2- and 7- position and subsequent cross-coupling with the phenylboronic ester prepared from **9** employing $Pd(PPh_3)_4$ as catalyst in THF and aqueous Na_2CO_3 gave a high selectivity for Iodine. **10** was converted to the diketone **12** by usual methods of subsequent oxidation, saponification and Friedel-Crafts acylation. Direct reaction of the dibromo-diketone **12** with 2-lithium biphenyl followed by a Friedel-Crafts alkylation gave **13** only in very low yields. However, bromine can be removed in a three-step sequence of reduction of the ketones to the corresponding alcohol, halogen metal exchange, quenching with a proton source, and re-oxidation of the hydroxyl groups to the diketone ***iso*-L4P-O2**, which can finally be reacted to **iso-L4P-sp2** in 60% yield.

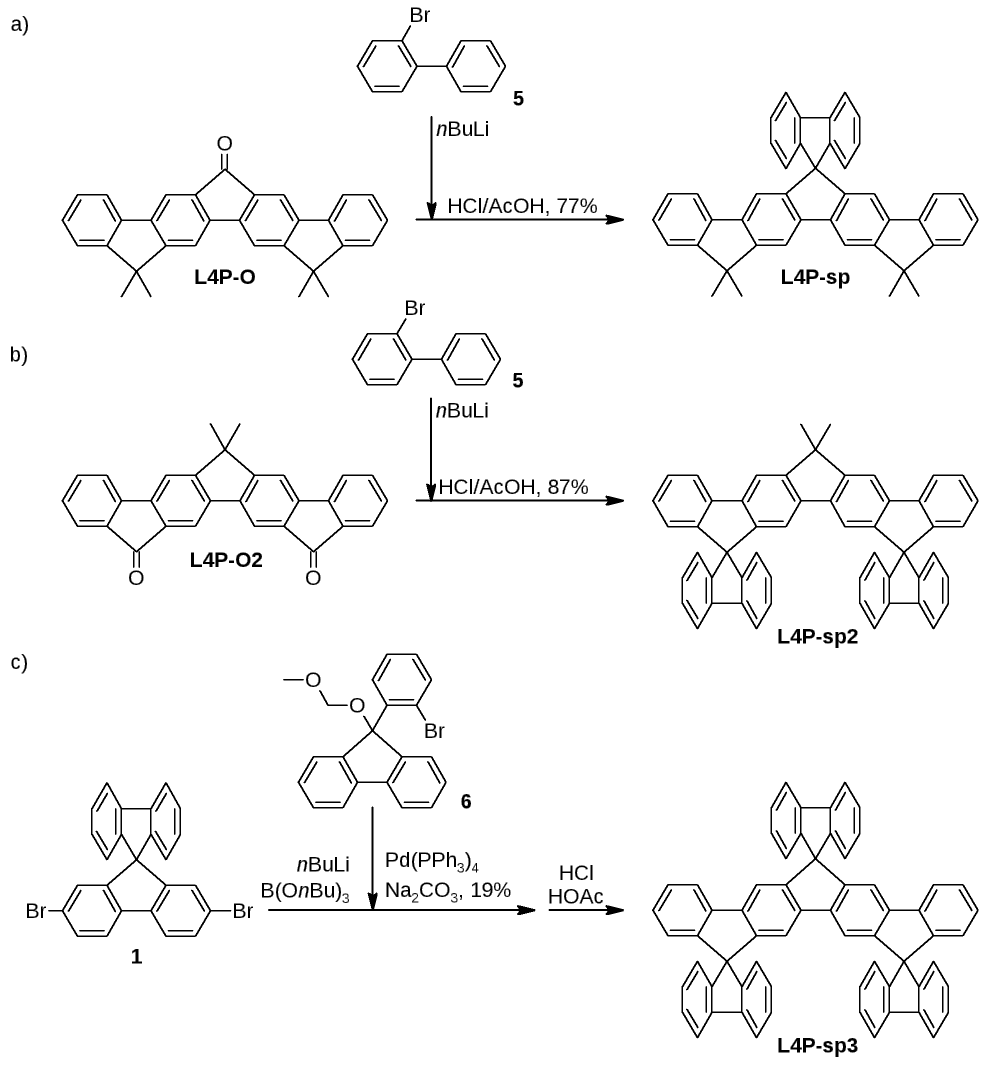

Figure 6.3. a) Synthesis of **L4P-sp**, b) synthesis of **L4P-sp2**, and c) synthesis of **L4P-sp3**.

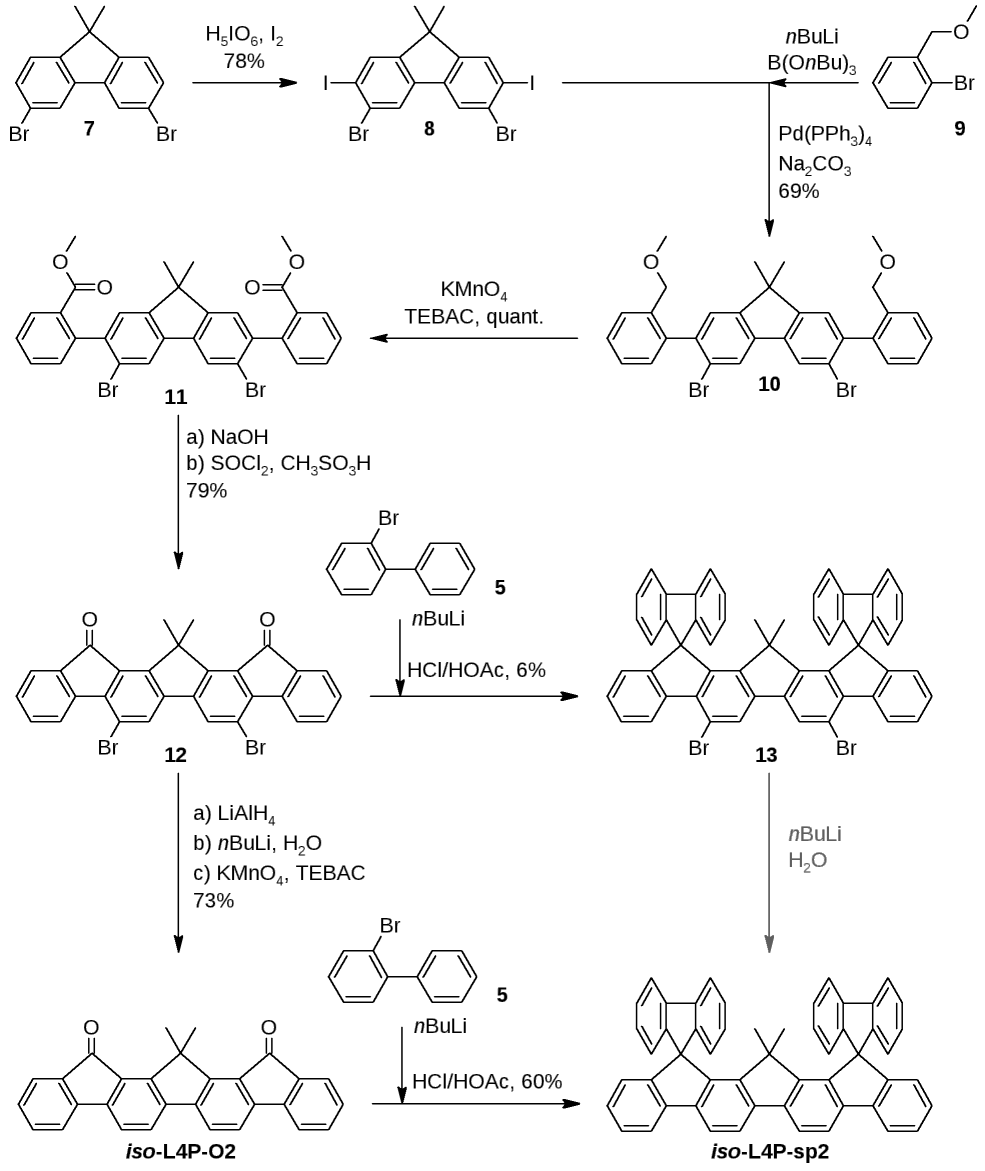

Figure 6.4. Synthesis of ***iso*-L4P-sp2**.

6.2.2 X-Ray Structures and Molecular Packing[40]

When going from solution to the solid state (in a device), intermolecular interactions have significant impact on the performance of a material. Thus, it is important to consider the effects of the molecular packing. Planar, rod-like organic π-conjugated oligomers tend to crystallize in a small number of molecular packing patterns that can be categorized by a few parameters describing their intermolecular orientation. In the simplest case the π-systems are oriented on top of each other forming a π-stack. As π-stacking is energetically unfavorable in many cases, displacement of the molecules with respect to each other may occur. The displacement along the long axis is referred to as pitching, characterized by a pitch distance or pitch angle (the angle between the stack and the normal of the molecular plane) and rolling, which relates to the displacement along the short molecular axis. If different stacks are rolling into opposite directions, typical herringbone-structures are formed.[190, 191] These intermolecular orientations and distances have an impact on the optical and electronic properties of the crystalline solid. While the electronic interactions are of very short range, the excitonic coupling is of farther range and less sensitive to small geometrical changes. Here, mainly the strength and orientation of the optical transition dipole is important. In π-stacked and herringbone arrangements with zero or low pitch, this can lead to the formation of H-aggregates, accompanied by a hypsochromic shift in absorption and a bathochomic shift in emission, as well as reduced radiative rates. Upon increasing the pitch angle, the interaction changes to J-aggregates, in which the lower-energy transition is allowed. This leads to a bathochomic shift in absorption and emission, as well as to increased radiative rates.[191] In case of hybrid devices as described above, the type of excitonic coupling is of great importance, as light emitting devices can have enhanced performance by the formation of J-aggregates. Furthermore, it should be taken into consideration, that dipolar coupling to an inorganic quantum well may be very inefficient, if all optical transition dipoles are oriented in the same mismatching direction.
For the three keto intermediates, as well as for nearly all final products (except ***iso*-L4P-sp2**) single crystals of sufficient quality to conduct X-ray crystal structure analysis were obtained by different techniques. In the case of ***iso*-L4P-sp2** only the brominated derivative **13** could be crystallized. Even different molecular arrangements for the same molecule (resp. different space groups) were obtained by different crystallization techniques in some cases. First, the crystal structures of all derivatives will be discussed in a more general way, afterwards potential effects of the molecular arrangement of the final products concerning the solid-state optical properties will be discussed. A useful characterization in terms of the above mentioned parameters may sometimes be difficult. Due to a large Z (resp. the large unit cell) adjacent molecules are not generated by translational symmetry but by cell symmetry. However, if the definition of the parameters is treated less strictly, the next-neighbor interactions can be described, as well.

[40] Collection of diffraction data and crystal structure refinement were carried out by Dr. Beatrice Braun (HU Berlin, Institut für Chemie).

6.2.2.1 Carbonyl Intermediates

The π-system of the three keto structures (figure 6.5) is very planar in the crystal, except for **L4P-O**, which displays a twist along the long axis of the π-system. **L4P-O** was crystallized from chlorobenzene at elevated temperatures with a space group of P-1 ($Z = 2$) in a layer structure. It forms stacks of molecules with the keto group pointing in alternating directions (see figure 6.6). The π-systems are not exactly on top of each other with respect to the short axis and the stacks have a pitch distance of roughly 1/4 of the molecular length. The distance between the planes of molecules generated by translational symmetry is 7.36 Å, so the $\pi - \pi$ distance is about 3.7 Å. **L4P-O2** was crystallized by sublimation in the space group $Pna2_1$ (Z = 4). The molecules are forming stacks in which the keto groups of adjacent molecules are pointing in opposite direction with a pitch distance of half a molecular length. The distance between the π-planes of translationally generated molecules amounts 6.690 Å, giving a $\pi - \pi$ distance of about 3.34 Å. Stacks of opposite pitch are forming a herringbone structure with an angle of 42 ° between the planes (figure 6.7). ***iso*-L4P-O2** was crystallized from chlorobenzene. It forms a layer structure in the space group of P-1 ($Z = 2$). The molecules are forming stacks with a pitch distance larger than half a molecular length (Figure 6.8). Related to that, the keto groups within a stack are pointing in the same direction. The distance between the π-planes is relatively short, amounting to only 3.10 Å. While the the CO-bonds in **L4P-O2** are nearly parallel, in ***iso*-L4P-O2** they are tilted by 36.7 ° with respect to each other.

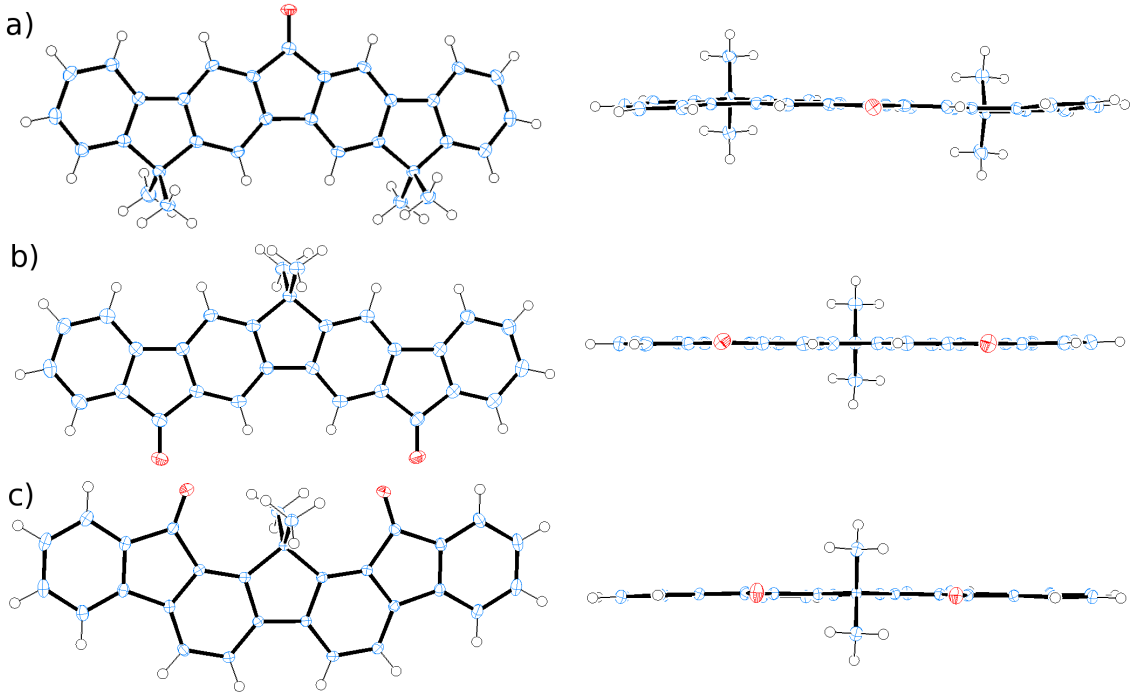

Figure 6.5. a) Molecular structures (based on single crystal X-ray diffraction) I. Asymmetric units (left) and view along the short axis of the π-system (right) of a) **L4P-O**, b) **L4P-O2**, and c) ***iso*-L4P-O2**. The thermal ellipsoids are drawn at 50% probability level.

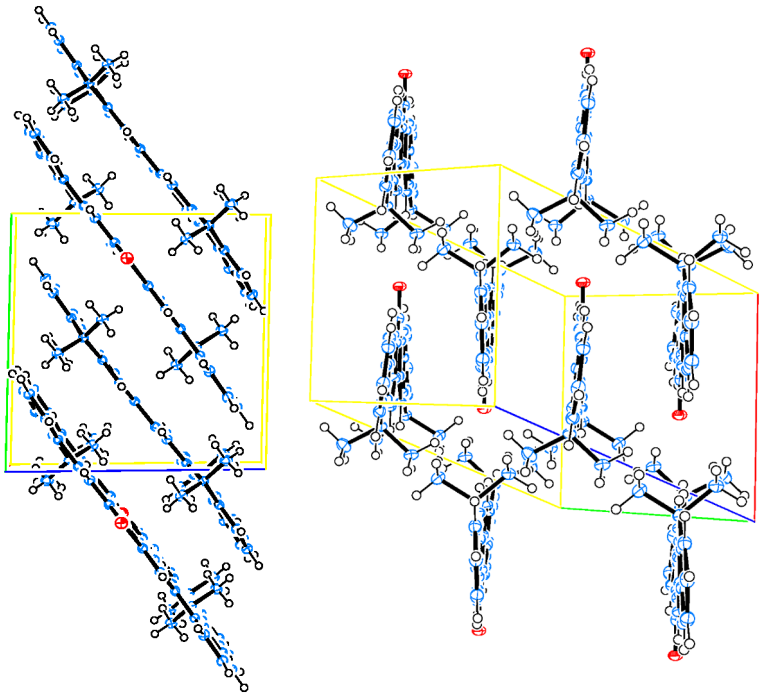

Figure 6.6. Arrangement of **L4P-O** in the crystal. Cell edges are marked in the following Colors: a: red, b: green, c: blue. Thermal ellipsoides are drawn at the 50% probability level.

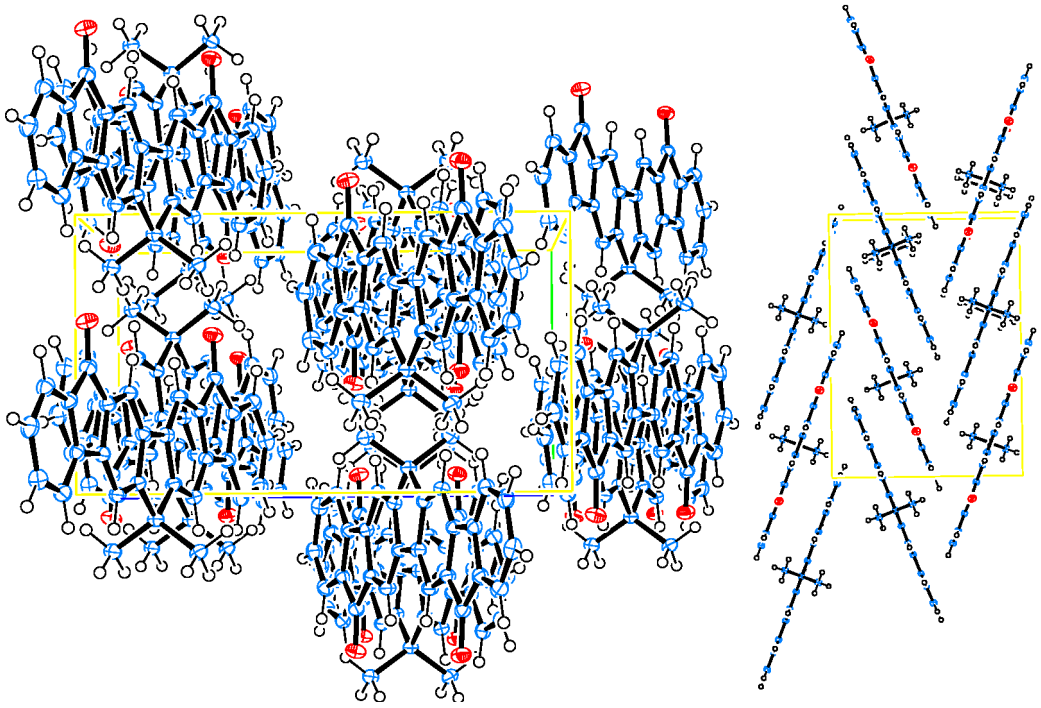

Figure 6.7. Arrangement of **L4P-O2** in the crystal. Cell edges are marked in the following Colors: a: red, b: green, c: blue. Thermal ellipsoides are drawn at the 50% probability level.

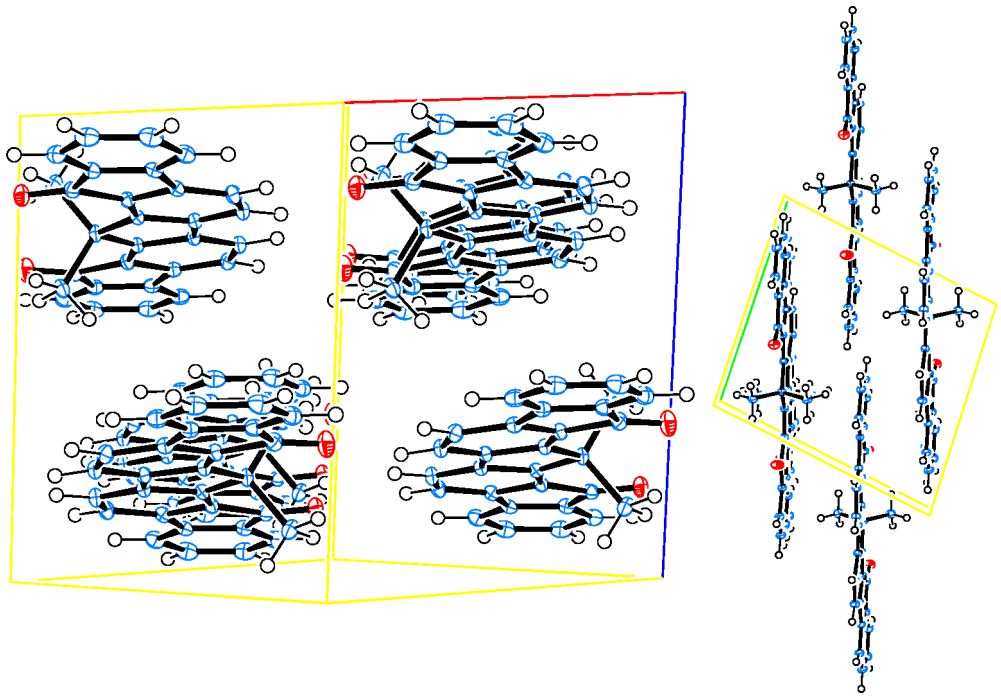

Figure 6.8. Arrangement of ***iso*-L4P-O2** in the crystal. Cell edges are marked in the following Colors: a: red, b: green, c: blue. Thermal ellipsoides are drawn at the 50% probability level.

6.2.2.2 Molecular Structures of the Spiro-LOPPs

The molecular geometry of the final products in the crystal (figures 6.9 and 6.10) can sometimes deviate form the ideal structure concerning the planarity of the backbone as well as the angle between the sprirobifluorene units (defined by the planes through the 3,6, and 9-carbon of the fluorenyl group) in the 12- and 15-positions in **L4P-sp2** and **L4P-sp3**. While in **L4P** (figure 6.9a) the backbone is relatively planar, **L4P-sp** (figure 6.9b) displays a wave-like deformation over the whole length of the molecule. **L4P-sp2** has a relatively planar backbone showing only small twist and bending, no matter if crystallized from chloroform / ethanol solution (figure 6.9c) or by sublimation (figure 6.9d). In the first case the angle between the spiro groups amounts to 6.8 ° in the latter one it is 13.6 °. In crystals of **L4P-sp3** grown by sublimation (figure 6.10a), the backbone shows relatively strong distortions, especially the outer methylene carbons moved out of plane giving rise to a twist throughout the entire backbone. The angle between the outer spiro groups amounts to 17.5 °. When crystals of **L4P-sp3** were grown from chloroform/ethanol, the backbone is not twisted, only showing wave-like bending and the outer spiro groups are nearly parallel (figure 6.10b). Finally **13** shows a distorted backbone (figure 6.10), as well. Mainly the outer methylene carbons are twisted versus the central one. The angle between the spiro groups amounts to 17.9 °, which is only half of the expected value, compared to the angle between the carbonyl bonds in ***iso*-L4P-O2**. This deformation might be explained by repulsion between the methyl groups and the spiro groups (the distance between the fluorenyl plane and the methyl carbon is 3.26 Å).

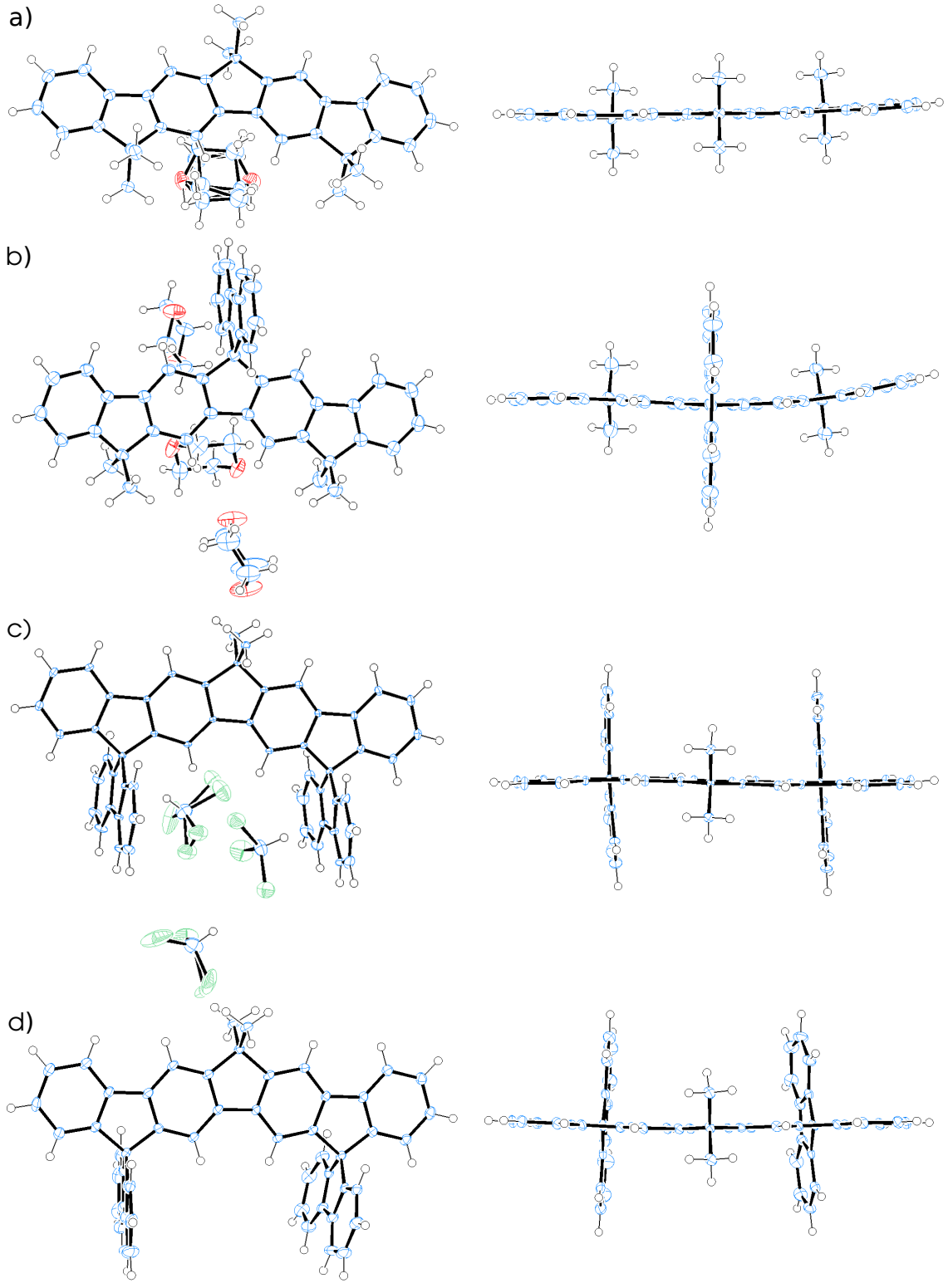

Figure 6.9. Molecular structures (based on single crystal X-ray diffraction) II. Asymmetric units (left) and view along the short axis of the π-system (right, solvent molecules omitted) of a) **L4P**·THF, b) **L4P-sp**·3 dioxane, c) **L4P-sp2**·3 ($CHCl_3$), d) **L4P-sp2** (sublimation). Thermal ellipsoides are drawn at the 50% probability level.

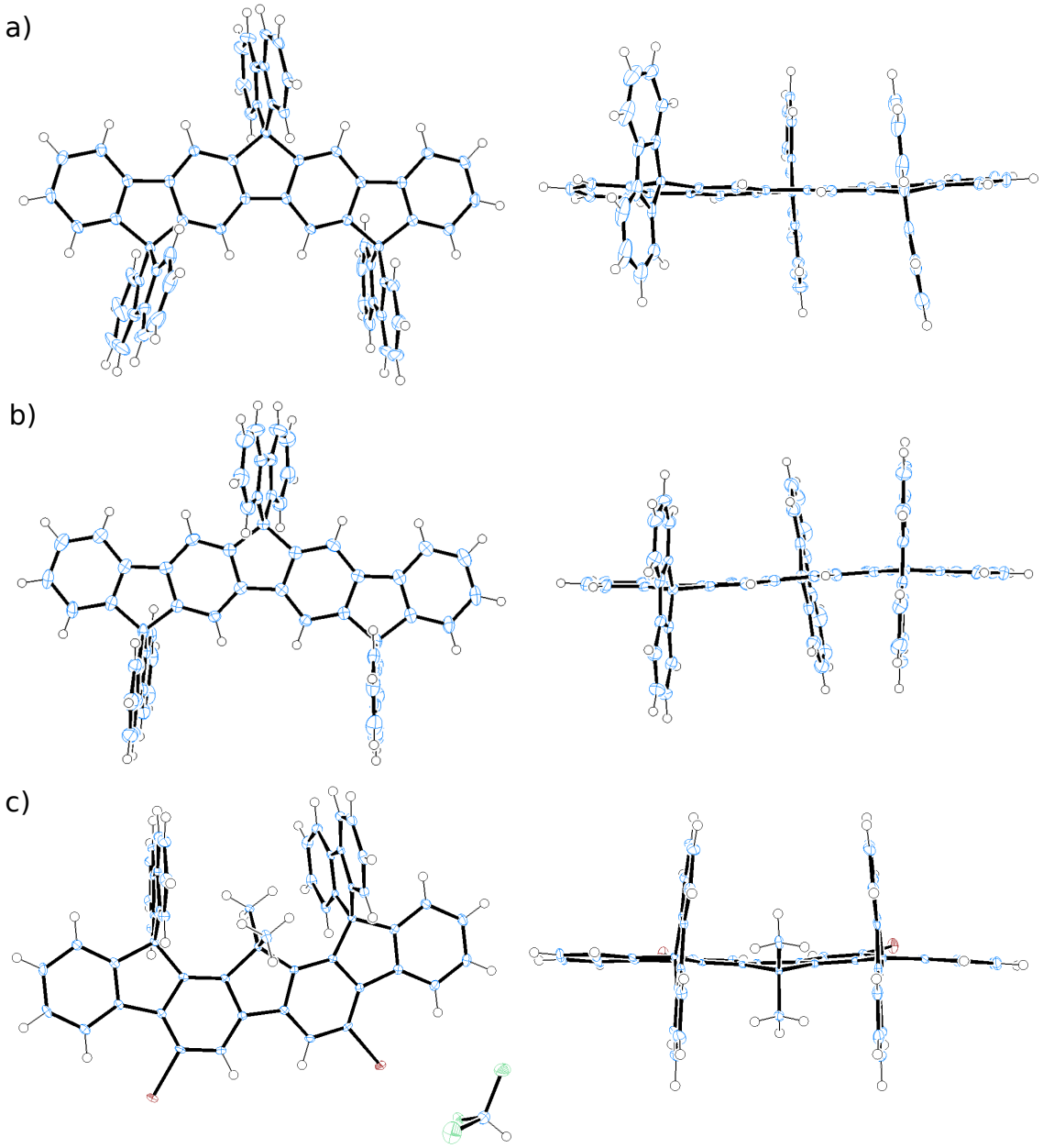

Figure 6.10. Molecular structures (based on single crystal X-ray diffraction) III. Molecular structures (left) and view along the short axis of the π-system (right, solvent molecules omitted) of a) **L4P-sp3** (sublimation), b) **L4P-sp3** ($CHCl_3$), c) **13**·($CHCl_3$). Thermal ellipsoides are drawn at the 50% probability level.

6.2.2.3 Arrangement of the Chromophores and Potential Excitonic Interactions

The crystal structure of **L4P**·(THF) (already published in ref. [104]) displays a space group of *Pbca* with $Z = 8$. There are two types of close interactions in **L4P**·(THF). In the first one (Figure 6.11c) the offset between the molecules with respect to their long axis (defined by the carbon atoms in position 2 and 10 in the cyclopenta[2,1-*b*:3,4-*b'*]difluorene core) is small and they are tilted by 18.4 °. Additionally the herringbone-like angle between the planes of the π-systems is about 80 °. In the second case (Figure 6.11d) the two molecules are nearly parallel with a distance of 3.47 Å, but with a large pitch offset: The overlap is only of the length of one indene unit with additional roll offset. The first interaction might give some H-type coupling, but due to the relatively large distance excimer emission is not expected to happen. The second interaction may lead to excitonic coupling in terms of J-aggregates.
L4P-sp·(dioxane) crystallizes in P -1 ($Z = 2$). The backbones of the molecules form a layer structure (Figure 6.12) with a distance of 8.5 Å between translationally generated layers, so the distance between adjacent layers can be estimated to be slightly above 4 Å. The structure can also be interpreted as an intersection of stacks of the two differently oriented molecules in the cell (Figure 6.12a) with a pitch distance of one molecular length concerning translationally generated molecules. There is no π-stacking and no herringbone-like interaction of the molecular backbone, however, the J-aggregate type coupling should still be possible.
From chloroform / ethanol **L4P-sp2**·($CHCl_3$) crystallizes in P -1, as well. Again, all molecular backbones are oriented parallel without π-stacking (see figure 6.13). Furthermore **L4P-sp3**($CHCl_3$) was crystallized from chloroform/ethanol in the space group of $C\ 2/c$. Also for this compound the arrangement of the chromophores is quite similar: all the backbones are parallel to each other and there is no direct π-stacking (figure 6.14).
Luckily for the two derivatives **L4P-sp2** and **L4P-sp3** single crystals were also obtained by sublimation (with only little temperature gradient), which is of greater relevance in terms of application in hybrid devices fabricated by vacuum deposition. In this case **L4P-sp2** crystallizes in $P\ 2_1\ /c$ ($Z = 4$). In the structure, herringbone-like interactions can be found similar to **L4P** (figure 6.15 a and c). The angle between the backbone planes of adjacent molecules is 88.5 ° and the long axis is tilted by 19.1 ° with respect to each other. Alternatively the structure can be interpreted in terms of stacks (Figure 6.15 b), but the pitch distance is larger than a molecular length, so there is no actual π-stacking. Upon sublimation **L4P-sp3** also crystallized in $P\ 2_1\ /c$ ($Z = 4$). The packing may be understood as a layer structure (figure 6.16 a). In each layer the backbones are rotated out of plane around the long axis of the molecule by 27 °. After every second layer, there is a twist of about 67 ° between the layers (figure 6.16 b). This structure is quite advantageous in terms of the above mentioned application in an hybrid device, because it can be expected that there is some transition dipole moment in every direction. Furthermore there is no π-stacking or herringbone structure. Thus the optical properties in the crystalline state should not change dramatically, especially since only J-aggregates can be formed.

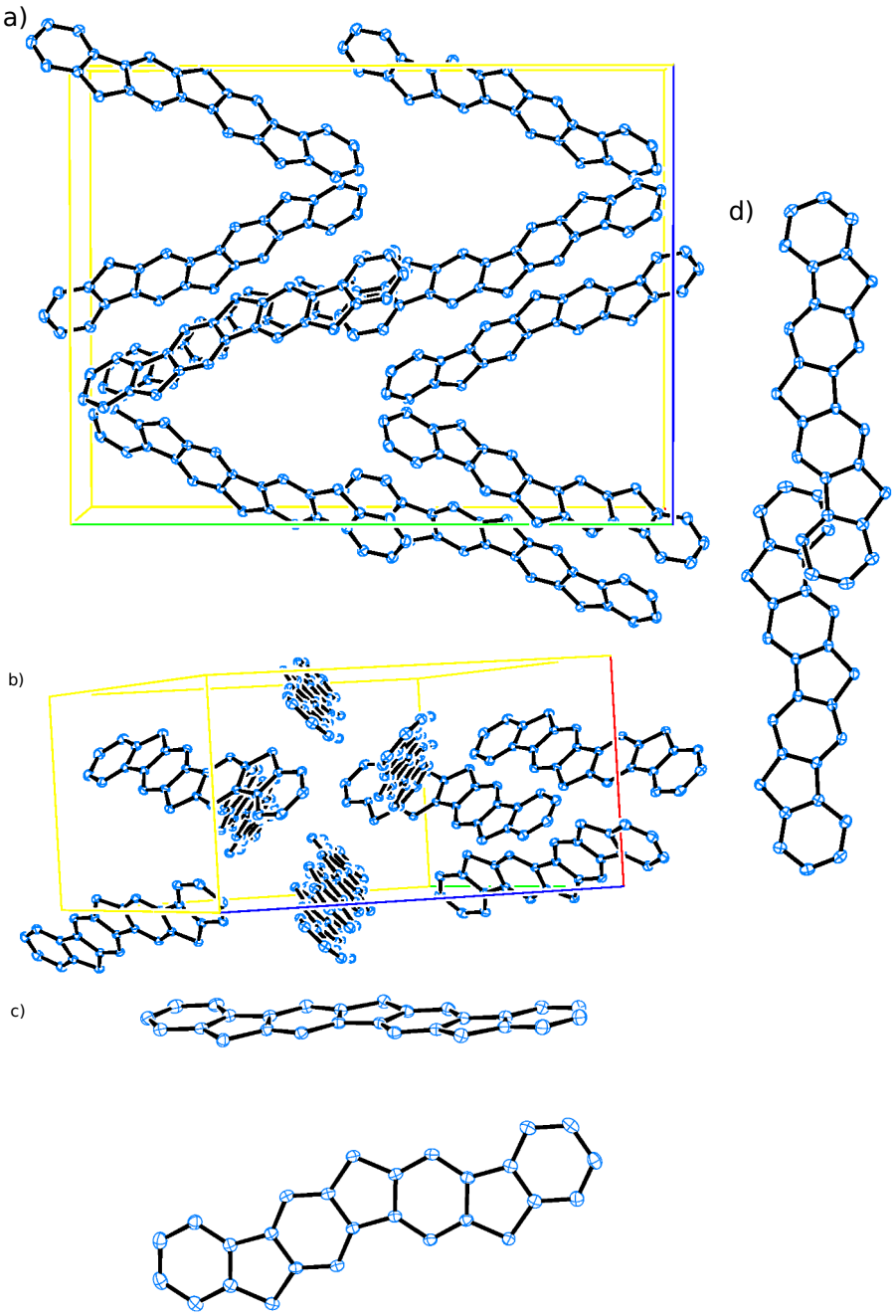

Figure 6.11. Backbone of **L4P** in the crystal. Substituents and solvent molecules are omitted for clarity. a), b) Arrangement in the crystal, c), d) interactions described in the text. Cell edges are marked in the following Colors: a: red, b: green, c: blue. Thermal ellipsoides are drawn at the 50% probability level.

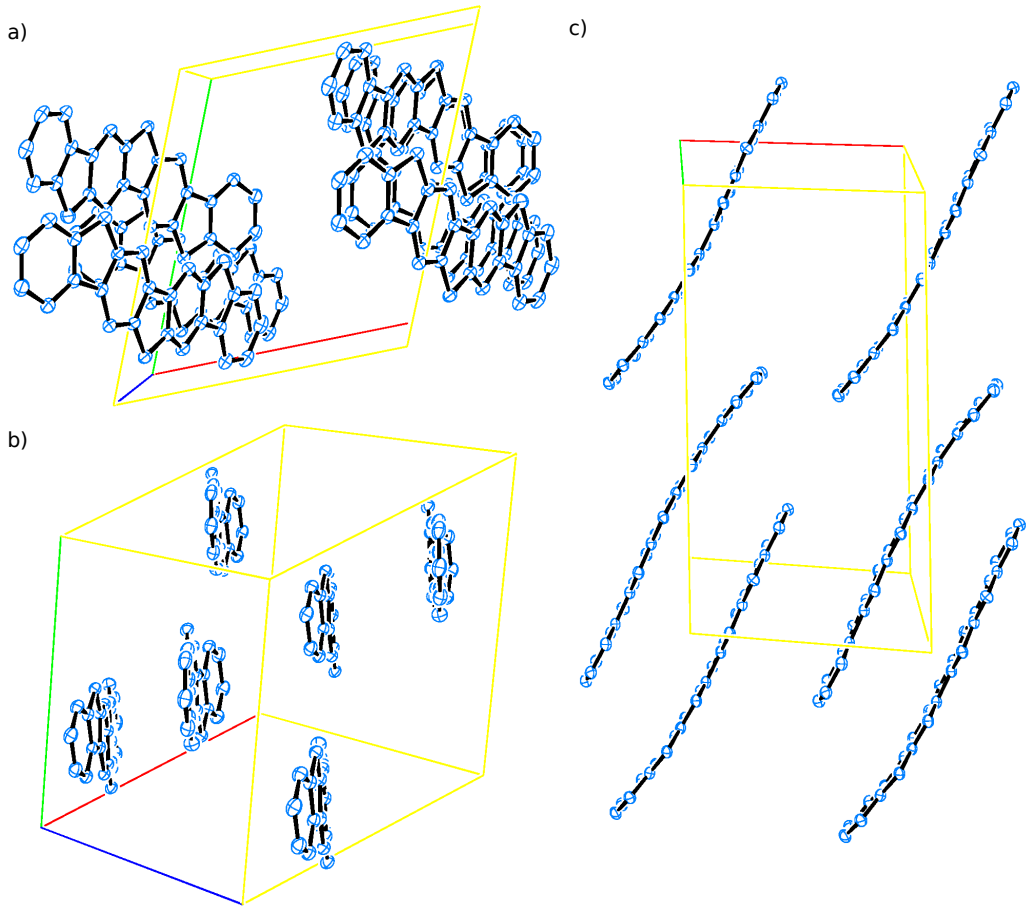

Figure 6.12. Backbone of **L4P-sp** in the crystal. Substituents and solvent molecules are omitted for clarity. a) View along stacks, b) view along the long axis of the molecules, c) view along the short axis of the molecules. Cell edges are marked in the following Colors: a: red, b: green, c: blue. Thermal ellipsoides are drawn at the 50% probability level.

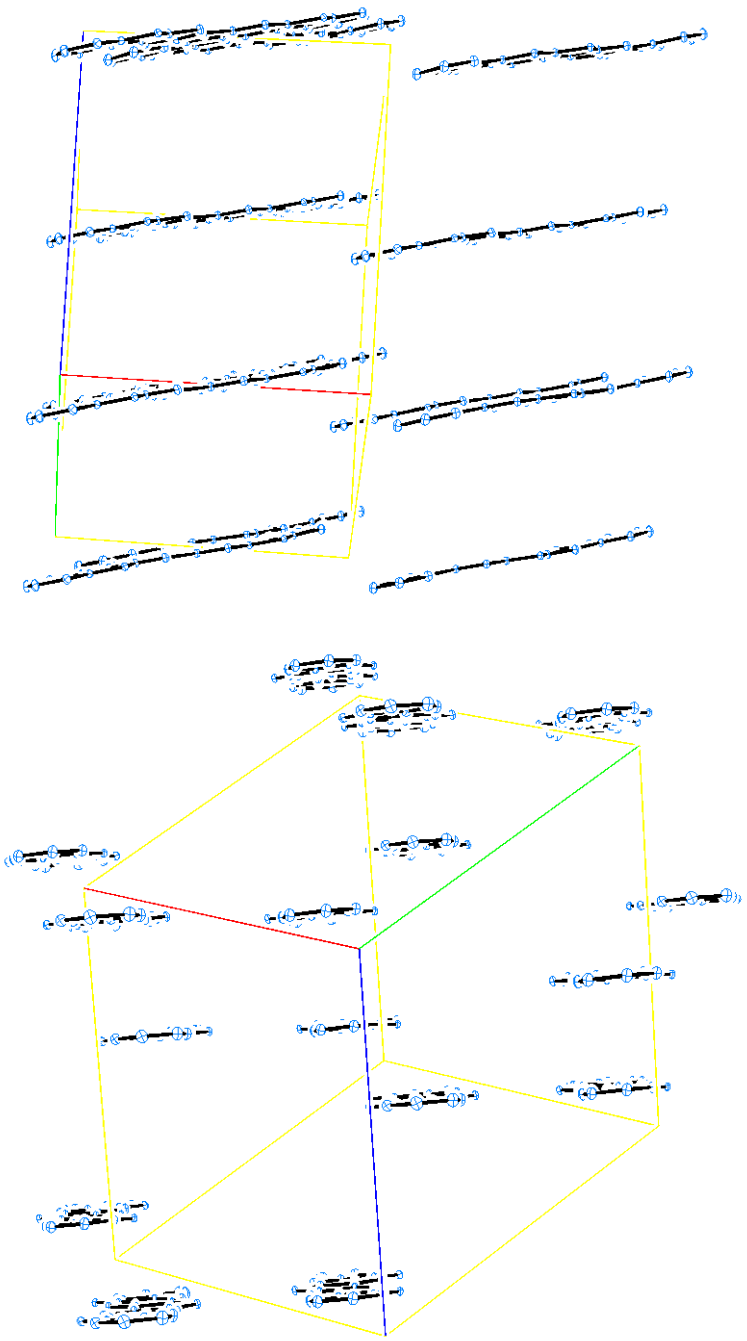

Figure 6.13. Arrangement of the backbone of **L4P-sp2**($CHCl_3$) in the crystal. Substituents and solvent molecules are omitted for clarity. Cell edges are marked in the following Colors: a: red, b: green, c: blue. Thermal ellipsoides are drawn at the 50% probability level.

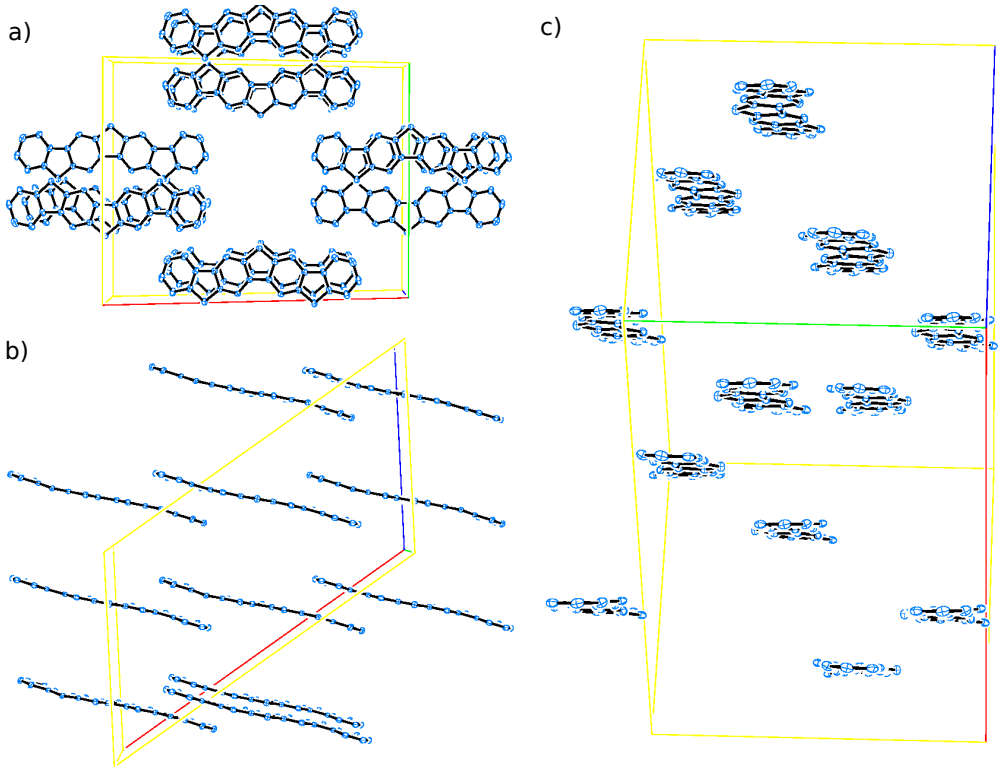

Figure 6.14. Arrangement of the backbone of **L4P-sp3**($CHCl_3$) in the crystal. Substituents and solvent molecules are omitted for clarity. a) View along stacks, b) view along short axis of the molecule, c) view along long axis. Cell edges are marked in the following Colors: a: red, b: green, c: blue. Thermal ellipsoides are drawn at the 50% probability level.

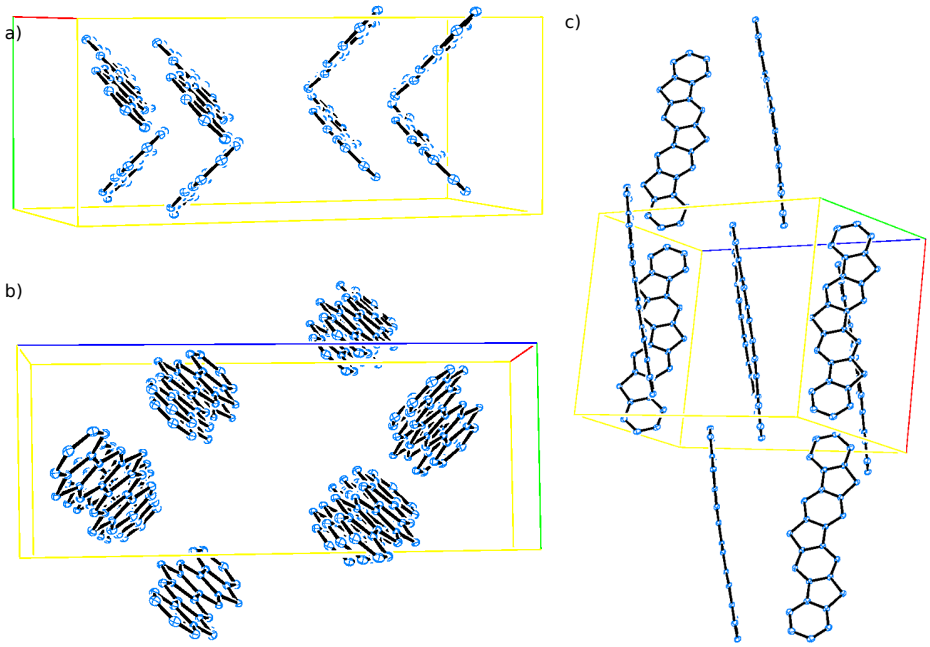

Figure 6.15. Arrangement of the backbone of **L4P-sp2** (from sublimation) in the crystal. Substituents are omitted for clarity. a) View along long axis of the molecules, b) view along stacks, c) herringbone-like interaction. Cell edges are marked in the following Colors: a: red, b: green, c: blue. Thermal ellipsoides are drawn at the 50% probability level.

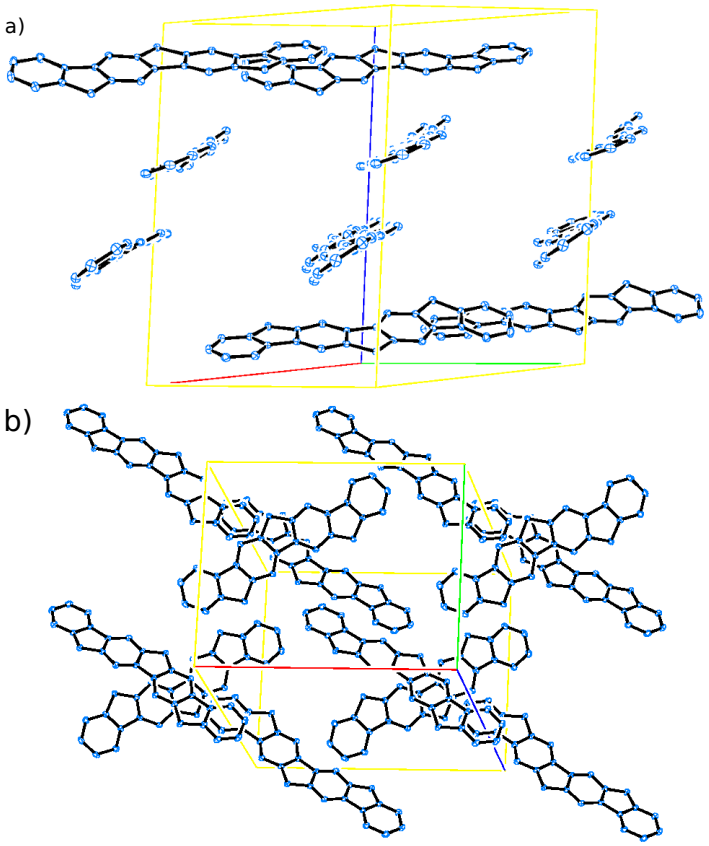

Figure 6.16. Arrangement of the backbone of **L4P-sp3** (from sublimation) in the crystal. Substituents are omitted for clarity. a) View parallel to layers, b) view perpendicular to layers. Cell edges are marked in the following Colors: a: red, b: green, c: blue. Thermal ellipsoides are drawn at the 50% probability level.

6.2.3 Optical Properties in Solution

Besides the final products also the keto intermediates display some interesting optical properties (see figure 6.17). The optical properties of the linear ketones **L4P-O** and **L4P-O2** have already been described.[117] Here, they are shown in comparison to underline the special behavior of ***iso*-L4P-O2**. The linear ones show a vibronically structured **L4P**-like absorption starting around 3.4 eV ($\pi \rightarrow \pi^*$) and a very weak low energy band between 2.5 and 3.3 eV ($n \rightarrow \pi^*$), as well as a low energy emission with less than 1% quantum yield. In contrast ***iso*-L4P-O2** does not posses a **L4P**-like absorption feature at all. The $\pi \rightarrow \pi^*$ absorption is hypsochromically shifted by about 0.2 eV compared to the linear ketones. The only feature that is similar is the absorption band above 4 eV, which might be addressed to some rather localized excitation of the carbonyl moieties. But especially the low energy transition shows unusual behavior. On the one hand, the absorption becomes relatively strong ($\varepsilon \approx 6000$ L mol^{-1} cm^{-1} between 2.6 an 2.7 eV), on the other hand the emission centered at 2.2 eV has a PL quantum yield of $\approx$ 22%. Both findings indicate that the normally symmetry forbidden $n \rightarrow \pi^*$-transition becomes partly allowed due to distortion of the orbital symmetry by the introduction of the 36.7 ° tilt angle between the carbonyl groups. As shown by the crystal structure analysis, the backbone of the molecule is still planar.

The optical properties of the spiro derivatives have also been investigated. Upon adding more spirobifluorene moieties in the bridges of **L4P**, the optical properties do not change dramatically. The spectra of **L4P**, **L4P-sp**, **L4P-sp2**, and

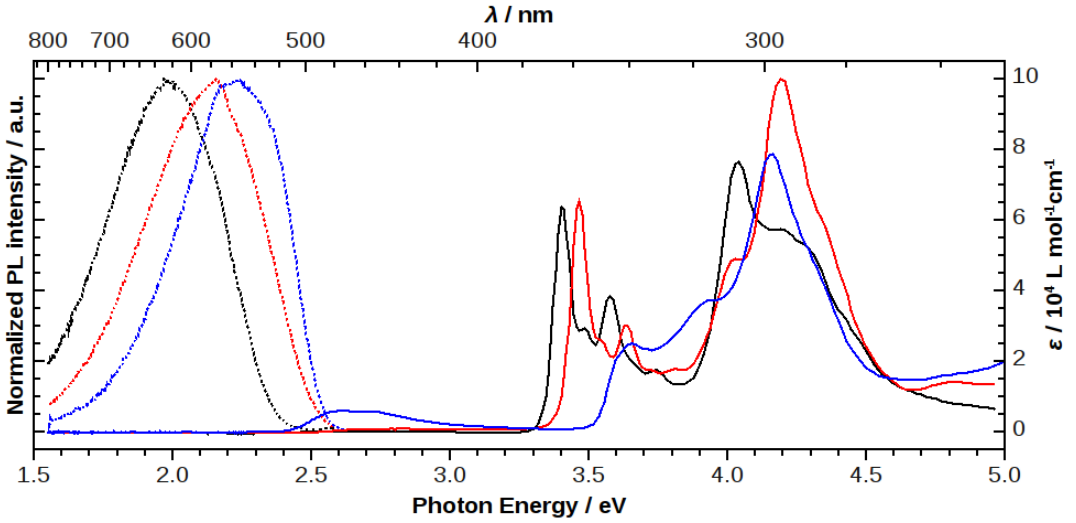

Figure 6.17. Absorption (solid line) and normalized photoluminescence (PL, dotted) spectra of **L4P-O** (black, λ_{Ex} = 330 nm), **L4P-O2** (red, λ_{Ex} = 330 nm), and ***iso*-L4P-O2** (blue, λ_{Ex} =337 nm) in CH_2Cl_2, 10^{-6} - 10^{-5} mol L^{-1}. PL spectra of **L4P-O** and **L4P-O2** are only shown below 2.6 eV to remove signals of highly emissive impurities. A cutoff filter (transmission below 430 nm) was used to remove the 2nd harmonic of the excitation source for all three samples.

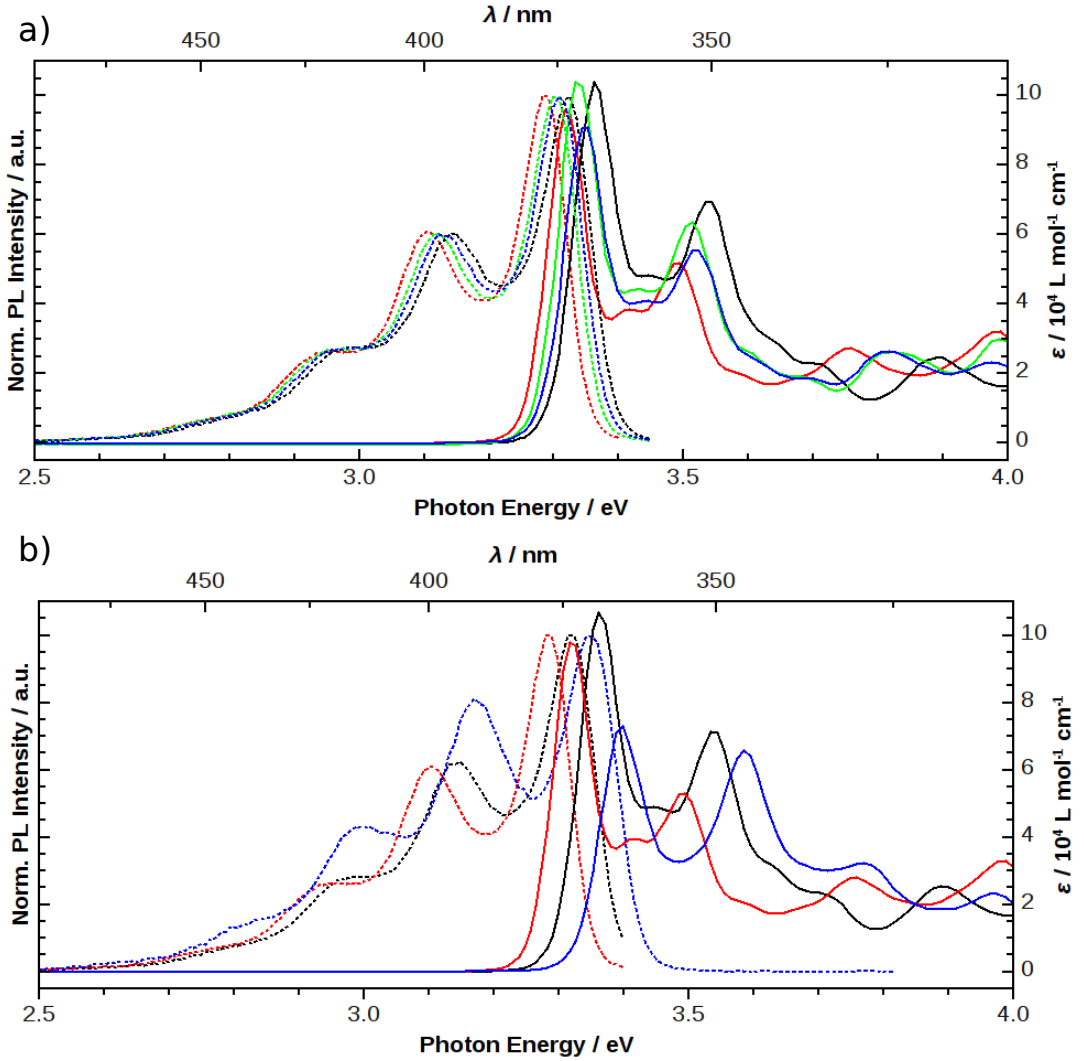

Figure 6.18. Absorption (solid line) and normalized PL (dotted) spectra of final products in CH_2Cl_2, 10^{-6} - 10^{-5} mol L^{-1}. a) **L4P** (black, λ_{Ex} = 352 nm), **L4P-sp** (blue, λ_{Ex} = 352 nm), **L4P-sp2** (green, λ_{Ex} = 352 nm), and **L4P-sp3** (red, λ_{Ex} = 360 nm). b) ***iso*-L4P-sp2** (blue, λ_{Ex} = 320 nm), **L4P** (black, λ_{Ex} = 352 nm), and **L4P-sp3** (red, λ_{Ex} = 360 nm).

Table 6.1. Absorption and PL data of the spiro-LOPPs

compound	λ_{max} / nm	ϵ_{max} / 10^3 L mol^{-1} cm^{-1} (λ / nm)	λ_{Em} / nm	λ_{Ex} / nm
L4P	369, 351	104 (369)	373, 394	352
L4P-sp	370, 352	91 (370)	375, 397	352
L4P-sp2	372, 353	104 (372)	375, 398	352
L4P-sp3	374, 355	98 (374)	377, 400	360
***iso*-L4P-sp2**	365, 346	73 (365)	370, 391	320

λ_{max}: Absorption maxima; ϵ_{max} (λ): Absorption coefficient and corresponding wavelength. λ_{Em}: Emission maxima; λ_{Ex}: Corresponding excitation wavelength.

L4P-sp3 (figure 6.18a) exhibit nearly the same shape with two main maxima due to vibronic progression in the absorption and emission (see also table 6.1). The Stokes-shift is small (around 40 meV) and the fluorescence quantum yield Φ_{PL} of all only-hydrocarbon derivatives is close to unity. However, with every additional spiro unit, absorption and emission are shifted bathochromically by about 2 nm. Since this bathochromic shift leads to reduced coupling to ZnO, ***iso*-L4P-sp2** was synthesized expecting transitions at slightly higher energies. And indeed, the absorption maximum of ***iso*-L4P-sp2** is blue shifted by 4 nm with respect to **L4P** (figure 6.18b, table 6.1). The Stokes-shift is still small and the fluorescence quantum yield is also about unity. The absorption coefficient of the first maximum decreases to 73000 L mol^{-1} cm^{-1} and the second (vibronic) maximum has higher weight. Optical characterization of some derivatives in the solid state have been carried out in the context of application in hybrid structures and are described in refs. in refs. [193–195].

6.2.4 Thin Film Growth[41]

L4P, **L4P-sp2**, and **L4P-sp3** have been grown on ZnO and Al_2O_3 surfaces by OMBD under UHV conditions. **L4P** growths in a Volmer-Weber mode and forms islands of up to 250 nm height at a nominal layer thickness of 6 nm, independent of the substrate temperature, which was kept between 90 and 300 K. **L4P-sp2** and **L4P-sp3** display two dimensional Frank-van der Merwe growth at 300 K substrate temperature and form smooth films at a nominal thickness of 3 nm. X-ray reflectometry (XRR) scans of a 20 nm film of **L4P-sp3** show, that the thicker film is also very smooth and the absence of Bragg-reflections indicate, that it is amorphous. Under vacuum or N_2, thin films ($\approx$ 3 nm) of **L4P-sp2** and **L4P-sp3** are stable. However, when exposed to air, films of **L4P-sp2** start to break up and form holes within hours. This process is significantly slower for **L4P-sp3**, which makes it very suitable for thin film applications.

[41] This section summarizes work, which was carried out by Moritz Eyer and Dr. Sylke Blumstengel in the group of Prof. Fritz Henneberger and by Anton Zykov in the group of Prof. Stefan Kowarik (Humboldt-Universität zu Berlin, Institut für Physik)

6.3 Conclusion

In summary, synthetic routes have been developed, that allow to subsequently replace every symmetry-equivalent alkyl group in **L4P** by a spirobifluorene group. With increasing number of spiro groups, the optical gap for absorption and emission slightly decreases, which is disadvantageous with respect to resonant energy transfer with ZnO. Thus, a synthetic route to a *para*-linked ladder-type quarterphenyl carrying all bridging units on one side of the ribbon (***iso*-L4P**) was developed, which results in a bending of the *para*-phenylene. And indeed, the optical gap increased compared to the 'linear' molecule, however the absorption coefficient is not as high. Nearly all derivatives have been analyzed by single crystal X-ray structure analysis. In the cases of **L4P-sp2** and **L4P-sp3** it could even be shown, that sublimation and crystallization from solution result in different crystal structures, of which the ones from sublimation might be advantageous in terms of application in light emitting devices.

6.4 Experimental

6.4.1 Analytical Instrumentation

6.4.1.1 Liquid Chromatography

Analytical LC was performed on a Waters Acquity UPLC equipped with a Waters LCT Premier XE Mass detector for high-resolution MS (HR-MS, ESI+-ionization) and with Waters Alliance systems (consisting of a Waters Separations Module 2695, a Waters Diode Array Detector 996 and a Waters LCT Premier XE Mass Detector).

6.4.1.2 UV-Vis Spectroscopy

Absorption spectra were recorded on a Varian Cary 50 Bio UV-Visible spectrometer and fluorescence spectra on a Varian Cary Eclipse Fluorescence spectrometer using 10.0 x 10.0 mm quartz cuvettes.

Fluorescence Quantum Yield The fluorescence quantum yield was determined according to

$$\Phi_S = \Phi_R \cdot \frac{\int I_S(\lambda_S) d\lambda_S}{\int I_R(\lambda_R) d\lambda_R} \cdot \frac{[1 - 10^{-E_R(\lambda_{Ex})}]}{[1 - 10^{-E_S(\lambda_{Ex})}]} \cdot \frac{n_S^2}{n_R^2}. \tag{6.1}$$

In the equation Φ depicts the fluorescence quantum yield, $\int I(\lambda) d\lambda$ the Area under the fluorescence spectrum, $E(\lambda_{Ex})$ the extinction (absorbance) at the excitation wavelength (which was kept the same for sample and reference), and n the refractive index of the solvents used. Index R denotes properties of reference, and S of the unknown sample. 9,10-Diphenylanthracene in cyclohexane, assuming $\Phi = 0.9$[42], was

[42] Ref. [126] p. 160.

used as reference.[126, 127]

6.4.2 Organic Synthesis

^{1}H-NMR and ^{13}C-NMR spectra were referenced to 7.26 ppm and 77.16 ppm, respectively, for $CDCl_3$ and 5.32 ppm and 53.8 ppm, respectively, for CD_2Cl_2.[43]

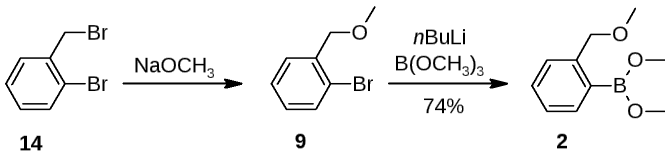

Dimethyl (2-(methoxymethyl)phenyl)boronate (2)
Under an argon atmosphere sodium (2.76 g, 120 mmol) was added to stirred methanol (150 mL) in a round bottom flask equipped with a reflux condenser. After all sodium was consumed, **14** (24.9 g, 100 mmol) was added to the mixture and stirring was continued for 2 h at room temperature. Water was added and the mixture was extracted with CH_2Cl_2. The organic phase was dried ($MgSO_4$) and the solvent was removed. Crude **9** was dissolved in THF (150 mL) under an Argon atmosphere and cooled to -78 °C, followed by the drop-wise addition of *n*BuLi (110 mmol, 44 mL, 2.5 M in hexanes). After stirring for 1 h at -78 °C, $B(OCH_3)_3$ (13.6 mL, 120 mmol, ϱ = 0.92 g cm^{-3}) was added. The reaction was allowed to warm to room temperature and it was stirred over night. The reaction was quenched with HCl (600 mL, 1 M) and extracted with diethyl ether. The organic phase was dried ($MgSO_4$) and the solvent was removed. 14.3 g (74 mmol, 74% yield)[44] of crude **2** were obtained.

[43] In some cases ^{13}-C-NMR spectra have not been recorded due to low solubility of the products.
[44] It was assumed, that the molecular mass of the product was the one of **2**, independent of the actual composition.

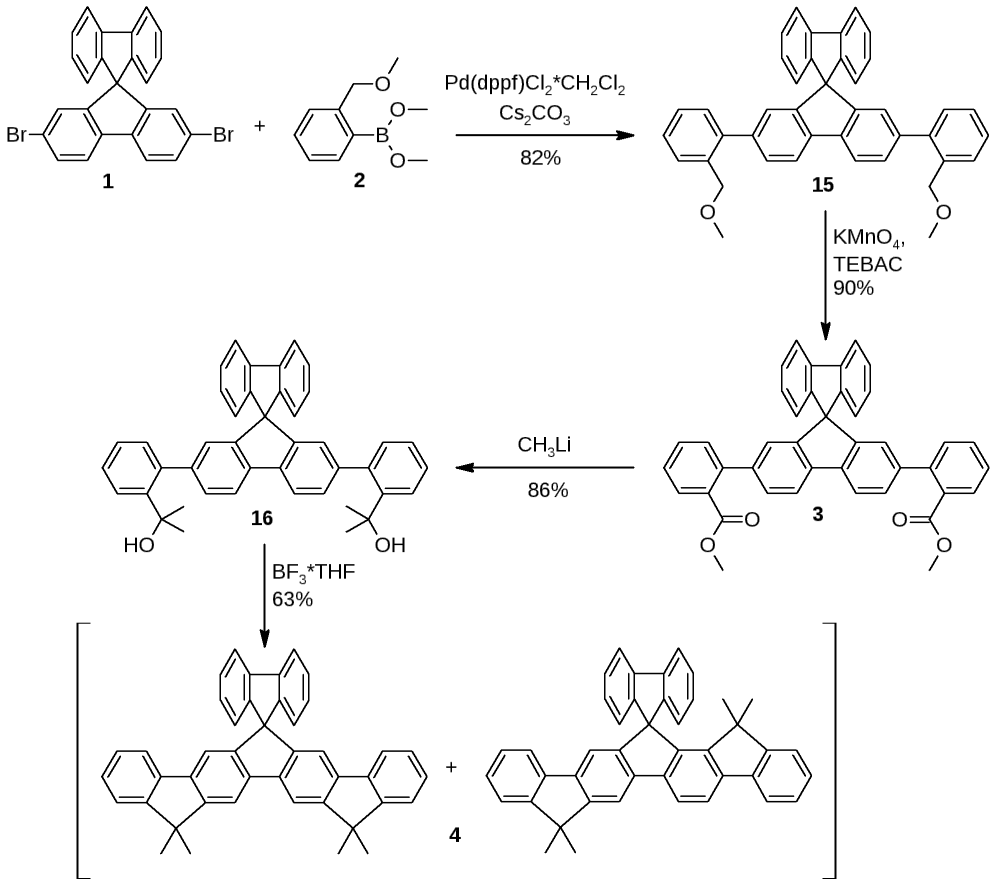

2,7-Bis(2-(methoxymethyl)phenyl)-9,9'-spirobi[fluorene] (15)
Under an argon atmosphere a mixture of **1** (3.5 mmol, 1.66 g), **2** (10.5 mmol, 2.06 g), Cs_2CO_3 (5.7 g, 17.5 mmol) and $Pd(dppf)Cl_2 \cdot CH_2Cl_2$ (0.175 mmol, 0.14 g) in THF / ethanol / DMF (20/20/5 mL) was stirred for 2 h at 70 °C. It was poured into water (600 mL). The mixture was acidified (HCl) and the precipitate was filtered off.[45] The crude product was dissolved in ethyl acetate, the solution was dried ($MgSO_4$) and the solvent was removed. After purification by column chromatography (cyclohexane/ethyl acetate) **15** (1.67 g, 3.0 mmol) was obtained in 86% yield.
^{1}H-NMR (300 MHz, $CDCl_3$) δ [ppm] = 7.93 (d, J = 7.8 Hz, 2H), 7.79 (d, J = 7.6 Hz, 2H), 7.43 (dd, J = 7.8, 1.6 Hz, 2H), 7.41 - 7.36 (m, 2H), 7.31 (td, J = 7.5, 1.1 Hz, 2H), 7.28 - 7.24 (m, 6H), 7.11 (td, J = 7.5, 1.0 Hz, 2H), 6.89 (d, J = 1.5 Hz, 2H), 6.86 (d, J = 7.6 Hz, 2H), 4.06 (s, 4H), 2.90 (s, 6H).
^{13}C-NMR (75 MHz, $CDCl_3$) δ [ppm] = 149.2, 148.8, 142.1, 140.6, 140.5, 135.2, 130.1, 129.1, 128.0, 127.9, 127.5, 125.3, 124.2, 120.1, 119.8, 72.7, 66.1, 57.7.

Dimethyl 2,2'-(9,9'-spirobi[fluorene]-2,7-diyl)dibenzoate (3)
A mixture of **15** (2.56 g, 4.6 mmol), TEBAC (6.3 g, 27.6 mmol), and $KMnO_4$ (4.36 g, 27.6 mmol) in CH_2Cl_2 (70 mL) was refluxed for 24 h. After cooling to room temperature the reaction was quenched with aqueous thiosulfate solution. It was extracted with CH_2Cl_2, the organic phase was dried ($MgSO_4$), and the solvent was

[45] If the product does not precipitate (e.g. if butylboronic esters were used), extraction with ethyl acetate or CH_2Cl_2 is necessary.

removed. The crude product was purified by column chromatography (CH_2Cl_2) to give **3** (2.41 g, 4.12 mmol) in 90% yield as colorless solid.
^{1}H-NMR (300 MHz, $CDCl_3$) δ [ppm] = 7.91 (dd, J = 7.9, 0.4 Hz, 2H), 7.80 (d, J = 7.6 Hz, 2H), 7.65 (dd, J = 8.0, 1.3 Hz, 2H), 7.46 - 7.37 (m, 4H), 7.36 - 7.27 (m, 6H), 7.10 (td, J = 7.5, 1.1 Hz, 2H), 6.83 (d, J = 7.6 Hz, 2H), 6.63 (d, J = 1.1 Hz, 2H), 3.30 (s, 6H).
^{13}C-NMR (75 MHz, $CDCl_3$) δ [ppm] = 169.4, 149.1, 148.7, 141.9, 141.9, 141.0, 140.8, 131.2, 131.1, 130.7, 129.7, 128.2, 127.9, 127.9, 127.2, 124.4, 124.3, 120.3, 120.1, 52.0.

2,2'-(9,9-Spirobi[fluorene]-2,7-diylbis(2,1-phenylene))bis(propan-2-ol) (16)
Under an argon atmosphere CH_3Li (8.0 mL, 24 mmol, 3 M in dimethoxymethane) was added to a stirred solution of **3** (1.17 g, 2.0 mmol) in dry THF (35 mL). After stirring the solution for 30 min at room temperature, water was added and the mixture was extracted with diethyl ether. The organic phase was dried ($MgSO_4$) and the solvent was removed. The crude product was purified by column chromatography (cyclohexane/ethyl acetate) to give **16** (0.96 g, 1.64 mmol, 82% yield) as a colorless solid.
^{1}H-NMR (300 MHz, CD_2Cl_2) δ [ppm] = 7.92 (dd, J = 7.8, 0.5 Hz, 2H), 7.80 - 7.76 (m, 2H), 7.57 (dd, J = 8.0, 1.1 Hz, 2H), 7.37 - 7.30 (m, 4H), 7.28 - 7.10 (m, 6H), 7.01 - 6.96 (m, 2H), 6.82 (d, J = 7.5 Hz, 2H), 6.63 (dd, J = 1.5, 0.5 Hz, 2H), 1.20 (s, 12H).
^{13}C-NMR (75 MHz, CD_2Cl_2) δ [ppm] = 148.8, 147.0, 143.8, 142.1, 140.6, 140.1, 131.9, 129.5, 128.2, 128.1, 127.6, 126.2, 126.2, 125.7, 124.0, 120.4, 119.8, 73.9, 32.6.

Isomeric mixture of L4P-sp (4)
$BF_3 \cdot THF$ (2.1 mL, 9.6 mmol, ϱ = 1.26 g/cm^3, 50% in THF) was added to a stirred solution of **16** (0,934 g, 1.6 mmol) in CH_2Cl_2 (100 mL). After stirring for 5 min, aqueous $NaHCO_3$ and ethanol were added. The mixture was extracted with CH_2Cl_2, the organic phase was dried ($MgSO_4$) and the solvent was removed. The crude product was purified by column chromatography (petroleum ether/CH_2Cl_2) and subsequent crystallization from toluene/hexane/ethanol to give 0.55 g (1.0 mmol, 63% yield) of isomeric mixture **4** containing 55% **L4P-sp** (by integration of the absorption trace of a UPLC chromatograpy run). **L4P-sp** was enriched to ≈ 95% by repeated crystallization from CCl_4/ethanol. For analytical data see below.

12,12,15,15-Tetramethyl-12,15-dihydrospiro[cyclopenta[2,1-*b*:3,4-*b'*] difluorene-6,9'-fluorene] L4P-sp
Under an argon atmosphere *n*BuLi (2.7 mL, 6.0 mmol, 2.2 M in cyclohexane) was added to a solution of **5** (1.4 g, 6.0 mmol) in THF (15 mL) at -78 °C. After stirring the mixture for 1 h at that temperature, it was added to a solution of **L4P-O** (0.42 g , 1.0 mmol) in THF (20 mL) and stirring was continued for 30 min at room temperature. The reaction was quenched with water and extracted with ethyl acetate. The organic phase was dried ($MgSO_4$) and the solvent was removed. The crude product was dissolved in AcOH (10 mL) at 100 °C. Upon adding HCl (1 mL, conc.) stirring at 100 °C was continued for 1 h. After cooling to room temperature, the precipitate was filtered off and dissolved in CH_2Cl_2. The solution was washed with

aqueous $NaHCO_3$, dried ($MgSO_4$) and the solvent was removed. The crude product was purified by column chromatography (petroleum ether/ethyl acetate) and crystallization from acetonitrile to give **L4P-sp** (0.42 g, 0.77 mmol) in 77% yield.
^{1}H-NMR (300 MHz, $CDCl_3$) δ [ppm] = 7.98 - 7.91 (m, 4H), 7.46 - 7.37 (m, 6H), 7.27 - 7.18 (m, 4H), 7.15 (td, J = 7.5, 1.1 Hz, 2H), 7.06 (d, J = 0.6 Hz, 2H), 6.88 (d, J = 7.6 Hz, 2H), 1.62 (s, 12H).
^{13}C-NMR (75 MHz, $CDCl_3$) δ [ppm] = 154.0, 153.9, 149.6, 148.6, 141.9, 141.6, 139.3, 139.2, 128.0, 127.8, 127.0, 127.0, 124.5, 122.5, 120.1, 120.1, 115.8, 114.0, 65.7, 46.7, 27.6.

6',6'-Dimethyl-6'*H*-dispiro[fluorene-9,12'-cyclopenta[2,1-*b*:3,4-*b*']difluorene-15',9"-fluorene] L4P-sp2
Under an argon atmosphere *n*BuLi (2.8 mL, 5.8 mmol, 2.2 M in cylcohexane) was added to a solution of **5** (1.4 g, 5.8 mmol) in dry THF (10 mL) at -78 °C. After stirring for 1 h, the solution was added to a suspension of **L4P-O2** (0.23 g, 0.58 mmol) in dry THF (10 mL) at -78 °C. The resulting mixture was stirred for 2 h at -78 °C and over night at room temperature. Water was added, the mixture was extracted with ethyl acetate, the organic phase was dried ($MgSO_4$) and the solvent was removed. The crude dialcohol was dissolved in 80 mL of AcOH at 100 °C and subsequently HCl (5 ml, conc.) was added. The reaction mixture was stirred for 2 h at 100 °C. After cooling to room temperature, water was added and the mixture was extracted with CH_2Cl_2. The organic phase was washed with aqueous $NaHCO_3$, dried ($MgSO_4$) and the solvent was removed. The crude product was purified by column chromatography (petroleum ether/ethyl acetate) and subsequent precipitation from petroleum ether to give **L4P-sp2** (0.34 g, 0.51 mmol) in 87% yield.
^{1}H-NMR (300 MHz, $CDCl_3$) δ [ppm] = 7.88 - 7.76 (m, 8H), 7.35 (td, J = 7.5, 1.0 Hz, 2H), 7.31 (td, J = 7.5, 1.1 Hz, 4H), 7.10 – 7.00 (m, 6H), 6.73 – 6.64 (m, 8H), 1.66 (s, 6H).
^{13}C-NMR (75 MHz, $CDCl_3$) δ [ppm] = 154.2, 149.3, 149.1, 148.0, 142.1, 141.8, 141.2, 139.5, 127.9, 127.8, 127.6, 124.2, 124.1, 120.1, 119.7, 115.7, 114.1, 65.7, 46.5, 27.8.

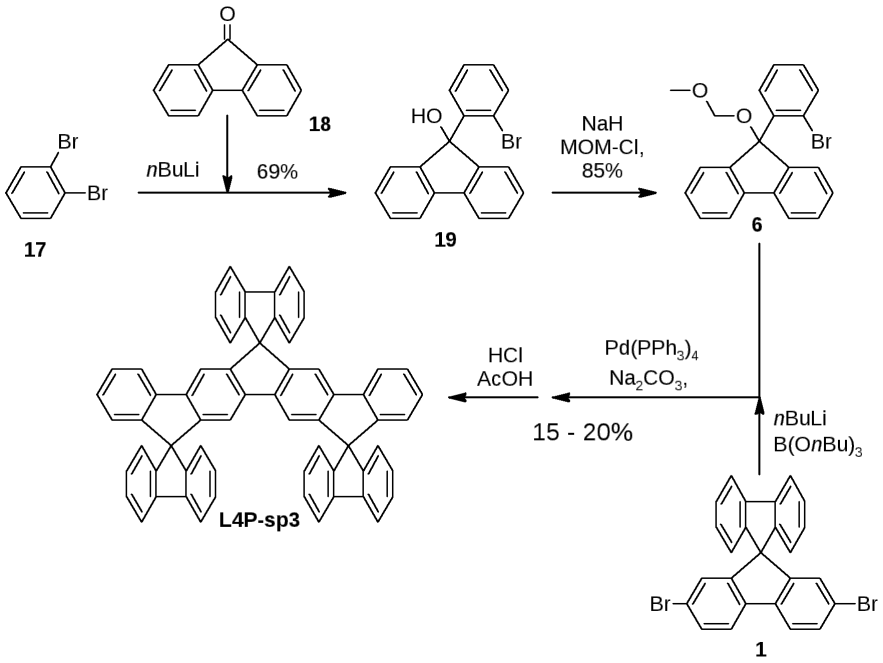

(9-(2-Bromophenyl)-9*H*-fluoren-9-yl)methanol (19)[46]
Dibromobenzene **17** (2.4 mL, 20.0 mmol, ϱ = 1.956 g/cm^3) was dissolved in dry THF/diethyl ether (30/30 mL) and cooled to -120 °C (using pentane and liquid N_2). A solution of *n*BuLi (9.0 mL, 19.8 mmol, 2.2 M in cyclohexane) and petroleum ether (15 mL) was added dropwise. The solution was stirred for 1 h at -120 °C. A solution of fluorenone **18** (3.2 g, 18 mmol) in dry THF/diethyl ether (10/20 mL) was added over a period of 30 min. The mixture was stirred for further 3 h at -120 °C. After allowing the reaction to warm to room temperature, it was quenched with aqueous NH_4Cl and extracted with diethyl ether. The organic phase was dried ($MgSO_4$) and the solvent was removed. A seed crystal[47], as well pentane were added and the product was crystallized over night. After filtration, **19** (4.64 g, 13.8 mmol, 69% yield) was obtained as colorless crystals.
^{1}H-NMR (300 MHz, $CDCl_3$) δ [ppm] = 8.45 (s, 1H), 7.74 - 7.63 (m, 2H), 7.53 - 7.34 (m, 4H), 7.25 - 7.08 (m, 5H), 2.50 (s, 1H).
^{13}C-NMR (75 MHz, $CDCl_3$) δ [ppm] = 176.8, 134.5, 129.4, 129.3, 128.5, 127.2, 124.1, 121.1, 120.4.

9-(2-Bromophenyl)-9-((methoxymethoxy)methyl)-9*H*-fluorene (6)[48]
Under an argon atmosphere NaH (0.74 g, 18.5 mmol, 60% dispersion in mineral oil) was dispersed in petroleum ether (10 mL) and cooled to 0 °C. 10 mL of dry THF, and subsequently a solution of **19** (2.1 g, 6.2 mmol) in dry THF (30 mL) was

[46]The synthesis of **19** was already described in ref [189]. Here, the procedure was slightly varied, especially concerning the purification.

[47]Column chromatography (cyclohexane/ethyl acetate) and subsequent crystallization from ethanol/hexane also yields analytically pure product.

[48]The synthesis of **6** was already described in ref. [189], however employing the stoichiometry of NaH and MOM-Cl, which was proposed there (more MOM-Cl than NaH) did never lead to the formation of significant amounts of product in our experiments after aqueous workup. Accordingly, excess NaH was used.

added slowly. After stirring the mixture for 2,5 h at 0 °C, chlormethylmethyl ether (MOM-Cl, 1.13 mL, 14.8 mmol, ϱ = 1.06 g/cm^3) was added and stirring was continued for another 2 h. The reaction was first quenched with $NaHCO_3$, afterwards water was added. The mixture was extracted with ethyl acetate. The organic phase was dried ($MgSO_4$) and the solvent was removed. The crude product was purified by column chromatography[49] (cyclohexane/ethyl acetate) to give **6** (2.0 g, 5.2 mmol, 85% yield) as colorless solid.
^{1}H-NMR (300 MHz, $CDCl_3$) δ [ppm] = 8.49 (s, 1H), 7.72 - 7.64 (m, 2H), 7.52 - 7.35 (m, 4H), 7.26 - 7.11 (m, 5H), 4.30 (s, 2H), 3.17 (s, 3H).
^{13}C-NMR (75 MHz, $CDCl_3$) δ [ppm] = 145.3, 141.0, 134.7, 129.4, 129.0, 128.9, 128.0, 127.0, 125.1, 120.8, 120.3, 119.9, 91.5, 55.9.

L4P-sp3 (small scale)
Under an argon atmosphere a solution of **1** (1.19 g, 2.5 mmol) in dry THF (50 mL, the solution was degassed by subsequently applying vacuum and argon 4 times) was cooled to -78 °C and *n*BuLi (2.6 mL, 5.7 mmol, 2.2 M in cyclohexane) was added. After stirring the mixture for 1 h, B(O*n*Bu)$_3$ (1.67 mL, 6.25 mmol, ϱ = 0.86 g/cm^3) was added and the solution was allowed to warm to room temperature. Meanwhile $Pd(PPh_3)_4$ (0.58 g, 0.50 mmol) was added to a solution of **6** (2.1 g, 5.5 mmol) in THF (15 mL, the solution was degassed by subsequently applying vacuum and argon 4 times) and stirred for 10 min under Argon at room temperature. Aqueous Na_2CO_3 (10 mL, 2.0 M) and the solution of the boronate were added. The temperature was raised to 65 °C. The reaction was stirred for 24 h at that temperature. It was quenched with water and extracted with ethyl acetate. The organic phase was dried ($MgSO_4$) and all volatiles were removed. The crude product was dissolved in AcOH (50 mL) at 100 °C and HCl (5 mL, conc.) was added. After stirring the mixture for 1 h at 100 °C, the precipitate was filtered off, dried and purified via column chromatography (petroleum ether/ethyl acetate) to give **L4P-sp3** (0.29 g, 0.37 mmol, 15% yield) as a colorless solid.
^{1}H-NMR (300 MHz, CD_2Cl_2) δ [ppm] = 8.07 - 8.01 (m, 2H), 7.88 - 7.83 (m, 4H), 7.57 - 7.53 (m, 2H), 7.52 (td, J = 7.5, 1.1 Hz, 2H), 7.37 (td, J = 7.5, 1.1 Hz, 4H), 7.24 (tt, J = 7.6, 1.2 Hz, 4H), 7.16 (d, J = 0.7 Hz, 2H), 7.10 (td, J = 7.5, 1.1 Hz, 4H), 7.04 (td, J = 7.5, 1.1 Hz, 2H), 6.92 - 6.87 (m, 2H), 6.83 (d, J = 0.7 Hz, 2H), 6.71 - 6.66 (m, 4H), 6.64 - 6.60 (m, 2H).
^{13}C-NMR (75 MHz, CD_2Cl_2) δ [ppm] = 149.5, 149.4, 149.3, 149.2, 149.0, 142.3, 142.1, 142.0, 142.0, 141.9, 128.3, 128.3, 128.1, 128.0, 127.9, 124.6, 124.2, 123.9, 120.6, 120.4, 120.3, 115.8, 115.6, 110.4, 66.0, 65.9.

L4P-sp3 (gram scale, high purity)
Under an argon atmosphere *n*BuLi (7.35 mL, 16.2 mmol, 2.2 M in cyclohexane) was added to a solution of **1** (3.34 g, 7.0 mmol) in THF (50 mL) at -78°C. After the mixture was stirred for 1.5 h at that temperature, B(O*n*Bu)$_3$ (4.75 mL, 17.6 mmol, ϱ = 0.86 g/cm^3) was added and stirring at -78 °C was continued for 10 min and for 1 h at room temperature. Under argon $Pd(PPh_3)_4$ (0.24 g, 0.21 mmol) was added to a solution of **6** (5.9 g, 15.5 mmol) in THF (30 mL) in the meantime. Aqueous Na_2CO_3

[49] **6** can also be purified by crystallization from hexane or hexane/ethanol.

(20 mL, 2.0 M) and subsequently the solution of the boronate were added. The mixture was refluxed over night. After cooling to room temperature the organic phase was separated and all volatiles were removed. The crude product was dissolved in AcOH (20 mL) at 100 °C and HCl (2 mL, conc.) was added. The mixture was stirred for 30 min at 100 °C. After cooling to room temperature, the precipitate was filtered off and washed with ethanol. The crude product was roughly purified by column chromatography (CH_2Cl_2), followed by crystallization ($CHCl_3$/ethanol), sublimation, crystallization (5x, $CHCl_3$/ethanol) and some further alternating steps of gradient sublimation and crystallization, to give **L4P-sp3** (1.1 g, 1.4 mmol, 20% yield) as colorless crystals.
NMR: see above.

2,7-Diiodo-3,6-dibromo-9,9-dimethylfluorene (8)[50]
A mixture of 3,6-dibromo-9,9-dimethylfluorene **7** (3.0 g, 8.5 mmol), iodine (4.3 g, 17.0 mmol), and periodic acid (1.0 g, 4.4 mmol) in $AcOH/H_2O/H_2SO_4$ (110/11/3 mL) was stirred over night at 80 °C. After cooling to room temperature, the mixture was poured on ice and extracted with CH_2Cl_2. Water was added to the organic phase and afterwards $NaHCO_3$ until the formation of CO_2 stopped. The organic phase was washed with aqueous $NaHCO_3$ and subsequently with aqueous $Na_2S_2O_3$. The organic phase was dried ($MgSO_4$) and the solvent was removed. The residue was washed with diethyl ether. 2,7-diiodo-3,6-dibromo-9,9-dimethylfluorene **8** (4.0 g, 6.6 mmol) was obtained in 78% yield.
^{1}H-NMR (300 MHz, $CDCl_3$) δ [ppm] = 7.91 (s, 2H), 7.88 (s, 2H), 1.43 (s, 6H).

3,6-dibromo-2,7-bis(2-(methoxymethyl)phenyl)-9,9-dimethyl-9*H*-fluorene (10)
Under an argon atmosphere, *n*BuLi (4.7 mL, 10.2 mmol, 2.2 M in cyclohexane) was added to a solution of **9** (1.87 g, 9.3 mmol) in THF (25 mL) at -78 °C. The mixture was stirred at that temperature for 1 h. Subsequently $B(O\,n\mathrm{Bu})_3$ (2.77 mL, 10.2 mmol, ϱ = 0.86 g/cm^3) was added and stirring was continued for 10 min at −78 °C and for 1 h at room temperature. Meanwhile a solution of **8** (2.25 g, 3.7 mmol) and $Pd(PPh_3)_4$ (0.65 g, 0.56 mmol) in THF (20 mL) was prepared under an argon atmosphere. After stirring this solution for 10 min, aqueous Na_2CO_3 (20 mL, 2 M), as well as the solution of the boronate were added. The reaction was refluxed over night. It was cooled to room temperature and the organic phase was separated. All volatiles were removed and the crude product was purified by column chromatography (petroleum ether/ethyl acetate) to give **10** (1.52 g, 2.56 mmol) in 69% yield.
^{1}H-NMR (300 MHz, $CDCl_3$) δ [ppm] = 8.01 (s, 2H), 7.58 (dd, J = 7.4, 1.1 Hz, 2H), 7.49 - 7.36 (m, 6H), 7.30 - 7.24 (m, 2H), 4.37 - 4.12 (m, 4H), 3.26 (s, 6H), 1.48 - 1.52 (m, 6H).
^{13}C-NMR (75 MHz, $CDCl_3$) δ [ppm] = 152.9, 141.0, 140.6, 139.0, 136.2, 130.0, 130.0, 128.5, 128.5, 128.3, 127.5, 125.8, 124.3, 122.3, 72.5, 58.5, 47.0, 27.0.

[50] The procedure was adapted from ref. [192].

Dimethyl 2,2'-(3,6-dibromo-9,9-dimethyl-9*H*-fluorene-2,7-diyl)di-benzoate (11)

A mixture of **10** (9.95 g, 16.8 mmol), TEBAC (23.0 g, 100.8 mmol) and $KMnO_4$ (15.9 g, 100.8 mmol) in CH_2Cl_2 (200 mL) was refluxed for 1 day. After cooling to room temperature, the reaction was quenched with aqueous $Na_2S_2O_3$ and diluted with CH_2Cl_2. Upon adding HCl to dissolve the MnO_2, the organic phase was immediately separated and dried ($MgSO_4$). The solvent was removed to give **11** in quantitative yield. The product was used without further purification.

^{1}H-NMR (300 MHz, $CDCl_3$) δ [ppm] = 8.04 (d, J = 7.8 Hz, 2H), 7.95 (s, 2H), 7.61 (td, J = 7.5, 1.5 Hz, 2H), 7.50 (td, J = 7.6, 1.3 Hz, 2H), 7.35 (d, J = 7.6 Hz, 2H), 7.28 (s, 2H), 3.64 (s, 3H), 3.63 (s, 3H), 1.49 (s, 6H).

^{13}C-NMR (75 MHz, $CDCl_3$) δ [ppm] = 167.7, 152.9, 142.5, 141.8, 138.8, 131.9, 131.4, 131.3, 130.7, 130.6, 130.3, 130.3, 128.1, 124.5, 124.1, 121.7, 52.2, 52.2, 47.0, 27.1, 27.1.

5,8-Dibromo-14,14-dimethyl-13*H*-cyclopenta[1,2-*a*:4,3-*a'*]difluorene-13, 15(14*H*)-dione (12)

A mixture of **11** (3.14 g, 5.07 mmol) and aqueous NaOH (8.0 g in 20 mL H_2O) in ethanol (200 mL) was stirred over night at 80 °C. After cooling to room temperature, the solution was concentrated and HCl (half conc.) was added. The mixture was extracted with CH_2Cl_2. The organic phase dried ($MgSO_4$) and all volatiles were removed. Afterwards the crude product was refluxed in $SOCl_2$ (90 mL). After 3 h the initially observed formation of gas had finished and methanesulfonic acid was added (18 mL). The mixture was refluxed for another 2 h and the formation of an orange precipitate started. After stirring over night at room temperature, the precipitate was filtered off and all volatiles were removed to yield **12** (2.23 g, 4.0 mmol, 79% yield) as an orange solid.

^{1}H-NMR (300 MHz, $CDCl_3$) δ [ppm] = 8.48 (dt, J = 7.7, 0.8 Hz, 2H), 7.93 (s, 2H), 7.78 - 7.71 (m, 2H), 7.58 (td, J = 7.6, 1.3 Hz, 2H), 7.39 (td, J = 7.4, 0.9 Hz, 2H), 1.91 (s, 6H).

5',8'dibromo-14',14'-dimethyl-14'*H*-dispiro[fluorene-9,13'-cyclopenta [1,2-*a*:4,3-*a'*]difluorene-15'-9"-fluorene (13)

Under an argon atmosphere *n*BuLi (6.4 mL, 14.2 mmol, 2.2 M in cyclohexane) was added to a solution of 2-bromobiphenyl **5** (3.3 g, 14.2 mmol) in THF (20 mL) at -78 °C. The solution was stirred for 45 min at that temperature. It was added to a suspension of **12** (1.31 g, 2.36 mmol) in THF (20 mL). After stirring the mixture for 15 min at room temperature, it was quenched with water and extracted with ethyl acetate. The organic phase was dried ($MgSO_4$) and the solvent was removed. The crude product was dissolved in AcOH (250 mL) at 100 °C. HCl (20 mL) was added and the mixture was refluxed over night. Water (50 mL) was added and the precipitate was filtered from the hot solution. Afterwards it was dissolved in CH_2Cl_2. The organic phase was washed with aqueous $NaHCO_3$, dried ($MgSO_4$) and the solvent was removed. The crude product was purified by column chromatography (cyclohexane/ethyl acetate) and subsequent crystallization from ethanol/chloroform and toluene to give **13** (0.11 g, 0.13 mmol) in 6% yield

^{1}H-NMR (300 MHz, CD_2Cl_2) δ [ppm] = 8.73 (d, J = 7.9 Hz, 2H), 8.07 (s, 2H), 7.77 (d, J = 7.6 Hz, 4H), 7.27 (qd, J = 7.8, 1.1 Hz, 6H), 6.97 (tt, J = 7.6, 1.2 Hz, 6H), 6.62 (d, J = 7.7 Hz, 4H), 6.17 (d, J = 7.6 Hz, 2H), -0.31 (s, 6H).

14,14-Dimethyl-13*H*-cyclopenta[1,2-*a*:4,3-*a'*]difluorene-13,15(14*H*)-dione *iso*-L4P-O2

Under an argon atmosphere $NaBH_4$ (2.15 g, 60 mmol) was added to a suspension of **12** (5.56 g, 10 mmol) in THF (300 mL). Upon refluxing the reaction for 4 h, the orange color disappeared and the mixture was cooled to room temperature. A major amount of solvent was removed and water was added carefully. After stirring for some more time, the mixture was extracted with ethyl acetate. The organic phase was dried ($MgSO_4$) and the solvent was removed. Under an Argon atmosphere the crude dialcohol was dissolved in THF (250 mL) and cooled to -78 °C. *n*BuLi (27 mL, 60 mmol, 2.2 M in cyclohexane) was added and after stirring for 1 h at -78 °C, the reaction was quenched with ethanol and was allowed to warm to room temperature. Water and brine were added and the mixture was extracted with ethyl acetate (in sum more than 3 L!). The organic phase was dried ($MgSO_4$) and the solvent was removed. Subsequently the crude product was suspended in CH_2Cl_2 (500 mL) and TEBAC (13.7 g, 60 mmol), as well as $KMnO_4$ (9.5 g, 60 mmol) were added carefully. The mixture was refluxed for 30 min. After cooling to room temperature the reaction was quenched carefully with aqueous $Na_2S_2O_3$, and diluted with water and CH_2Cl_2. Upon adding some HCl, the organic phase was separated. Some ethanol was added and the major amount of solvent was removed. The precipitate was filtered off and dried under vacuum to yield ***iso*-L4P-O2** (2.9 g, 7.3 mmol, 73% yield) as an orange solid.

^{1}H-NMR (500 MHz, CD_2Cl_2) δ [ppm] = 7.86 (d, J = 7.7 Hz, 2H), 7.68 - 7.65 (m, 2H), 7.61 (d, J = 7.7 Hz, 2H), 7.61 - 7.59 (m, 2H), 7.53 (td, J = 7.4, 1.2 Hz, 2H), 7.33 (td, J = 7.4, 1.0 Hz, 2H), 1.89 (s, 6H).

^{13}C-NMR (126 MHz, CD_2Cl_2) δ ppm] = 193.9, 154.9, 145.1, 144.9, 140.8, 135.0, 134.4, 129.7, 129.3, 125.5, 124.3, 120.4, 119.9, 49.7, 21.5.

14',14'-Dimethyl-14'*H*-dispiro[fluorene-9,13'-cyclopenta[1,2-*a*:4,3-*a'*] difluorene-15',9"-fluorene] *iso*-L4P-sp2

Under an argon atmosphere *n*BuLi (5.5 mL, 12.0 mmol, 2.2 M in cyclohexane) was added to a solution of **5** (2.80 g, 12 mmol) in THF (50 mL) at -78 °C. After stirring for 1.5 h at -78 °C, this solution was added to a solution of ***iso*-L4P-O2** (0.80 g, 2.0 mmol) in THF (200 mL) and stirring was continued for 10 min at room temperature and 1 h at 65 °C. After cooling to room temperature, brine was added and the mixture was extracted with ethyl acetate. The organic phase was dried ($MgSO_4$) and the solvent was removed. The crude product was dissolved in AcOH (250 mL) at 100 °C and HCl (40 mL) was added. After stirring the mixture for 1.5 h at 100 °C, it was cooled to room temperature and the precipitate was filtered off. The crude product was crystallized from $CHCl_3$/ethanol to yield 0.80 g (1.20 mmol, 60% yield) of ***iso*-L4P-sp2** as colorless crystals.

^{1}H-NMR (300 MHz, CD_2Cl_2) δ [ppm] = 7.93 (s, 4H), 7.80 - 7.74 (m, 6H), 7.28 (td, J = 7.6, 1.1 Hz, 4H), 7.25 - 7.19 (m, 2H), 6.97 (td, J = 7.5, 1.1 Hz, 4H), 6.94 - 6.87

(m, 2H), 6.65 - 6.60 (m, 4H), 6.21 - 6.16 (m, 2H), -0.26 (s, 6H).
^{13}C-NMR (75 MHz, CD_2Cl_2) δ [ppm] = 150.6, 149.2, 141.6, 141.3, 140.5, 140.3, 128.1, 127.9, 127.8, 127.53, 124.3, 122.8, 120.8, 120.3, 119.7, 119.7, 22.4.

6.4.3 Crystal Structure Analysis

The diffraction data were collected on a STOE IPDS 2Θ diffractometer at 100 K. Crystallographic data are depicted in the crystallographic table. The structures were solved by direct methods (SHELXS-97)[124] and were refined with the full-matrix least-squares method on F^2 (SHELX-97 and SHELXL-2013)[51]. The hydrogen atoms were placed at the calculated positions and were refined by using a riding model. The data, which contain the supplementary crystallographic information, can be obtained free of charge from The Cambridge Crystallographic Data Centre via `www.ccdc.cam.ac.uk/data_request/cif`.

[51] [124]; Sheldrick, G. M., *SHELXL, Crystal Structure Refinement*, **2013** University of Göttingen, Germany.

compound	**L4P-O**	**L4P-O2**	***iso*-L4P-O2**	**L4P-sp**	**13**
Formular	$C_{31}H_{24}O$	$C_{29}H_{18}O_2$	$C_{29}H_{18}O_2$	$C_{43}H_{32}{\cdot}3\,(C_4H_8O_2)$	$C_{53}H_{32}Br_2{\cdot}CHCl_3$
Formular weight / g·mol^{-1}	412.50	398.43	398.43	813.00	947.95
λ / Å	0.71073	0.71073	0.71073	0.71073	0.71073
Crystal system	triclinic	orthorhombic	triclinic	triclinic	monoclinic
Space group	P-1	$Pna2_1$	P-1	P-1	$P2_1/n$
a / Å	8.2469(4)	18.8710(4)	8.4042(5)	10.6215(5)	13.7531(6)
b / Å	11.3875(6)	7.6790(2)	10.9413(6)	12.2581(6)	17.4523(7)
c / Å	11.9372(6)	13.5948(4)	11.2219(7)	18.6568(9)	18.2022(6)
α / °	87.578(4)	90	81.353(5)	80.597(4)	90
β / °	74.069(5)	90	89.882(5)	87.527(4)	110.296(1)
γ / °	85.189(6)	90	69.816(4)	66.356(4)	90
V / Å^3	1073.97(10)	1970.03(9)	956.13(10)	2194.6(2)	4097.7(3)
Z	2	4	2	2	4
Density / g·cm^{-3}	1.276	1.343	1.384	1.230	1.537
μ / mm^{-1}	0.075	0.083	0.086	0.079	2.213
$F(000)$	436.0	832.0	416.0	868.0	1912.0
Θ range / °	2.499 - 26.721	2.158 - 27.388	2.498 - 29.236	3.265 - 27.049	2.285 - 25.394
Reflections collected	16459	30176	18417	32957	49276
Independent reflections	4552	4430	5154	9281	7521
Completeness to Θ	1.00	0.99	0.99	0.96	1.00
R_{int}	0.073	0.098	0.063	0.115	0.030
GoF on F^2	0.809	1.012	0.982	0.994	1.040
R_1 [I > 2σ(I)]	0.039	0.046	0.040	0.061	0.026
wR_2 [I > 2σ(I)]	0.088	0.118	0.104	0.153	0.073
R_1 (all data)	0.0799	0.0517	0.0558	0.0857	0.0290
wR_2 (all data)	0.0808	0.1147	0.0977	0.1397	0.0707
$\Delta\rho_{max}/\Delta\rho_{min}$ / e·Å^{-3}	0.19 / -0.29	0.29 / -0.22	0.34 / -0.26	1.06 / -0.57	0.55 / -0.66
CCDC	-	-	-	-	-

compound	**L4P-sp2**	**L4P-sp2 ($CHCl_3$)**	**L4P-sp3**	**L4P-sp3 ($CHCl_3$)**[a]
Formular	$C_{53}H_{34}$	$C_{53}H_{34}$·3 ($CHCl_3$)	$C_{63}H_{36}$	$C_{63}H_{36}$·3 ($CHCl_3$)
Formular weight / g·mol^{-1}	670.80	1028.91	792.92	792.92
λ / Å	0.71073	0.71073	0.71073	0.71073
Crystal system	monoclinic	triclinic	monoclinic	monoclinic
Space group	$P2_1/c$	P-1	$P2_1/c$	$C2/c$
a / Å	15.0681(4)	13.4200(6)	16.6603(6)	27.0895(11)
b / Å	9.7445(4)	13.8860(6)	14.2737(3)	18.0988(7)
c / Å	24.5112(8)	14.7898(6)	17.8191(6)	15.7797(7)
α / °	90	111.455(2)	90	90
β / °	98.232(3)	92.712(2)	97.392(3)	122.641(1)
γ / °	90	104.062(2)	90	90
V / Å^3	3561.9(2)	2459.76(19)	4202.2(2)	6514.7(5)
Z	4	2	4	4
Density / g·cm^{-3}	1.251	1.389	1.253	-
μ / mm^{-1}	0.071	0.550	0.071	0.046
$F(000)$	1408.0	1052.0	1656.0	1544.0
Θ range / °	2.31 - 27.50	2.188 - 34.415	4.64 - 27.50	2.251 - 25.100
Reflections collected	14572	66710	33682	37433
Independent reflections	6511	18477	9613	5797
Completeness to Θ	0.80	0.89	1.00	1.00
R_{int}	0.0963	0.0666	0.0524	0.0769
GoF on F^2	0.948	1.030	0.886	0.918
R_1 [I > 2σ(I)]	0.0614	0.0998	0.0418	0.0769
wR_2 [I > 2σ(I)]	0.1423	0.2738	0.0848	0.2338
R_1 (all data)	0.0953	0.1302	0.0739	0.1047
wR_2 (all data)	0.1537	0.3008	0.0917	0.2545
$\Delta\rho_{max}/\Delta\rho_{min}$ / e·Å^{-3}	0.26 / -0.31	3.11 / -1.97	0.29 / -0.25	0.336 / -0.239
CCDC	-	-	-	-

[a]Solvent molecules were excluded for refinement of the structure.

7 Integration in Hybrid Structures[52]

In this chapter the application and characterization of LOPPs in HIOS, carried out in intense collaboration with other groups in the Department of Physics (HU Berlin), is presented. The most important issue in this context is the exciton transfer from inorganic QW structures to organic emitters. The QW structure was grown by epitaxial methods on a sapphire substrate consisting of a 500 nm thick lower barrier layer of $Zn_{0.9}Mg_{0.1}O$, a 3.5 nm ZnO QW, and a 2 nm upper barrier of $Zn_{0.9}Mg_{0.1}O$ (compare figure 7.1a). Organic layers of LOPPs were deposited by OMBD. As **L4P** forms crystals upon vacuum deposition on ZnO, **L4P-sp3** was chosen to study energy transfer from the ZnO QW, since it forms smooth layers. Apart from a slight red-shift, the absorption spectrum of **L4P-sp3** in the solid state is very similar to that in solution and overlaps well with the room temperature PL of the QW. Regarding the steady state PL of the hybrid system at 5 K, a PL excitation spectrum recorded at the **L4P-sp3** emission wavelength does not only display features of the molecule, but also of the QW PL excitation spectrum, which clearly indicates energy transfer from the QW to the organic emitter. This was further investigated by transient PL measurements. The QW alone has a PL decay time constant of 200 ps at 5 K. In the hybrid structure with a layer of **L4P-sp3** (figure 7.1), the time constant was reduced to 56 ps. From that a time constant of 77 ps and an efficiency of 0.72 can be calculated for the exciton transfer. However, the intensity of the **L4P-sp3** emission was very low. Since this can not be explained by the bulk properties of **L4P-sp3**, a loss channel related to the interface was very likely. This was revealed by UPS measurements to characterize the electronic structure at the interface. From the UPS data and from the optical absorption of the components, it

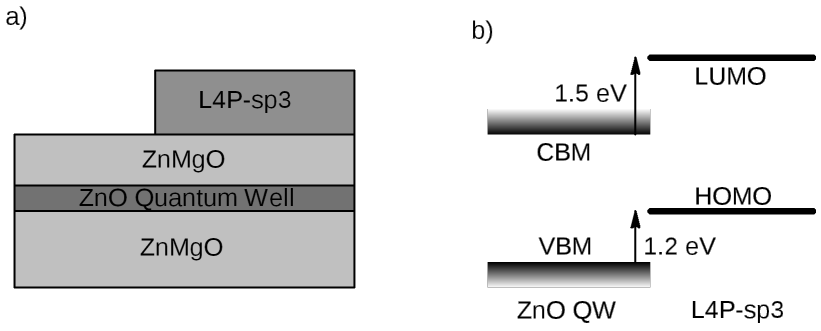

Figure 7.1 HIOS consisting of a ZnO quantum well (QW) and **L4P-sp3**. a) Device structure, b) energy level diagram, displaying type II energy level alignment.

[52]The studies presented in this chapter were mainly carried out in the groups of Prof. Fritz Henneberger and Prof. Norbert Koch (HU Berlin, Institut für Physik) and published in refs. [193–195].

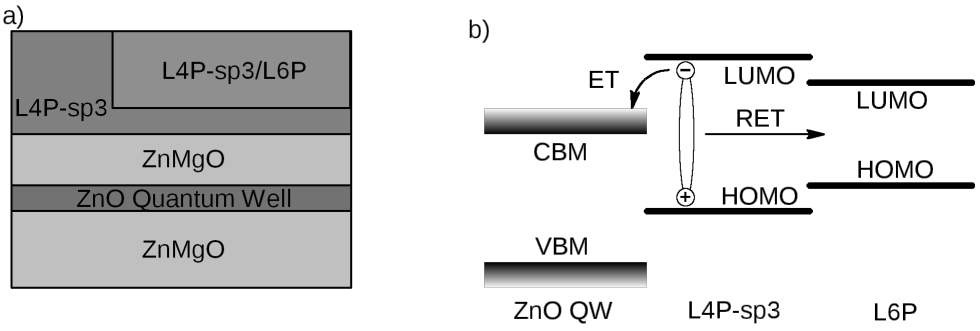

Figure 7.2 HIOS consisting of a ZnO QW and a **L4P-sp3** - **L6P** cascade. a) Device structure, b) energy level diagram with an exciton located in the layer of **L4P-sp3** and competing processes of electron transfer (ET) and resonant energy transfer (RET).

can be estimated, that the HOMO of **L4P-sp3** is situated 1.2 eV above the valence band maximum (VBM) of ZnO and the LUMO 1.5 eV above the conduction band minimum (CBM). The type II energy level alignment gives rise to exciton dissociation at the interface and thus quenches the emission of the organic component. This process can also be exemplified by PL transients. While the decay time of **L4P-sp3** on an inert substrate is 500 ps, it shortens to 95 ps in the hybrid structure.[194]

There are some strategies to suppress the exciton dissociation at the interface. The most obvious one is, to change the energy levels of the inorganic or the organic material, or to adjust the energy level alignment by the introduction of a dipole layer or by an interlayer of strong donors. This will be discussed later. Another way to suppress exciton dissociation is again to find a desirable process, that is faster than quenching. Here, a second RET to an emitter with a slightly lower optical gap is employed, to funnel the excitons away from the interface. This hybrid structure consists of a similar ZnO QW with a 0.5 nm layer of **L4P-sp3** and on top of that a 3.5 nm layer of 10% **L6P** blended into **L4P-sp3** (figure 7.2). This structure displays nearly only **L6P** emission. The transfer time constant between the QW and the organic layer is 65 ps and the corresponding efficiency 0.77 at 5 K. Furthermore the decay time of the **L6P** emission in this structure is 400 ps, which is nearly equal to the one on an inert substrate. The efficiency of energy transfer from **L4P-sp3** is above 0.9, but can not exactly be determined due to the time resolution of the setup. It is worth to note, that exciton transfer from the inorganic to the organic part even takes place at room temperature with an efficiency of 0.32. The structure is still emitting with a higher efficiency than the QW alone.[194]

As stated above, an alternative way to suppress charge separation at the organic-inorganic interface is to lower the work function of ZnO. By evaporation of $[RuCp^*Mes]_2$ on different surfaces of ZnO single crystals, the work function was significantly shifted. For example from 3.7 eV for ZnO(0001) to 2.2 eV with approximately one monolayer of the donor. The change in the work function is related to an electron transfer from the donor, which forms monomeric singly charged $[RuCp^*Mes]^+$ ions, to ZnO. The electron transfer was evidenced by a shift of the Ru $3d_{5/2}$ peaks in the

XPS spectrum towards higher binding energies. The change of the work function originates from the dipole between the positively charged dopands and the negatively charged ZnO. While for the HIOS with **L4P-sp3** directly on ZnO an offset between the frontier orbital levels and the ZnO bands of 1.1 - 1.2 eV was detected by UPS measurements, the offset with the interlayer is reduced to roughly 0.1 eV (see figure 7.3). These hybrid structures have also been characterized by transient PL spectroscopy. For the case of **L4P-sp3** directly on the ZnO/ZnMgO QW an energy transfer time of 115 ps (efficiency of 0.65) was found. But the lifetime of excited **L4P-sp3** was decreased from 500 ps on an inert substrate to 60 ps in the hybrid structure. With the donor interlayer the decay time increased to 265 ps again, which is accompanied by a seven fold increase of the emission intensity.[195]

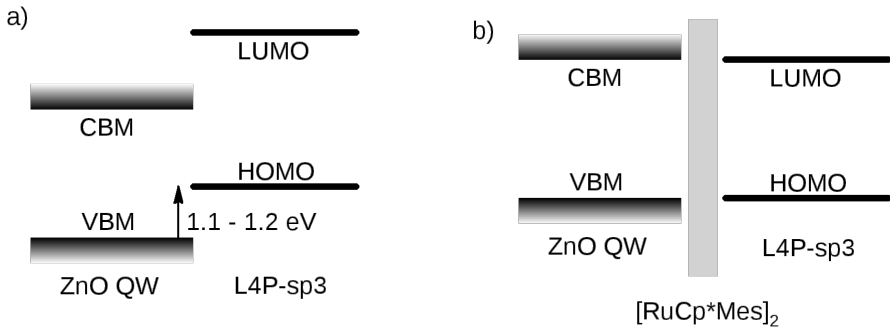

Figure 7.3 HIOS consisting of a ZnO QW and **L4P-sp3**. Energy level alignment a) without and b) with an interlayer of $[RuCp^{*}Mes]_2$.

In another study strong coupling between the 0,0 and 0,1-transition of **L4P-sp2** with the cavity mode of a $\lambda/2$ cavity consisting of **L4P-sp2** dispersed in a polymer matrix and SiO_x/ZrO_x Bragg reflectors with a reflectivity maximum of 96.9% was demonstrated. Furthermore, a structure with higher reflectivity (99.8%) and a longer cavity showed single-mode laser action upon optical pumping.[193]

8 Conclusion and Outlook

To summarize the outcome of this work, the different challenges presented at the end of the introduction chapter are addressed again in relation to the results, which have been described in detail in the previous chapters:

- **Appropriate chromophor.** By the choice of LOPPs and adjustment of the oligomer length to n = 4 phenylene units, a structural motif for the organic emitter was found, that provides narrow and strong optical transitions in the region of the ZnO emission as well as a high PL quantum yield.

- **Site selective functionalization.** Site selective functionalization of the non-equivalent methylene bridges was demonstrated for different substituents. It was shown, that formally each of the non-equivalent methyl groups in **L4P** can subsequently be replaced by spirobifluorene units or by fluorine substituents. To replace two or four methyl groups, the ketones **L4P-O** and **L4P-O2** are the key intermediates. It is worth mentioning, that the synthesis of the former one was achieved by unusual protection of the ketone in the bridging step. However, to substitute all six methyl groups, a modular route could not be developed and the derivatives were produced via very specific ways.

- **Inertness.** The issue of inertness was elaborated far more than initially planned, since photodegradation turned out to be a serious problem at the beginning of the investigations. Degradation studies on **L4P** in solution showed that in $CHCl_3$ or CH_2Cl_2 relatively rapid aromatic formylation can occur, in other solvents autocatalytic formation of singlet oxygen was identified as the main source of degradation. Furthermore, considerations of the optical properties of the model compounds **L4P-O** and **L4P-O2** revealed, that the yellow-to-green defect emission in LOPPs can not be explained by the fluorenone defect alone.
  In degradation studies on 2,7-diphenylfluorenes it turned out, that the photochemistry is very much dependent on the substituent in the methylene bridge, which concerns both the reaction rates as well as the reaction mechanism and the final products.

- **Energy level alignment.** Tuning of the energy levels in the organic part of HIOS is in principle possible. By introducing fluorine substituents in the methylene bridges, an overall shift of the frontier orbital energies of about 1 eV was observed in a series of **L4P**, **L4P-F2**, **L4P-F4**, and **L4P-F6**. However, the optical properties of these compounds are not favorable.

- **Vacuum processing and layer formation.** All derivatives throughout this work having the term '**L4P**' in the label, have been proven to undergo sublimation without or nearly without degradation. The growth on oxide surfaces can

be influenced by introduction of spirobifluorene units from crystalline islands (**L4P**) to smooth layers (**L4P-sp3**).

- **Spectral overlap.** The absorption of **L4P** and the PL of the ZnO QW overlap very well. But with every additional spirobifluorene unit, the optical transitions are shifted to slightly lower energies. To overcome this problem, an on-purpose synthesis for the 'bent' ***iso*-L4P** was developed.
- **Molecular orientation.** There are only very preliminary studies about the structure of different L4Ps on surfaces, which are not discussed here, but a large number of single crystal X-ray structures was generated. These revealed surprising deviations from the ideal structure (planar π-system) of the spiro-L4Ps, as well as polymorphism for different methods of crystallization. For the fluorinated derivatives some conclusions about the intermolecular interactions could be made.

According to the preceding list, most of the issues presented in the beginning have in principle been solved or a better understanding was gained, as for example in the case of photodegradation. In early stages of this work the focus was mainly on the optimization of one specific property, for example the optical gap or the absolute position of the frontier orbital energies. However, it turned out that optimization of one property may lead undesired effects in the other properties of importance. For example the introduction of fluorine in the methylene bridge leads to a lowering of the frontier orbital energies, but the optical properties and the inertness towards photochemical degradation suffer. On the other hand, by introduction of the spirobifluorene units both inertness and processability were improved. Furthermore the unwanted red-shift was compensated by the 'bent' ***iso*-L4P** structure.

Some of the derivatives have also successfully been integrated in HIOS to demonstrate efficient inorganic-to-organic energy transfer and light emission, as well as strong coupling and laser action. It is now a crucial issue to extend this concept to electrically pumped quantum wells, which might also consist of other inorganic semiconductors. In that case, the knowledge, which was gained here can be utilized for target-oriented development of organic emitters for the respective materials. Apart from that, the potential for coupling with ZnO has not yet fully been exploited, as the last generation of L4Ps (namely *iso*-L4Ps) have not been employed in hybrid structures.
In addition, the molecular structures can further be developed. Tuning of the energy levels without influencing the optical properties is still an interesting topic both from scientific point of view, as well as towards applications. The optical properties of the fluorinated L4Ps in the solid state and in solution are currently under investigation by means of time resolved PL and quantum chemical calculations. Insight from this analysis may lead to improved molecular design. In another attempt L4P-structures are being developed, that carry the acceptor groups in a different symmetry (see structure **3** in figure 8.1). The introduction of trifluoromethyl groups into aromatic positions of **L4P** without the creation of a dipole over the molecule might lead to a reduction of the frontier orbital energies while conserving the optical properties. The synthesis of structures that are as electron deficient leads to

normally unexpected side reactions or in some cases to very low reactivity, however diketone **1** could be synthesized and can among others be reacted to **3**. Unfortunately the product mixture could not yet be separated to analyze the final product. Another project is the covalent linkage of L4Ps on oxide surfaces, for example by carboxylic or phosphonic acids (labeled as AG in **4**), to control the orientation of the molecules with respect to the surface or to create stable thin films. To keep the synthetic routes versatile, a modular approach was chosen. The surface-binding group should be connected to the core of the molecule via an alkyl spacer of variable length, which is connected to a binding site at the molecule. A (phenolic) alcohol was chosen as binding site, which can be reacted in an ether synthesis and which is protected as methyl ether through the synthesis of the core. These groups can either be connected to the ends of the *p*-phenylene (**4** in figure 8.1) or to the spirobifluorene units synthesized from a keto-L4P and an appropriate bisphenol derivative.

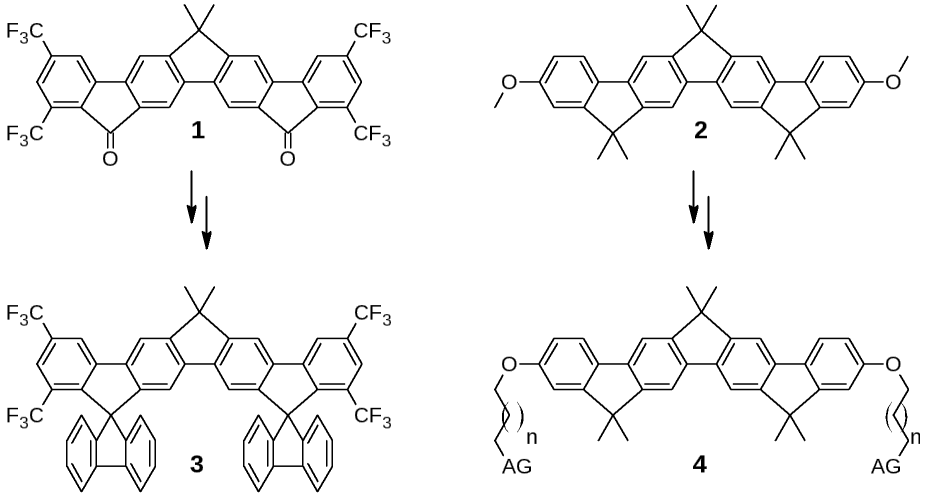

Figure 8.1. Structures for further optimization of L4Ps for HIOS.

Literature

[1] J. C. Maxwell, *Phil. Trans. R. Soc. Lond.* **1865**, *155*, 459 –512.

[2] H. Hertz, *Ann. Phys.* **1888**, *270*, 551 –569.

[3] A. Einstein, *Ann. Phys.* **1905**, *322*, 132 –148.

[4] D. Giulini, N. Straumann, *Physikalische Blätter* **2000**, *56*, 37 –41.

[5] B. Valeur, *Molecular Fluorescence - Principles and Applications*, Wiley-VCH, Weinheim, **2001**, Chapter 2, 3.

[6] P. W. Atkins, *Physikalische Chemie*, Wiley-VCH, Weinheim, 3rd ed., **2001**, Chapter 16.1.

[7] S.-S. Sun in *Introduction to Organic Electronic and Optoelectronic Materials and Devices*, CRC Press, Boca Raton, **2008**, Chapter 3.

[8] C. K. Chiang, C. B. Fincher Jr., Y. W. Park, A. J. Heeger, H. Shirakawa, E. J. Louis, S. C. Gau, A. G. MacDiarmid, *Pys. Rev. Lett.* **1977**, *39*, 1098 –1101.

[9] H. Shirakawa, E. J. Lois, A. G. MacDiarmid, C. K. Chiang, A. J. Heeger, *J.C.S. Chem. Comm* **1977**, *578 - 580.*

[10] C. K. Chiang, A. Druy, S. C. Gau, A. J. Heeger, E. J. Louis, A. G. MacDiarmid, Y. W. Park, H. Shirakawa, *J. Am. Chem. Soc.* **1978**, *100*, 1013 –1015.

[11] R. F. Service, *Science* **1997**, *278*, 383 –384.

[12] J. A. Rogers, Z. Bao, K. Baldwin, A. Dodabalapur, B. Crone, V. R. Raju, V. Kuck, H. Katz, K. Amundson, J. Ewing, P. Drzaic, *P. Natl. Acad. Sci.* **2001**, *98*, 4835 –4840.

[13] S. R. Forrest, *Nature* **2004**, *428*, 911 –918.

[14] G. H. Gelinck, H. E. A. Huitema, E. van Veenendaal, E. Cantatore, L. Schrijnemakers, J. B. P. H. van der Putten, T. C. T. Genus, M. Beenhakkers, J. B. Giesbers, B.-H. Huisman, E. J. Meijer, E. M Benito, F. J. Touwslager, A. W. Marsman, B. J. E. van Rens, D. M. de Leeuw, *Nat. Mat.* **2004**, *3*, 106 –110.

[15] M. H. Lee, S. M. Seop, J. S. Kim, J. H. Hwang, H. J. Shin, S. K. Cho, K. W. Min, W. K. Kwak, S. I. Jung, C. S. Kim, W. S. Choi, S. C. Kim, E. J. Yoo, *SID Symposium Digest of Technical Papers* **2009**, *40*, 802 –804.

[16] *Organic Electronics, Materials, Processing, and Devices*, (Ed.: F. So), CRC Press, Boca Raton, **2010**.

[17] L. S. Miller in *Electronic Materials - From Silicon to Organics*, (Eds.: L. S. Miller, J. B. Mullin), Plenum Press, New York, **1991**, Chapter 2.

[18] A. Barr in *Electronic Materials - From Silicon to Organics*, (Eds.: L. S. Miller, J. B. Mullin), Plenum Press, New York, **1991**, Chapter 3.

[19] L. S. Miller in *Electronic Materials - From Silicon to Organics*, (Eds.: L. S. Miller, J. B. Mullin), Plenum Press, New York, **1991**, Chapter 5.

[20] T. U. Kampen, *Low Molecular Weight Organic Semiconductors*, Wiley-VCH, Weinheim, **2010**, Chapter 2.

[21] R. R. Søndergaard, M. Hösel, F. C. Krebs, *J. Polym. Sci. Pol. Phys.* **2013**, *51*, 16 –34.

[22] A. J. Moulé, K. Meerholz, *Adv. Mater.* **2008**, *20*, 240 –245.

[23] H. N. Tsao, K. Müllen, *Chem. Soc. Rev.* **2010**, *39*, 2372 –2386.

[24] J. S. Brooks, *Chem. Soc. Rev.* **2010**, *39*, 2667 –2694.

[25] R. E. Martin, F. Diederich, *Angew. Chem. Int. Ed.* **1999**, *38*, 1350 –1377.

[26] H. Meier, U. Stalmach, H. Kolshorn, *Acta Polymer.* **1997**, *48*, 379 –384.

[27] D. J. Walton in *Electronic Materials - From Silicon to Organics*, (Eds.: L. S. Miller, J. B. Mullin), Plenum Press, New York, **1991**, Chapter 30.

[28] P. M. Beaujuge, J. M. J. Fréchet, *J. Am. Chem. Soc.* **2011**, *133*, 20009 – 20029.

[29] A. Pron, P. Gawrys, M. Zagorska, D. Djurado, R. Demadrille, *Chem. Soc. Rev.* **2010**, *39*, 2577 –2632.

[30] A. Tsumura, H. Koezuka, T. Ando, *Appl. Phys. Lett.* **1986**, *49*, 1210 –1212.

[31] H. Klauk, *Chem. Soc. Rev.* **2010**, *39*, 2643 –2666.

[32] B. Kippelen, J.-L. Brédas, *Energy Environ. Sci.* **2009**, *2*, 251 –261.

[33] K. Glaser, A. Pütz, J. Mescher, D. Bahro, A. Colsmann in *Organic Photovoltaics*, (Eds.: C. Brabec, U. Scherf, V. Dyakonov), Wiley-VCH, Weinheim, 2nd ed., **2014**, Chapter 14.

[34] B. O'Regan, M. Grätzel, *Nature* **1991**, *353*, 737 –740.

[35] M. Pagliaro, G. Palmisano, R. Ciriminna, *Flexible Solar Cells*, Wiley-VCH, Weinheim, **2008**, Chapter 5.

[36] J. Weickert, L. Schmidt-Mende in *Organic Photovoltaics*, (Eds.: C. Brabec, U. Scherf, V. Dyakonov), Wiley-VCH, Weinheim, 2nd ed., **2014**, Chapter 15.

[37] A. W. Nelson in *Electronic Materials - From Silicon to Organics*, (Eds.: L. S. Miller, J. B. Mullin), Plenum Press, New York, **1991**, Chapter 7.

[38] C. W. Tang, S. A. VanSlyke, *Apl. Phys. Lett.* **1987**, *51*, 913 –915.

[39] J. H. Burroughes, D. D. C. Bradley, A. R. Brown, R. N. Marks, K. Mackay, R. H. Friend, P. L. Burns, A. B. Holmes, *Nature* **1990**, *347*, 539 –541.

[40] G. Gustafsson, Y. Cao, G. M. Treacy, F. Klavetter, N. Colaneri, A. J. Heeger, *Nature* **1992**, *357*, 477 –479.

[41] X. Gong, D. Moses, A. J. Heeger in *Organic Light-Emitting Devices*, (Eds.: K. Müllen, U. Scherf), Wiley-VCH, Weinheim, **2006**, Chapter 4.

[42] M.-K. Fung, C.-S. Lee, S.-T. Lee in *Organic Light-Emitting Devices*, (Eds.: K. Müllen, U. Scherf), Wiley-VCH, Weinheim, **2006**, Chapter 5.

[43] Y. Shirota in *Organic Light-Emitting Devices*, (Eds.: K. Müllen, U. Scherf), Wiley-VCH, Weinheim, **2006**, Chapter 7.

[44] H. Yersin, W. J. Finkenzeller in *Highly Efficient OLEDs with Phosphorescent Materials*, (Ed.: H. Yersin), Wiley-VCH, Weinheim, **2008**, Chapter 1.

[45] X.-H. Yang, F. Jaiser, D. Neher in *Highly Efficient OLEDs with Phosphorescent Materials*, (Ed.: H. Yersin), Wiley-VCH, Weinheim, **2008**, Chapter 6.

[46] V. M. Agranovich, Y. N. Gartstein, M. Litinskaya, *Chem. Rev.* **2011**, *111*, 5179 –5214.

[47] B. Valeur, *Molecular Fluorescence - Principles and Applications*, Wiley-VCH, Weinheim, **2001**, Chapter 4.

[48] V. M. Agranovich, D. M. Basko, G. C. La Rocca, F. Bassani, *Synth. Met.* **2001**, *116*, 349 –351.

[49] S. Blumstengel, S. Sadofev, C. Xu, J. Puls, F. Henneberger, *Phys. Rev. Lett.* **2007**, *97*, 237401.

[50] S. Blumstengel, S. Sadofev, C. Xu, J. Puls, R. L. Johnson, H. Glowatzki, N. Koch, F. Henneberger, *Phys. Rev. B* **2008**, *77*, 085323.

[51] G. Itskos, G. Heliotis, G. Lagoudakis, J. Lupton, N. P. Barradas, E. Alves, S. Pereira, I. M. Watson, M. D. Dawson, J. Feldmann, R. Murray, D. D. C. Bradley, *Phys. Rev. B* **2007**, *76*, 035344.

[52] J. J. Rindermann, G. Pozina, B. Monemar, L. Hultman, H. Amano, P. G. Lagoudakis, *Phys. Rev. Lett.* **2011**, *107*, 236805.

[53] R. Smith, B. Liu, J. Bai, T. Wang, *Nano Lett.* **2013**, *13*, 3042 –3047.

[54] T. N. Lin, L. T. Huang, G. W. Shu, C. T. Yuan, J. L. Shen, C. A. J. Lin, W. H. Chang, C. H. Chiu, D. W. Lin, C. C. Lin, H. C. Kuo, *Opt. Lett.* **2013**, *38*, 2897 –2899.

[55] R. M. Smith, B. Liu, J. Bai, T. Wang, *Apl. Phys. Lett.* **2014**, *105*, 171111.

[56] M. Achermann, M. A. Petruska, D. D. Koleske, M. H. Crawford, V. I. Klimov, *Nano Lett.* **2006**, *6*, 1396 –1400.

[57] H. M. Nguyen, O. Seitz, W. Peng, Y. N. Gartstein, Y. J. Chabal, A. V. Malko, *ACS Nano* **2012**, *6*, 5574 –5582.

[58] K. Ema, M. Inomata, Y. Kato, H. Kunugita, *Phys. Rev. Lett.* **2008**, *100*, 257401.

[59] M. Tabachnyk, B. Ehrler, S. Gélinas, M. L. Böhm, B. J. Walker, K. P. Musselman, N. C. Greenham, R. H. Friend, A. Rao, *Nat. Mater.* **2014**, *13*, 1033 –1038.

[60] S. Blumstengel, H. Glowatzki, S. Sadofev, N. Koch, S. Kowarik, J. P. Rabe, F. Henneberger, *Phys. Chem. Chem. Phys.* **2010**, 11642 –11646.

[61] A. Janotti, C. G. Van de Walle, *Rep. Prog. Phys.* **2009**, *72*, 126501.

[62] H. Sawada, R. Wang, A. W. Sleight, *J. Solid State Chem.* **1996**, *122*, 148 –150.

[63] R. G. Gordon, *MRS Bulletin* **2000**, 52 –57.

[64] T. Minami, *Semicond. Sci. Technol.* **2005**, *20*, S35 –S44.

[65] S. Sadofev, S. Blumstengel, J. Cui, J. Puls, S. Rogaschewski, P. Schäfer, Y. G. Sadofyev, F. Henneberger, *Apl. Phys. Lett.* **2005**, *87*, 091903.

[66] S. Blumstengel, S. Sadofev, F. Henneberger, *New J. Phys.* **2008**, *10*, 065010.

[67] A. C. Grimsdale, K. Müllen, *Macromol. Rapid Commun.* **2007**, *28*, 1676 – 1702.

[68] U. Scherf, K. Müllen, *Makromol. Chem. Rapid Commun.* **1991**, *12*, 489 –497.

[69] U. Scherf, K. Müllen, *Synthesis* **1992**, 23 –38.

[70] J. Grimme, U. Scherf, *Macrornol. Chem. Phys.* **1996**, *197*, 2297 –2304.

[71] J. Jacob, S. Sax, M. Gaal, E. J. W. List, A. C. Grimsdale, K. Müllen, *Macromolecules* **2005**, *38*, 9933 –9938.

[72] N. Cocherel, C. Poriel, J. Rault-Berthelot, F. Barrière, N. Audebrand, A. M. Z. Slawin, L. Vignau, *Chem. Eur. J.* **2008**, *14*, 11328 –11342.

[73] H. Usta, A. Facchetti, T. J. Marks, *Org. Lett* **2008**, *10*, 1385 –1388.

[74] J. Rissler, H. Bässler, F. Gebhard, P. Schwerdtfeger, *Phys. Rev. B* **2001**, *64*, 045122.

[75] T. Pauck, H. Bässler, J. Grimme, U. Scherf, K. Müllen, *Chem. Phys.* **1996**, *210*, 219 –227.

[76] E. J. W. List, J. Partee, J. Shinar, U. Scherf, K. Müllen, E. Zojer, W. Graupner, G. Leising, *Synth. Met.* **2000**, *111 - 112*, 509 –513.

[77] G. Leising, S. Tasch, C. Brandstätter, W. Graupner, S. Hampel, E. J. W. List, F. Meghdadi, C. Zenz, P. Schlichting, U. Rohr, Y. Geerts, U. Scherf, K. Müllen, *Synth. Met.* **1997**, *91*, 41 –47.

[78] B. Kobin, L. Grubert, S. Blumstengel, F. Henneberger, S. Hecht, *J. Mater. Chem.* **2012**, *22*, 4383 –4390.

[79] B. Kobin, Diploma thesis, Humboldt-Universität zu Berlin, **2011**.

[80] S. Forrest, *Chem. Rev.* **1997**, *97*, 1793 –1896.

[81] Y. Ohmori, T. Tsukagawa, H. Kajii, *Displays* **2001**, *22*, 61 –64.

[82] R. Resel, *J. Phys.: Condens. Matter* **2008**, *20*, 184009.

[83] A. C. Grimsdale, K. Müllen, *Adv. Polym. Sci.* **2008**, *212*, 1 –48.

[84] J. Grimme, M. Kreyenschmidt, F. Uckert, K. Müllen, U. Scherf, *Adv. Mater.* **1995**, *7*, 292 –295.

[85] F. Schindler, J. Jacob, A. C. Grimsdale, U. Scherf, K. Müllen, J. M. Lupton, J. Feldmann, *Angew. Chem. Int. Ed.* **2005**, *44*, 1520 –1525.

[86] Q. Zheng, S. K. Gupta, G. S. He, L.-S. Tan, P. N. Prasad, *Adv. Funct. Mater.* **2008**, *18*, 2770 –2779.

[87] Q. Zheng, B. J. Jung, J. Sun, H. E. Katz, *J. Am. Chem. Soc.* **2010**, *132*.

[88] M. Kimura, C. Hosokawa, M. Funahashi, Aromatic Amine Derivative and Electroluminescence Device Utilizing the same, Patent, EP 1860097 A1, **2007**.

[89] K. Brunner, A. van Dijken, H. Börner, J. J. A. M. Bastiaansen, N. M. M. Kiggen, B. M. W. Langeveld, *J. Am. Chem. Soc.* **2004**, *126*, 6035 –6042.

[90] J. Ipaktschi, R. Hosseinzadeh, P. Schlaf, E. Dreiseidler, R. Goddard, *Helv. Chim. Acta* **1998**, *81*, 1821 –1834.

[91] Y. S. ans W. Xu, D. Zhu, *Tetrahedron Lett.* **2010**, *51*, 4894 –4897.

[92] C.-S. Li, Y.-H. Tsai, W.-C. Lee, W.-J. Kuo, *J. Org. Chem.* **2010**, *75*, 4004 –4013.

[93] S. Kajigaeshi, T. Kadowaki, A. Nishida, S. Fujisaki, *Bull. Chem. Soc. Jpn.* **1986**, *59*, 97 –103.

[94] J. H. Markgraf, B. Y. Choi, *Synth. Commun.* **1999**, *29*, 2405–2411.

[95] L. Lafferentz, F. Ample, H. Yu, S. Hecht, C. Joachim, L. Grill, *Science* **2009**, *323*, 1193 –1197.

[96] N. I. Nijegorodov, W. S. Downey, M. B. Danailov, *Spectrochimica Acta Part A* **2000**, *56*, 783 –795.

[97] J. B. Birks, *Photophysics of Aromatic Molecules*, Wiley, London, **1970**.

[98] G. G. Guilbault, *Practical Fluorescence*, Marcel Dekker, New York, **1973**.

[99] I. B. Berlman, *Handbook of Fluorescence Spectra of Aromatic Molecules*, Academic Press, New York, **1971**.

[100] J. R. Lakowicz, *Principles of Fluorescence Spectroscopy*, Kluwer, 2nd ed., **1999**.

[101] C. Chi, G. Wegner, *Macromol. Rapid Commun.* **2005**, *26*, 1532 –1537.

[102] J. Rault-Berthelot, J. Simonet, *J. Electroanal. Chem.* **1985**, *182*, 187 –192.

[103] R. Resel, M. Oehzelt, O. Lengyel, T. Haber, T. Schülli, A. Thierry, G. Hlawacekd, C. Teichert, S. Berkebile, G. Koller, M. Ramsey, *Surf. Sci.* **2006**, *600*, 4645 –4649.

[104] B. Kobin, L. Grubert, S. Mebs, B. Braun, S. Hecht, *Isr. J. Chem.* **2014**, *54*, 789 –795.

[105] P. Kirsch, *Modern Fluoroorganic Chemistry*, Wiley-VCH, Weinheim, **2004**.

[106] P. W. Miller, N. J. Long, R. Vilar, A. D. Gee, *Angew. Chem. Int. Ed.* **2008**, *47*, 8998 –9033.

[107] S. M. Ametamey, M. Honer, P. A. Schubiger, *Chem. Rev.* **2008**, *108*, 1501 –1516.

[108] F. Hof, D. M. Scofield, W. B. Schweizer, F. Diederich, *Angew. Chem. Int. Ed.* **2004**, *43*.

[109] H.-J. Schneider, *Chem. Sci.* **2012**, *3*, 1381 –1394.

[110] K. Reichenbächer, H. I. Süss, J. Hulliger, *Chem. Soc. Rev.* **2005**, *34*, 22 –30.

[111] Y. Sakamoto, T. Suzuki, M. Kobayashi, Y. Gao, Y. Fukai, Y. Inoue, F. Sato, S. Tokito, *J. Am. Chem. Soc* **2004**, *126*, 8138 –8140.

[112] H. Pinto, R. Jones, J. P. Goss, P. R. Briddon, *J. Phys. Condens. Matter* **2009**, *21*, 402001.

[113] K.-F. Braun, S. W. Hla, *J. Chem. Phys.* **2008**, *129*, 064707.

[114] K. Ohkubo, Y. Sakamoto, T. Suzuki, T. Tsuzuki, D. Kumaki, S. Tokito, *Chem. Eur. J.* **2008**, *14*, 4472 –4474.

[115] Y. Ie, M. Nitani, Y. Aso, *Chem. Lett.* **2007**, *36*, 1326 –1327.

[116] S. C. Sondej, J. A. Katzenellenbogen, *J. Org. Chem.* **1986**, *51*, 3508 –3513.

[117] B. Kobin, F. Bianchi, S. Halm, J. Leistner, S. Blumstengel, F. Henneberger, S. Hecht, *Adv. Funct. Mater.* **2014**, *24*, 7717 –7727.

[118] B. A. Haag, C. Sämann, A. Jana, P. Knochel, *Angew. Chem. Int. Ed.* **2011**, *50*, 7290 –7294.

[119] H. G. O. Becker, W. Berger, G. Domschke, *Organikum*, *Vol. 20*, Wiley-VCH, Weinheim, **1999**, p. 352.

[120] A. L. Spek, *Acta Cryst. D* **2009**, *D65*, 148 –155.

[121] J. Pommerehne, H. Vestweber, W. Guss, R. F. Mahrt, H. Bässler, M. Porsch, J. Daub, *Adv. Mater* **1995**, *7*, 551 –554.

[122] B. Milián-Medina, S. Varghese, R. Ragni, H. Boerner, E. Ortí, G. M. Farinola, J. Gierschner, *J. Chem. Phys.* **2011**, *135*, 124509.

[123] B. M. Medina, D. Beljonne, H.-J. Egelhaaf, J. Gierschner, *J. Chem. Phys.* **2007**, *126*, 111101.

[124] G. M. Sheldrick, *Acta Cryst.* **2008**, *A64*, 112 –122.

[125] I. B. Berlman, *Handbook of Fluorescence Spectra of Aromatic Molecules*, Academic Press, New York, **1965**.

[126] B. Valeur, *Molecular Fluorescence - Principles and Applications*, Wiley-VCH, Weinheim, **2001**, Chapter 6.

[127] J. R. Lakowicz, *Principles of Fluorescence Spectroscopy*, Springer, 3rd ed., **2006**.

[128] *Organic Light Emitting Devices*, (Eds.: K. Müllen, U. Scherf), Wiley-VCH, Weinheim, **2006**.

[129] R. H. Friend, R. W. Gymer, A. B. Holmes, J. H. Burroughes, R. N. Marks, C. Taliani, D. D. C. Bradley, D. A. D. Santos, J. L. Brédas, M. Logdlund, W. R. Salaneck, *Nature* **1999**, *397*.

[130] J. Huber, K. Müllen, J. Salbeck, H. Schenk, U. Scherf, T. Stehlin, R. Stern, *Acta Polymer.* **1994**, *45*, 244 –247.

[131] U. Scherf, E. J. W. List, *Adv. Mater.* **2002**, *14*, 477 –487.

[132] S. Gamerith, C. Gadermaier, U. Scherf, E. J. W. List in *Physics of Organic Semiconductors*, (Ed.: W. Brütting), Wiley-VCH, Weinheim, **2005**, Chapter 6, pp. 153 –181.

[133] S. Gamerith, C. Gadermaier, U. Scherf, E. J. W. List, *Phys. Status Solidi* **2004**, *201*, 1132 –1151.

[134] V. N. Bliznyuk, S. A. Carter, J. C. Scott, G. Klärner, R. D. Miller, D. C. Miller, *Macromolecules* **1999**, *32*, 361 –369.

[135] E. Zojer, A. Pogantsch, E. Hennebicq, D. Beljonne, J.-L. Brédas, P. Scandiucci de Freitas, U. Scherf, E. J. W. List, *J. Chem. Phys.* **2002**, *117*, 6794 –6802.

[136] E. J. W. List, R. Guentner, P. Scandiucci de Freitas, U. Scherf, *Adv. Mater.* **2002**, *14*, 374 –378.

[137] J. M. Lupton, M. R. Craig, E. W. Meijer, *Appl. Phys. Lett.* **2002**, *80*, 4489 –4491.

[138] S. I. Hintschich, C. Rothe, S. Sinha, A. P. Monkman, P. Scandiucci de Freitas, U. Scherf, *J. Chem. Phys.* **2003**, *119*, 12017 –12022.

[139] M. Sims, D. D. C. Bradley, M. Ariu, M. Koeberg, A. Asimakis, M. Grell, D. G. Lidzey, *Adv. Func. Mater.* **2004**, *14*, 765 –781.

[140] C. Gadermaier, L. Romaner, T. Piok, E. J. W. List, B. Souharce, U. Scherf, G. Cerullo, G. Lanzani, *Phys. Rev. B* **2005**, *72*, 045208.

[141] C. Chi, C. Im, V. Enkelmann, A. Ziegler, G. Lieser, G. Wegner, *Chem. Eur. J.* **2005**, *11*, 6833 –6845.

[142] K. Becker, J. M. Lupton, J. Feldmann, B. S. Nehls, F. Galbrecht, D. Gao, U. Scherf, *Adv. Funct. Mater.* **2006**, *16*, 364 –370.

[143] C. Chi, C. Im, G. Wegner, . *Chem. Phys.* **2006**, *124*, 024907.

[144] Y.-S. Wu, J. Li, X.-C. Ai, L.-M. Fu, J.-P. Zhang, Y.-Q. Fu, J.-J. Zhou, L. Li, Z.-S. Bo, *J. Phys. Chem. A* **2007**, *111*, 11473 –11479.

[145] J. Kang, J. Jo, Y. Jo, S. Y. Lee, P. E. Keivanidis, G. Wegner, D. Y. Yoon, *Polymer* **2008**, *49*, 5700 –5704.

[146] S. Kappaun, H. Scheiber, R. Trattnig, E. Zojer, E. J. W. List, C. Slugovc, *Chem. Commun.* **2008**, 5170 –5172.

[147] W. Graupner, M. Sacher, M. Graupner, C. Zenz, G. Grampp, A. Hermetter, G. Leising in *Electrical, Optical, and Magnetic Properties of Organic Solid-State Materials IV*, (Eds.: J. R. Reynolds, A. K.-Y. Jen, M. F. Rubner, L. Y. Chiang, L. R. Dalton), Materials Research Society, Warrendale, PA, **1998**, p. 789.

[148] E. J. W. List, J. Partee, J. Shinar, U. Scherf, K. Müllen, E. Zojer, K. Petritsch, G. Leising, W. Graupner, *Phys. Rev. B* **2000**, 10807 –10814.

[149] L. Liu, S. Qiu, B. Wang, W. Zhang, P. Lu, Z. Xie, M. Hanif, Y. Ma, J. Shen, *J. Phys. Chem. B* **2005**, *109*, 23366 –23370.

[150] L. Romaner, G. Heimel, H. Wiesenhofer, P. Scandiucci de Freitas, U. Scherf, J.-L. Brédas, E. Zojer, E. J. W. List, *Chem. Mater.* **2004**, *16*, 4667 –4674.

[151] B. W. Zhao, T. Cao, J. M. White, *Adv. Funct. Mater.* **2004**, *14*, 783 –790.

[152] R. Grisorio, G. P. Suranna, P. Mastrorilli, C. F. Nobile, *Adv. Funct. Mater.* **2007**, *17*, 538 –548.

[153] L. Liu, S. Tang, M. Liu, Z. Xie, W. Zhang, P. Lu, M. Hanif, Y. Ma, *J. Phys. Chem. B* **2006**, *110*, 13734 –13740.

[154] R. Grisorio, G. Allegretta, P. Mastrorilli, G. P. Suranna, *Macromolecules* **2011**, *44*, 7977 –7986.

[155] R. Abbel, M. Wolffs, R. A. A. Bovee, J. L. J. van Dongen, X. Lou, O. Henze, W. J. Feast, E. W. Meijer, A. P. H. J. Schenning, *Adv. Mater.* **2009**, *21*, 597 –602.

[156] G. Goldschmiedt, F. Schranzhofer, *Monatshefte für Chemie* **1895**, *16*, 807 –827.

[157] K. Reimer, F. Tiemann, *Chem. Ber.* **1876**, *9*, 824 –828.

[158] L. Kürti, B. Czakó in, Elsevier, Burlington, San Diego, London, **2005**, p. 378.

[159] N. J. Turro, V. Ramamurthy, J. C. Scaiano, *Modern Molecular Photochemistry of Organic Molecules*, University Science Books, Sausalito, CA, **2010**, Chapter 4.23 - 4.26.

[160] A. G. Griesbeck, T. T. El-Idreesy, W. Adam, O. Krebs in *CRC Handbook of Organic Photochemistry and Photobiology*, (Eds.: W. Horspool, F. Lenci), CRC Press Boca Raton, FL, 2nd ed., **2004**, Chapter 8.

[161] C. S. Foote, *Acc. Chem. Res.* **1968**, *1*, 104 –110.

[162] S. K. W. Ando, *Chem. Commun.* **1978**, 120 –121.

[163] *CRC Handbook of Organic Photochemistry and Photobiology*, (Eds.: W. Horspool, F. Lenci), CRC Press Boca Raton, FL, 2nd ed., **2004**, Chapter 4, 8, 25, 45, 108.

[164] H. Marciniak, M. Teicher, U. Scherf, S. Trost, T. Riedl, M. Lehnhardt, T. Rabe, W. Kowalksy, S. Lochbrunner, *Phys. Rev. B* **2012**, *85*, 214204.

[165] S. M. Fonseca, J. Pina, L. G. Arnaut, J. Seixas de Melo, H. D. Burrows, N. Chattopadhyay, L. Alcácer, A. Charas, J. Morgado, A. P. Monkman, U. Asawapirom, U. Scherf, R. Edge, S. Navaratnam, *J. Phys. Chem. B* **2006**, *110*, 8278 –8283.

[166] N. J. Turro, V. Ramamurthy, J. C. Scaiano, *Modern Molecular Photochemistry of Organic Molecules*, University Science Books, Sausalito, CA, **2010**, Chapter 14.6.

[167] W.-L. Yu, J. Pei, W. Huang, A. J. Heeger, *Adv. Mater.* **2000**, *12*, 828 –831.

[168] S. Setayesh, A. C. Grimsdale, T. Weil, V. E. andK. Müllen, F. Meghdadi, E. J. W. List, G. Leising, *J. Am. Chem. Soc.* **2001**, *123*, 946 –953.

[169] J.-H. Lee, D.-H. Hwang, *Chem. Commun.* **2003**, 2836 –2837.

[170] D.-H. Hwang, M.-J. Park, J.-H. Lee, *Mater. Sci. Eng. C* **2004**, *24*, 201 –204.

[171] D. Vak, C. Chun, C. L. Lee, J.-J. Kim, D.-Y. Kim, *J. Mater. Chem.* **2004**, *14*, 1342 –1346.

[172] Y. Wu, J. Li, Y. Fu, Z. Bo, *Org. Lett.* **2004**, *6*, 3485 –3487.

[173] Y. Wu, J. Zhang, Z. Fei, Z. Bo, *J. Am. Chem. Soc.* **2008**, *130*, 7192 –7193.

[174] *IUPAC. Compendium of Chemical Terminology, 2nd ed. (the "Gold Book")*, (Eds.: Compiled, by A. D. McNaught, A. Wilkinson), Blackwell Scientific Publications, Oxford, **1997**, doi:10.1351/goldbook.S05900.

[175] *IUPAC. Compendium of Chemical Terminology, 2nd ed. (the "Gold Book")*, (Eds.: Compiled, by A. D. McNaught, A. Wilkinson), Blackwell Scientific Publications, Oxford, **1997**, doi:10.1351/goldbook.R05180.

[176] M. D. Barnett, G. H. Daub, F. N. Hayes, D. G. Ott, *J. Am. Chem. Soc.* **1959**, *81*, 4583 –4586.

[177] J. Xu, S. Semin, D. Niedzialek, P. H. J. Kouwer, E. Fron, E. Coutino, M. Savoini, Y. Li, J. Hofkens, H. Uji-I, D. Beljonne, T. Rasing, A. E. Rowan, *Adv. Mater.* **2013**, *25*, 2084 –2089.

[178] C. K. Bradscher, L. Beaver, N. Tokura, *J. Am. Chem. Soc.* **1956**, *78*, 3196 –3198.

[179] H. Mauser, *Formale Kinetik*, Bertelsmann Universitätsverlag, Düsseldorf, **1974**.

[180] H. Mauser, *Formale Kinetik*, Bertelsmann Universitätsverlag, Düsseldorf, **1974**, Chapter 3.

[181] U. Mitschke, P. Bäuerle, *J. Mater. Chem.* **2000**, *10*, 1471 –1507.

[182] L. Liu, S. Qiu, B. Wang, H. Wang, Z. Xie, Y. Ma, *J. Phys. Chem. C* **2009**, *113*, 5799 –5804.

[183] B. Wang, M. Forster, E. Preis, H. Wang, Y. Ma, U. Scherf, *J. Polym. Sci. A: Pol. Chem.* **2009**, *47*, 5137 –5143.

[184] Y. Wu, J. Zhang, Z. Bo, *Org. Lett.* **2007**, *9*, 4435 –4438.

[185] D. Thirion, C. Poriel, J. Rault-Berthelot, F. Barrière, O. Jeannin, *Chem. Eur. J.* **2010**, *16*, 13646 –13658.

[186] D. Thirion, M. Romain, J. Rault-Berthelot, C. Poriel, *J. Mater. Chem.* **2012**, *22*, 7149 –7157.

[187] M. Romain, D. Tondelier, J.-C. Vanel, B. Geffroy, O. Jeannin, J. Rault-Berthelot, R. Métivier, C. Poriel, *Angew. Chem. Int. Ed.* **2013**, *52*, 14147 –14151.

[188] R. G. Clarkson, M Gomberg, *J. Am. Chem. Soc.* **1930**, *52*, 2881 –2891.

[189] T. Kowada, T. Kuwabara, K. Ohe, *J. Org. Chem.* **2010**, *75*, 906 –913.

[190] M. D. Curtis, J. Cao, J. W. Kampf, *J. Am. Chem. Soc.* **2004**, *126*, 4318 –4328.

[191] J. Gierschner, S. Y. Park, *J. Mater. Chem. C* **2013**, *1*, 5818 –5832.

[192] T. Watanabe, K. Ueno, K. Suzuki, Y. Iwasaki (CANON KABUSHIKI KAISHA), Patent, WO 2008/146825, **2008**.

[193] M. Höfner, B. Kobin, S. Hecht, F. Henneberger, *ChemPhysChem* **2014**, 3805 –3808.

[194] F. Bianchi, S. Sadofev, R. Schlesinger, B. Kobin, S. Hecht, N. Koch, F. Henneberger, S. Blumstengel, *Appl. Phys. Lett.* **2014**, *105*, 233301.

[195] R. Schlesinger, F. Bianchi, S. Blumstengel, C. Christodoulou, R. Ovsyannikov, B. Kobin, K. Moudgil, S. Barlow, S. Hecht, S. R. Marder, F. Henneberger, N. Koch, *submitted* **2015**.